2014

Novel Syntheses and Surface Modifications of Electrode Materials for Superior Lithium-Ion Batteries

Jianqing Zhao
Louisiana State University and Agricultural and Mechanical College

NOVEL SYNTHESES AND SURFACE MODIFICATIONS OF ELECTRODE MATERIALS FOR SUPERIOR LITHIUM-ION BATTERIES

A Dissertation

Submitted to the Graduate Faculty of the
Louisiana State University and
Agricultural and Mechanical College
in partial fulfillment of the
requirements for the degree of
Doctor of Philosophy

in

The Department of Mechanical & Industrial Engineering

by
Jianqing Zhao
B.S., Nanjing University of Aeronautics and Astronautics, 2006
M.S., Nanjing University of Aeronautics and Astronautics, 2011
December 2014

ACKNOWLEDGMENTS

My first sincere expression of gratitude must go to my advisor, Prof. Ying Wang, for her patient and continuous provision of the insight, encouragement, advice and experience necessary for me to proceed through the doctoral program. An undertaking of my PhD program cannot be easily progressed without her supervision and instruction.

I greatly appreciate my committee numbers, Prof. Wenjin Meng, Prof. Guoqiang Li, and Prof. Dorel Moldovan for their support, guidance and useful suggestions. With their help I can carry out my research effectively and efficiently.

Special thanks give to my collaborators, Saad Aziz, Hilary Eikhuemelo, Zhiqiang Xie, Guoying Qu, Boliang Zhang, Yiying Yue, Sarah Ellis, Prof. John Flake, Prof. Shengmin Guo, Prof. Qinglin Wu and Prof. Kerry Dooley at Louisiana State University (LSU); Ruiming Huang, Yuan Chen, M. Reza Khoshi, Prof. Huixin He and Prof. Jenny Lockard at Rutgers-Newark, The State University of New Jersey; Wenpei Gao and Prof. Jian-Min Zuo at University of Illinois at Urbana-Champaign; Dr. Xiao Feng Zhang at Hitachi High Technologies America, Inc.; and Prof. Scott T. Misture at Alfred University. I also want to thank Prof. Rongying Jin's groups for experimental assistances, and Dr. Dongmei Cao in Materials Characterization Center, Dr. Ying Xiao in the Department of Biological Science and Dr. Xiaochu Wu in the School of Veterinary Medicine for their assistance in facility use, and my labmates, Xinning Luan and Dongsheng Guan at LSU. I would like to acknowledge the financial support from ME Scholarship (LSU), ME One-Time Enhancement Award (LSU), Graduate Student Travel Award (LSU), and ECS Student Travel Grant Award from the Battery Division in The Electrochemical Society.

There are many challenges in life. You choose for yourself, and others are fully trusted upon you. Particular acknowledgments belong to my parents, Ms. Jie Li and all my friends for their love, support and understanding in dealing with all the challenges I have faced.

TABLE OF CONTENTS

LIST OF FIGURES

LIST OF TABLES

LIST OF ABBREVIATIONS

ALD	Atomic layer deposition
CV	Cyclic Voltammetry
DEZ	Diethylzinc, $Zn(CH_2CH_3)_2$
EIS	Electrochemical impedance spectroscopy
EDS	Energy dispersive spectroscopy
FESEM	Field emission scanning electron microscopy
HRTEM	High-resolution transmission electron microscopy
LMNCO	$Li[Li_{0.2}Mn_{0.54}Ni_{0.13}Co_{0.13}]O_2$
PVDF	Polyvinylidene fluoride
SAED	Select area electron diffraction
SEI	Solid-electrolyte interphase
SEM	Scanning electron microscope
TEM	Transmission electron microscopy
TMA	Trimethylalumium, $Al(CH_3)_3$
TBAOH	Tetrabutylammonium hydroxide
XPS	X-ray photoelectron spectroscopy
XRD	X-ray diffraction
ZTB	Zirconium tert-butoxide, $Zr(OC(CH_3)_3)_4$

ABSTRACT

Rechargeable lithium-ion battery is one of the most promising energy conversion and storage systems that offers high energy and powder densities, long service life and assuring safety. Performance of lithium-ion batteries crucially relies on electrochemical characteristics of electrode materials, i.e., anode and cathode materials. This dissertation work aims at developing novel electrode materials with high capacity, excellent cycling stability and remarkable rate capability for next-generation lithium-ion batteries. The effects of surface modifications for $LiMn_2O_4$ cathode materials are studied by depositing ultrathin conformal amphoteric oxides via atomic layer deposition (ALD). In the case of ZnO coating, the thickness of ZnO ALD layers can be finely optimized at atomic scale by varying ALD growth cycles. Six ZnO ALD layers demonstrate to have the optimal thickness (~ 1 nm) for the best electrochemical performance of $LiMn_2O_4$ cathodes either at room temperature or elevated temperature. Furthermore, the effects of crystalline ZrO_2 ALD coating on improving elevated-temperature performance of either micro-sized or nano-sized $LiMn_2O_4$ particles are evaluated.

Other work concentrates on boosting electrochemical performance of Li-excess layered transition metal oxides, which are emerging lithium-ion battery cathode materials with very high theoretical capacities but suffering from drastic initial capacity loss and poor rate capability. To solve these issues, one strategy involves preparing hierarchical functional surface modifications on $Li[Li_{0.2}Mn_{0.54}Ni_{0.13}Co_{0.13}]O_2$ nanoparticles, which consist of nano-sized $LiCoO_2$ shell and sub-nano-sized ZrO_2 ALD coating. The other route is to completely convert Li-excess layered $Li[Li_{0.2}Mn_{0.54}Ni_{0.13}Co_{0.13}]O_2$ to a $Li_4Mn_5O_{12}$-type spinel product via ex-situ ion-exchanges and a post-annealing process. The enhanced electrochemical performance of Li-excess layered cathode materials is achieved from the synergetic effects of ALD oxide coating and core-shell structure, ex-situ layered-to-spinel phase transformation, and nanoarchitecture with high surface area. In addition to cathode materials, multi-shell spherical $Mn_{0.54}Ni_{0.13}Co_{0.13}(CO_3)_{0.8}$ carbonate anode material is synthesized by a hydrothermal approach, which is combined with its lithiated yolk-shell-structured $Li[Li_{0.2}Mn_{0.54}Ni_{0.13}Co_{0.13}]O_2$ cathode for a full battery cell exhibiting excellent electrochemical performance.

CHAPTER 1. INTRODUCTION

1.1 Background and Rationale

The purpose of this chapter is to introduce the essential background and rationale for my PhD research. It starts with an overview of energy supply around the world, since the global energy crisis has promoted rapid development of various energy technologies. The following section provides research background and knowledge related to configuration and work mechanism of rechargeable lithium-ion battery. The criteria for choosing cathode material in lithium-ion battery are also discussed, followed by summarizing characteristics of different cathode materials. Then, surface modifications for enhanced electrochemical performance of cathode materials are reviewed, in which atomic layer deposition method is emphasized since it is an emerging technique for surface modifications on lithium-ion battery electrodes. The chapter is ended with presenting the objective and scope for the whole report.

1.1.1 Overview of energy supply

Increasing consumption of fossil fuels in modern civilization has resulted in many problematic consequences. The unavoidable CO_2 emission and noxious byproducts, including sulfide and nitride resulted from burning fossil fuels, cause many problems such as global warming and air pollution, which are threatening health of human kind and environment of our planet. On the other hand, the supply of fossil fuels is finite, and its distribution is globally uneven [1]. To date, as shown in Figure 1.1, traditional fossil fuels, including coal, gas and oil, are still the primary energy supplies in the world [2,3]. It is urgent to find new and sustainable energy alternatives now. Where will the new energy breakthrough go?

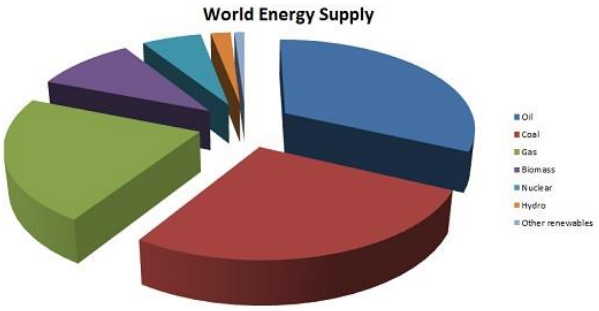

Figure 1.1 Distribution of world energy supply in 2013 [2].

Exploitation and production of renewable energy have been considered as the most promising solution for current energy limitation and crisis. Prospects for nuclear power sources are attractive, but they suffer from potential radiation threat, high operation and maintenance costs, low efficiency and political dependence. Furthermore, whether nuclear energy can be considered as renewable energy is still

under debate. The hydro power has been extensively employed to yield electricity together with tidal and wave energy. The constancy and predictability of water flows allow for controllable utilization of hydro power sources. However, the artificial plug-in hydroelectric power stations may significantly affect diversity of species in the surrounding ecosystem either in rivers or in oceans, which has already caused extinction of numerous living beings. Over the last several decades, research on different energy supply, such as biofuels, geothermal energy and wind power, has attracted tremendous attention and financial support. Particular attention and efforts are also paid to solar power technique, because solar energy from sunshine is endless and abundant. However, to date, these fast-developing energy research fields are limited in large-scale production of energy [4].

One technology that is critical for the future of renewable energy is energy storage, i.e., how to effectively store energy from various renewable energy supplies, which are limited in large-scale production. Governments from different countries have recognized this and responded by increasing research support on developing novel electrochemical devices with high storage capacity and output, high efficiency in energy conversion and long serve life. There are two efficient electrochemical devices, the rechargeable lithium-ion battery and electrochemical supercapacitor, show the promising ability to serve as the clean energy supply for the internal engines in vehicles by offering electricity [5]. The electrochemical technology enables to secure a sustainable energy supply for all need and reduce the further exacerbation on air pollution from the combustion of fossil fuels. In comparison with supercapacitors, the lithium-ion batteries are more preferable due to its higher energy density than that in supercapacitors [6]. Scientists and engineers will together conduct interdisciplinary research to advance the capacity, performance and longevity of lithium-ion batteries. The technology of lithium-ion batteries have been widely regarded as one of the most promising solutions for the ever-fading fossil-fuel energy in the modern society, being capable of providing energy for portable electronics and electric vehicles.

1.1.2 The principle of lithium-ion battery

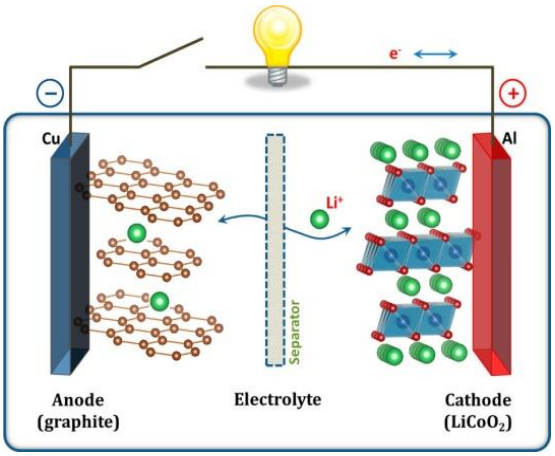

Figure 1.2 Schematic illustration of the lithium-ion battery based on $LiCoO_2/Li^+$ -based electrolyte/graphite [1].

Lithium-ion battery has shown various advantages in terms of high specific capacity and operating voltage, outstanding rate capability and long-term cycling performance, safety, and environmental benignity in comparison with traditional lead-acid battery, nickel-metal hydride battery and nickel-cadmium battery [7]. For example, the operating voltage of $LiCoO_2$-based lithium-ion batteries is ~3.7 V, which is almost three times of that in lead-acid battery. The first commercial rechargeable lithium ion battery was released in 1991 by SONY. Since then, it has rapidly occupied the market as major power sources for portable electronic devices and equipment, and starts to be used as power sources in hybrid electric vehicles and other electric transportations.

Lithium-ion battery is one of the most promising and efficient energy conversion and storage devices. As shown in Figure 1.2, there are three primary functional components in a lithium-ion battery: cathode, anode and electrolyte [8]. The cathode and anode are separated by a separator, immersed in the electrolyte and placed on the current collectors - Cu for anode and Al for cathode. Common cathode materials include $LiCoO_2$, $LiMn_2O_4$, $LiFePO_4$, and $LiMn_{1/3}Co_{1/3}Ni_{1/3}O_2$. Anode materials include graphite, tin-based or silicon-based materials, graphene, and $Li_4Ti_5O_{12}$, and so on. Electrolyte is usually lithium salt, such as $LiPF_6$ and $LiClO_4$, dissolved in organic solvents consisting of ethylene carbonate (EC), dimethyl carbonate (DMC), and diethyl carbonate (DEC), etc. Energy conversion and storage of lithium-ion battery depends on reversible migration of lithium ions between cathode and anode along with simultaneous charge transfer through external circuit. The corresponding reactions in a lithium-ion battery composed of $LiCoO_2$ cathode and graphite anode are described below [8]:

Cathode:

$$LiCoO_2 \underset{Discharge}{\overset{Charge}{\rightleftarrows}} Li_{1-x}CoO_2 + xLi^+ + xe^-$$

Anode:

$$6C + xLi^+ + xe^- \underset{Discharge}{\overset{Charge}{\rightleftarrows}} Li_xC_6$$

Total reactions in battery:

$$LiCoO_2 + 6C \underset{Discharge}{\overset{Charge}{\rightleftarrows}} Li_{1-x}CoO_2 + Li_xC_6$$

During the initial charging, lithium ions are extracted from $LiCoO_2$ cathode; meanwhile, the corresponding lithium ions are inserted into graphite anode. The subsequent discharge reaction occurs through migration of lithium ions from the anode to the cathode. Overall, the specific storage capacity and energy conversion efficiency of lithium-ion battery mainly rely on electrochemical properties of electrode materials.

1.1.3 Cathode materials for lithium-ion battery

Recently, the rapidly increasing demand for electricity-powered vehicles has prompted considerable developments of high-performance lithium-ion batteries

worldwide. The breakthrough as well as the bottleneck of lithium-ion batteries is to design and fabricate novel electrode materials with superior performance. The lithium-silicon (Li-Si) and lithium-tin (Li-Sn) anode materials have provided excellent cycling stability, high rate capability, and high specific capacity with a theoretic capacity of 4000 and 990 mAh/g, respectively. However, the state-of-the-art development of cathode materials in lithium-ion batteries cannot meet the high energy and power densities required for plug-in hybrid electric vehicles (HEVs) and electric vehicles (EVs), since cathode materials usually have much lower capacity than anode materials. Cathode materials for high-performance lithium-ion batteries are subject to the following criteria [9,10]:

1. Chemical and physical availability, and mechanical stability: First of all, lithium-containing compound as the cathode material candidate must be able to be reversibly reduced and oxidized for lithiathion and delithiation. For instance, various transition metal oxides serve as cathode materials for lithium-ion batteries due to their facile reduction and oxidization of transition metals. Secondly, cathode materials are required to have high electronic conductivity and lithium ion diffusion coefficient for fast transfer of lithium ions and electrons in cathodes. Poor conductivity would affect rate capability of cathodes significantly, resulting in low power density and poor cycling performance of lithium-ion batteries. In addition, cathode materials should possess excellent mechanical stability to keep the host structure stable during Li-ion intercalation/deintercalation processes and against corrosion and reaction from electrolyte.
2. High operating voltage and flat voltage plateau: Cathode materials are preferred to have relative high chemical potential vs. lithium metal, which would contribute to high operating voltage of lithium-ion batteries. Furthermore, as power sources of electronic devices and electric vehicles, a flat voltage plateau from cathode materials is necessary.
3. High energy and power densities: Cathode materials should allow a large amount of lithium ions to be inserted and extracted, leading to high specific practical capacity and favorable high-rate performance.
4. Wide applicable temperature range: Due to extensive applications of lithium-ion batteries in different fields with respect to ordinary life, military facilities, transportations and space systems, cathode materials are required to be stable when they are subjected to elevated or low temperatures. For general applications in daily life, the expected range is between 0 ^{o}C and 40 ^{o}C. However, challenging operations come from high-end applications of lithium-ion batteries. For example, lithium-ion batteries in electric vehicles need to withstand elevated temperature above 50 ^{o}C, and those used in space stations may experience temperature amplitude as high as several hundreds of Celsius degrees.
5. Excellent cycling performance: Sophisticated battery engineering, including controlling size and morphology of cathode materials as well as configuration of lithium-ion battery, has almost helped to accomplish maximum capacities of traditional cathode materials during initial electrochemical cycles. However, capacity fading of lithium-ion batteries always takes place during long-term usage.

Hence, commercial applications of lithium-ion batteries require a robust battery system with excellent cycleability of cathode materials to reduce maintenance cost.

6. Low cost and environmental friendliness: These two factors rely on raw materials used for cathode materials. Nontoxic and cheap materials are preferred for large-scale production of cathode materials.
7. Other aspects such as safety, flexibility and microminiaturization of lithium-ion batteries are dependent on syntheses of cathode material and design of battery structure.

Table 1.1 summaries characterisitics of different commercial cathode materials, and detailed information of these materials is described as follows.

Table 1.1 Characteristics of commercial cathode materials

Parameters	Layered $LiCoO_2$	Layered $LiNi_{1/3}Co_{1/3}Mn_{1/3}O_2$	Olivine $LiFePO_4$	Spinel $LiMn_2O_4$
Theoretical capacity (mAh/g)	272	274	170	148
Practical capacity（mAh/g）	135～140	155～165	160～170	100～115
Surface area（m^2/g）	0.4～0.6	0.2～0.4	12～20	0.4～0.8
Operating voltage（V）	3.7	3.5	3.5	3.7
Cycling stability	≥300	≥800	≥2000	≥500
Material sources	Insufficient	Insufficient	Abundant	Sufficient
Cost	Very expensive	Expensive	Very cheap	Cheap
Environmental friendliness	Toxic	Toxic	Nontoxic	Nontoxic
Safety	Poor	Median	Excellent	Outstanding
Applications	Electric devices	Electric devices, HEVs, EVs	Electric devices	Electric devices, HEVs, EVs

1.1.3.1 Layered $LiMO_2$ (M=Co, Ni and Mn)

Figure 1.3 illustrates crystal structure of ideal layered cathode materials, including $LiCoO_2$, $LiNiO_2$, $LiMnO_2$ and $LiNi_{1/3}Co_{1/3}Mn_{1/3}O_2$, within which cations occupy in the 6-coordinated octahedral crystal site formed by oxygen anions. The MO_2 slabs and lithium layers are stacked alternatively [10]. Lithium cobalt oxide ($LiCoO_2$) is a typical material in this series, which was discovered by Goodenough *et al*. in 1979 and has been commercialized as the cathode material in lithium-ion batteries for more than twenty years since being manufactured by SONY 1991 [7,11].

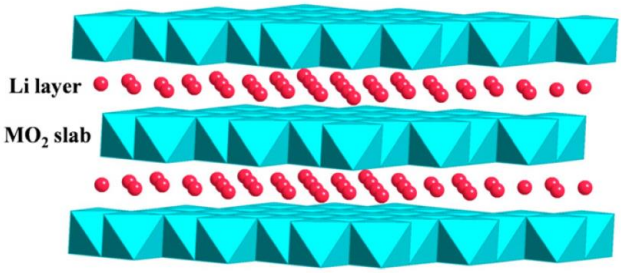

Figure 1.3 Crystal structure of layered $LiMO_2$ [10].

The theoretical capacity of $LiCoO_2$ is 272 mAh/g, but it can only deliver half of its theoretical capacity (~140 mAh/g). Phase transition of $LiCoO_2$ occurs when half of lithium ions are extracted under a charge voltage above 4.2V, leading to significant structural instability, limited capacity and poor cycleability of this material [12]. Moreover, cobalt element in $LiCoO_2$ is toxic and expensive, and has limited resource in the earth, which can cause environmental problems and increased cost for large-scale applications of lithium-ion batteries. Formation of Li–Co–Ni–Mn–O layered compound can be regarded as an effective way to reduce pollution and costs by partial substitution of Co ions with more abundant and environmental friendly Ni and Mn ions [13]. For instance, $LiNi_{1/3}Co_{1/3}Mn_{1/3}O_2$, one of the derivatives from $LiCoO_2$, has been extensively employed in commercial lithium ion batteries.

1.1.3.2 Olivine $LiFePO_4$

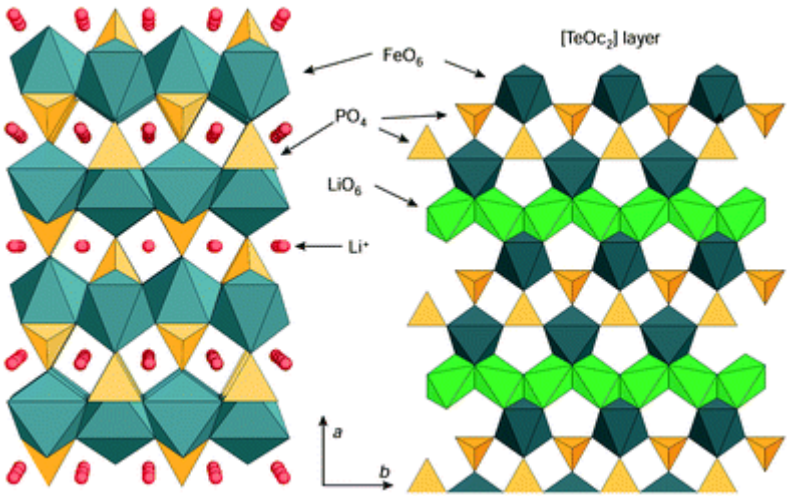

Figure 1.4 Crystal structure of olivine $LiFePO_4$ [14].

The olivine lithium iron phosphate ($LiFePO_4$) as an alternative cathode material was first reported by Padhi *et al*. in 1997 [15]. In comparison with $LiCoO_2$, $LiFePO_4$ shows a higher theoretical capacity of 170 mAh/g, excellent cycling stability, lower cost, and better safety and environmental benignity. The most challenging issue of this material is its extremely poor electronic conductivity in nature, causing poor rate capability at high current densities. Crystal structure of $LiFePO_4$ is composed of LiO_6

and FeO_6 octahedral and PO_4 tetrahedral with the space group Pmna. As shown in Figure 1.4, LiO_6 octahedral share edges to form LiO_6 chains parallel to (111) direction, where one-dimensional lithium ion mobility is high in this framework [8,14]. In order to improve high-rate performance of $LiFePO_4$, many approaches have been investigated to circumvent this main drawback by ameliorating intrinsic character of bulk $LiFePO_4$ or using extrinsic modifications, including metallic cation doping in its crystal [16,17], carbon coating or fabricating a carbonaceous matrix [18-24], mixing with noble metal particles [25] and introducing conductive inorganic compounds [26,27] or organic polymers [28]. Creating large surface area in nano-scale electrode materials can contribute to high-rate capability by shortening the diffusion path of lithium ions and maximizing the interfacial contact between active particles and the surrounding electrolyte [29-31]. The two-phase $LiFePO_4$/C composite has been considered as an optimum structure design by combining host $LiFePO_4$ particles with guest carbon framework into one incorporated entity for lithium ion storage [24]. Overall, improving electronic conductivity and creating high surface area for $LiFePO_4$ are two crucial factors for achieving high energy and power capabilities of lithium-ion batteries.

1.1.3.3 Spinel $LiMn_2O_4$

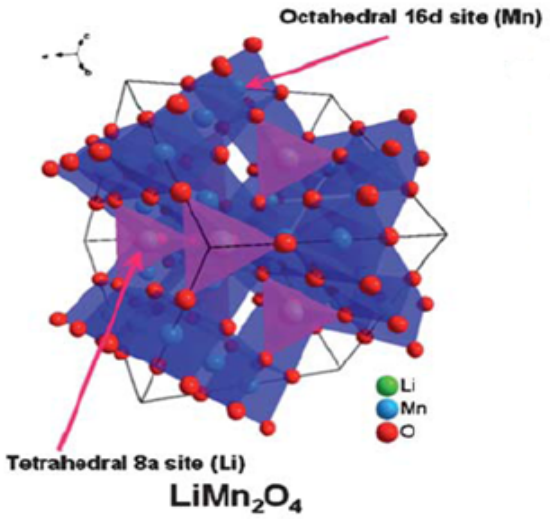

Figure 1.5 Crystal structure of spinel $LiMn_2O_4$ [32].

In 1983, M. Thackeray *et al*. proposed spinel $LiMn_2O_4$ as an alternative cathode material [33]. In comparison with $LiCoO_2$ and $LiFePO_4$, $LiMn_2O_4$ shows outstanding electronic and lithium ion conductivity, and possesses a three-dimensional open structure, contributing to high structural stability and rate capability, respectively. Its spinel structure with space group Fd3-m is shown in Figure 1.5 [32]. The edge-shaped octahedral Mn_2O_4 structure is composed of the face-sharing of tetrahedral lithium (8a) sites and empty octahedral (16c) sites, providing structural stability and a series of intersecting tunnels for facile lithium ion diffusion in three dimensions.

In addition to its remarkable cycleability and rate capability, $LiMn_2O_4$ cathode material also displays various advantages in terms of abundant manganese resource, environmental benignity, safety and cost-effective application for rechargeable lithium ion batteries [32,34-36]. However, significant capacity fading of pristine $LiMn_2O_4$ limits its practical application, especially at elevated temperature. The following three factors - manganese (Mn) element dissolution, phase transition and electrolyte decomposition, contribute to poor capacity retention of $LiMn_2O_4$ during electrochemical cycling [37,38]. Mn dissolution during electrochemical cycling results from the attack of acidic hydrofluoric acid (HF) formed by residual H_2O and hexafluorophosphate ($LiPF_6$) in organic electrolyte. This irreversible decomposition of $LiMn_2O_4$ has been considered as the main cause of its capacity fading [39]. The presence of Mn^{3+} ions in $LiMn_2O_4$ leads to an unexpected Jahn-Teller distortion, causing crystal structure transformation and severe structural instability of $LiMn_2O_4$. In the case of low-voltage discharge, the Jahn-Teller effect induces phase transition of $LiMn_2O_4$ from cubic structure to tetragonal symmetry, resulting in high disorder of lithium ion distribution [40]. The high oxidation ability of Mn^{3+}/Mn^{4+} redox pairs at the end of high-voltage charging process triggers decomposition of electrolyte, and the formed solid electrolyte interphase (SEI) on the surface of working electrode considerably increases the charge transition resistance and affects the lithium ion diffusivity [41,42]. The three factors summarized above together lead to inferior cycleability of $LiMn_2O_4$ cathode material, especially at elevated temperature. Although pure $LiMn_2O_4$ suffers from significant capacity fading, this problem can be overcome by surface modifications of the material, and thus it becomes a promising cathode material for high-performance lithium-ion batteries.

1.1.3.4 Lithium-excess layered cathode materials

Recently, Li-excess layered $Li[Li_xM_{1-x}]O_2$ (M = Mn, Ni, and Co) materials, i.e., xLi_2MnO_3-(1-x)$LiMO_2$ (M=Mn,Ni,Co), have attracted much research attention due to its high theoretical capacity (> 250 mAh/g) and high operating potential (> 4.5 V) [43-48]. The xLi_2MnO_3-(1-x)$LiMO_2$ (M=Mn,Ni,Co) can be considered as a solid solution composite, composed of Li-inactive Li_2MnO_3 and Li-active $LiMO_2$ with different molar ratios in an integrated layered structure, as presented in Figure 1.6 with a group space *R-3m* [47,49]. There is a super lattice structure in Figure 1.6, which is arisen from $LiMn_6$ cation arrangements in the transition metal layers of Li_2MnO_3 component (group space *C2m*) [43,48,50]. The high capacity of Li-excess cathodes has been demonstrated from the electrochemical activation of inert Li_2MnO_3 upon the initial charge > 4.5 V *vs.* Li/Li^+. In this electrochemical activation process, oxygen will be lost irreversibly together with lithium ion extraction and decomposition of Li_2MnO_3 to Li_2O and MnO_2; hence, the oxidation state of transition metal ions is lowered in comparison with that in the original material at the end of corresponding first discharge to 2.0 V *vs.* Li/Li^+ [44,51,52]. The initial Li_2MnO_3 activation contributes to high capacity of this series of materials in subsequent electrochemical cycles but also low Coulombic efficiency in the first cycle.

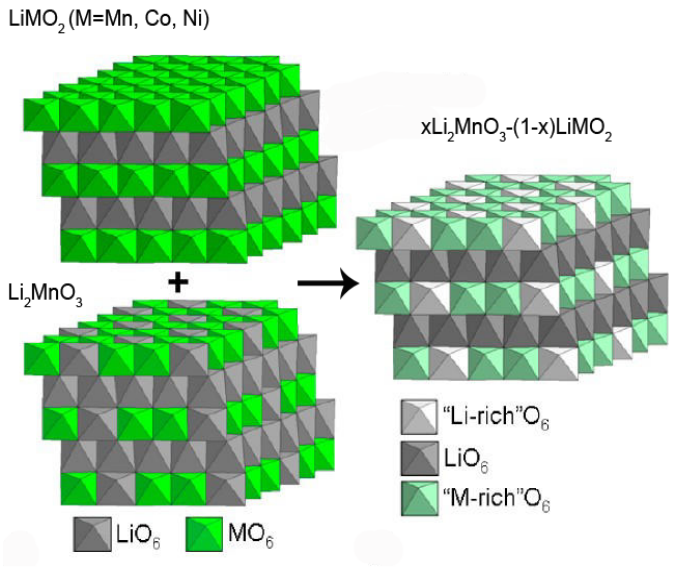

Figure 1.6 Crystal structure of Li-excess layered cathode materials, $Li[Li_xM_{1-x}]O_2$ (M = Mn, Ni, and Co) [43].

$Li[Li_{0.2}Mn_{0.54}Ni_{0.13}Co_{0.13}]O_2$ (LMNCO), one of the most promising materials among Li-excess layered cathode materials, consists of Li_2MnO_3 and $LiMn_{1/3}Ni_{1/3}Co_{1/3}O_2$ with a molar ratio of 1:1, i.e., $0.5Li_2MnO_3$-0.5 $LiMn_{1/3}Ni_{1/3}Co_{1/3}O_2$. The theoretical capacity of LMNCO is up to 321 mAh/g, which is much higher than that of commercial cathode materials (Table 1.1). In spite of the high capacity of layered cathode materials, more efforts are needed to overcome their irreversible capacity loss in the initial charge/discharge, inferior rate capability and poor reversibility caused by a layered-to-spinel phase conversion. In contrast, it has recently been reported that the phase transition in Li-excess layered cathode materials during and after activating the Li_2MnO_3 component when electrochemically cycled can significantly contribute to the unexpectedly enhanced high-rate capability [53-55]. Both Li_2MnO_3 and $LiMn_{1/3}Ni_{1/3}Co_{1/3}O_2$ components simultaneously undergo phase conversion from original layered to reconstructed spinel structures but through different pathways. Within Li_2MnO_3 domain, removal of Li^+ and O^{2-} during initial electrochemical activation triggers phase transition from layered Li_2MnO_3 to spinel phase due to the existence of lithium ion and oxygen vacancies. As a result, layered Li_2MnO_3 transforms to numerous spinel grains integrated in an amorphous matrix [56]. It has been suggested that structural rearrangement within $LiMn_{1/3}Ni_{1/3}Co_{1/3}O_2$ region takes place through migration of transition metal ions to lithium ion layers, yielding spinel grains on the surface of predominant layered structure during initial electrochemical cycles [43,57]. Such structural evolution can progress via continuous lithiation and delithiation, and consumes the parent layered phase to grow spinel phase until a complex layered-spinel composite structure is stabilized [58,59]. The formation of the spinel phase in Li-excess layered cathode materials has been demonstrated by high resolution STEM observations [43], high resolution TEM images with selected area electron diffraction patterns [53], in situ X-ray diffraction

patterns [58], X-ray absorption spectroscopic and Raman studies [59,60] , and is also reflected on charge/discharge curves [61], differential capacity plots [53], and cyclic voltammetric (CV) profiles [53, 62]. Although such phase transformations break down the parent layered lattice and induces lattice strains, newly-formed spinel phase exhibits higher capacity and better rate capability, owing to its lithium-active characteristic, higher electronic conductivity and facile lithium ion diffusivity in the spinel phase [53]. The intergrowth of spinel-layered phases tends to alleviate electrochemical inferiority of Li-excess layered cathode materials. However, structural details of these phases in the cycled electrodes have not been reported yet. Crystal phase of the formed spinel in Li-excess layered oxides is still referred as "spinel" or "spinel-like". Effects of such a layered-to-spinel phase transformation (whether to improve or deteriorate performance of spinel-layered composite cathodes) are currently not clear. It is very important to explore these effects for understanding fundamental electrochemical behaviors of the emerging high-capacity Li-excess layered cathode materials. One the other hand, battery performance depends on not only intrinsic characteristics but also the designed morphologies and structures of electrode materials. Another approach to realize combination of high energy and high power in battery is to assemble high-capacity electrode materials in nanoarchitectures.

In summary, each cathode material has its advantages and disadvantages. For commercial applications of high-performance lithium-ion batteries in HEVs and EVs, high energy and power densities are two critical requirements for cathode materials together with other important factors in terms of affordable cost, environmental benignity, and practical safety. Although $LiCoO_2$-based lithium-ion batteries have been extensively used in various fields, layered $LiMO_2$ cathode materials suffer from structural instability, toxic and high-cost Co source and safety problem. As for $LiFePO_4$, its olivine structure and inherent insulating property severely affect lithium ion diffusion and electron transfer, resulting in poor rate capability. In comparison with other cathode materials, Mn-based cathode materials, including spinel $LiMn_2O_4$ and emerging Li-excess layered cathode materials, can be considered as the most promising cathodes for next generation lithium-ion batteries due to their high specific capacity and rate capability, abundant and nontoxic Mn resource, and outstanding safety.

1.1.4 Surface modifications of cathode materials

Currently, commercial cathode materials, such as $LiCoO_2$, $LiMn_2O_4$, $LiFePO_4$ and $LiCo_{1/3}Ni_{1/3}Mn_{1/3}O_2$, are very limited in their specific capacities lower than 170 mAh/g. On the other hand, high-capacity Li-excess layered cathode materials (theoretical capacity >250 mAh/g) suffer inherently from structural instability, poor cycleability and high rate capability [63]. Upon charge/discharge cycling of pristine cathode materials, changes in electrode volume, phase transformations of cathode materials, electrode-electrolyte chemical reactions and electrolyte decomposition inevitably take place in working electrodes. Among these deleterious factors, a passivating solid-electrolyte interphase (SEI) layer is formed on the surface of

cathode materials by electrode-electrolyte chemical reactions and electrolyte decomposition, which are induced by the high oxidization ability of transition metal redox in cathode materials, such as Co^{3+}/Co^{4+}, Mn^{3+}/Mn^{4+}, Ni^{2+}/Ni^{3+}, Ni^{3+}/Ni^{4+} and Fe^{2+}/Fe^{3+} [64]. Such unexpected SEI layer affects lithium ion diffusivity and electronic conductivity of cathode materials drastically, leading to an irreversible loss of capacity and poor rate capability. Therefore, the essential challenge here is to develop a strategy that will preserve cycling performance at an acceptable rate in a safe and affordable lithium-ion battery. The doping technique by introducing foreign ions into the internal structure of cathode materials can significantly enhance lithium ion diffusion and electronic conductivity of bulk cathode materials but do not address the problem of SEI formation. In comparison with the doping approach, surface modifications on cathode materials show are more effective for modifying the electrode-electrolyte interphase to prevent formation of SEI layer, and can thus reduce capacity fading and improve charge transfer across electrode/electrolyte interfaces.

Surface coatings not only effectively restrict formation of SEI film via fabricating an artificial interlayer between cathode materials and surrounding electrolyte, but also simultaneously serve as lithium ion or/and electron conductors, HF scavenger in electrolyte and structural supporter for the host cathode materials. The expected multifunction from surface modifications requires high qualities from the as-prepared surface coatings in terms of high mechanical strength and chemical stability, uniformity, conformality and controllable thickness [64].

1.1.4.1 Traditional surface coatings on cathode materials

Surface modifications have been widely employed on different cathode materials to improve electrochemical performance of lithium-ion batteries. Wet chemical process followed by solid state reaction is considered as a traditional route to deposit various coating materials, such as oxides [65-69], phosphates [70], fluoride [71], carbon-based materials [67,72], lithium-active cathode materials [69], lithium-conductive composite [73,74] and polymers [75], and so on. Lu *et al*. reported a novel synthetic approach to fabricate Li_2TiO_3 coated layered LMO_2 cathode materials, in which TiO_2-coated $MC_2O_4 \cdot xH_2O$ were prepared first by a solvothermal method, and then the precursors were lithiated in high-temperature solid-state reaction to yield the coated product. The Li^+-conductive Li_2TiO_3 coatings improve the intrinsic Li^+-ion conductivity and structural stability of layered cathode materials, and also act as a barrier to prevent decomposition of electrolyte on the surface of active particles, contributing to enhanced rate capability and cycling performance of layered LMO_2 cathode materials [73]. Hwang *et al*. demonstrated that ZrO_2 coatings can enhance electrochemical performance of $LiCoO_2$ in a high voltage range up to 4.5 V. In comparison with bare $LiCoO_2$ electrode, ZrO_2-coated $LiCoO_2$ delivers better cycling stability, rate capability and thermal stability under a wide voltage range of 3.0 - 4.5 V, which are attributed to different surface microstructure and improved structural stability of $LiCoO_2$ after being coated with ZrO_2 [66].

Increasing electronic conductivity is essential to improve charge-discharge rate capability of insulting olivine $LiFePO_4$ cathode material, and carbon-based materials in combination with other functional coatings have been utilized for $LiFePO_4$. Zhang *et al*. employed a carbothermal reduction method to prepare V_2O_3-modified $LiFePO_4$/C powders. V_2O_3/carbon composite surface coatings can effectively improve the reversibility, specific capacity and rate capability of $LiFePO_4$, due to its high electronic conductivity higher than 10^3 S/cm [57]. Hybrid coating of nano-Li_3PO_4 and carbon on the surface of $LiFePO_4$ particles was synthesized in a two-step solid-state reaction by Zhao *et al*, which also contributed to improved high-rate performance of $LiFePO_4$ cathodes [74].

In the case of Mn-based cathode materials, such as spinel $LiMn_2O_4$ and Li-excess layered $Li[Li_{0.2}Mn_{0.54}Ni_{0.13}Co_{0.13}]O_2$, most research efforts focus on reducing capacity fading of cathodes at high rates and elevated temperature by restricting transition metal dissolution, electrolyte decomposition and phase transformation. Oxide (ZnO, ZrO_2, TiO_2, MgO, SnO_2 and Al_2O_3) and phosphate ($FePO_4$ and $AlPO_4$) coatings have been widely used to modify $LiMn_2O_4$ and lithium-rich layered cathode materials. TiO_2-coated $LiMn_2O_4$ was synthesized using a carrier transfer method [68], in which TiO_2 particles were transferred to the surface of $LiMn_2O_4$ using XC-72 active carbon powders as the dispersant. Such TiO_2 modification can lower charge transfer resistance and reduce Mn dissolution, and increase lithium ion diffusion of $LiMn_2O_4$ cathodes, contributing to better cycling performance in comparison with bare $LiMn_2O_4$ electrodes. Due to chemical stability and lithium activity of $FePO_4$, Qing *et al*. reported that amorphous $FePO_4$ coating resulted in improved cycling performance of $LiMn_2O_4$ [70]. Surface modification on lithium-excess layered cathode materials has also been reported as an effective method to reduce irreversible capacity loss during initial electrochemical cycle by suppressing elimination of oxygen ion vacancies and side reactions between active materials and electrolyte. Shi *et al*. reported enhanced cycling stability of $Li[Li_{0.2}Mn_{0.54}Ni_{0.13}Co_{0.13}]O_2$ by surface modification of MgO, which was prepared in a melting impregnation method [71]. The cathode coated with 2 wt.% MgO exhibited excellent cycling stability with a capacity retention of 96.4% at a current density of 200 mA/g after 100 cycles at room temperature and 94.3% after 50 cycles at 60 ˚C, respectively. Conductive materials, such as carbon [72] and conductive polymers [75], show significant effects on improving cycleability and rate capability for Li-excess layered cathode materials, due to their high electronic conductivity and elasticity. Furthermore, fabrication of core-shell structures consisting of Li-excess layered cathode material as the core and Li-stoichiometric active material as the shell is an alternative route to achieve high performance of Li-excess layered cathode materials. Electrochemically-active shells can improve electronic conductivity, lithium ion diffusivity, thermal stability, and cycling stability of core Li-excess cathode materials. Q. Qiao *et al.* have shown that coating $LiMnPO_4$ on the surface of Li-rich layered $Li[Li_{0.17}Ni_{0.25}Mn_{0.58}]O_2$ followed by heat treatment can increase reaction kinetics and structural stability of core material, resulting in better rate capability and cycleability in comparison with bare cathode [76].

Traditional surface modifications have contributed to significantly enhanced electrochemical performance of cathode materials, but there are still several limitations: (1) Surface coatings formed by traditional methods always lack conformality and uniformity, and the coating thickness cannot be precisely controlled; (2) Synthetic approaches are time-consuming and energy-consuming. For example, wet-chemical and solid-state reactions require a large amount of solvents and high temperature sintering, respectively; (3) Conventional coating-deposition approaches cannot be used to modify composite electrodes, which are composed of cathode materials, conductive additives and polymer binders at a certain weight ratio.

1.1.4.2 Oxide ALD coatings on cathodes

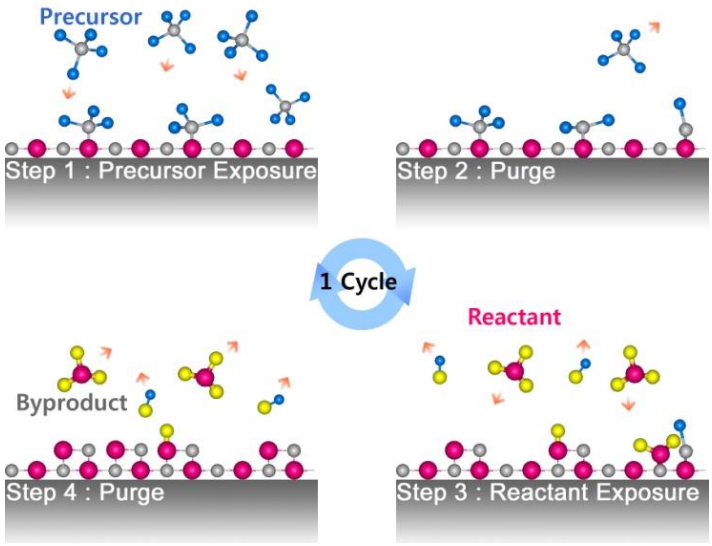

Figure 1.7 Schematic diagram of atomic layer deposition [89].

Among various coating materials, surface modifications via amphoteric oxide coatings, such as Al_2O_3, ZnO, ZrO_2, MgO, Cr_2O_3 and SnO_2, can be easily synthesized and have proved very effective on improving electrochemical performance of electrode materials in comparison with other materials [39,77]. The amphoteric oxide coating can not only neutralize acidic HF to suppress disproportionate transition metal dissolution but also separate cathode materials from electrolyte to alleviate decomposition of electrolyte [78]. In addition, the oxide film serves as a solid framework to restrict inherent phase transition of cathode materials, leading to better structural stability [79]. However, electrochemical performance of cathodes can be affected by quality of oxide coatings in terms of adhesion to cathode materials, conformality, uniformity, thickness, specific surface area and crystallinity [80-82]. There are quite a few approaches for preparing oxide coatings, such as sol-gel processing [81], colloidal suspension [82,83], pulsed laser deposition [79], sono-chemical method [84], chemical deposition [85] and atomic layer deposition (ALD) [86-88]. The emerging atomic layer deposition technique is very promising for

overcoming limitations of traditional surface modifications, though ALD is limited by mainly yielding oxide coatings [64].

In comparison with other methods, ALD approach is unique in the sense that it produces ultrathin films with high conformality and precise thickness control at atomic scale. As shown in Figure 1.7 [89], ALD is a thin film deposition technique subjected to a sequence of chemisorption and self-terminating surface reactions [90-97]. In a typical ALD run, initial hydroxylation on the surface of the substrate using an oxidative precursor, such as H_2O and ozone, yields conformal and complete surface coverage of hydroxyl groups on the substrate, followed by purging residual H_2O and ozone and by-products with inert gas flux. Subsequently, an organometallic precursor is introduced to react with hydroxyl groups, and thus a monolayer of oxide grows on the surface of substrate bridged by oxygen bonds. After the second purging step to remove extra organometallic precursor and by-products, continuative hydroxylation takes place to replace organic groups on the surface of organometallic precursor with hydroxyl groups for growing the second layer of oxide. As a result, sequential ALD cycles proceed step-wise in self-limiting surface reactions as mentioned above, separated by purge steps, and the coating layers grow precisely monolayer by monolayer at atomic scale [87,93]. Hence, films grown using ALD are typically uniform, dense, homogenous, pinhole-free, and extremely conformal to the underlying substrate, and the thickness of coatings can be precisely controlled at atomic level. It is also noted that the ALD coating is chemically bonded to the substrate, while there is merely physical contact between the coating synthesized via wet chemical methods and the substrate. Another distinct advantage of ALD technique for surface modification of lithium ion batteries is that it allows for direct coating on the composite electrode with high aspect ratio [91,95,97]. In the process of ALD growth on the composite electrodes, gas-phase precursors can facilely penetrate into the porous frame of composite electrode composed of electrode material, conductive carbon and polymer binder, resulting in deposition of oxide on the whole external and internal surface of the electrode. Although it is difficult to validate specific morphology and structure of oxide coatings in the ALD-modified electrode, oxide ALD thin film depositing on the electrode for improved electrochemical performance have been reported for both cathode and anode materials [87,91,95,98]. ALD approach also offers the flexibility of depositing coatings on either individual cathode particles or the whole composite electrode. In this report, ALD growth of ultrathin and highly-conformal ZnO, ZrO_2 and Al_2O_3 coatings with controllable atomic-scale thickness are investigated systematically, and their effects on improving electrochemical properties of $LiMn_2O_4$ and $Li[Li_{0.2}Mn_{0.54}Ni_{0.13}Co_{0.13}]O_2$ cathodes are also discussed.

1.2 Motivation and Scope

Rechargeable lithium-ion battery has been demonstrated as an excellent electrochemical energy conservation and storage system. Electrochemical performance of lithium-ion batteries mainly depends on properties of two electrodes:

cathode and anode. Tremendous research efforts have been focused on developing safe and environmentally friendly electrode materials that have high operating voltage, high energy density, excellent rate capability and cycling stability [1,98]. As mentioned earlier, lithium alloys as anode materials for lithium ion batteries, such as lithium-silicon (Li-Si) and lithium-tin (Li-Sn), promise to provide excellent cycling stability, high rate capability, and higher specific capacity than conventional carbon materials with a theoretic capacity of 4000 and 990 mAh/g, respectively [99,100]. On the other hand, common cathode materials have much lower theoretical capacity than anodes and suffer from structural instability when cycled at high voltage and elevated temperature. For example, traditional Li-stoichiometric cathode materials, e.g., layered $LiCoO_2$, spinel $LiMn_2O_4$, and olivine $LiFePO_4$, have low reversible specific capacity up to 170 mAh/g and are limited by inferior cycleability at elevated temperature [63]. Development of high-performance lithium ion batteries requires breakthrough improvement in electrochemical performance of cathode materials.

Two main strategies are usually used to significantly improve electrochemical performance of cathode materials: One aims at achieving specific capacity of conventional cathode materials ($LiCoO_2$, $LiMn_2O_4$, $LiFePO_4$, and $LiMn_{1/3}Co_{1/3}Ni_{1/3}O_2$) up to their theoretical capacities together with excellent cycling stabilities even in elevated-temperature environment; the other focuses on synthesis of new cathode materials, including high-voltage $LiMn_{1.5}Ni_{0.5}O_2$ cathode (The operation voltage vs. Li^+/Li is up to 5.0 V) [13] and high-capacity Li-excess layered cathode materials (the theoretical capacity is up to 321 mAh/g) [101], for superior lithium-ion batteries. My research projects concentrate on Mn-based cathode materials: (1) surface modifications of commercial spinel $LiMn_2O_4$ cathode materials by depositing ultrathin and conformal amphoteric oxide coatings on $LiMn_2O_4$ electrodes via atomic layer deposition to enhance its elevated-temperature cycling performance; and (2) synthesis and systematic investigation of novel high-capacity Li-excess layered cathode material, $Li[Li_{0.2}Mn_{0.54}Ni_{0.13}Co_{0.13}]O_2$, for superior lithium-ion batteries.

This dissertation contains eight chapters to present all research achievements in my doctoral program.

In Chapter 1, an overview of various energy conversion/storage systems is presented, followed by general information on lithium-ion rechargeable battery, including its working mechanism, anode and cathode materials, and surface modifications of cathodes for improved electrochemical performance. Background and rationale of my Ph.D. research are also summarized in this chapter.

Chapter 2 focuses on atomic layer deposition of ZnO surface coatings on micro-sized $LiMn_2O_4$ particles for enhanced electrochemical performance of $LiMn_2O_4$. ZnO ALD coated $LiMn_2O_4$ electrodes show enhanced cycleability in comparison with bare $LiMn_2O_4$ electrodes both at room temperature and elevated temperature. Furthermore, cycling performance of $LiMn_2O_4$ cathodes is easily optimized by manipulating ZnO coating thickness via varying ALD growth cycles.

Chapter 3 reveals intriguing growth of crystalline ZrO_2 ALD coatings on micro-sized $LiMn_2O_4$ particles, and summarizes its effect on enhancing rate capability of $LiMn_2O_4$ cathodes at elevated temperature. In addition, different effects from

various ALD oxide coatings (ZnO, ZrO_2 and Al_2O_3) on improving electrochemical performance of $LiMn_2O_4$ cathodes are discussed.

Chapter 4 presents the interesting structure and effect of ZrO_2 ALD coatings on $LiMn_2O_4$ nanoparticles. It is found that epitaxial growth leads to crystalline ZrO_2 ALD coatings on the surface of nano-sized $LiMn_2O_4$ at low temperature. Remarkable high-rate performance of ZrO_2-coated $LiMn_2O_4$ nanoparticles is achieved in this work.

Chapter 5 reports synthesis of novel high-capacity $Li[Li_{0.2}Mn_{0.54}Ni_{0.13}Co_{0.13}]O_2$ nanoparticles and their surface modification via hierarchical functional layers for considerably improved electrochemical performance. The hierarchical functional layers consist of nano-sized $LiCoO_2$ shell and sub-nano-sized ZrO_2 ALD coating deposited on core $Li[Li_{0.2}Mn_{0.54}Ni_{0.13}Co_{0.13}]O_2$ nanoparticles. The synergetic effect from ALD oxide coating and core-shell structure results in high reversibility, cycleabilitiy and rate capability of Li-excess layered cathode materials for superior lithium-ion batteries.

Chapter 6 resolves the important unanswered issues related to the layered-to-spinel phase transition within Li-excess transition metal oxides, which are emerging Li-ion battery cathode materials with very high theoretical capacities but suffering from drastic initial capacity loss. In highly contrast to the limited layered-to-spinel phase transformation occurred during in-situ electrochemical cycles, a new ex-situ approach is developed to intentionally and controllably induce a complete phase transition of Li-excess layered $Li[Li_{0.2}Mn_{0.54}Ni_{0.13}Co_{0.13}]O_2$ via ion-exchanges and a post-annealing process. Fundamental mechanism of such phase transition and crystal structure of the resultant spinel product are explored using a wide set of characterizations, including in-situ X-ray diffraction and in-situ high-resolution transition electron microscopy. Most importantly, the final $Li_4Mn_5O_{12}$-type spinel product demonstrates remarkably improved rate capability and cycling stability in comparison with the original Li-excess layered cathode materials.

Chapter 7 illustrates the effects of nanostructured electrode materials on improving electrochemical performance for both Li-excess layered cathode material and transition metal carbonate anode material. A full lithium-ion battery cell is assembled based on nanoarchitectured ternary manganese-nickel-cobalt compounds, in which multi-shell spherical $Mn_{0.54}Ni_{0.13}Co_{0.13}(CO_3)_{0.8}$ serves as anode and the subsequently lithiated Li-excess $Li[Li_{0.2}Mn_{0.54}Ni_{0.13}Co_{0.13}]O_2$ with a yolk-shell structure acts as cathode. Such a full lithium-ion battery demonstrates high practical capacity for new-generation lithium-ion batteries.

Finally, chapter 8 summarizes my research contributions to the developments of high-energy and high-power lithium-ion batteries through novel syntheses and surface modifications of various electrode materials.

1.3 References

1. J. B. Goodenough, K. S. Park, The Li-ion Rechargeable Battery: A Perspective. *Journal of American Chemical Society* 135 (2013) 1167-1176.

2. Greenband, Peak Water Worries Energy Experts. *Greenband*: http://www.greenbang.com/peak-water-worries-energy-experts_22514.html (2013).

3. D. Mohindra, Despite Rise of Renewables, Fossil Fuel Still Fastest Growing Energy Source. *World Economic Forum*: http://www.weforum.org/news/despite-rise-renewables-fossil-fuel-still-fastest-growing-energy-source?news=page (2013).

4. M. Caine, New Energy Sources: Possibilities and Prospects. *Theenergycollective*: http://theenergycollective.com/markecaine/173971/new-energy-sources-possibilities-and-prospects (2013).

5. D. Johnson, Battery Combines Li-Ion Energy, Ultracapacitor Power. *SPIE*: http://spie.org/x93835.xml (2013).

6. P. Patel, A Battery-Ultracapacitor Hybrid-A Device for Power Tools may also Help Regenerative Braking. *MIT Technology Review*: http://www.technologyreview.com/news/417053/a-battery-ultracapacitor-hybrid, (2010).

7. Wikipedia, The Free Encyclopedia, *WIKIPEDIA*: http://en.wikipedia.org/wiki/Lithium-ion_battery (2013).

8. M. C. Yang, Strategies to Improve the Electrochemical Performance of Li-Ion Batteries, *Dissertation*, University of Floride (2012).

9. M. S. Whittingh, Lithium Batteries and Cathode Materials. *Chemical Reviews* 104 (2004) 4271-4301.

10. B. Xu, D. Qian, Z. Wang, Y. S. Meng, Recent Progress in Cathode Materials Research for Advanced Lithium Ion Batteries. *Material Science and Engineering: R: Report* 73 (2012) 51-65.

11. K. Mizushima, P. C. Jones, P. J. Wiseman, J. B. Goodenough, Li_xCoO_2 ($0<x<-1$): A New Cathode Material for Batteries of High Energy Density. *Materials Research Bulletin* 15 (1980) 783-789.

12. G. G. Amatucci, J. M. Tarascon, L. C. Klein, CoO_2, The End Member of the Li_xCoO_2 Solid Solution. *Journal of The Electrochemical Society* 143 (1996) 1114-1123.

13. X. Zhang, F. Cheng, J. Yang, J. Chen, $LiNi_{0.5}Mn_{1.5}O_4$ Porous Nanorods as High-Rate and Long-Life Cathodes for Li-Ion Batteries. *Nano Letters* 13 (2013) 2822-2825.

14. L. X. Yuan, Z. H. Wang, W. X. Zhang, X. L. Hu, J. T. Chen, Y. H. Huang, J. B. Goodenough, *Energy & Environmental Science* 4 (2011) 269-284.

15. L. X. Yuan, Z. H. Wang, W. X. Zhang, X. L. Hu, J. T. Chen, Y. H. Huang, J. B. Goodenough, Development and Challenges of $LiFePO_4$ Cathode Material for Lithium-Ion Batteries. *Energy & Environmental Science* 4 (2011) 269-284.

16. S. Y. Chung, J. T. Bloking, Y. M. Chiang, Electronically Conductive Phospho-Olivines as Lithium Storage Electrodes. *Nature Materials* 1 (2002) 123-128.

17. M. Thackeray, Lithium-Ion Batteries: An Unexpected Conductor. *Nature Materials* 1 (2002) 81-82.

18. C. Y. Lai, Q. J. Xu, H. H. Ge, G. D. Zhou, J. Y. Xie, Improved Electrochemical Performance of $LiFePO_4$/C for Lithium-Ion Batteries with Two Kinds of Carbon Sources. *Solid State Ionics* 179 (2008) 1736-1739.

19. J. M. Chen, C. H. Hsu, Y. R. Lin, M. H. Hsiao, G. T.-K. Fey, High-Power $LiFePO_4$ Cathode Materials with A Continuous Nano Carbon Network for Lithium-Ion Batteries. *Journal of Power Sources* 184 (2008) 498-502.

20. J. Liu, J. W. Wang, X. D. Yan, X. F. Zhang, G. L. Yang, A. F. Jalbout, R. S. Wang, Long-Term Cyclability of $LiFePO_4$/Carbon Composite Cathode Material for Lithium-Ion Battery Applications. *Electrochimica Acta* 54 (2009) 5656-5659.

21. C. M. Doherty, R. A. Caruso, B. M. Smarsly, C. J. Drummond, Colloidal Crystal Templating to Produce Hierarchically Porous $LiFePO_4$ Electrode Materials for High Power Lithium Ion Batteries. *Chemistry of Materials* 21 (2009) 2895-2903.

22. C. M. Doherty, R. A. Caruso, B. M. Smarsly, P. Adelhelm, C. J. Drummond, Hierarchically Porous Monolithic $LiFePO_4$/Carbon Composite Electrode Materials for High Power Lithium Ion Batteries. *Chemistry of Materials* 21 (2009) 5300-5306.

23. X. L. Wu, L. Y. Jiang, F. F. Cao, Y. G. Guo, L. J. Wan, $LiFePO_4$ Nanoparticles Embedded in a Nanoporous Carbon Matrix: Superior Cathode Material for Electrochemical Energy-Storage Devices. *Advanced Materials* 21 (2009) 2710-2714.

24. F. Y. Cheng, Z. L. Tao, J. Liang, J. Chen, Template-Directed Materials for Rechargeable Lithium-Ion Batteries. *Chemistry of Materials* 20 (2008) 667-681.

25. F. Croce, A. D' Epifanio, J. Hassoun, A. Deptula, T. Olczac, B. Scrosati, A Novel Concept for the Synthesis of an Improved $LiFePO_4$ Lithium Battery Cathode. *Electrochemical Solid-State Letters* 5 (2002) A47-A50.

26. G. M. Song, Y. Wu, Q. Xu, G. Liu, Enhanced Electrochemical Properties of $LiFePO_4$ Cathode for Li-Ion Batteries with Amorphous NiP Coating. *Journal of Power Sources* 195 (2010) 3913-3917.

27. Y. Cui, X. L. Zhao, R. S. Guo, Improved Electrochemical Performance of $La_{0.7}Sr_{0.3}MnO_3$ and Carbon Co-Coated $LiFePO_4$ Synthesized by Freeze-Drying Process. *Electrochimica Acta* 55 (2010) 922-926.

28. Y. H. Huang, J. B. Goodenough, High-Rate $LiFePO_4$ Lithium Rechargeable Battery Promoted by Electrochemically Active Polymers. *Chemistry of Materials* 20 (2008) 7237-7241.

29. J. Zhao, J. He, J. Zhou ,Y. Guo, T. Wang, S. Wu, X. Ding, R. Huang, H. Xue, Facile Synthesis for $LiFePO_4$ Nanospheres in Tridimensional Porous Carbon Framework for Lithium Ion Batteries. *The Journal of Physical Chemistry C*, 115 (2011) 2888-2894.

30. R. Dominko, M. Bele, J. M. Goupil, M. Gaberscek, D. Hanzel, I. Arcon, J. Jamnik, Wired Porous Cathode Materials: A Novel Concept for Synthesis of $LiFePO_4$. *Chemistry of Materials* 19 (2007) 2960-2969.

31. J. F. Qian, M. Zhou, Y. L. Cao, X. P. Ai, H. X. Yang, Template-Free Hydrothermal Synthesis of Nanoembossed Mesoporous $LiFePO_4$ Microspheres for High-Performance Lithium-Ion Batteries. *The Journal of Physical Chemistry C* 114 (2010) 3477-3482.

32. O. K. Park, Y. Cho, S. Lee, H. C. Yoo, H.-K. Song, J. Cho, Who Will Drive Electric Vehicles, Olivine or Spinel? *Energy & Environmental Science* 4 (2011) 1621-1633.

33. M. M. Thackeray, W. I. F. David, P. G. Bruce, J. B. Goodenough, Lithium Insertion into Manganese Spinels. *Materials Research Bulletin* 18 (1983) 461-472.

34. J. M. Tarascon, M. Armand, Issues and Challenges Facing Rechargeable Lithium Batteries. *Nature* 414 (2001) 359-367.

35. A. Manthiram, Materials Challenges and Opportunities of Lithium Ion Batteries. *The Journal of Physical Chemistry Letters* 2 (2011) 176-184.

36. H. W. Lee, P. Muralidharan, R. Ruffo, C. M. Mari, Y. Cui, D. K. Kim, Ultrathin Spinel $LiMn_2O_4$ Nanowires as High Power Cathode Materials for Li-Ion Batteries. *Nano Letters* 10 (2010) 3852-3856.

37. K. Y. Chung, H. S. Lee, W. S. Yoon, J. McBreen, X. Q. Yang J. Electrochem. Soc. 153 (2006) A774-A780.

38. K. Y. Chung, H. S. Lee, W. S. Yoon, J. McBreen, X. Q. Yang, Studies of $LiMn_2O_4$ Capacity Fading at Elevated Temperature Using In Situ Synchrotron X-Ray Diffraction. *Journal of The Electrochemical Society* 153 (2006) A774-A780.

39. S. T. Myung, K. Amine, Y. K. Sun, Surface Modification of Cathode Materials from Nano- to Microscale for Rechargeable Lithium-Ion Batteries. *Journal of Materials Chemistry* 20 (2010) 7074-7095.

40. H. Wang, T. A. Tan, P. Yang, M. O. Lai, L. Lu, High-Rate Performances of the Ru-Doped Spinel $LiNi_{0.5}Mn_{1.5}O_4$: Effects of Doping and Particle Size. *The Journal of Physical Chemistry C* 115 (2011) 6102-6110.

41. F. Simmen, A. Hintennach, M. Horisberger, T. Lippert, P. Novák, C. W. Schneider, A. Wokaun, Aspects of the Surface Layer Formation on $Li_{1+x}Mn_2O_{4-\delta}$ during Electrochemical Cycling. *Journal of The Electrochemical Society* 157 (2010) A1026-A1029.

42. M. Hirayama, H. Ido, K. Kim, W. Cho, K. Tamura, J. Mizuki, R. Kanno, Dynamic Structural Changes at $LiMn_2O_4$/Electrolyte Interface during Lithium Battery Reaction, *Journal of The American Chemical Society* 132 (2010) 15268-15276.

43. A. Boulineau, L. Simonin, J.-F.Colin, E. Canévet, L. Daniel, S. Patoux, Evolutions of $Li_{1.2}Mn_{0.61}Ni_{0.18}Mg_{0.01}O_2$ during the Initial Charge/Discharge Cycle Studied by Advanced Electron Microscopy. *Chemistry of Materials* 24 (2012) 3558-3566.

44. A. R. Armstrong, M. Holzapfel, P. Novák, C. S. Johnson, S. H. Kang, M. M. Thackeray, P. G. Bruce, Demonstrating Oxygen Loss and Associated Structural Reorganization in the Lithium Battery Cathode $Li[Ni_{0.2}Li_{0.2}Mn_{0.6}]O_2$. *Journal of The American Chemical Society* 128 (2006) 8694-8698.

45. T. A. Arunkumar, Y. Wu, A. Manthiram, Factors Influencing the Irreversible Oxygen Loss and Reversible Capacity in Layered $Li[Li_{1/3}Mn_{2/3}]O_2$-$Li[M]O_2$ (M = $Mn_{0.5-y}Ni_{0.5-y}Co_{2y}$ and $Ni_{1-y}Co_y$) Solid Solutions. *Chemistry of Materials* 19 (2007) 3067-3073.

46. T. A. Arunkumar, E. Alvarez, A. Manthiram, Structural, Chemical, and Electrochemical Characterization of Layered $Li[Li_{0.17}Mn_{0.33}Co_{0.5-y}Ni_y]O_2$ Cathodes. *Journal of The Electrochemical Society* 154 (2007) A770-A775.

47. Y. Wu, A. Manthiram, Structural Stability of Chemically Delithiated Layered $(1-z)Li[Li_{1/3}Mn_{2/3}]O_2$-$zLi[Mn_{0.5-y}Ni_{0.5-y}Co_{2y}]O_2$ Solid Solution Cathodes. *Journal of Power Sources* 183 (2008) 749-754.

48. K. A. Jarvis, Z. Deng, L. F. Allard, A. Manthiram, P. J. Ferreira, Atomic Structure of a Lithium-Rich Layered Oxide Material for Lithium-Ion Batteries: Evidence of a Solid Solution. *Chemistry of Materials* 23 (2011) 3614-3621.

49. Q. Y. Wang, J. Liu, A. Vadivel Murugan, A. Manthiram, High Capacity Double-Layer Surface Modified $Li[Li_{0.2}Mn_{0.54}Ni_{0.13}Co_{0.13}]O_2$ Cathode with Improved Rate Capability. *Journal of Materials Chemistry* 19 (2009) 4965-4972.

50. M. Jiang, B. Key, Y. S. Meng, C. P. Grey, Electrochemical and Structural Study of the Layered, "Li-Excess" Lithium-Ion Battery Electrode Material $Li[Li_{1/9}Ni_{1/3}Mn_{5/9}]O_2$. *Chemistry of Materials* 21 (2009) 2733-2745.

51. Y. S. Jung, A. S. Cavanagh, Y. Yan, S. M. George, A. Manthiram, Effects of Atomic Layer Deposition of Al_2O_3 on the $Li[Li_{0.20}Mn_{0.54}Ni_{0.13}Co_{0.13}]O_2$ Cathode for Lithium-Ion Batteries. *Journal of The Electrochemical Society* 158 (2011) A1298-A1302.

52. S. H. Yu, T. Yoon, J. Mun, S. Park, Y. S. Kang, J. H. Park, S. M. Oh, Y. E. Sung, Continuous Activation of Li_2MnO_3 Component upon Cycling in $Li_{1.167}Ni_{0.233}Co_{0.100}Mn_{0.467}Mo_{0.033}O_2$ Cathode Material for Lithium Ion Batteries. *Journal of Materials Chemistry A* 1 (2013) 2833-2839.

53. B. Song, H. Liu, Z. Liu, P. Xiao, M. On Lai, L. Lu, High Rate Capability Caused by Surface Cubic Spinels in Li-Rich Layer-Structured Cathodes for Li-Ion Batteries. *Scientific Reports* 3 (2013) 3094.

54. M. N. Ates, Q. Jia, A. Shah, A. Busnaina, S. Mukerjee, K. M. Abraham, Mitigation of Layered to Spinel Conversion of A Li-Rich Layered Metal Oxide Cathode Material for Li-Ion Batteries. *Journal of The Electrochemical Society* 161 (2013) A290-A301.

55. D. Wang, I. Belharouak, G. Zhou, K. Amine, Nanoarchitecture Multi-Structural Cathode Materials for High Capacity Lithium Batteries. *Advanced Functional Materials* 23 (2013)1070-1075.

56. M. Gu, I. Belharouak, J. Zheng, H. Wu, J. Xiao, A. Genc, K. Amine, S. Thevuthasan, D. R. Baer, J. G. Zhang, N. D. Browning, J. Liu, C. Wang,

Formation of the Spinel Phase in the Layered Composite Cathode Used in Li Ion Batteries. *ACS Nano* 7 (2013) 760-767.

57. F. Lin, I. M. Markus, D. Nordlund, T. C. Weng, M. D. Asta, H. L. Xin, M. M. Doeff, Surface Reconstruction and Chemical Evolution of Stoichiometric Layered Cathode Materials for Lithium-Ion Batteries. *Nature Communications* 5 (2014) 3529.

58. D. Mohanty, S. Kalnaus, R. A. Meisner, K. J. Rhodes, J. Li, E. A. Payzant, D. L. Wood III, C. Daniel, Structural Transformation of A Lithium-Rich $Li_{1.2}Co_{0.1}Mn_{0.55}Ni_{0.15}O_2$ Cathode during High Voltage Cycling Resolved by In Situ X-Ray Diffraction. *Journal of Power Sources* 229 (2013) 239-248.

59. S. Hy, W. N. Su, J. M. Chen, B. J. Hwang, Soft X-Ray Absorption Spectroscopic and Raman Studies on $Li_{1.2}Ni_{0.2}Mn_{0.6}O_2$ for Lithium-Ion Batteries. *The Journal of Physical Chemistry C* 116 (2012) 25242-25247.

60. F. Amalraj, M. Talianker, B. Markovsky, D. Sharon, L. Burlaka, G. Shafir, E. Zinigrad, O. Haik, D. Aurbach, J. Lampert, M. S. Dobrick, A. Garsuch, Study of the Lithium-Rich Integrated Compound $xLi_2MnO_3 \cdot (1\text{-}x)LiMO_2$ (x around 0.5; M=Mn,Ni,Co;2:2:1) and Its Electrochemical Activity as Positive Electrode in Lithium Cells. *Journal of The Electrochemical Society* 160 (2012) A324-A337.

61. D. Wang, I. Belharouak, G. Zhou, K. Amine, Nanoarchitecture Multi-Structural Cathode Materials for High Capacity Lithium Batteries. *Advanced Functional Materials* 23 (2013) 1070-1075.

62. B. Song, M. O. Lai, Z. Liu, H. Liu, L. Lu, Graphene-Based Surface Modification on Layered Li-Rich Cathode for High-Performance Li-Ion Batteries. *Journal of Materials Chemistry A* 1 (2013) 9954-9965.

63. P. He, H. Yu, D. Li, H. Zhou, Layered Lithium Transition Metal Oxide Cathodes towards High Energy Lithium-Ion Batteries. *Journal of Materials Chemistry* 22 (2012) 3680-3695.

64. X. Meng , X. Q. Yang, X. Sun, Emerging Applications of Atomic Layer Deposition for Lithium-Ion Battery Studies. *Advanced Materials* 24 (2012) 3589-3615.

65. S. J. Shi, J. P. Tu, Y. Y. Tang, X. Y. Liu, Y. Q. Zhang, X. L. Wang, C. D. Gu, Enhanced Cycling Stability of $Li[Li_{0.2}Mn_{0.54}Ni_{0.13}Co_{0.13}]O_2$ by Surface Modification of MgO with Melting Impregnation Method. *Electrochimica Acta* 88 (2013) 671-679.

66. B. Hwang, C. Chen, M. Cheng, R. Santhanam, K. Ragavendran, Mechanism study of enhanced electrochemical performance of ZrO_2-coated $LiCoO_2$ in high voltage region. *Journal of Power Sources* 195 (2010) 4255-4265.

67. Y. Zhang, G. Shao, Z. Ma, G. Wang, J. Du, Influence of Surface Modification by Vanadium Oxide and Carbon on the Electrochemical Performance of $LiFePO_4$/C. *Ionics* 19 (2013) 1091-1097.

68. C. Lai, W. Ye, H. Liu, W. Wang, Preparation of TiO_2-Coated $LiMn_2O_4$ by Carrier Transfer Method. *Ionics* 15 (2009) 389-392.

69. Z. Qiao, O. Sha, Z. Tang, J. Yan, S. Wang, H. Liu, Q. Xu, Y. Su, Surface Modification of $LiNi_{0.5}Mn_{1.5}O_4$ by $LiCoO_2/Co_3O_4$ Composite for Lithium-Ion Batteries. *Materials Letters* 87 (2012) 176-179.

70. C. Qing, Y. Bai, J. Yang, W. Zhang, Enhanced Cycling Stability of $LiMn_2O_4$ Cathode by Amorphous $FePO_4$ Coating. *Electrochimica Acta* 56 (2011) 6612-6618.

71. S. Shi, J. Tu, Y. Tang, Y. Zhang, X. Liu, X. Wang, C. Gu, Enhanced Electrochemical Performance of LiF-Modified $LiNi_{1/3}Co_{1/3}Mn_{1/3}O_2$ Cathode Materials for Li-Ion Batteries. *Journal of Power Sources* 225 (2013) 338-346.

72. Y. Deng, S. Liu, X. Liang, Study of Carbon Surface-Modified $Li[Li_{0.2}Mn_{0.54}Ni_{0.13}Co_{0.13}]O_2$ for High-Capacity Lithium Ion Battery Cathode. *Journal of Solid State Electrochemistry* 17 (2013) 1067-1075.

73. J. Lu, Q. Peng, W. Wang, C. Nan, L. Li, Y. Li, Nanoscale Coating of $LiMO_2$ (M = Ni, Co, Mn) Nanobelts with Li^+-Conductive Li_2TiO_3: Toward Better Rate Capabilities for Li-Ion Batteries. *Journal of The American Chemical Society* 135 (2013) 1649-1652.

74. S. Zhao, H. Ding, Y. Wang, B. Li, C. Nan, Improving Rate Performance of $LiFePO_4$ Cathode Materials by Hybrid Coating of Nano-Li_3PO_4 and Carbon. *Journal of Alloys and Compounds*. 566 (2013) 206-211.

75. C. Wu, X. Fang, X. Guo, Y. Mao, J. Ma, C. Zhao, Z. Wang, L. Chen, Surface Modification of $Li_{1.2}Mn_{0.54}Co_{0.13}Ni_{0.13}O_2$ with Conducting Polypyrrole. Journal of Power Sources 231 (2013) 44-49.

76. Q. Q. Qiao, H. Z. Zhang, G. R. Li, S. H. Ye, C. W. Wang, X. P. Gao, Surface Modification of Li-Rich Layered $Li(Li_{0.17}Ni_{0.25}Mn_{0.58})O_2$ oxide with Li-Mn-PO_4 as the Cathode for Lithium-Ion Batteries. *Journal of Materials Chemistry A* 1 (2013) 5262-5268.

77. C. Li, H. P. Zhang, L. J. Fu, H. Liu, Y. P. Wu, E. Rahm, R. Holze, H. Q. Wu Cathode Materials Modified by Surface Coating for Lithium Ion Batteries. *Electrochimica Acta* 51 (2006) 3872-3883.

78. S. B. Park, H. C. Shin, W. G. Lee, W. I. Cho, H. Jang, Improvement of Capacity Fading Resistance of $LiMn_2O_4$ by Amphoteric Oxides. *Journal of Power Sources* 180 (2008) 597-601.

79. D. W. Shin, J. W. Choi, J. P. Ahn, W. K. Choi, Y. S. Cho, S. J. Yoon, ZrO_2-Modified $LiMn_2O_4$ Thin-Film Cathodes Prepared by Pulsed Laser Deposition. *Journal of The Electrochemical Society* 157 (2010) A567-A570.

80. S. Lim, J. Cho, PVP-Assisted ZrO_2 Coating on $LiMn_2O_4$ Spinel Cathode Nanoparticles Prepared by MnO_2 Nanowire Templates. *Electrochemical Communications* 10 (2008) 1478-1481.

81. H. M. Wu, I. Belharouak, A. Abouimrane, Y. K. Sun, K. Amine, Surface Modification of $LiNi_{0.5}Mn_{1.5}O_4$ by ZrP_2O_7 and ZrO_2 for Lithium-Ion Batteries. *Journal of Power Sources* 195 (2010) 2909-2913.

82. J. S. Kim, C. S. Johnson, J. T. Vaughey, S. A. Hackney, K. A. Walz, W. A. Zeltner, M. A. Anderson, M. M. Thackeray, The Electrochemical Stability of Spinel Electrodes Coated with ZrO_2, Al_2O_3, and SiO_2 from Colloidal Suspensions. *Journal of The Electrochemical Society* 151 (2004) A1755-A1761.

83. K. A. Walz, C. S. Johnson, J. Genthe, L. C. Stoiber, W. A. Zeltner, M. A. Anderson, M. M. Thackeray, Elevated Temperature Cycling Stability and Electrochemical Impedance of $LiMn_2O_4$ Cathodes with Nanoporous ZrO_2 and TiO_2 Coatings. *Journal of Power Sources* 195 (2010) 4943-4951.

84. H. Sclar, O. Haik, T. Menachem, J. Grinblat, N. Leifer, A. Meitav, S. Luski, D. Aurbach, The Effect of ZnO and MgO Coatings by a Sono-Chemical Method, on the Stability of $LiMn_{1.5}Ni_{0.5}O_4$ as a Cathode Material for 5 V Li-Ion Batteries. *Journal of The Electrochemical Society* 159 (2012) A228-A237.

85. C. Qing, Y. Bai, J. Yang, W. Zhang, Enhanced Cycling Stability of $LiMn_2O_4$ Cathode by Amorphous $FePO_4$ Coating. *Electrochimica Acta* 56 (2011) 6612-6618.

86. D. Guan, J. A. J eevarajan, Y. Wang, Enhanced Cycleability of $LiMn_2O_4$ Cathodes by Atomic Layer Deposition of Nanosized-Thin Al_2O_3 Coatings. *Nanoscale* 3 (2011) 1465-1469.

87. J. Zhao, Y. Wang, Ultrathin Surface Coatings for Improved Electrochemical Performance of Lithium Ion Battery Electrodes at Elevated Temperature. *The Journal of Physical Chemistry C* 116 (2012) 11867-11876.

88. D. Guan, Y. Wang, Ultrathin Surface Coatings to Enhance Cycling Stability of $LiMn_2O_4$ Cathode in Lithium-Ion Batteries. *Ionics* 19 (2013) 1-8.

89. Nanodevice laboratory, *website of Hyungjun's Kim's research group*: http://nanodevice.yonsei.ac.kr/?mid=topic_nanopattern.

90. K. Leung, Y. Qi, K. R. Zavadil, Y. S. Jung, A. C. Dillon, A. S. Cavanagh, S. H. Lee, S. M. George, Using Atomic Layer Deposition to Hinder Solvent Decomposition in Lithium Ion Batteries: First-Principles Modeling and Experimental Studies. *Journal of The American Chemical Society* 133 (2011) 14741-14754.

91. Y. S. Jung, A. S. Cavanagh, L. A. Riley, S. H. Kang, A. C. Dillon, M. D. Groner, S. M. George, S. H. Lee, Ultrathin Direct Atomic Layer Deposition on Composite Electrodes for Highly Durable and Safe Li-Ion Batteries. *Advanced Materials* 22 (2010) 2172-2176.

92. L. A. Riley, S.V. Atta, A. S. Cavanagh, Y. Yan, S. M. George, P. Liu, A. C. Dillon, S. H. Lee, Electrochemical Effects of ALD Surface Modification on Combustion Synthesized $LiNi_{1/3}Mn_{1/3}Co_{1/3}O_2$ as a Layered-Cathode Material. *Journal of Power Sources* 196 (2011) 3317-3324.

93. Y. S. Jung, A. S. Cavanagh, A. C. Dillon, M. D. Groner, S. M. George, S. H. Lee, Enhanced Stability of $LiCoO_2$ Cathodes in Lithium-Ion Batteries Using Surface Modification by Atomic Layer Deposition. *Journal of The Electrochemical Society* 157 (2010) A75-A81.

94. I. D. Scott, Y. S. Jung, A. S. Cavanagh, Y. Yan, A. C. Dillon, S. M. George, S. H. Lee, Ultrathin Coatings on Nano-$LiCoO_2$ for Li-Ion Vehicular Applications. *Nano Letters* 11 (2011) 414-418.

95. S. H. Jin, G. H. Jun, S. H. Hong, S. Jeon, Conformal Coating of Titanium Suboxide on Carbon Nanotube Networks by Atomic Layer Deposition for Inverted Organic Photovoltaic Cells. *Carbon* 50 (2012) 4483-4488.

96. X. Meng, D. Geng, J. Liu, R. Li, X. Sun, Controllable Synthesis of Graphene-Based Titanium Dioxide Nanocomposites by Atomic Layer Deposition. *Nanotechnology* 22 (2011) 165602.

97. J. T. Lee, F. M. Wang, C. S. Cheng, C. C. Li, C. H. Lin, Low-Temperature Atomic Layer Deposited Al_2O_3 Thin Film on Layer Structure Cathode for Enhanced Cycleability in Lithium-Ion Batteries. *Electrochimica Acta* 55 (2010) 4002-4006.

98. R. Mukherjee, R. Krishnan, T. M. Lu, N. Koratkar, Nanostructured Electrodes for High-Power Lithium Ion Batteries. *Nano Energy* 1 (2012) 518-533.

99. L. Hu, N. Liu, M. Eskilsson, G. Zheng, J. McDonough, L. Wågberg, Y. Cui, Silicon-Conductive Nanopaper for Li-ion Batteries, *Nano Energy* 2 (2013) 138-145.

100. I. Meschini, F. Nobili, M. Mancini, R. Marassi, R. Tossici, A. Savoini, M. L. Focarete, F. Croce, High-Performance Sn@Carbon Nanocomposite Anode for Lithium Batteries. *Journal of Power Sources* 226 (2013) 241-248.

101. F. Amalraj, D. Kovacheva, M. Talianker, L. Zeiri, J. Grinblat, N. Leifer, G. Goobes, B. Markovsky, D. Aurbach, Synthesis of Integrated Cathode Materials $x\mathrm{Li_2MnO_3}\cdot(1\text{-}x)\,\mathrm{LiMn_{1/3}Ni_{1/3}Co_{1/3}O_2}$ $(x = 0.3\,,\,0.5\,,\,0.7)$ and Studies of Their Electrochemical Behavior. *Journal of The Electrochemical Society* 157 (2010) A1121-A1130.

CHAPTER 2. ULTRATHIN ZnO SURFACE COATINGS ON $LiMn_2O_4$ CATHODES FOR IMPROVED ELECTROCHEMICAL PERFORMANCE OF LITHIUM-ION BATTERY ELECTRODES AT ELEVATED TEMPERATURE

2.1 Introduction

Lithium manganese oxide ($LiMn_2O_4$) has been considered as a promising cathode alternative to the commercial lithium cobalt oxide ($LiCoO_2$) for rechargeable lithium-ion batteries (LIBs) due to its nontoxicity, low cost, excellent rate capability for applications in portable electronic devices and plug-in electric vehicle [1,2]. However, this electrode material suffers from the Mn dissolution, crystal structure transformation and electrolyte decomposition during electrochemical cycling, especially at the elevated temperature. The poor capacity retention of $LiMn_2O_4$ cathode material limits its practical applications [3-6]. Mn dissolution during electrochemical cycling is caused by the attack from the acidic hydrofluoric acid (HF) formed by the residual H_2O and hexafluorophosphate ($LiPF_6$) in the electrolyte. This irreversible decomposition of $LiMn_2O_4$ yields impurity phases of the rock salt phase (Li_2MnO_3) and tetragonal phase ($Li_2Mn_2O_4$), which is the key factor for the capacity fading [7,8]. Phase transition of the spinel $LiMn_2O_4$ also occurs, and the crystal structure of $LiMn_2O_4$ changes from the cubic to tetragonal symmetry during long-term cycling. Such structural degradation resulted from the Jahn-Teller effect considerably increases the disorder of lithium ions [9]. The strong oxidation ability of Mn^{4+} at the end of charge reaction will bring about the decomposition of electrolyte on the surface of the working electrode. The formed solid electrolyte interphase (SEI) can cause increased charge transition resistance and distinct electrochemical polarization on the electrode [2]. The factors mentioned above will together result in poor capacity retention of $LiMn_2O_4$ [7].

The surface modification technique has been reported as an effective approach to improve the cycling performance of $LiMn_2O_4$ by coating different conductive carbon materials, phosphates, amphoteric oxides and composite oxides [3-5,10-14]. In order to circumvent the key issue of Mn dissolution for $LiMn_2O_4$, various oxides such as Al_2O_3, ZnO, ZrO_2, MgO, SiO_2, TiO_2, Cr_2O_3 and SnO_2 have been employed as surface coatings to protect $LiMn_2O_4$ particles from the HF's attack in electrolyte [6-9, 15-22]. The oxide coating on $LiMn_2O_4$ scavenges trace hydrogen fluoride acids (HF) in LIBs, and thus slows down dissolution of manganese ions and degradation of organic electrolyte at cathode, resulting in better electrochemical performance of $LiMn_2O_4$. Most surface modifications of lithium transition metal oxides reported in literature are carried out with wet chemical methods such as sol-gel processing or solution processing [5,23], such as soaking cathode materials into a nano-alumina sol [24]. Other methods include melting impregnation method and pulsed laser deposition [20,25]. However, these methods are not well-controlled processes. The resulted coatings lack conformality, uniformity, and completeness. One is not capable of controlling or tuning the coating thickness and quantity by using these methods, which limits the repeatability, reliability, and optimization of these processes.

Moreover, wet chemistry methods require a large amount of solvent and precursor, and a post-heat-treatment to obtain the desired coatings. In addition, nanostructured battery electrodes have received tremendous attention lately, owning to their high surface area and high capacities. However, coatings resulted from wet processing are usually 50-100 nm thick [26], which is too thick to be coated onto nanostructured electrodes. Moreover, the conventional thick oxide coatings on the cathode materials would hinder Li ion diffusivity, resulting in both low energy and power density of the working electrodes [27]. Therefore, it is necessary to explore new surface coatings that are much thinner and have high conformality for next-generation battery technology.

In this study, we deposit ultra-thin and highly-conformal oxide coatings onto $LiMn_2O_4$ by using the atomic layer deposition (ALD) method with precise thickness control at atomic scale. ALD requires only a minimal amount of precursor and can be used to deposit ultra-thin and highly-conformal surface coatings [28,29]. The basic advantage of ALD lies in the fact that the film growth is surface controlled, rather than source controlled as in many other deposition methods such as chemical vapor deposition (CVD). This is achieved by using sequential exposures, separating the (usually binary) reaction between the precursor compounds into two half-reactions. During each half-reaction, only one monolayer of the reactant chemisorbs (or is chemically bound) on the surface. Further layers which are only physisorbed are removed by an inert gas purge before the other reactant is introduced. As a result, the process proceeds step-wise in self-limiting surface reactions, separated by purge steps. Hence, films grown using ALD are typically uniform, dense, homogenous, pinhole-free, and extremely conformal to the underlying substrate. Moreover, ALD has excellent step coverage (~100%) and refilling ability on particles and porous structures [27, 29-31].

2.2 Objectives of Project

To date, there are only a few reports about surface modifications of lithium-ion battery electrodes via ALD coatings and most of them focused on $LiCoO_2$ [32-39]. To the best of our knowledge, there is no report about the effect of ALD coatings on electrochemical properties of $LiMn_2O_4$ so far, except a communication paper we published recently [6]. In the present work, we fabricate ZnO ALD modified $LiMn_2O_4$ cathodes to enhance cycling performances of cathodes at both room temperature (25ºC) and elevated temperature (55ºC). The ZnO ALD coatings are either deposited onto individual $LiMn_2O_4$ particles or onto entire $LiMn_2O_4$ composite electrode. Both these two types of ALD-modified cathodes show enhanced cycleability compared to bare cathodes at room temperature and elevated temperature. Furthermore, cycling performances of coated cathodes are optimized by manipulating the coating thickness via varying ALD growth cycles. Electrode composed of $LiMn_2O_4$ particles coated with 6 ZnO ALD layers shows the best cycling performance even at the elevated temperature (55°C), which can be considered as a very promising electrode applied to the elevated temperature environment.

2.3 Experimental Section

2.3.1 Atomic layer deposition of ZnO coating on $LiMn_2O_4$ particles and bare composite electrode

Atomic layer deposition of ZnO coatings on $LiMn_2O_4$ particles (Alfa Aesar, 99.5%) was carried out in a Savannah 100 ALD system (Camabridge NanoTech Inc.) at 120°C using $Zn(CH_2CH_3)_2$ (diethylzinc, DEZ) and H_2O as precursors with exposure time of 0.015 s, waiting time of 5 s and purge time of 40 s. The principle of ZnO ALD growth from H_2O and DEZ is subjected to the two self-terminating reactions as follows [36, 40, 41]:

$$ZnOH^* + Zn(CH_2CH_3)_2 \rightarrow ZnO–ZnCH_2CH_3^* + CH_3CH_3$$
$$ZnCH_2CH_3^* + H_2O \rightarrow ZnOH^* + CH_3CH_3$$

$LiMn_2O_4$ particles were coated with 2, 6, 10 and 50 ZnO ALD layers via corresponding ALD growth cycles, respectively.

The bare composite electrodes (abbreviated as B-E) were composed of 80% bare $LiMn_2O_4$ particles, 10% acetylene black (conductive carbon, Alfa Aesar, 99.5%) and 10% poly-vinylidenefluoride (PVDF, Alfa Aesar) as the binder, dissolved in N-methyl-2-pyrrolidone (NMP) solvent. The resultant viscous slurry was coated onto the aluminum current collector using the AFA-III automatic film applicator (MTI) with the thickness setting of 500 μm and then dried at 120°C overnight under vacuum. The dried electrodes were pressed to an effective thickness of 50 μm by using the EQ-MR100A rolling press machine (MTI). Approximately 10 mg active material was loaded in the circular working electrode with a diameter of 18.9 mm. The bare composite electrodes were coated with 2, 6 and 10 ZnO ALD layers, respectively (abbreviated as 2 ZnO ALD-E, 6 ZnO ALD-E and 10 ZnO ALD-E). Other comparative composite electrodes were prepared by mixing $LiMn_2O_4$ particles coated with 2, 6 and 10 ZnO ALD layers with conductive carbon and PVDF binder at the same weight ratio of 80:10:10, respectively. (abbreviated as 2 ZnO ALD LMO-E, 6 ZnO ALD LMO-E and 10 ZnO ALD LMO-E).

2.3.2 Characterizations

The crystallographic structure of bare and ZnO ALD coated $LiMn_2O_4$ powders were examined by using a Rigaku MiniFlex X-ray diffractometer with Cu K_α radiation at a scan rate of 4^o/min. The particle size and surface morphology were observed using a FEI Quanta 3D FEG field emission scanning electron microscopy (FESEM). Transmission electron microscopy (TEM) images were captured on a JEM-2010 instrument microscopy at an acceleration voltage of 200 kV, to investigate the characteristics of the ZnO coatings. Surface compositions of $LiMn_2O_4$ particles coated with 6 ZnO ALD layers and $LiMn_2O_4$ composite electrode coated with 6 ZnO ALD layers were analyzed via X-ray photoelectron spectroscope (XPS) using an

AXIS 165 spectrometer with a twin-anode Al K_α (1486.6 eV) X-ray source. All the XPS spectra were calibrated according to the binding energy of the C1s peak at 284.8 eV.

2.3.3 Electrochemical measurements

Different $LiMn_2O_4$-based composite electrodes were integrated into two-electrode CR2032-type coin cells for electrochemical measurements, with $LiMn_2O_4$-based composite electrode as cathode, metallic lithium foil as anode, Celgard-2320 membrane as separator; electrolyte was 1 M $LiPF_6$ dissolved in ethylene carbonate (EC) and dimethyl carbonate (DMC) and diethyl carbonate (DEC) at a volumetric ratio of 1:1:1. The coin cells were assembled in an argon-filled glove box (OMNI-Lab system, Vacuum Atmosphere Co.). Galvanostatic charge and discharge were performed in a voltage range of 3.4-4.5 V at a current density of 120 mA/g using an 8-channel battery analyzer (MTI Corporation) at room temperature (25^{o}C) and elevated temperature (55^{o}C). Electrochemical specific storage capacities of working electrodes were calculated based on the mass of cathode materials. In addition, cyclic voltammetry (CV) curves of 6 ZnO ALD LMO-E were measured at a scan rate of 0.1mVs^{-1} between 3.4 and 4.5 V using an electrochemical analyzer (CHI605C) at 25^{o}C and 55^{o}C, respectively.

2.4 Results and Discussion

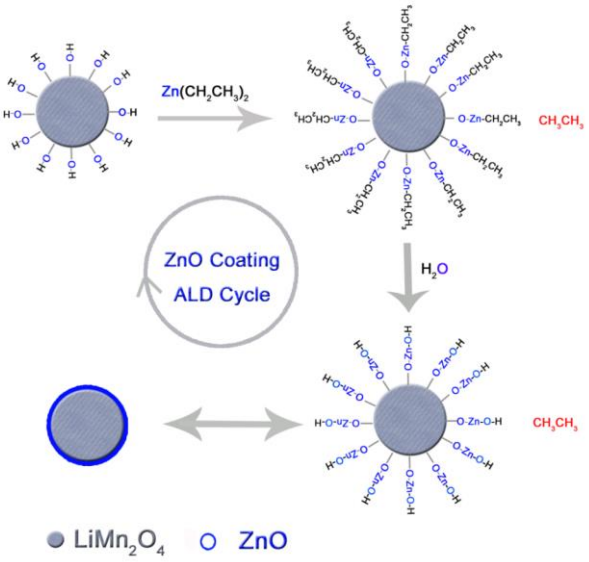

Figure 2.1 Schematic representation for ZnO ALD growth on the surface of $LiMn_2O_4$ particle using $Zn(CH_2CH_3)_2$ and H_2O as precursors.

Ultrathin ZnO coatings can be deposited onto the surface of $LiMn_2O_4$ particles via ALD with high conformality and exquisite thickness control at the Angstrom or monolayer level. As shown in the schematic representation of ZnO ALD growth in Figure 2.1, ZnO film grows monolayer by monolayer due to the sequential and

self-limiting surface reactions. The self-limiting aspect of ALD leads to excellent step coverage and conformal deposition on high aspect ratio structures. Another advantage of ALD approach is that it allows for direct deposition of ZnO on either as-prepared composite electrodes or individual electrode material particles, providing commercial feasibility for mass industrial production for lithium ion batteries [6, 28, 32].

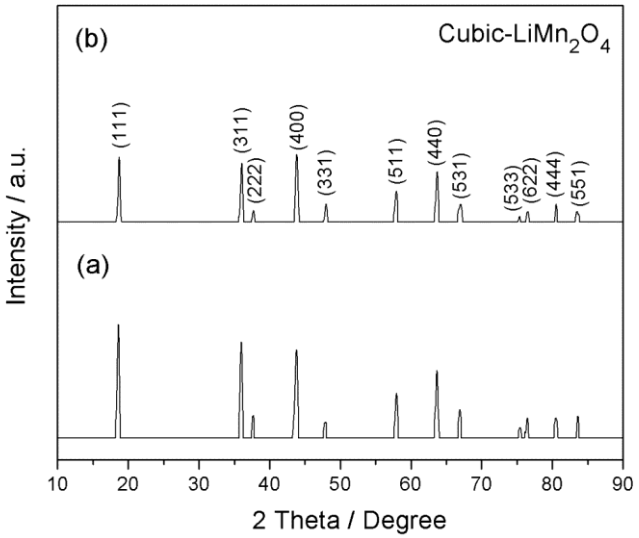

Figure 2.2 XRD patterns of (a) bare $LiMn_2O_4$ particles and (b) $LiMn_2O_4$ particles coated with 6 ZnO ALD layers.

X-ray diffraction (XRD) pattern of $LiMn_2O_4$ particles coated with 6 ZnO ALD layers (via 6 ALD growth cycles) is displayed in Figure 2.2 in comparison with that of bare $LiMn_2O_4$ particles. All distinct XRD peaks from the sample of 6 ZnO ALD LMO ($LiMn_2O_4$ particles coated with 6 ZnO ALD layers) are well indexed to the spinel cubic structure of $LiMn_2O_4$ with a *F3dm* space group (JCPDS: 35-0782). The ZnO phase is not detectable even when 50 ZnO ALD layers are coated on pristine $LiMn_2O_4$ particles, which can be ascribed to the amorphous phase and low weight ratio of ZnO.

Figure 2.3 reveals the morphology and composition of $LiMn_2O_4$ particles before and after ZnO ALD coatings. Figure 2.3a and b present SEM images of bare $LiMn_2O_4$ particles and $LiMn_2O_4$ particles coated with 6 ZnO ALD layers, respectively. As can be seen from Figure 2.3a, $LiMn_2O_4$ particles have an average particle size of ~5 μm with smooth polyhedron profile. Figure 2.3b shows the shape and morphology of $LiMn_2O_4$ particles coated with 6 ZnO ALD layers, which are almost identical to bare $LiMn_2O_4$ particles in Figure 2.3a. There is no visible difference in the SEM image after the $LiMn_2O_4$ particles are coated with ZnO ALD film, possibly because the ALD coating is ultrathin and highly-conformal and thus preserves the morphology of $LiMn_2O_4$ particles. Even when $LiMn_2O_4$ particles are coated with 50 ZnO ALD layers, the coated particles retain the same morphology and shape of bare particles as observed under SEM, suggesting the high conformality of ALD coating.

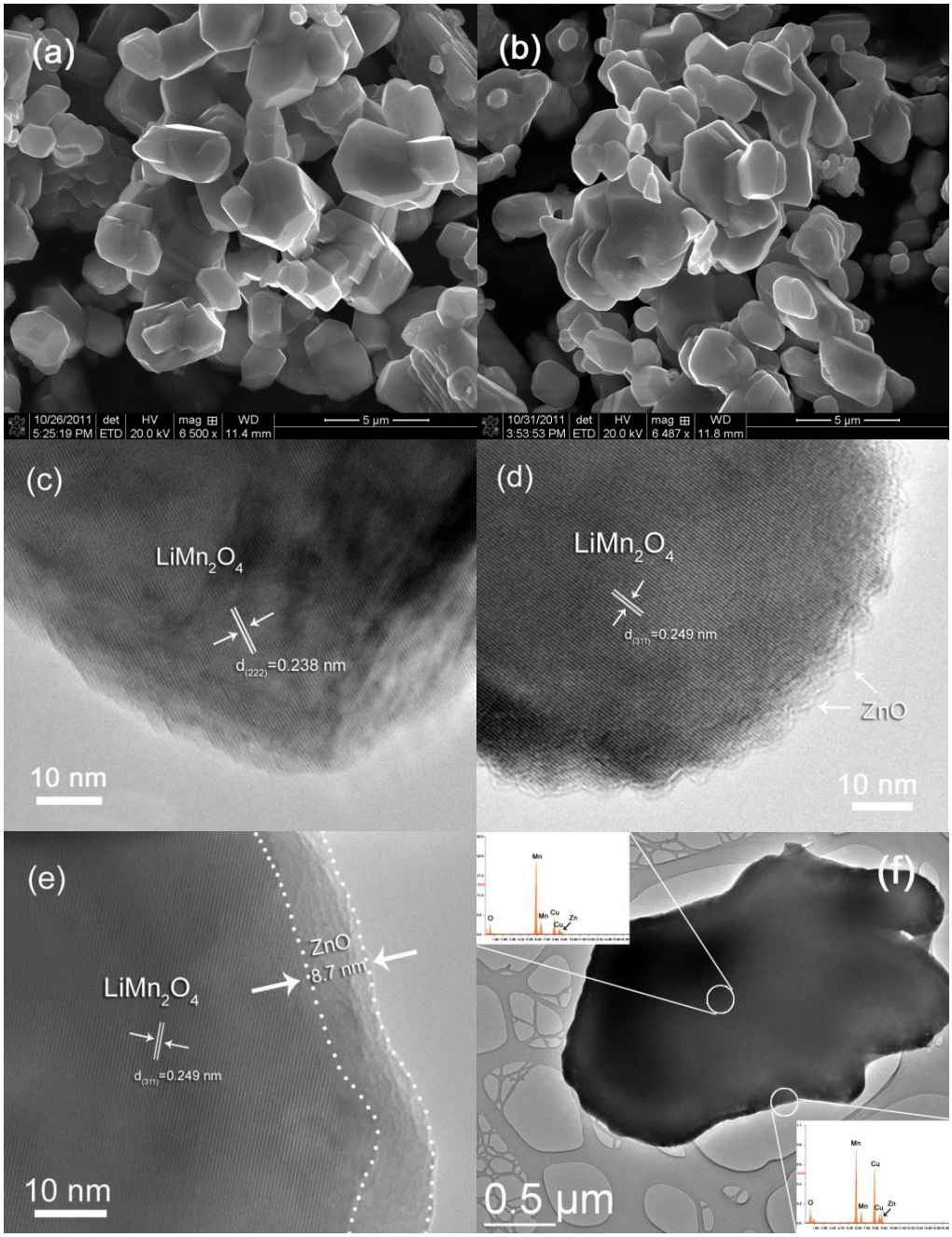

Figure 2.3 SEM images of (a) bare $LiMn_2O_4$ particle and (b) $LiMn_2O_4$ particle coated with 6 ZnO ALD layers; and HRTEM images of (c) bare $LiMn_2O_4$ particle, (d) $LiMn_2O_4$ particle coated with 6 ZnO ALD layers, (e) $LiMn_2O_4$ particle coated with 50 ZnO ALD layers, and (f) TEM image of $LiMn_2O_4$ particle coated with 50 ZnO ALD layers (Insets: EDS captured at the center and edge of this particle).

To study the details of ALD coatings, high-resolution TEM (HRTEM) is used to examine uncoated and ALD-coated $LiMn_2O_4$ particles. Figure 2.3c and d present HRTEM images of a bare $LiMn_2O_4$ particle and a $LiMn_2O_4$ particle coated with 6 ZnO ALD layers. It is noted that bare $LiMn_2O_4$ particle is crystalline, as lattice fringes are observed in Figure 2.3c with $d_{(222)}$ = 0.238 nm, while TEM image of the ZnO

coated $LiMn_2O_4$ (Figure 2.3d) reveals that a very thin and amorphous ALD coating fully and conformally enwraps around the crystalline $LiMn_2O_4$ particle. To obtain more information about ALD coatings, $LiMn_2O_4$ particles are coated with thicker ZnO ALD film (50 ALD layers using 50 ALD growth cycles) and are examined under HRTEM, as presented in Figure 2.3e and f. Figure 2.3e clearly shows that an amorphous and homogeneous ALD film is conformally coated on the crystalline $LiMn_2O_4$ particle. Thickness of the coating is estimated to 8.7 nm, corresponding to an ALD growth rate of 1.7 Å/cycle. In order to confirm the deposition of ZnO on the surface of $LiMn_2O_4$, energy dispersive X-ray spectroscopy (EDS) is used to examine the compositions at the center and the edge of coated $LiMn_2O_4$ respectively, as shown in the inset graphs of Figure 2.3f. Both EDS spectra reveal the elements of O, Mn, Zn, and Cu. The Cu peaks are from the copper grid where the TEM sample is placed on. It is noted that the atomic percent of Zn on the edge is 10.9 %, larger than 7.1% in the center, confirming the formation of ZnO coating on the surface of $LiMn_2O_4$ particle. Therefore, from the SEM and TEM results in Figure 2.3, we can conclude that ZnO ALD coatings are ultrathin, dense, uniform, highly-conformal, and provide full coverage of $LiMn_2O_4$ particles.

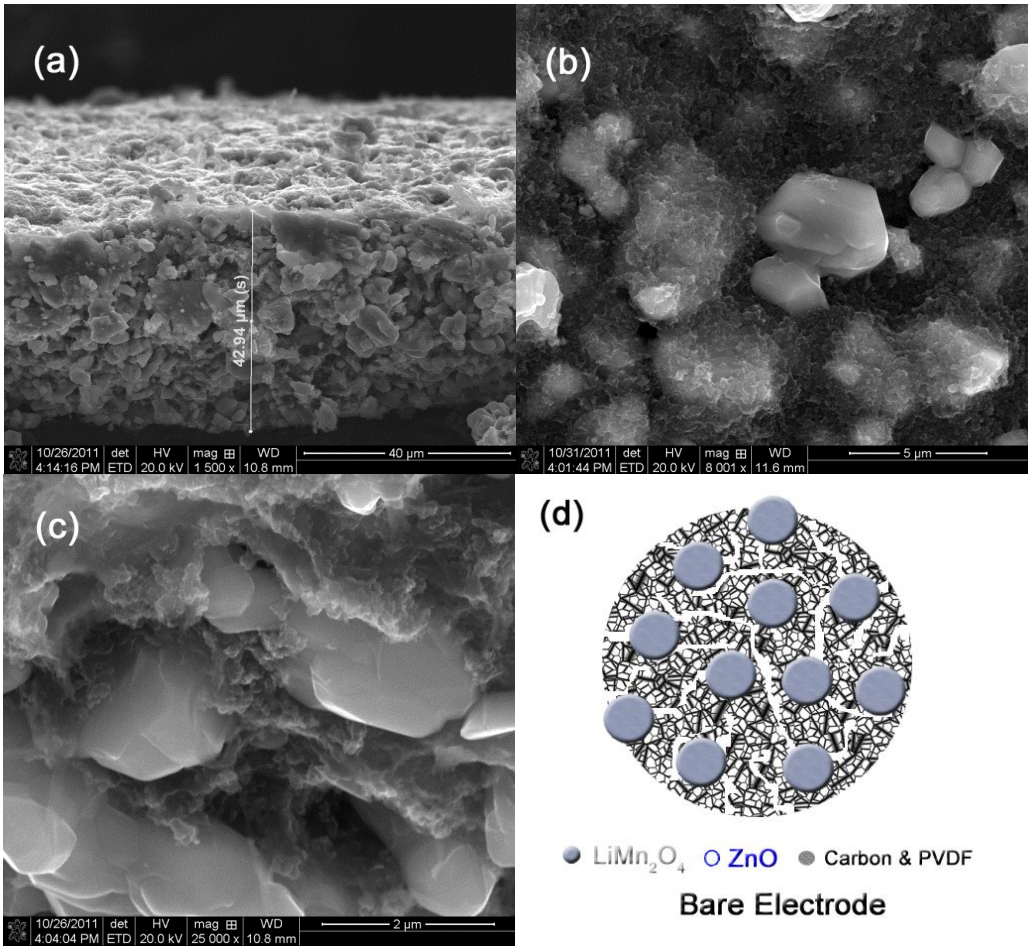

Figure 2.4 (a) cross-section SEM image, (b) surface view, (c) enlarged cross-section SEM image, and (d) schematic representation of bare $LiMn_2O_4$ composite electrode.

Before integrating into lithium-ion battery cells, $LiMn_2O_4$ cathode is fabricated by mixing 80% $LiMn_2O_4$ particles, 10% acetylene black as conducting material, and 10% poly-vinylidenefluoride (PVDF) as a binder. Figure 2.4a, 4b, and 4c show the SEM images of cross-section view, surface view, and enlarged cross-section view of $LiMn_2O_4$ cathode, respectively. The cathode shows an even thickness of ~ 43 μm (Figure 2.4a). As seen from the surface morphology (Figure 2.4b) and the cross-section profile of $LiMn_2O_4$ cathode (Figure 2.4c), $LiMn_2O_4$ particles are immersed in a porous network composed of smaller carbon and PVDF particles. Figure 2.4d exhibits a schematic illustrating this morphology and structure of $LiMn_2O_4$ cathode.

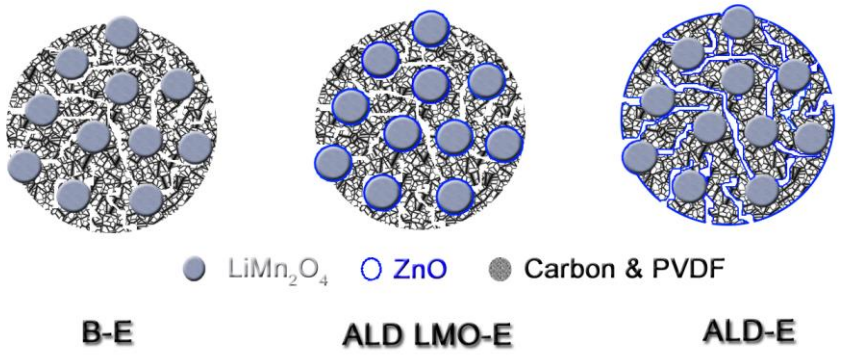

Figure 2.5 Schematic representations of bare $LiMn_2O_4$ composite electrode (left), electrode composed of ALD-coated $LiMn_2O_4$ particles and uncoated carbon/PVDF (center), and ALD-coated $LiMn_2O_4$ composite electrode (right).

We have prepared three types of $LiMn_2O_4$-based electrodes as shown in the schematics in Figure 2.5. One is bare electrode consisting of bare $LiMn_2O_4$ particles, carbon and PVDF, denoted by "B-E". The second type of electrode is composed of ALD-coated $LiMn_2O_4$ particles, carbon and PVDF, denoted by "ALD LMO-E". The third is obtained by depositing ALD coating onto the entire bare electrode, which is marked with "ALD-E". Since ALD allows for the growth of conformal films even on substrates with complex surface geometries [6, 32, 35, 36], ZnO film will penetrate into the porous electrode, and coat onto both micron-sized $LiMn_2O_4$ particles and porous framework bridged by carbon and PVDF in the case of "ALD-E", as illustrated in the right picture of Figure 2.5. $LiMn_2O_4$ particles are partially covered by ALD coatings, because $LiMn_2O_4$ particles are tightly enwrapped by carbon and PVDF network as shown in the cross-section SEM image of electrode (Figure 2.4c). Therefore, in these three different electrodes, there are various interfaces between $LiMn_2O_4$ particles, ALD coatings, carbon and PVDF composites, and surrounding electrolyte, to affect electron transport and Li-ion diffusion during delithiation and lithiation reactions, resulting in different electrochemical behaviors of these electrodes. It is noted that SEM images captured from electrode composed of $LiMn_2O_4$ particles coated with 6 ZnO ALD layers and uncoated carbon/PVDF network, $LiMn_2O_4$

composite electrode coated with 6 ZnO ALD layers, and $LiMn_2O_4$ composite electrode coated with 50 ZnO ALD layers are all similar to the SEM image of bare $LiMn_2O_4$ composite electrode, indicating that ZnO ALD coatings on the composite electrodes are ultrathin, homogeneous and highly-conformal.

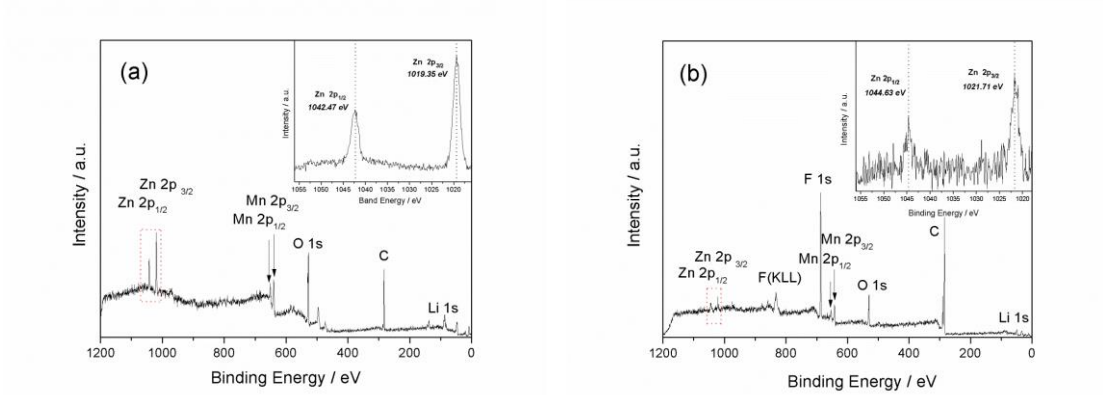

Figure 2.6 XPS spectra of (a) $LiMn_2O_4$ particles coated with 6 ZnO ALD layers, and (b) $LiMn_2O_4$ composite electrode coated with 6 ZnO ALD layers.

To confirm the formation of ZnO on the surface of $LiMn_2O_4$ particles and $LiMn_2O_4$ electrode, X-ray photoelectron spectroscopy (XPS) is used to analyze the surface compositions of $LiMn_2O_4$ particles coated with 6 ZnO ALD layers and $LiMn_2O_4$ composite electrode coated with 6 ZnO ALD layers, respectively, as shown in Figure 2.6. Both spectra show the Zn $2p_{3/2}$ and $2p_{1/2}$ peaks from ZnO, indicating the existence of ZnO on the surface of the samples. However, the binding energies of the Zn $2p_{3/2}$ and $2p_{1/2}$ in XPS spectrum of 6 ZnO ALD LMO are 1019.4 eV and 1042.5 eV (Figure 2.6a), respectively, shifting ~2 eV to the lower binding energy in comparison with the standard values of ZnO (1021.7 eV and 1044.7 eV) in NIST XPS Database, while the binding energies of Zn $2p_{3/2}$ of 1021.7 eV and $2p_{1/2}$ of 1044.6 eV observed for 6 ZnO ALD-E sample in Figure 2.6b are consistent with standard values of ZnO. This difference is possibly due to different chemical and bonding environments of ZnO ALD coatings on $LiMn_2O_4$ particles and $LiMn_2O_4$ composite electrode. In ALD coating, substrate material and ZnO coating film are bridged by the chemical bond, oxygen bond (Substrate-O-ZnO) illustrated in Figure 2.1. In 6 ZnO ALD-E the ZnO is mainly deposited on conductive carbon due to the hydrophobic selection property of PVDF to hydroxyl groups (Figure 2.5) [35], while in 6 ZnO ALD LMO the ZnO is grown tightly on $LiMn_2O_4$ particles. We speculate that the different electronic distribution and polarity of substrate materials ($LiMn_2O_4$ and Carbon) influence the chemical environment of ZnO coating via oxygen bond, contributing to the peak shift of Zn 2p in 6 ZnO ALD LMO.

The three types of electrodes shown in Figure 2.5 are then integrated into CR2032-type coin cells with lithium as anode for electrochemical testing. Electrochemical measurements are performed for bare electrode (“B-E”), electrodes coated with ALD films of various thicknesses (2, 6, 10 ZnO ALD layers) (samples denoted by “2 ZnO ALD-E”, “6 ZnO ALD-E”, “10 ZnO ALD-E”), and electrode composed of $LiMn_2O_4$ particles coated with 2, 6 and 10 ZnO ALD layers and

carbon/PVDF (marked with "2 ZnO ALD LMO-E, 6 ZnO ALD LMO-E and 10 ZnO ALD LMO-E"). Figure 2.7 summarizes cycling performances of these electrodes cycled at a current density of 120 mA/g in a voltage range of 3.4 - 4.5 V at 25°C and 55°C. All ALD-modified $LiMn_2O_4$ electrodes exhibit higher final capacities than bare cathode after 100 electrochemical cycles. ZnO coatings have been reported as the most effective HF scavenger among Al_2O_3, ZrO_2 and SnO_2 to protect $LiMn_2O_4$ particles from the detrimental Mn dissolution.[15] The ZnO thin film can serve as an amorphous interphase between electrode and electrolyte to prevent from electrolyte decomposition and formation of the insulating solid electrolyte interphase (SEI) on the surface of working electrode [2, 28].

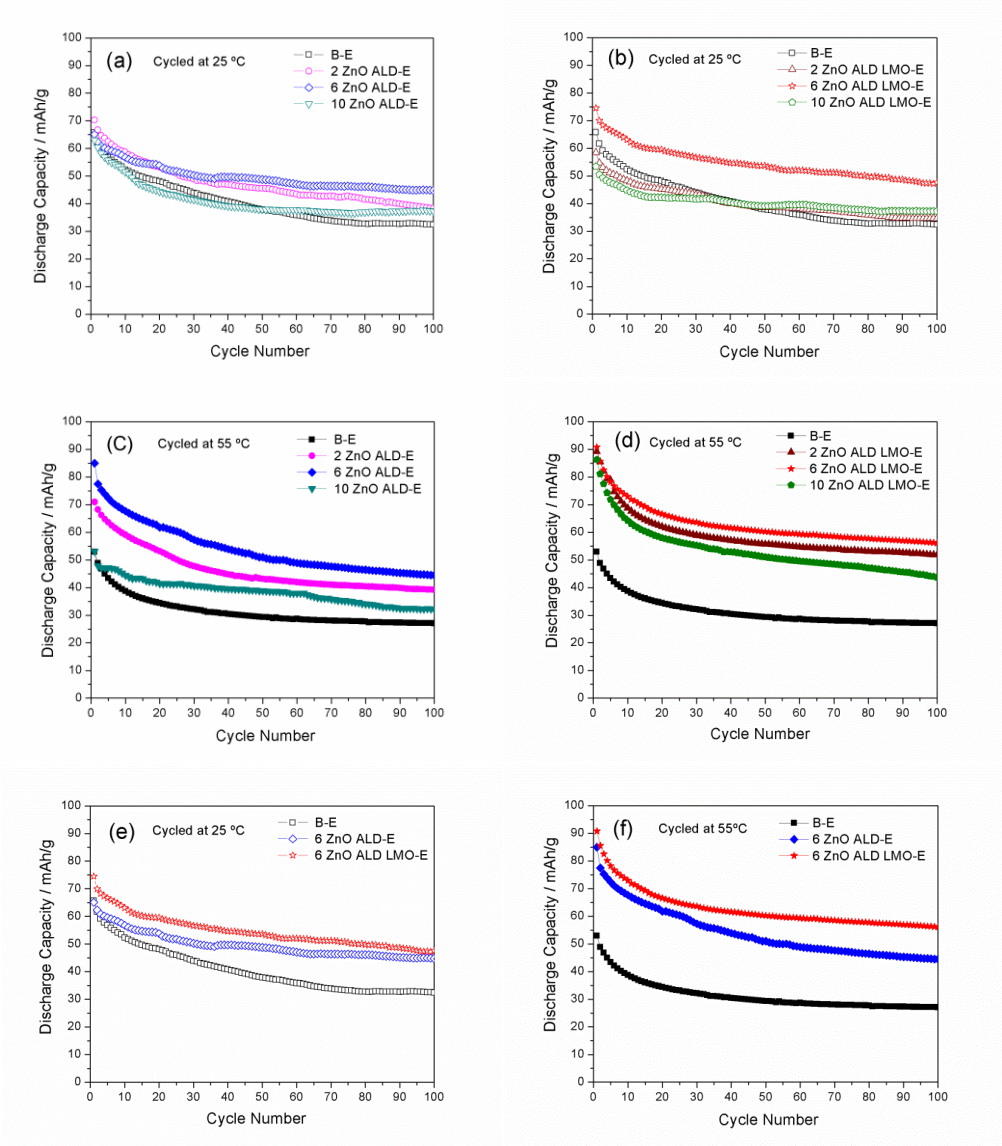

Figure 2.7 Cycling performances of various electrodes at a current density of 120 mA/g in a voltage range of 3.4 - 4.5 V *vs*. Li/Li^+. (a), (b) and (e): cycled at 25ºC; (c), (d) and (f): cycled at 55ºC. "B-E": bare $LiMn_2O_4$ composite electrode; "*n* ZnO ALD-E": $LiMn_2O_4$ composite electrode coated with *n* ZnO ALD layers; "*n* ZnO ALD LMO-E": electrode composed of $LiMn_2O_4$ particles coated with *n* ZnO ALD layers and uncoated carbon/PVDF network.

It has been estimated from the TEM results in Figure 2.3 that the growth rate of this ZnO ALD is 1.7 Å/cycle and thus one ALD layer is 1.7 Å thick. As shown in Figure 2.7a and 7c, the electrode coated with 6 ZnO ALD layers (1.02 nm thick) delivers the best cycling performance and the highest final capacity among the electrodes coated with ZnO ALD films of different thicknesses, either at 25^{o}C or 55^{o}C. This "6 ZnO ALD-E" delivers a final capacity of 44.5 mAh/g after 100 electrochemical cycles at 1 *C* at 55^{o}C, much higher than the final capacity of 27.0 mAh/g delivered by bare electrode at 55^{o}C. When ZnO is coated on $LiMn_2O_4$ particles as shown in Figure 2.7b and 7d, 6 ZnO ALD layers are also the optimal thickness for the best cycling performance either at room temperature or elevated temperature. When the ALD coating is too thin, it is not sufficient to scavenge the harmful HF generated during electrochemical cycling and thus the effect of surface coating to enhance the performance of electrode is less distinct, as observed for electrodes coated with 2 ALD layers. On the other hand, an overly thick ZnO ALD coating will slow down the diffusion of lithium ions at the interface between electrode and electrolyte and will thus reduce the capacities of the electrode [27], as observed for electrodes coated with 10 ALD layers. Therefore, it is feasible to accurately tune the thickness of ALD coatings for ultimate optimization of lithium-ion battery performances, because ALD offers precise thickness control at atomic level. In addition, the protective effect of ZnO ALD coatings to the $LiMn_2O_4$ electrode is even more obvious when the electrode is cycled at elevated temperature than cycled at room temperature, by comparing Figure 2.7a and 7c for ZnO coated electrodes as well as Figure 2.7b and 7d for ZnO modified $LiMn_2O_4$ particles. In comparison with ALD oxide coatings on different nano-sized cathode materials, such as $LiCoO_2$ [27, 35, 36] and $LiNi_{1/3}Mn_{1/3}Co_{1/3}O_2$ [34], the initial capacity drops during first several cycles in this work are probably due to the micron-sized $LiMn_2O_4$ particles which have an average size of 5 μm, inevitable Mn dissolution in $LiMn_2O_4$-based cathodes and the resultant electrochemical polarization of the cathodes at a relatively high current density of approximate 1 *C*. It is found in our other work that there is much less distinct initial capacity degradation for nano-sized $LiMn_2O_4$ and this work has been submitted elsewhere. There is also ongoing work in our laboratory to alleviate the initial capacity drops via heat treatments of micro-sized $LiMn_2O_4$. Furthermore, at the elevated temperature, $LiMn_2O_4$ suffers from faster capacity fading, because high temperature accelerates side reactions and electrolyte decomposition in battery cells which will induce more severe Mn dissolution [42].

Figure 2.7a-7d indicate that ZnO coating on $LiMn_2O_4$ particles is more sensitive for improved electrochemical performance than ZnO depositing on composite electrodes. Figure 2.7e and 7f present cycling performances of bare electrode ("B-E"), $LiMn_2O_4$ electrode coated with 6 ZnO ALD layers ("6 ZnO ALD-E"), and the electrode composed of $LiMn_2O_4$ particles coated with 6 ZnO ALD layers and carbon/PVDF ("6 ZnO ALD LMO-E") at 25ºC and 55ºC, respectively. Differences in the morphology and structure of these three electrodes are illustrated in Figure 2.5 earlier. It is interesting to note that "6 ZnO ALD LMO-E" shows even better cycling performance and higher capacities than "6 ZnO ALD-E". As shown in Figure 2.7e, "6

ZnO ALD LMO-E" delivers an initial discharge capacity of 74.6 mAh/g at 25ºC, higher than the initial capacities of 65.1 mAh/g from "6 ZnO ALD-E" and 65.7 mAh/g from "B-E" at 25ºC. The increased capacity of "6 ZnO ALD LMO-E" can be attributed to the following factors: (1) ZnO film is fully coated onto $LiMn_2O_4$ particles in "6 ZnO ALD LMO-E", while ZnO film is partially coated onto $LiMn_2O_4$ particles within the ZnO coated carbon/PVDF network in "6 ZnO ALD-E" as shown in Figure 2.5; this difference in ZnO ALD coverage of $LiMn_2O_4$ particles may contribute to the higher capacities of "6 ZnO ALD LMO-E" than "6 ZnO ALD-E"; (2) The semi-conducting ZnO film can average the distribution of electrons and lithium ions around the whole $LiMn_2O_4$ surface to take full advantages of the active sites for Li^+ insertion and extraction; the polarization from the concentration difference of Li^+ and electrons can be reduced in the working electrode; (3) The conformal and dense ZnO coatings, as shown in Figure 2.1 and Figure 2.3d, can serve as a solid framework to restrain the phase transition of $LiMn_2O_4$ from cubic to tetragonal structure, and thus to prevent the harmful Jane-Taller effect; (4) Dissolution of Mn ions into the internal structure of carbon and PVDF network can be reduced due to the complete ZnO coverage on $LiMn_2O_4$ particles in "6 ZnO ALD LMO-E", while ZnO coverage on $LiMn_2O_4$ particles is partial in "6 ZnO ALD-E" (Figure 2.5). Therefore, "6 ZnO ALD LMO-E" delivers the highest discharge capacity. However, the capacity retention of "6 ZnO ALD LMO-E" after 100 cycles is slightly less good than that of "6 ZnO ALD-E", possibly due to less ZnO content in "6 ZnO ALD LMO-E" to completely consume the HF. As shown in Figure 2.5, the composite electrode can be coated with more ZnO than $LiMn_2O_4$ particles, because the electrode composed of micron-sized $LiMn_2O_4$ particles buried in porous carbon/PVDF network has larger surface area than micron-sized $LiMn_2O_4$ particles.

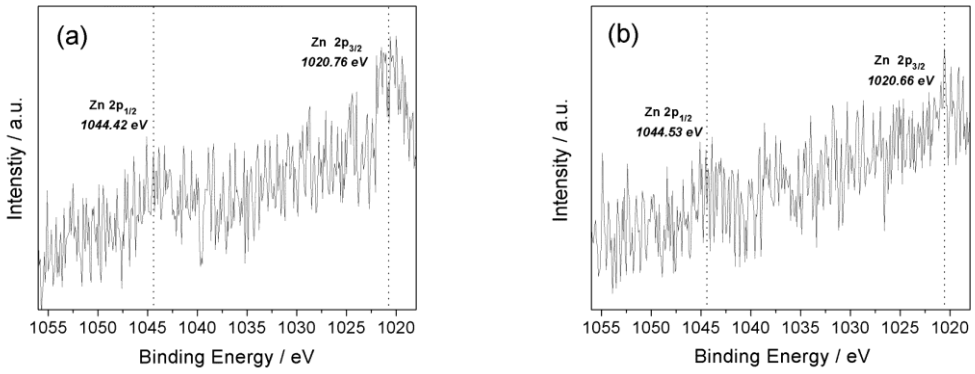

Figure 2.8 XPS spectra of Zn 2p from $LiMn_2O_4$ composite electrodes coated with (a) 10 ZnO ALD layers and (b) 6 ZnO ALD layers after 100 cycles at 55ºC.

At elevated temperature, $LiMn_2O_4$ electrode will suffer from faster capacity fading because high temperature accelerates chemical kinetics in battery cell and aggravates negative factors in terms of Mn dissolution, phase transition and electrolyte decomposition [7]. On the other hand, higher temperature also leads to

enhanced electrical conductivity and faster lithium ion diffusion in $LiMn_2O_4$ electrode, which can contribute to less polarization and subsequently improved energy and powder densities of $LiMn_2O_4$. Figure 2.7c, 7d and 7f illuminate this competitive relationship between such negative and positive influences on different composite electrodes. Bare electrode displays more severe capacity loss at 55^{o}C compared to that at 25^{o}C, as shown in Figure 2.7. The capacity fading of "B-E" is mainly ascribed to the intensified Mn dissolution which becomes the predominant factor at elevated temperature without any protective surface coatings on the composite electrode [7, 16]. "2 ZnO ALD-E" exhibits similar electrochemical behaviors at 55^{o}C and 25^{o}C without much change in cycleability when the sample is subjected to higher temperature, indicating that the ultrathin ZnO coating (2 ALD layers, 0.34 nm thick) can adequately impede Mn dissolution at elevated temperature. The effect of ALD coatings to enhance performance of $LiMn_2O_4$ at higher temperature is more phenomenal when thickness of ALD coatings is optimized to be 6 ALD layers (1.02 nm). "6 ZnO ALD-E" shows a higher initial capacity (84.9 mAh/g) at 55^{o}C than that at 25^{o}C. It is speculated that when Mn dissolution at elevated temperature is effectively restrained by 6 ZnO ALD layers as it works at room temperature, the enhanced conductivity and Li-ion diffusion rate in electrode at higher temperature becomes the leading beneficial factor resulting in increased capacity. In the case of "10 ZnO ALD-E", the initial capacity at 55^{o}C is lower than that at 25^{o}C, because a overly thick ZnO coating may slow down Li^+ diffusion at elevated temperature [16, 27], though this sample shows very good capacity retention after 100 electrochemical cycles. After 100 electrochemical cycles at 55^{o}C, the obvious existence of residual ZnO coating in "10 ZnO ALD-E" is validated by XPS analysis of Zn 2p peaks in Figure 2.8a. The apparently lower Zn 2p peaks can be observed from "6 ZnO ALD-E" after 100 electrochemical cycles at 55^{o}C (Figure 2.8) in comparison with that measured from the primary electrode coated with 6 ZnO ALD layers before cycling (Figure 2.6b), indicating that 6 ZnO ALD layers can be considered as the critical coating thickness to completely neutralize the HF but not influence the lithium ion diffusivity. In summary, a surface coating composed of 6 ZnO ALD layers (1.02 nm thick) has optimal thickness for enhancing the performance of $LiMn_2O_4$ electrode, and the positive effect of this coating is more distinct at elevated temperature. Furthermore, when this optimal 6 ZnO ALD layers are coated onto $LiMn_2O_4$ particles instead of the entire composite electrode, the effect of this coating to enhance the performance of electrode at elevated temperature is even more phenomenal. The sample "6 ZnO ALD LMO-E" delivers an initial capacity of 90.8 mAh/g at 55 ^{o}C, which is higher than that of "6 ZnO ALD-E" (84.9 mAh/g) and 1.7 times larger than that of "B-E" (52.9 mAh/g) at 55^{o}C. "6 ZnO ALD LMO-E also delivers the highest final capacity of 56.1 mAh/g at 55^{o}C, higher than that of "6 ZnO ALD-E" (44.5 mAh/g) and that of "B-E" (27.0 mAh/g) at 55^{o}C. Moreover, under a low current density of 0.1 *C*, "6 ZnO ALD LMO-E" delivers a high initial discharge capacity of 119.1 mAh/g at 55^{o}C, confirming its outstanding electrochemical performance at elevated temperature.

In order to further evaluate the effect of ZnO ALD coating on $LiMn_2O_4$ particles at elevated temperature, the cyclic voltammetric (CV) measurements of "6 ZnO ALD LMO-E" are carried out at a scan rate of 0.1 mV/s between 3.4 and 4.5 V *vs*. Li, at 25^{o}C and 55^{o}C, respectively, as shown in Figure 2.9a. It can be seen that the anodic peak current located at 4.18 V at 55^{o}C is larger than the peak at 4.17 V at 25^{o}C, indicating that more lithium ions can be extracted from the $LiMn_2O_4$ structure due to the enhanced electrical conductivity from $3.82*10^{-6}$ (25^{o}C) to $3.04*10^{-5}$ S/cm (55^{o}C) of "6 ZnO ALD LMO-E" when it is subjected to elevated temperature. In the corresponding reduction cycle, the cathodic peak current at a high voltage of 4.06 V at 55^{o}C is also much higher than that at 4.08 V at 25^{o}C, suggesting more intercalation of lithium ions into the host $LiMn_2O_4$ at 55^{o}C. It should be noted that the improved conductivity and lithium ion diffusion rate at higher temperature stimulate the activity of lithium ions in the high voltage sites, resulting in improved specific capacity. The distinct peak at 4.5 V at 55^{o}C indicates that decomposition of the electrolyte derived by the higher oxidation of Mn^{4+} due to the deep delithiation reaction is accelerated at elevated temperature.

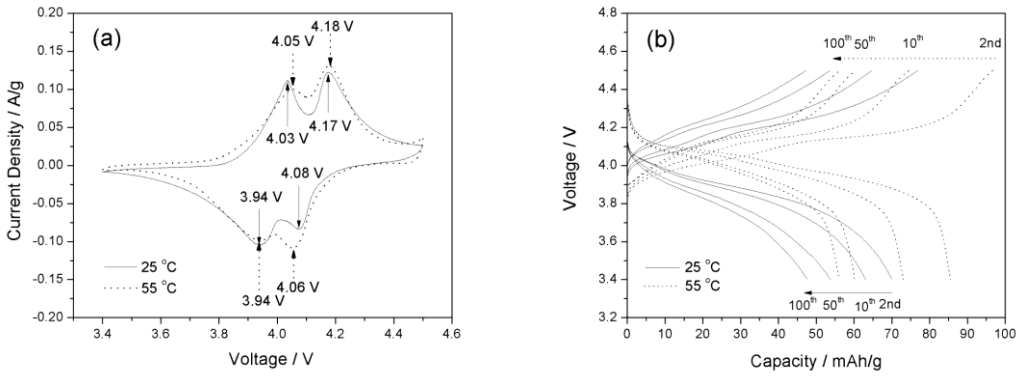

Figure 2.9 Electrochemical performances of the electrode composed of $LiMn_2O_4$ particles coated with 6 ZnO ALD layers and carbon/PVDF network ("6 ZnO ALD LMO-E"): (a) CV curves at a scan rate of 0.1 mV/s at 25 ºC and 55ºC, (b) charge/discharge curves from different electrochemical cycles at a current density of 120 mAh/g in a voltage range of 3.4 - 4.5 V *vs*. Li/Li^+ at 25ºC and 55ºC.

Figure 2.9b exhibits charge/discharge profiles of "6 ZnO ALD LMO-E" from different electrochemical cycles at 25^{o}C and 55^{o}C. As for the 2nd cycle at 55^{o}C, the charge curve presents two potential plateaus located at 4.03 V and 4.16 V, and the corresponding discharge curve displays plateaus at 4.08 V and 3.95 V, consistent with the CV curve. In contrast, the two pairs of weak voltage plateaus in charge and discharge curves at 25^{o}C are not well-matched with the redox peaks in the CV curve. The increased polarization can be attributed to the low conductivity of working electrode and the usage of high current density in charge/discharge reactions at 25^{o}C, whereas the CV measurement was performed at a slow scan rate. The extended high-voltage plateaus can be clearly observed in the charge/discharge curves at 55^{o}C

at the 2^{nd}, 5^{th}, 50^{th} and 100^{th} electrochemical cycles compared to those of charge/discharge curves at 25°C. The enhanced mobility of lithium ions at high voltage at increased temperature thus contributes to the considerably improved capacity of the "6 ZnO ALD LMO-E" at 55°C.

3.5 Conclusions

We have deposited ultra-thin and highly-conformal ZnO coatings (as thin as 0.34-1.7 nm) onto $LiMn_2O_4$ by using the atomic layer deposition method, for enhanced electrochemical performances of electrode materials. Thickness of ZnO ALD coatings can be tuned and precisely controlled by varying ALD growth cycles, with a growth rate of 1.7 Å per cycle in this study. ZnO ALD coatings are deposited either onto the entire $LiMn_2O_4$ composite electrode or individual $LiMn_2O_4$ particles. All the ALD-modified electrodes demonstrate enhanced cycleability compared to bare electrodes at both 25°C and 55°C. Among electrodes coated with ALD films of different thicknesses, $LiMn_2O_4$ electrode coated with 6 ZnO ALD layers (1.02 nm thick) shows the best cycling performance, demonstrating that it is facile to accurately tuning thickness of ALD coatings and thus optimize the electrochemical performances of ALD-modified electrodes simply via varying ALD growth cycles. Furthermore, electrode composed of $LiMn_2O_4$ particles coated with 6 ZnO ALD layers and uncoated carbon/PVDF network shows even better electrochemical performances than $LiMn_2O_4$ composite electrode coated with 6 ZnO ALD layers at both 25°C and 55°C, and the effect of ZnO ALD coatings is more phenomenal at the elevated temperature. The electrode composed of $LiMn_2O_4$ particles coated with 6 ZnO ALD layers delivers the highest final capacity of 56.1 mAh/g after 100 electrochemical cycles at 1 *C* at 55°C, much higher than the final capcity of 27.0 mAh/g delivered by bare electrode at 55°C, showing the effect of ZnO ALD coatings to enhance the electrochemical performance of $LiMn_2O_4$ is more phenomenal at the elevated temperature. The ultra-thin and high-quality ZnO ALD coating can effectively alleviate dissolution of manganese ions into electrolyte by scavenging HF, and retards the electrolyte decomposition by isolating $LiMn_2O_4$ from the electrolyte. And lastly, the methods presented in this study can be generalized to other cathode materials and other coatings as long as the coatings can be fabricated via ALD. For example, ALD surface coatings will be used to improve electrochemical performances of high-capacity cathodes such as lithium-rich layered oxides $Li[Li,Mn,Ni,Co]O_2$ in our laboratory.

2.6 References

1. A. Manthiram, Materials Challenges and Opportunities of Lithium Ion Batteries. *The Journal of Physical Chemistry Letters* 2 (2011) 176-184

2. M. Hirayama, H. Ido, K. Kim, W. Cho, K. Tamura, J. Mizuki, R. Kanno, Dynamic Structural Changes at $LiMn_2O_4$/Electrolyte Interface during Lithium Battery Reaction, *Journal of The American Chemical Society* 132 (2010) 15268-15276.

3. X. M. Liu, Z. D. Huang, S. Oh, P. C. Ma, P. C. H. Chan, G. K. Vedam, K. Kang, J. K. Kim, Sol-Gel Synthesis of Multiwalled Carbon Nanotube-$LiMn_2O_4$ Nanocomposites as Cathode Materials for Li-Ion Batteries. *Journal of Power Sources* 195 (2010) 4290-4296.

4. C. Qing, Y. Bai, J. Yang, W. Zhang, Enhanced Cycling Stability of $LiMn_2O_4$ Cathode by Amorphous $FePO_4$ Coating. *Electrochimica Acta* 56 (2011) 6612-6618.

5. J. Y. Shi, C. W. Yi, K. J. Kim, Improved Electrochemical Performance of $AlPO_4$-Coated $LiMn_{1.5}Ni_{0.5}O_4$ Electrode for Lithium-Ion Batteries. *Journal of Power Sources* 195 (2010) 6860-6866.

6. D. Guan, J. A. J eevarajan, Y. Wang, Enhanced Cycleability of $LiMn_2O_4$ Cathodes by Atomic Layer Deposition of Nanosized-Thin Al_2O_3 Coatings. *Nanoscale* 3 (2011) 1465-1469.

7. Y. K. Sun, K. J. Hong, J. Prakash, The Effect of ZnO Coating on Electrochemical Cycling Behavior of Spinel $LiMn_2O_4$ Cathode Materials at Elevated Temperature. *Journal of The Electrochemical Society* 150 (2003) A970-A972.

8. Y. K. Sun, K. J. Hong, J. Prakash, K. Amine, Electrochemical Performance of Nano-sized ZnO-coated $LiNi_{0.5}Mn_{1.5}O_4$ Spinel as 5 V Materials at Elevated Temperatures. *Electrochemical Communications* 4 (2002) 344-348.

9. J. Tu, X. B. Zhao, J. Xie, G. S. Cao, D. G. Zhuang, T. J. Zhu, J. P. Tu, Enhanced Low Voltage Cycling Stability of $LiMn_2O_4$ Cathode by ZnO Coating for Lithium Ion Batteries. *Journal of Alloys and Compounds* 432 (2007) 313-317.

10. C. Li, H. P. Zhang, L. J. Fu, H. Liu, Y. P. Wu, E. Rahm, R. Holze, H. Q. Wu Cathode Materials Modified by Surface Coating for Lithium Ion Batteries. *Electrochimica Acta* 51 (2006) 3872-3883.

11. X. Li, Y. Xu, Enhanced Cycling Performance of Spinel $LiMn_2O_4$ Coated with $ZnMn_2O_4$ Shell. *Journal of Solid State Electrochemistry* 12 (2008) 851-855.

12. H. Li, Z. Wang, L. Chen, X. Huang, Research on Advanced Materials for Li-ion Batteries. *Advanced Materials* 21 (2009) 4593-4607.

13. M. M. Thackeray, C. S. Johnson, J. S. Kim, K. C. Lauzze, J. T. Vaughey, N. Dietz, D. Abraham, S. A. Hackney, W. Zeltner, M. A. Anderson, ZrO_2- and Li_2ZrO_3-stabilized Spinel and Layered Electrodes for Lithium Batteries. *Electrochemical Communications* 5 (2003) 752-758.

14. H. M. Wu, I. Belharouak, A. Abouimrane, Y. K. Sun, K. Amine, Surface Modification of $LiNi_{0.5}Mn_{1.5}O_4$ by ZrP_2O_7 and ZrO_2 for Lithium-Ion Batteries. *Journal of Power Sources* 195 (2010) 2909-2913.

15. S. B. Park, H. C. Shin, W. G. Lee, W. I. Cho, H. Jang, Improvement of Capacity Fading Resistance of $LiMn_2O_4$ by Amphoteric Oxides. *Journal of Power Sources* 180 (2008) 597-601.

16. J. S. Kim, C. S. Johnson, J. T. Vaughey, S. A. Hackney, K. A. Walz, W. A. Zeltner, M. A. Anderson, M. M. Thackeray, The Electrochemical Stability of Spinel Electrodes Coated with ZrO_2, Al_2O_3, and SiO_2 from Colloidal Suspensions. *Journal of The Electrochemical Society* 151 (2004) A1755-A1761.

17. Y. M. Lin, H. C. Wu, Y. C. Yen, Z. Z. Guo, M. H. Yang, H. M. Chen, H. S. Sheu, N. L. Wu, Enhanced High-Rate Cycling Stability of $LiMn_2O_4$ Cathode by ZrO_2 Coating for Li-Ion Battery. *Journal of The Electrochemical Society* 152 (2005) A1526-A1532.

18. S. B. Park, S. M. Lee, H. C. Shin, W. I. Cho, H. Jang, An Alternative Method to Improve the Electrochemical Performance of a Lithium Secondary Battery with $LiMn_2O_4$. *Journal of Power Sources* 166 (2007) 219-225.

19. K. A. Walz, C. S. Johnson, J. Genthe, L. C. Stoiber, W. A. Zeltner, M. A. Anderson, M. M. Thackeray, Elevated Temperature Cycling Stability and Electrochemical Impedance of $LiMn_2O_4$ Cathodes with Nanoporous ZrO_2 and TiO_2 Coatings. *Journal of Power Sources* 195 (2010) 4943-4951.

20. D. W. Shin, J. W. Choi, J. P. Ahn, W. K. Choi, Y. S. Cho, S. J. Yoon, ZrO_2-Modified $LiMn_2O_4$ Thin-Film Cathodes Prepared by Pulsed Laser Deposition. *Journal of The Electrochemical Society* 157 (2010) A567-A570.

21. S. Lim, J. Cho, PVP-Assisted ZrO_2 Coating on $LiMn_2O_4$ Spinel Cathode Nanoparticles Prepared by MnO_2 Nanowire Templates. *Electrochemical Communications* 10 (2008) 1478-1481.

22. H. Şahan, H. Göktepe, Ş. Patat, A. Ülgen, Effect of the Cr_2O_3 coating on Electrochemical Properties of Spinel $LiMn_2O_4$ as a Cathode Material for Lithium Battery Applications. *Solid State Ionics* 181 (2010) 1437-1444.

23. S. W. Lee, K. S. Kim, H. S. Moon, H. J. Kim, B. W. Cho, W. I. Cho, J. B. Ju, J. W. Park, Electrochemical Characteristics of Al_2O_3-Coated Lithium Manganese Spinel as a Cathode Material for a Lithium Secondary Battery. *Journal of Power Sources* 126 (2004) 150-155.

24. J. Y. Liu, N. Liu, D. T. Liu, Y. Bai, L. H. Shi, Z. X. Wang, L. Q. Chen, V. Hennige, A. Schuch, Improving the Performances of $LiCoO_2$ Cathode Materials by Soaking Nano-Alumina in Commercial Electrolyte. *Journal of The Electrochemical Society* 154 (2007) A55-A63.

25. J. Tu, X. B. Zhao, G. S. Cao, D. G. Zhuang, T. J. Zhu, J. P. Tu, Enhanced Cycling Stability of $LiMn_2O_4$ by Surface Modification with Melting Impregnation Method. *Electrochimica Acta* 51 (2006) 6456-6462.

26. R. Beetstra, U. Lafont, J. Nijenhuis, E. M. Kelder, J. R. van Ommen, Atmospheric Pressure Process for Coating Particles Using Atomic Layer Deposition. *Chemical Vapor Deposition* 15 (2009)227-233.

27. I. D. Scott, Y. S. Jung, A. S. Cavanagh, Y. Yan, A. C. Dillon, S. M. George, S. H. Lee, Ultrathin Coatings on Nano-$LiCoO_2$ for Li-Ion Vehicular Applications. *Nano Letters* 11 (2011) 414-418.

28. H. J. Shin, D. K. Jeong, J. G. Lee, M. M. Sung, J. Y. Kim, Formation of TiO_2 and ZrO_2 Nanotubes Using Atomic Layer Deposition with Ultraprecise Control of the Wall Thickness. *Advanced Materials* 16 (2004) 1172-1200.

29. M. Kemell, V. Pore, J. Tupala, M. Ritala, M. Leskela, Atomic Layer Deposition of Nanostructured TiO_2 Photocatalysts via Template Approach. *Chemistry of Materials* 19 (2007) 1816-1820.

30. S. M. George, Atomic Layer Deposition: An Overview. *Chemical Reviews* 110 (2010) 111-131.

31. R. G. Gordon, D. Hausmann, E. Kim, J. Shepard, A Kinetic Model for Step Coverage by Atomic Layer Deposition in Narrow Holes or Trenches. *Chemical Vapor Deposition* 9 (2003) 73-78.

32. Y. S. Jung, A. S. Cavanagh, L. A. Riley, S. H. Kang, A. C. Dillon, M. D. Groner, S. M. George, S. H. Lee, Ultrathin Direct Atomic Layer Deposition on Composite Electrodes for Highly Durable and Safe Li-Ion Batteries. *Advanced Materials* 22 (2010) 2172-2176

33. X. Meng, D. Geng, J. Liu, R. Li, X. Sun, Controllable Synthesis of Graphene-Based Titanium Dioxide Nanocomposites by Atomic Layer Deposition. *Nanotechnology* 22 (2011) 165602.

34. L. A. Riley, S.V. Atta, A. S. Cavanagh, Y. Yan, S. M. George, P. Liu, A. C. Dillon, S. H. Lee, Electrochemical Effects of ALD Surface Modification on Combustion Synthesized $LiNi_{1/3}Mn_{1/3}Co_{1/3}O_2$ as a Layered-Cathode Material. *Journal of Power Sources* 196 (2011) 3317-3324.

35. J. T. Lee, F. M. Wang, C. S. Cheng, C. C. Li, C. H. Lin, Low-Temperature Atomic Layer Deposited Al_2O_3 Thin Film on Layer Structure Cathode for Enhanced Cycleability in Lithium-Ion Batteries. *Electrochimica Acta* 55 (2010) 4002-4006.

36. Y. S. Jung, A. S. Cavanagh, A. C. Dillon, M. D. Groner, S. M. George, S. H. Lee, Enhanced Stability of $LiCoO_2$ Cathodes in Lithium-Ion Batteries Using Surface Modification by Atomic Layer Deposition. *Journal of The Electrochemical Society* 157 (2010) A75-A81.

37. X. Meng, Y. Zhong, Y. Sun, M. N. Banis, R. Li, X. Sun, Nitrogen-Doped Carbon Nanotubes Coated by Atomic Layer Deposited SnO_2 with Controlled Morphology and Phase. *Carbon* 49 (2011) 1133-1144.

38. M. Q. Snyder, S. A. Trebukhova, B. Ravdel, M. C. Wheeler, J. DiCarlo, TrC. P. ipp, W. J. DeSisto, Synthesis and Characterization of Atomic Layer Deposited Titanium Nitride Thin Films on Lithium Titanate Spinel Powder as a Lithium-Ion Battery Anode. *Journal of Power Sources* 165 (2007) 379-385.

39. L. A. Riley, A. S. Cavanagh, S. M. George, Y. S. Jung, Y. F. Yan, S. H. Lee, A. C. Dillon, Conformal Surface Coatings to Enable High Volume Expansion Li-Ion Anode Materials. *ChemPhysChem* 11 (2010) 2124-2130.

40. A. W. Ott, R. P. H. Chang, Atomic layer-controlled growth of transparent conducting ZnO on plastic substrates. *Materials Chemistry and Physics* 58 (1999) 132-138.

41. J. W. Elam, S. M. George, Growth of ZnO/Al_2O_3 Alloy Films Using Atomic Layer Deposition Techniques. *Chemistry of Materials* 15 (2003) 1020-1028.

42. M. M. Thackeray, Structural Considerations of Layered and Spinel Lithiated Oxides for Lithium Ion Batteries. *Journal of The Electrochemical Society* 142 (1995) 2558-2563.

CHAPTER 3. LOW TEMPERATURE PREPARATION OF CRYSTALLINE ZrO_2 COATINGS FOR IMPROVED ELEVATED-TEMPERATURE PERFORMANCES OF $LiMn_2O_4$ CATHODES IN LITHIUM–ION BATTERY

3.1 Introduction

The manganese dissolution caused by hydrofluoric acidic (HF) in organic electrolyte has been proposed as the major cause for the significant capacity fading of spinel $LiMn_2O_4$ Li-ion battery cathode material at elevated temperature [1]. This disproportionate degradation of $LiMn_2O_4$ results in considerably adverse effect on cycling performance for high temperature applications. The decomposition of electrolyte driven by high oxidation ability of Mn^{3+}/Mn^{4+} redox takes another responsibility for capacity loss when $LiMn_2O_4$ is in high-potential charge/discharge reactions [1]. Artificial preparation of a protective surface coating on $LiMn_2O_4$ particles is an effective approach to minimize the solubility of the spinel $LiMn_2O_4$ electrode and prevent from direct contact with electrolyte [2]. Amphoteric oxide coatings, such as Al_2O_3, ZnO, ZrO_2, SnO_2, TiO_2 and SiO_2 [2-4], have been extensively investigated and reported for the improvement of electrochemical performance. However, the electrochemical performance can be vulnerably affected by qualities of oxide coatings in terms of the adhesion to host materials, conformality, uniformity, thickness, specific surface area and crystallinity [5-7]. In comparison with surface coatings synthesized via traditional wet chemical methods that lack conformality, completeness, uniformity and can be as thick as 10-100 nm, the atomic layer deposition (ALD) technique has been demonstrated to achieve ultrathin coatings that are uniform, dense, homogenous, and extremely conformal for surface modifications of Li-ion battery electrodes [8-11]. ALD is a thin film deposition technique which utilizes a sequence of chemisorption self-terminating surface reactions, and thus the thickness of ALD coatings can be precisely controlled at atomic scale. It is also noted that the ALD coating is chemically bonded to the substrate, while there is merely physical contact between the coating synthesized via wet chemical methods and the substrate. Another distinguishing advantage of ALD technique for surface modification of electrode materials for lithium-ion batteries is that ALD offers the flexibility of conformal coatings on either individual particles or the whole composite electrode. ALD coating on electrode for improved electrochemical performance has been demonstrated on both Li-ion battery cathode and anode materials [6,8,12].

3.2 Objectives of Project

ZrO_2 can serve as a remarkable HF scavenger to suppress Mn dissolution and act as an artificial interface to reduce the deleterious reaction between $LiMn_2O_4$ and electrolyte [5]. Furthermore, crystalline ZrO_2 coating prepared by sol-gel method has shown good stability at elevated temperature [13]. To the best of our knowledge, there is no report about ZrO_2 ALD coatings for Li-ion battery electrodes yet. In the present work, ultrathin crystalline ZrO_2 films for surface modifications of $LiMn_2O_4$ are deposited via ALD at low temperature (120°C) without any thermal post-treatment, while most oxides deposited via ALD at low temperature are amorphous. ZrO_2 ALD coating has advantages of using minimal amount of precursors, while synthesis of

ZrO_2 films via conventional wet chemical methods requires a large amount of precursors and solvents and subsequent heat treatments at much higher temperature for obtaining and manipulating crystallinity of ZrO_2 films [13,14]. Electrochemical performance of $LiMn_2O_4$ cathodes modified with ultrathin and crystalline ZrO_2 coatings are optimized by tailoring the coating thickness at atomic scale via simply varying number of ALD growth cycles. Furthermore, the electrode composed of ZrO_2-ALD-coated $LiMn_2O_4$ particles and uncoated carbon/PVDF shows even higher capacities and better cycling stability and high-rate performance at elevated temperature.

3.3 Experimental Section

3.3.1 Preparation of bare composite electrode

The $LiMn_2O_4$ powders (99.5%) were purchased from Alfa Aesar without any further treatment. The bare composite electrode was composed of 80 % pristine $LiMn_2O_4$ particles, 10 % acetylene black (conductive carbon, Alfa Aesar, 99.5%) and 10 % poly-vinylidenefluoride (PVDF, Alfa Aesar) as the binder. The bare composite electrode was denoted as B-E.

3.3.2 Atomic layer deposition of ZrO_2 coating on $LiMn_2O_4$ particles and bare composite electrode

Atomic layer deposition of ZrO_2 coating on $LiMn_2O_4$ particles and bare composite electrodes was carried out in a Savannah 100 ALD system (Camabridge NanoTech Inc.) at 120°C using $Zr(OC(CH_3)_3)_4$ (Zirconium tert-butoxide, ZTB) and H_2O as precursors with exposure time of 0.25 and 0.015 s, waiting time of 5 and 5 s and purge time of 60 and 40 s, respectively. The two self-terminating reactions involved in this ZrO_2 ALD growth are described in the following reactions:

$$Zr(OH)^* + Zr(OC(CH_3)_3)_4 \rightarrow Zr\text{-}O\text{-}Zr\text{-}(O\text{-}C(CH_3)_3)_3{}^*+ (CH_3)_3COH$$
$$Zr\text{-}O\text{-}(CH_3)_3{}^*+ H_2O \rightarrow ZrOH^*+ CH_2{=}C(CH_3)_2$$

3.3.3 Characterizations

The crystallographic structure of ZrO_2 ALD coated $LiMn_2O_4$ particles were examined by using a Rigaku MiniFlex X-ray diffractometer with Cu K_α radiation at a scan rate of 2^o/min. The particle size of bare $LiMn_2O_4$ particles and surface morphology of bare composite electrode were observed using a FEI Quanta 3D FEG field emission scanning electron microscopy (FESEM). Transmission electron microscopy (TEM) images were captured on a JEM-2010 instrument microscopy at an acceleration voltage of 200 kV, to investigate the characteristics of the ZrO_2 coatings. Surface compositions of $LiMn_2O_4$ particles coated with 6 ZrO_2 ALD layers and $LiMn_2O_4$ composite electrode coated with 6 ZrO_2 ALD layers were analyzed via X-ray photoelectron spectroscope (XPS) using an AXIS 165 spectrometer using a

twin-anode Al K_α (1486.6 eV) X-ray source. All the XPS spectra were calibrated according to the binding energy of the C1s peak at 284.8 eV.

3.3.4 Electrochemical measurements

Different electrodes were integrated into two-electrode CR2032-type coin cells for electrochemical measurements, with metallic lithium foil as anode, Celgard-2320 membrane as separator; electrolyte was 1 M $LiPF_6$ dissolved in ethylene carbonate (EC) and dimethyl carbonate (DMC) and diethyl carbonate (DEC) at a volumetric ratio of 1:1:1. Galvanostatic charge and discharge were performed at different current densities in a voltage range of 3.4 - 4.5 V using an 8-channel battery analyzer (MTI Corporation) at room temperature (25ºC) and elevated temperature (55°C). The electrochemical impedance spectroscopy (EIS) of different ZrO_2 ALD modified $LiMn_2O_4$ electrodes were performed on VersaSTAT MC electrochemical analyzer (Princeton Applied Research) in a frequency range of 100 kHz-10 mHz by applying an AC amplitude of 5 mV.

3.4 Results and Discussion

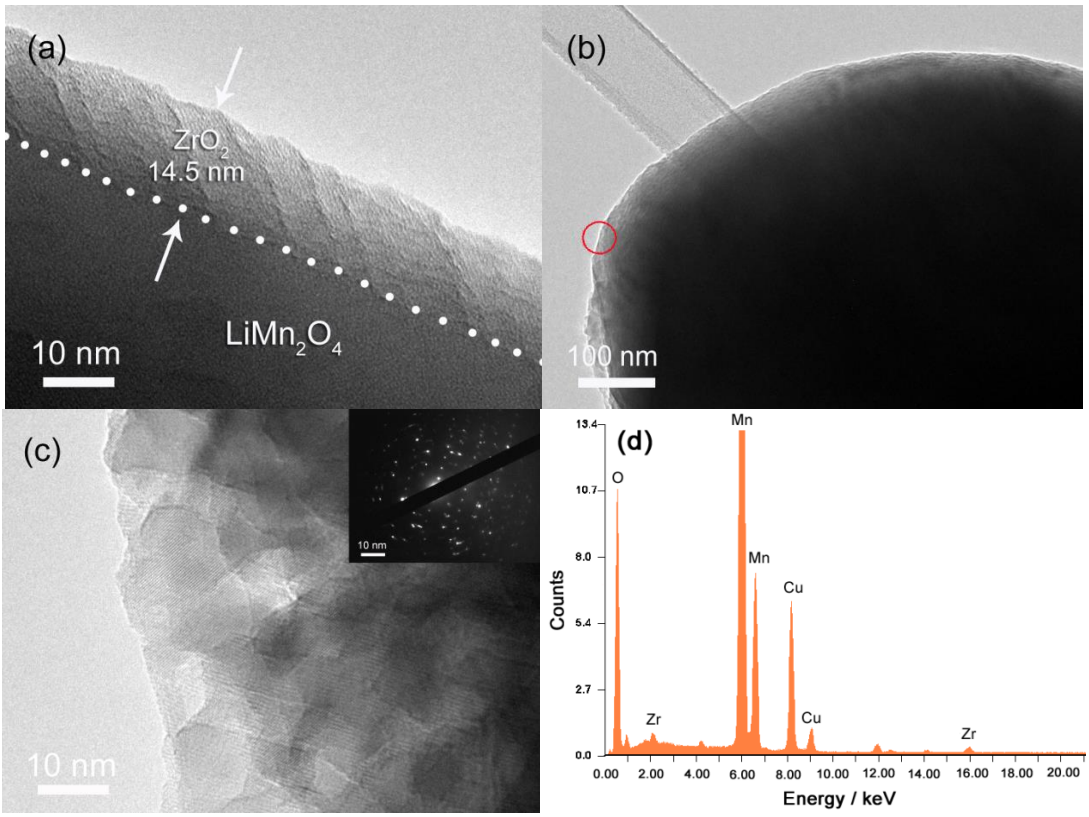

Figure 3.1 (a) HR-TEM image of $LiMn_2O_4$ particle coated with 50 ZrO_2 ALD layers, (b) TEM image of $LiMn_2O_4$ particle coated with 300 ZrO_2 ALD layers, (c) HR-TEM image with the selected area electron diffraction (SAED) pattern (inset) and (d) energy dispersive spectroscopy (EDS) pattern captured from the sample in red circle in (b).

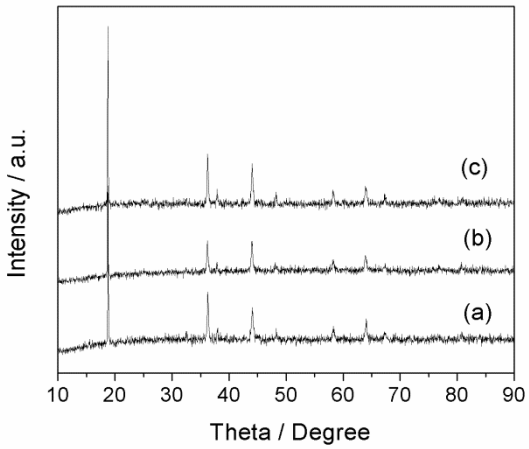

Figure 3.2 XRD patterns of (a) bare $LiMn_2O_4$ particles, (b) $LiMn_2O_4$ particles coated with 300 ZrO_2 ALD layers and (c) composite electrode ($LiMn_2O_4$:Carbon:PVDF=8:1:1 in weight ratio) coated with 300 ZrO_2 ALD layers. Three XRD patterns only present show spinel cubic $LiMn_2O_4$ phase with a *Fd-3m* space group (JCPDS: 35-0782). No ZrO_2 phase can be detected.

Figure 3.1a shows a high-resolution transmission electron microscopy (HR-TEM) image of $LiMn_2O_4$ particle coated with 50 ZrO_2 ALD layers. The uniform ZrO_2 thin film with ordered lattice fringes is deposited on the surface of $LiMn_2O_4$ particle via ALD at 120°C, indicating that ALD can be used for low-temperature preparation of crystallized ZrO_2 coating on $LiMn_2O_4$. This ZrO_2 coating composed of 50 ALD layers has a thickness of 14.5 nm, corresponding to a ZrO_2 ALD growth rate of 2.9Å/cycle. To further study the details of ZrO_2 ALD film, a thicker ZrO_2 film composed of 300 ZrO_2 ALD layers is deposited onto $LiMn_2O_4$ particle and its TEM image is presented in Figure 3.1b showing the conformality and homogeneity of the ZrO_2 ALD coating. Figure 3.1c and 1d display the HR-TEM image, selected area electron diffraction (SAED) pattern and energy dispersive spectroscopy (EDS) profile captured from the part in the red circle in Figure 3.1b. The HR-TEM image in Figure 3.1c reveals that the homogeneous ZrO_2 ALD film is composed of numerous single-crystal ZrO_2 particles with an average particle size of ~15 nm. It is intriguing to note that ZrO_2 ALD coating is changed from uniform crystalline thin film (50 ALD layers in Figure 3.1a) to thicker film composed of single-crystal particles (300 ALD layers in Figure 3.1c). Kim et al. have indicated that the crystal structure of as-deposited ZrO_2 film by ALD depends on the ZrO_2 film thickness [15]. The phase of ZrO_2 in this work cannot be clearly identified from the SAED pattern (inset in Figure 3.1c) or X-ray diffraction (XRD) pattern (Figure 3.2) due to the coexistence of tetragonal and monoclinic phases in ZrO_2 phase [15], nanoscale of ZrO_2 particles and low weight ratio of ZrO_2 coating as shown from the EDS spectrum (Figure 3.1d), in the case of nanosized-thin ZrO_2 coatings deposited on micro-sized $LiMn_2O_4$ particles with an average particle size of ~5 μm. There is ongoing work in our laboratory to study mechanism of ZrO_2 ALD growth and phase transition in ZrO_2 ALD coatings.

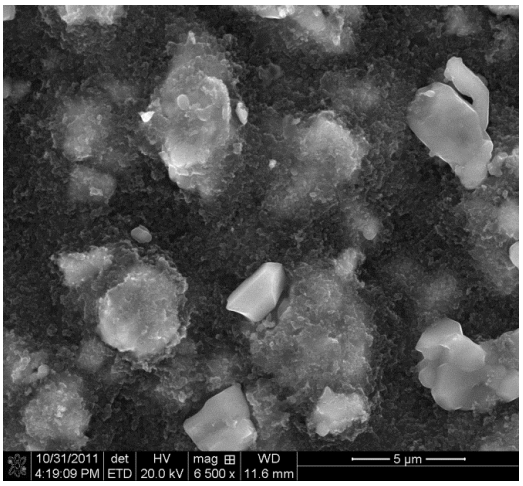

Figure 3.3 SEM image showing surface morphology of the bare composite electrode composed of 80 % pristine $LiMn_2O_4$ particles, 10 % acetylene black and 10 % poly-vinylidenefluoride (PVDF) as the binder.

Low-temperature ALD approach has been demonstrated for preparation of ZrO_2 coatings of high quality with respect to crystallinity, conformability and homogeneity (Figure 3.1). In a typical ALD process on as-prepared composite electrode composed of $LiMn_2O_4$ particles embedded in porous carbon/PVDF framework (Figure 3.3), all surface area of electrode is exposed to the vaporized H_2O and organometallic precursors, resulting in deposition of conformal ZrO_2 coating on pristine composite electrode.

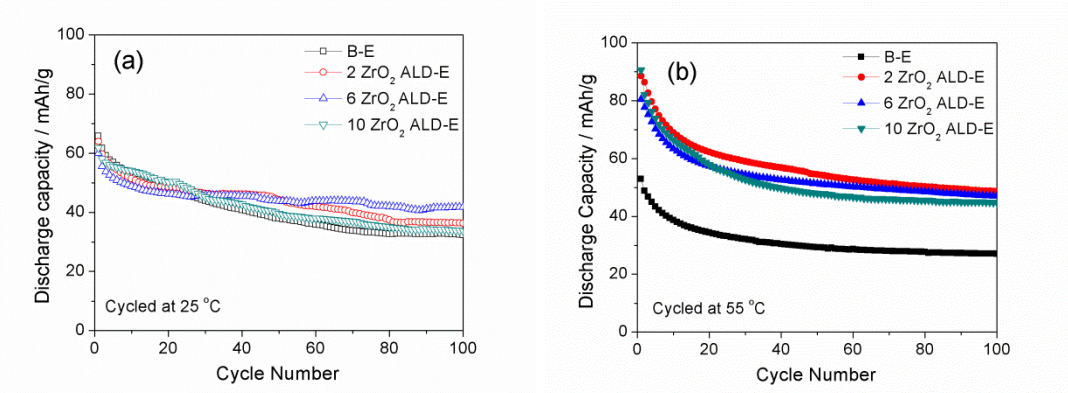

Figure 3.4 Cycling performance of ZrO_2 ALD-modified cathode electrodes with 2, 6 and 10 ZrO_2 ALD layers as comparison with bare electrode at 25ºC and 55ºC, respectively.

In order to optimize the electrochemical performance of ZrO_2 ALD-modified composite electrodes, $LiMn_2O_4$ composite electrodes are coated with 2, 6 and 10 ZrO_2 ALD layers (denoted as 2 ZrO_2 ALD-E, 6 ZrO_2 ALD-E and 10 ZrO_2 ALD-E), respectively. Figure 3.4a and 4b summarizes cycling performances of these different electrodes subject to room temperature (25ºC) and elevated temperature (55°C). The protective ZrO_2 ALD coatings significantly improve cycleability of ZrO_2 coated

electrodes, while the bare composite electrode suffers from fast capacity fading due to the HF's acidic attack in electrolyte, especially at 55°C. The optimal thickness of ZrO_2 surface coating for $LiMn_2O_4$ composite electrode is 1.74 nm composed of 6 ZrO_2 ALD layers. The 6 ZrO_2 ALD-E exhibits the best cycling stability during 100 electrochemical cycles in comparison with B-E, 2 ZrO_2 ALD-E and 10 ZrO_2 ALD-E both at room temperature and elevated temperature. We speculate that two ZrO_2 ALD layers with a thickness of 0.58 nm are not sufficient to rapidly consume the HF in electrolyte, and the thicker ZrO_2 coating of 10 ZrO_2 ALD layers (2.9 nm) elongates the path way for lithium ion diffusion through the stacked coating, which affects the lithium ion diffusivity [7].

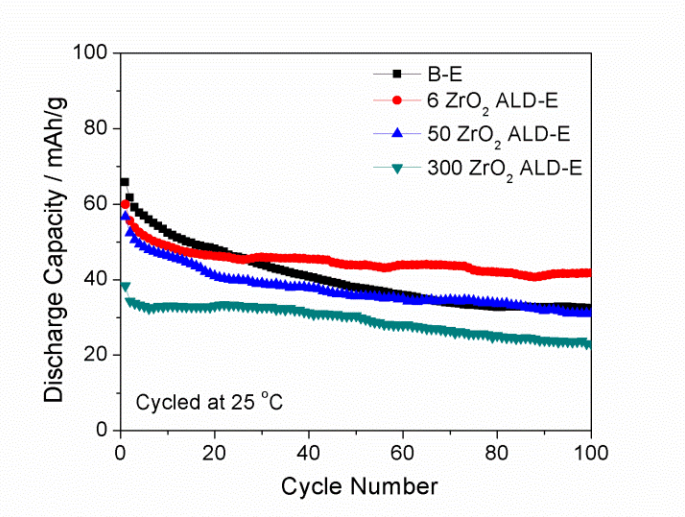

Figure 3.5 Cycling performance of bare $LiMn_2O_4$ composite electrode and $LiMn_2O_4$ composite electrodes coated with 6, 50, and 300 ZrO_2 ALD layers corresponding to the thickness of 1.74, 14.5 and 87 nm at a current density of 120 mA/g in a voltage range of 3.4-4.5 V at room temperature (25°C).

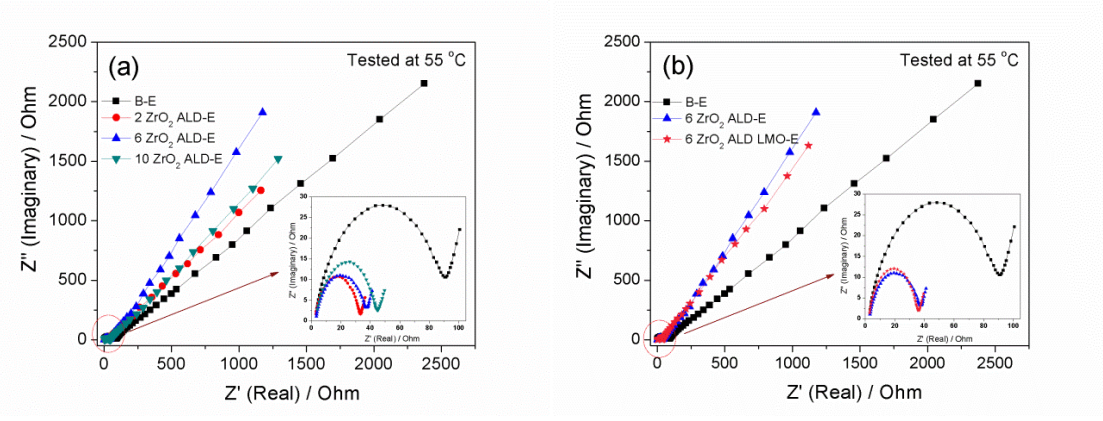

Figure 3.6 Electrochemical impedance spectra of different ZrO_2-ALD-modified $LiMn_2O_4$ electrodes in comparison with bare electrode in a frequency range of 100 kHz - 10 mHz by applying an AC amplitude of 5 mV at 55°C. "B-E": bare $LiMn_2O_4$ composite electrode; "*n* ZrO_2 ALD-E": $LiMn_2O_4$ composite electrode coated with *n* ALD layers; "6 ZrO_2 ALD LMO-E": electrode composed of $LiMn_2O_4$ particles coated with 6 ZrO_2 ALD layers and uncoated carbon/PVDF network.

Figure 3.5 reveals that ZrO_2 coating thicker than 2 nm contribute to the inferior electrochemical performance, although it can completely neutralize acidic HF and thus prevent Mn dissolution in $LiMn_2O_4$. If we compare the capacity retention profiles at 25°C in Figure 3.4a and 55°C in Figure 3.4b, ZrO_2 ALD coating not only contributes to the improved cycling performance but also to the increased discharge capacity at elevated temperature. The thermal effect at elevated temperature will lead to volumetric expansion and improved conductivity of ZrO_2 coating, resulting in faster lithium ion diffusion and electron transition at high kinetics, which is consistent with the electrochemical impedance spectra (EIS) in Figure 3.6.

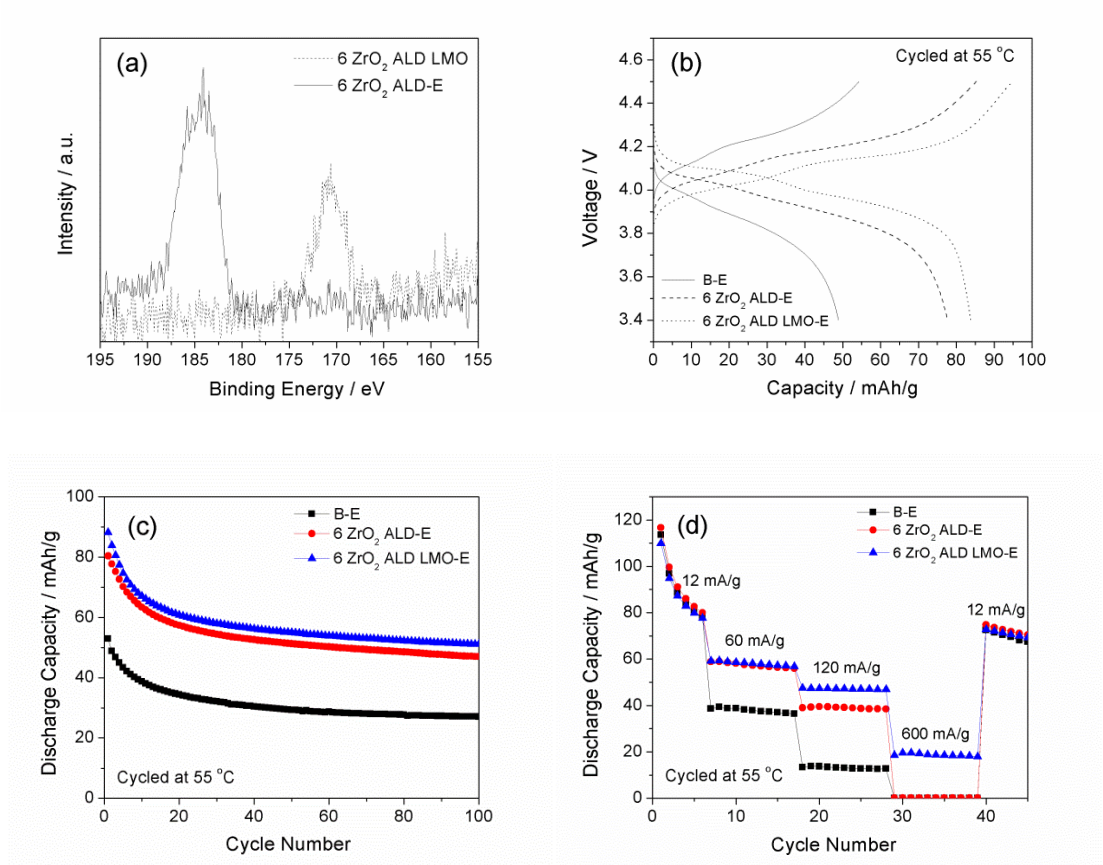

Figure 3.7 (a) XPS pattern of Zr 3d peaks measured from 6 ZrO_2 ALD LMO (dashed line) and 6 ZrO_2 ALD-E (solid line); (b) galvanostatic charge/discharge, (c) cycling performance and (d) rate performances of 6 ZrO_2 ALD-E and 6 ZrO_2 ALD LMO-E in comparison with B-E at 55ºC.

Thickness of ZrO_2 ALD coatings can be optimized at atomic scale to maximize electrochemical performances of ZrO_2-modified $LiMn_2O_4$ electrodes, and 6 ZrO_2 ALD layers demonstrate to have optimal thickness for surface modification of $LiMn_2O_4$ (Figure 3.4). For comparison purposes, 6 ZrO_2 ALD layers are directly coated on bare $LiMn_2O_4$ particles (marked as 6 ZrO_2 ALD LMO). Figure 3.7a shows the X-ray photoelectron spectroscopy (XPS) patterns of Zr 3d captured from 6 ZrO_2 ALD LMO and 6 ZrO_2 ALD-E, respectively. The two Zr 3d XPS spectra indicate different chemical and bonding environments of ZrO_2 ALD coatings on $LiMn_2O_4$

particles and composite electrode. The Zr 3d peak located at 184.1 eV for 6 ZrO_2 ALD-E confirms the formation of ZrO_2 coating on the composite electrode. In contrast, 6 ZrO_2 ALD LMO delivers a lower binding energy of 170.6 eV for Zr 3d peak. Due to the hydrophobic nature of carbon/PVDF composite in 6 ZrO_2 ALD-E [12], we speculate that different initial loading densities of hydroxyl groups (-OH) on the surface of composite electrode and $LiMn_2O_4$ particles in ALD hydroxylation procedure will affect the subsequent ZrO_2 growth. As presented in Figure 3.1a, another possible reason for the XPS peak shift of 6 ZrO_2 ALD LMO is the oriented crystal growth of crystalline Li-Mn-Zr-O composite following the lattice orientation of $LiMn_2O_4$ particle.

We also fabricate the electrode composed of 6 ZrO_2 ALD LMO particles and uncoated carbon/PVDF at the same weight ratio of 80:10:10 (marked as 6 ZrO_2 ALD LMO-E). Figure 3.7b and 7c show galvanostatic charge and discharge curves and cycling performance of 6 ZrO_2 ALD-E and 6 ZrO_2 ALD LMO-E at 55^oC in comparison with bare composite electrode, respectively. When this optimal 6 ZrO_2 ALD layers are coated onto $LiMn_2O_4$ particles instead of the entire composite electrode, the effect of this coating to enhance the performance of electrode at elevated temperature is even more phenomenal. The increased temperature is damaging to the electrochemical performance owning to faster kinetics for Mn dissolution and electrolyte decomposition, but is favourable for electrochemical performance due to improved electron and lithium ion transportation at higher temperature. The thermal effect can also lead to volumetric expansion of ZrO_2 coating and improved electrical conductivity of crystalline ZrO_2 film. The enhanced electrochemical performance of 6 ZrO_2 ALD LMO-E can be attributed to the following reasons: (1) The uniform ZrO_2 coating on $LiMn_2O_4$ particles with improved conductivity can average electron and lithium ion distributions on the surface of $LiMn_2O_4$, resulting in less electrochemical polarization at elevated temperature in comparison with partial ZrO_2 coverage of $LiMn_2O_4$ in 6 ZrO_2 ALD-E [11,16]; The two pairs of symmetric charge/discharge plateau of 6 ZrO_2 ALD LMO-E in Figure 3.3b reveal the remarkable reversibility of ZrO_2 coated $LiMn_2O_4$. (2) The strong chemical bonding between $LiMn_2O_4$ and ZrO_2 via oxygen bond ($LiMn_2O_4$-O-ZrO_2) can contribute to reducing the oxygen activity of $Mn^{3+/}Mn^{4+}$ redox at the $LiMn_2O_4$ surface at high potentials to suppress the electrolyte decomposition [14]; (3) The crystalline ZrO_2 thin film with highly ordered lattice fringe in expanded structure at elevated temperature is more facile for lithium ion diffusion into $LiMn_2O_4$ particles. The slope of warburg impedance of 6 ZrO_2 ALD LMO-E in EIS pattern is approximately $\pi/4$ (Figure 3.6), indicating reversible lithiation and delithiation within ZrO_2-coated $LiMn_2O_4$, which contributes to outstanding high-rate performance of 6 ZrO_2 ALD LMO-E in comparison with B-E and 6 ZrO_2 ALD-E (Figure 3.7d). The crystalline structure of conformal ZrO_2 coating can be considered as an essential factor for enhanced electrochemical performance of $LiMn_2O_4$ electrodes at elevated temperature.

3.5 Conclusions

In conclusion, ultrathin and crystalline ZrO_2 coatings have been facilely deposited on both $LiMn_2O_4$ particles and composite electrode at low temperature using atomic layer deposition. The thickness of ZrO_2 coating can be precisely tailored at 2.9 Å per ALD cycle at atomic scale. The optimal thickness of ZrO_2 for maximized electrochemical performance is 1.74 nm (6 ZrO_2 ALD layers). Surface modification of $LiMn_2O_4$ with crystalline ZrO_2 coating has led to the remarkably enhanced electrochemical performance of $LiMn_2O_4$ at elevated temperature.

3.6 References

1. K. Y. Chung, H. S. Lee, W. S. Yoon, J. McBreen and X. Q. Yang, Studies of $LiMn_2O_4$ Capacity Fading at Elevated Temperature Using In Situ Synchrotron X-Ray Diffraction. *Journal of The Electrochemical Society* 153 (2006) A774-A778.

2. C. Li, H. P. Zhang, L. J. Fu, H. Liu, Y. P. Wu, E. Rahm, R. Holze, H. Q. Wu Cathode Materials Modified by Surface Coating for Lithium Ion Batteries. *Electrochimica Acta* 51 (2006) 3872-3883.

3. L. Yu, X. Qiu, J. Xi, W. Zhu and L. Chen, Enhanced High-Potential and Elevated-Temperature Cycling Stability of $LiMn_2O_4$ Cathode by TiO_2 Modification for Li-Ion Battery. *Electrochimica Acta* 51 (2006) 6406-6411.

4. D. Guan, J. A. J eevarajan, Y. Wang, Enhanced Cycleability of $LiMn_2O_4$ Cathodes by Atomic Layer Deposition of Nanosized-Thin Al_2O_3 Coatings. *Nanoscale* 3 (2011) 1465-1469.

5. S. Lim, J. Cho, PVP-Assisted ZrO_2 Coating on $LiMn_2O_4$ Spinel Cathode Nanoparticles Prepared by MnO_2 Nanowire Templates. *Electrochemical Communications* 10 (2008) 1478-1481.

6. Y. S. Jung, A. S. Cavanagh, L. A. Riley, S. H. Kang, A. C. Dillon, M. D. Groner, S. M. George, S. H. Lee, Ultrathin Direct Atomic Layer Deposition on Composite Electrodes for Highly Durable and Safe Li-Ion Batteries. *Advanced Materials* 22 (2010) 2172-2176.

7. I. D. Scott, Y. S. Jung, A. S. Cavanagh, Y. Yan, A. C. Dillon, S. M. George, S. H. Lee, Ultrathin Coatings on Nano-$LiCoO_2$ for Li-Ion Vehicular Applications. *Nano Letters* 11 (2011) 414-418.

8. X. Meng, Y. Zhong, Y. Sun, M. N. Banis, R. Li, X. Sun, Nitrogen-Doped Carbon Nanotubes Coated by Atomic Layer Deposited SnO_2 with Controlled Morphology and Phase. *Carbon* 49 (2011) 1133-1144.

9. Y. S. Jung, A. S. Cavanagh, A. C. Dillon, M. D. Groner, S. M. George, S. H. Lee, Enhanced Stability of $LiCoO_2$ Cathodes in Lithium-Ion Batteries Using Surface Modification by Atomic Layer Deposition. *Journal of The Electrochemical Society* 157 (2010) A75-A81.

10. L. A. Riley, S.V. Atta, A. S. Cavanagh, Y. Yan, S. M. George, P. Liu, A. C. Dillon, S. H. Lee, Electrochemical Effects of ALD Surface Modification on Combustion Synthesized $LiNi_{1/3}Mn_{1/3}Co_{1/3}O_2$ as a Layered-Cathode Material. *Journal of Power Sources* 196 (2011) 3317-3324.

11. J. Zhao, Y. Wang, Ultrathin Surface Coatings for Improved Electrochemical Performance of Lithium Ion Battery Electrodes at Elevated Temperature. *The Journal of Physical Chemistry C* 116 (2012) 11867-11876.

12. J. T. Lee, F. M. Wang, C. S. Cheng, C. C. Li, C. H. Lin, Low-Temperature Atomic Layer Deposited Al_2O_3 Thin Film on Layer Structure Cathode for Enhanced Cycleability in Lithium-Ion Batteries. *Electrochimica Acta* 55 (2010) 4002-4006.

13. H. M. Wu, I. Belharouak, A. Abouimrane, Y. K. Sun, K. Amine, Surface Modification of $LiNi_{0.5}Mn_{1.5}O_4$ by ZrP_2O_7 and ZrO_2 for Lithium-Ion Batteries. *Journal of Power Sources* 195 (2010) 2909-2913.

14. M. M. Thackeray, C. S. Johnson, J. S. Kim, K. C. Lauzze, J. T. Vaughey, N. Dietz, D. Abraham, S. A. Hackney, W. Zeltner, M. A. Anderson, ZrO_2- and Li_2ZrO_3-stabilized Spinel and Layered Electrodes for Lithium Batteries. *Electrochemical Communications* 5 (2003) 752-758.

15. H. Kim, K. C. Saraswat and P. C. McIntyre, Comparative Study on Electrical and Microstructural Characteristics of ZrO_2 and HfO_2 Grown by Atomic Layer Deposition. *Journal of Materials Research* 20 (2005) 3125-3132.

16. K. A. Walz, C. S. Johnson, J. Genthe, L. C. Stoiber, W. A. Zeltner, M. A. Anderson, M. M. Thackeray, Elevated Temperature Cycling Stability and Electrochemical Impedance of $LiMn_2O_4$ Cathodes with Nanoporous ZrO_2 and TiO_2 Coatings. *Journal of Power Sources* 195 (2010) 4943-4951.

CHAPTER 4. ATOMIC LAYER DEPOSITION OF EPITAXIAL ZrO_2 COATING ON $LiMn_2O_4$ NANOPARTICLES FOR HIGH-RATE LITHIUM-ION BATTERIES AT ELEVATED TEMPERATURE

4.1 Introduction

High power lithium ion batteries have attracted tremendous attentions due to their growing applications in hybrid electric vehicles (HEVs) and full electric vehicles (EVs) [1,2]. Capacities and rate capabilities of lithium ion batteries can be improved by using nanostructured electrode materials. In comparison with micro-sized materials, nanomaterials provide much shorter lithium ion diffusion path and offer more active sites for lithium ion insertion and extraction due to the larger surface-to-volume ratio. Excellent cycling stability and high rate capability have been achieved for both nanostructured cathode and anode nanomaterials [3,4]. Nanosized spinel $LiMn_2O_4$ has been demonstrated as a promising cathode material for applications in high-rate lithium ion batteries due to its advantages such as high power and energy densities, low cost, environmental friendliness and safety [5-7]. However, $LiMn_2O_4$ suffers from inevitable manganese (Mn) dissolution, phase transition and electrolyte decomposition during lithiation and delithiation processes, resulting in significant capacity fading during long-term cycling, especially at elevated temperature [8-11]. Mn^{2+} dissolution into the electrolyte is attributed to the attack from hydrofluoric acid (HF) formed by hexafluorophosphate ($LiPF_6$) and residual H_2O in the commercial electrolyte [12]. This disproportionate degradation of $LiMn_2O_4$ is considered as the major factor leading to poor capacity retention in cycling performance. The phase and structural stability of $LiMn_2O_4$ is important for having reversible charge and discharge reactions. Phase transition of $LiMn_2O_4$ can be effectively alleviated via choosing suitable operating voltage range for lithium ion intercalations to preserve highly ordered distribution of lithium ions in $LiMn_2O_4$ structure [9]. Decomposition of organic electrolyte on the surface of cathode is induced by the high oxidation effect of $Mn^{3+/}Mn^{4+}$ redox, which considerably increases the charge transition resistance and affects the lithium ion diffusion by forming the solid electrolyte interphase (SEI) layer [10]. The three factors summarized above together attribute to the inferior cycleability of $LiMn_2O_4$ cathode material, especially at elevated temperature. Therefore, interface between $LiMn_2O_4$ particles and surrounding electrolyte plays a critical role for electron and lithium ion transfer in the cathode [13]. Artificial preparation of a protective coating on $LiMn_2O_4$ particle is an effective approach to optimize electrochemical performance of $LiMn_2O_4$ electrode [12,14,15]. Electrochemical performance of $LiMn_2O_4$ cathode can be improved by coating it with various amphoteric oxide coatings, such as Al_2O_3, ZnO, ZrO_2, SiO_2, TiO_2, Cr_2O_3 and SnO_2 [16-21]. The protective oxide film serves as an effective HF scavenger to suppress Mn dissolution. Furthermore, the oxide coating separates $LiMn_2O_4$ particles from electrolyte to alleviate decomposition of electrolyte, and acts as a solid framework to restrict the unexpected phase transition of $LiMn_2O_4$, contributing to better structural stability and cycleability [11].

Due to the large surface area and complex structure, surface coatings on nanostructured materials synthesized via traditional wet chemical methods usually lack conformality, completeness and uniformity, and the thickness of coating layer cannot be precisely controlled at the sub-nano scale. Electrochemical performance of oxide-coated electrodes can be affected by qualities of surface coatings such as adhesion between coatings and host materials, conformality, uniformity, thickness, specific surface area and crystallinity of surface coatings [22]. Atomic layer deposition (ALD) is an advanced thin film deposition technique involving a sequence of chemisorption and self-terminating surface reactions [23-25]. In a typical ALD run, the initial hydroxylation on the surface of the substrate using H_2O precursor yields conformal and full coverage of the host material with hydroxyl groups, followed by purging the residual H_2O and by-products with inert gas flux. Subsequently, the organometallic precursor is introduced to react with hydroxyl groups, and thus a monolayer of oxide grows on the surface of substrate bridged by oxygen bonds. After the second purging step to remove extra organometallic precursor and by-products, the continuative hydroxylation takes place to replace organic groups on the surface of organometallic precursor with hydroxyl groups for the second monolayer growth of oxide coating. As a result, sequential ALD cycles proceed step-wise in self-limiting surface reactions as mentioned above, separated by purge steps, and the oxide film grows monolayer by monolayer at atomic scale. Hence, films grown using ALD are typically uniform, dense, homogenous, pinhole-free, and extremely conformal to the underlying substrate, and the thickness of coatings can be precisely controlled at atomic level [26-31]. It is also noted that the ALD coating is chemically bonded to the substrate, while there is merely physical contact between the coating synthesized via conventional wet chemical methods and the substrate. Another distinct advantage of ALD technique is that it allows for direct low-temperature (< 200°C) preparation of crystalline oxide coatings without post heat treatment, such as ZrO_2 [32,33]and V_2O_5 [34].

4.2 Objectives of Project

ZrO_2 coating deposited on $LiMn_2O_4$ nanoparticles via conventional sol-gel method has been demonstrated as a remarkable HF scavenger to suppress Mn dissolution and as an artificially robust interface to significantly reduce the deleterious reaction between $LiMn_2O_4$ and electrolyte [19]. Among various oxide coatings, ZrO_2 has shown excellent structural and thermal stability at elevated temperature [11]. ZrO_2 ALD coating for surface modification of micro-sized $LiMn_2O_4$ particles has been demonstrated to improve specific capacity and cycling stability of $LiMn_2O_4$ cathode at elevated temperature in our previous work [32]. The effect of ZrO_2 ALD coating on enhancing electrochemical performance of $LiMn_2O_4$ cathode is more phenomenal at elevated temperature than at room temperature. As nanostructured battery electrodes have attracted tremendous attention due to their enhanced surface area and improved high-rate performance compared to micro-sized electrode materials, in this work we deposit ultrathin ZrO_2 coating on nanosized $LiMn_2O_4$ particles via ALD to explore the

interesting growth and crystalline/amorphous phases of ZrO_2 ALD films and to further improve high-rate electrochemical performance of $LiMn_2O_4$ at elevated temperature. Cycling performance of ZrO_2-coated $LiMn_2O_4$ nanoparticles is optimized by tuning the coating thickness at atomic scale via varying ALD growth cycles, indicating that the optimal thickness of ZrO_2 coating is ~1 nm grown via 6 ZrO_2 ALD layers. The ZrO_2 ALD-modified cathode shows improved specific capacity and enhanced cycleability compared to bare composite electrode at high charge/discharge rate at elevated temperature, which can be considered as a promising electrode for high-power lithium ion batteries in elevated-temperature environment.

4.3 Experimental Section

4.3.1 Atomic layer deposition of ZrO_2 coating on $LiMn_2O_4$ nanoparticles

$LiMn_2O_4$ nanoparticles were purchased from MTI Corporation (marked as LMO). Atomic layer deposition of ZrO_2 coating on $LiMn_2O_4$ nanoparticles was carried out in a Savannah 100 ALD system (Cambridge NanoTech Inc.) at 120°C using $Zr(OC(CH_3)_3)_4$ (Zirconium tert-butoxide, ZTB) and H_2O as precursors with exposure time of 0.25 and 0.015 s, waiting time of 5 and 5 s and purge time of 60 and 40 s, respectively. The two self-terminating reactions involved in this ZrO_2 ALD growth are described in the following reactions [32]:

$$Zr(OH)^* + Zr(OC(CH_3)_3)_4 \rightarrow Zr\text{-}O\text{-}Zr\text{-}(O\text{-}C(CH_3)_3)_3^* + (CH_3)_3COH$$
$$Zr\text{-}O\text{-}C(CH_3)_3^* + H_2O \rightarrow Zr(OH)^* + CH_2{=}C(CH_3)_2.$$

$LiMn_2O_4$ nanoparticles coated with *n* ZrO_2 ALD layers were marked as *n* ZrO_2 ALD LMO. The heat treatment of 6 ZrO_2 ALD LMO was performed at 450°C for 3 h in air (denoted as 6 ZrO_2 ALD LMO HT).

4.3.2 Characterizations

The crystallographic structure of $LiMn_2O_4$ nanoparticles was examined by X-ray diffraction (XRD) using a Rigaku MiniFlex X-ray diffractometer with Cu K_α radiation at a scan rate of 2^o/min. Surface morphology, particle size and energy dispersive spectroscopic (EDS) mappings of bare and ZrO_2 ALD modified $LiMn_2O_4$ nanoparticles were observed using a FEI Quanta 3D FEG field emission scanning electron microscopy (FESEM). Transmission electron microscopy (TEM) images with EDS were captured on a FEI Tecnai G2 FEG instrument at an acceleration voltage of 300 kV, to examine morphology and structure of ZrO_2 coatings. Surface compositions of $LiMn_2O_4$ nanoparticles coated with 50 ZrO_2 ALD layers were analyzed via X-ray photoelectron spectroscopy (XPS) using an AXIS 165 spectrometer using a twin-anode Al K_α (1486.6 eV) X-ray source with the charge neutralization function being turned on. All the XPS spectra were calibrated according to the binding energy of the C1s peak at 284.8 eV.

4.3.3 Electrochemical measurements

Bare composite electrode (marked as B-E) was composed of 80 % pristine $LiMn_2O_4$ nanoparticles, 10 % acetylene black (conductive carbon, Alfa Aesar, 99.5%) and 10 % poly-vinylidenefluoride (PVDF, Alfa Aesar) as the binder. ZrO_2 ALD modified composite electrodes were denoted as *n* ZrO_2 ALD LMO-E consisting of $LiMn_2O_4$ nanoparticles coated with *n* ZrO_2 ALD layers, conductive carbon and PVDF binder at the same weight ratio of 8:1:1. These cathodes were assembled into two-electrode CR2032-type coin cells for electrochemical measure, with metallic lithium foil as anode, Celgard-2320 membrane as separator; electrolyte was 1 M $LiPF_6$ dissolved in ethylene carbonate (EC) and dimethyl carbonate (DMC) and diethyl carbonate (DEC) at a volumetric ratio of 1:1:1. Galvanostatic charge and discharge were performed at different current densities in a voltage range of 3.4 - 4.5 V using an 8-channel battery analyzer (MTI Corporation) at elevated temperature (55°C).

4.4 Results and Discussion

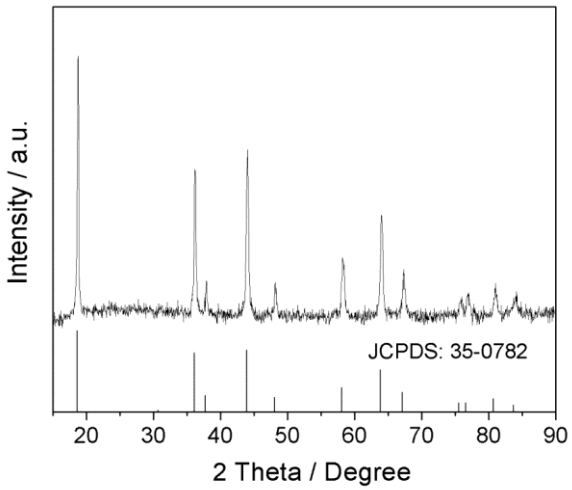

Figure 4.1 XRD pattern of bare $LiMn_2O_4$ nanoparticles.

Figure 4.1 shows the XRD pattern of bare $LiMn_2O_4$ nanoparticles. All distinct XRD peaks are indexed as the spinel cubic structure of $LiMn_2O_4$ with a *Fd3m* space group (JCPDS: 35-0782), indicating the high purity and crystallinity of $LiMn_2O_4$ nanoparticles.

The pristine $LiMn_2O_4$ nanoparticles have an average particle size of ~250 nm with a smooth polyhedron shape as observed in FESEM image in Figure 4.2a. To study details of ZrO_2 ALD coating, $LiMn_2O_4$ nanoparticles are coated with thick ALD film via 50 ALD growth cycles (marked as 50 ZrO_2 ALD LMO). Morphology and structure of 50 ZrO_2 ALD LMO are examined under TEM as presented in Figure 4.2b. The shape and morphology of $LiMn_2O_4$ nanoparticles coated with 50 ZrO_2 ALD layers are almost identical to those of bare $LiMn_2O_4$ particles, indicating conformality

of ZrO_2 ALD coating. Figure 4.2b shows conformal and homogeneous ZrO_2 ALD coating on the surface of $LiMn_2O_4$ nanoparticles. The corresponding EDS spectrum in Figure 4.2c captured from the marked circle in Figure 4.2b confirms the existence of ZrO_2 coating. The Cu peaks are from the copper grid where the TEM sample is placed. 50 ALD growth cycles contribute to a thickness of ~10 nm for ZrO_2 ALD coating, corresponding to the ZrO_2 ALD growth rate of ~2.0 Å/cycle. As such, the thickness of ZrO_2 ALD coating on $LiMn_2O_4$ nanoparticles can be precisely tailored at atomic scale. Furthermore, in contrast to deposition of crystalline ZrO_2 film on micro-sized $LiMn_2O_4$ particles, ZrO_2 ALD coating on $LiMn_2O_4$ nanoparticles is partially amorphous and partially crystalline. More details for ZrO_2 ALD growth on the surface of $LiMn_2O_4$ nanoparticle are obtained after obtaining HRTEM image of ZrO_2 film as shown in Figure 4.2d. It can be seen that ZrO_2 coating on $LiMn_2O_4$ nanoparticle is composed of two distinct layers in different textures and structures. The external layer of ZrO_2, as shown as layer 2, is amorphous with a uniform thickness of ~2 nm, while the layer inside (layer 1) shows formation of epitaxial layer of ZrO_2 following the orientation or lattice fringes of $LiMn_2O_4$ nanoparticles. These two distinct ZrO_2 layers on the underlying $LiMn_2O_4$ illustrate the evolution of ZrO_2 ALD coating on $LiMn_2O_4$ nanoparticles from amorphous to crystalline phase.

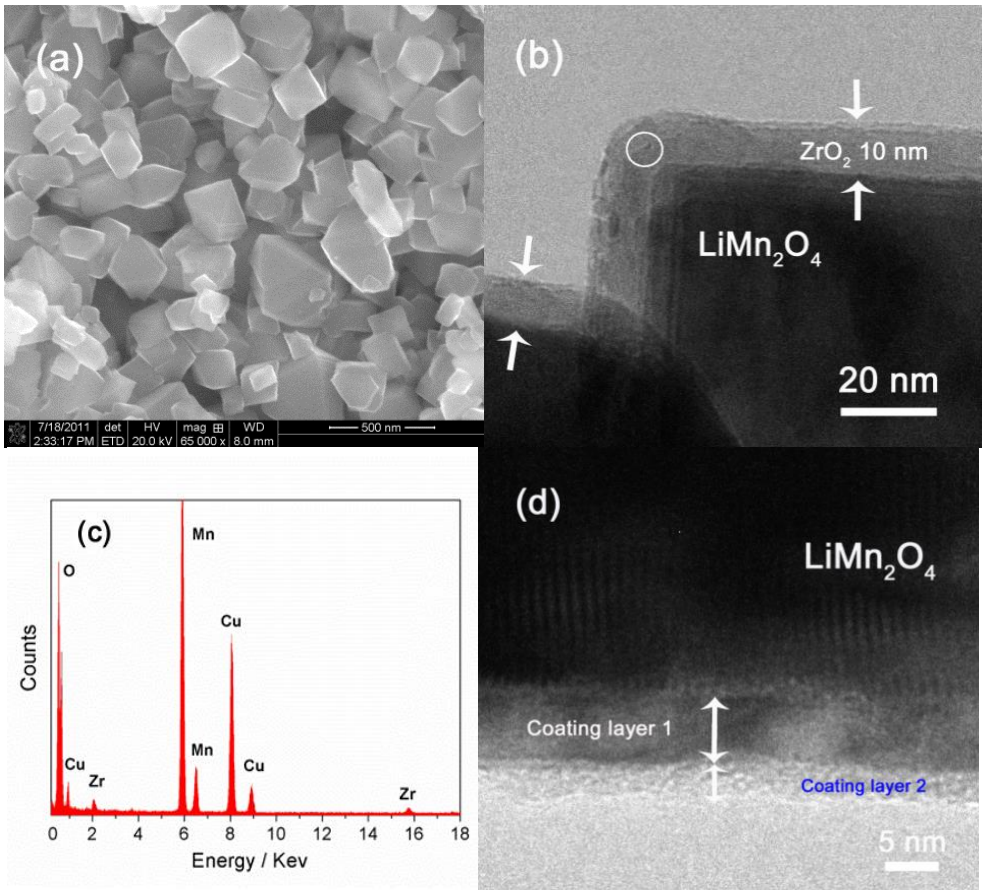

Figure 4.2 (a) FESEM image of bare $LiMn_2O_4$ nanoparticles; and (b) TEM image, (c) EDS spectrum captured from the area in the marked circle in (b) and (d) HRTEM image of $LiMn_2O_4$ nanoparticles coated with 50 ZrO_2 ALD layers.

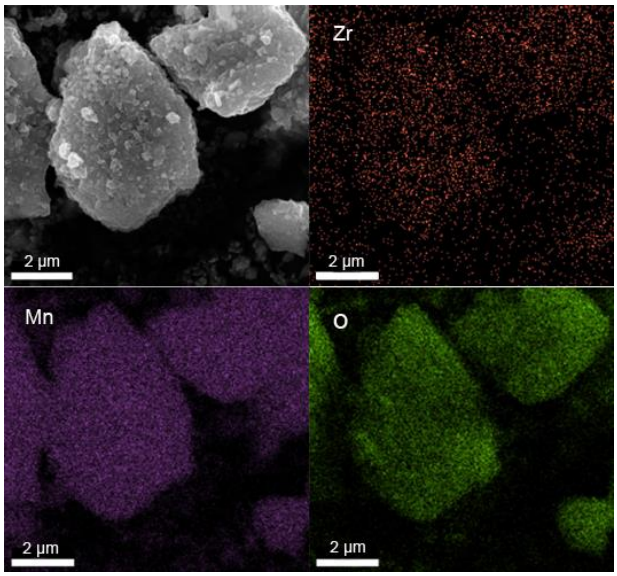

Figure 4.3 SEM image of agglomerated $LiMn_2O_4$ nanoparticles coated with 50 ZrO_2 ALD layers, and the corresponding elemental mappings of Zr (red image), Mn (purple image) and O (green image).

Furthermore, Figure 4.3 shows the EDS mappings of Zr, Mn and O elements from agglomerated $LiMn_2O_4$ nanoparticles with 50 ZrO_2 ALD coating layers, indicating the uniform ZrO_2 ALD coating on every individual $LiMn_2O_4$ nanoparticle. In comparison with facile deposition of crystalline ZrO_2 film on micro-sized $LiMn_2O_4$ particles using the same ZrO_2 ALD process [32], ZrO_2 ALD film on nano-sized $LiMn_2O_4$ particles is more difficult to grow epitaxially. We speculate that factors such as morphology, particle size, surface energy and grain size of different $LiMn_2O_4$ particles will influence the ZrO_2 ALD growth process, because ZrO_2 ALD growth starts from chemical bonds with the surface of $LiMn_2O_4$. There is ongoing work in our laboratory to study the effect of ZrO_2 ALD coating on various nanostructured cathode materials.

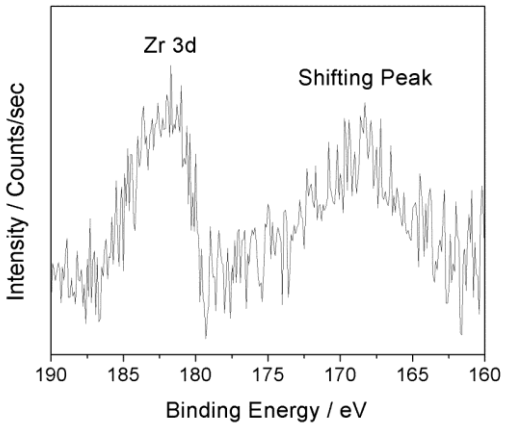

Figure 4.4 XPS spectrum for Zr 3d of $LiMn_2O_4$ nanoparticles coated with 50 ZrO_2 ALD layers.

To confirm the epitaxial growth of ZrO_2 coating on the surface of $LiMn_2O_4$ nanoparticles, X-ray photoelectron spectroscopy (XPS) is further employed to analyze surface composition of $LiMn_2O_4$ particles coated with 50 ZrO_2 ALD layers. In order to minimize electronic charging effect in XPS measurement, the charge neutralization function is turned on. Figure 4.4 presents the Zr 3d XPS pattern captured from 50 ZrO_2 ALD LMO particles. Two distinct Zr peaks located at the binding energies of 182 and 168 eV are detected, which are speculated to be from the two formed layers in ZrO_2 coating in Figure 4.2d. The representative Zr 3d peak positioned at 182 eV (consistent with the standard value of ZrO_2 in NIST XPS database) can be attributed to the stoichiometric and amorphous external ZrO_2 layer (layer 2 in Figure 4.2d). On the other hand, the other broad peak at 168 eV that has some shift from the standard binding energy of Zr 3d in ZrO_2 may be from the crystalline ZrO_2 layer (layer 1 in Figure 4.2d) which may have lattice change due to possible epitaxial growth of ZrO_2 coating on the surface of $LiMn_2O_4$ particles, indicating the complex chemical bonding environment for Zr element in the ZrO_2 ALD coating (50 ZrO_2 ALD layers) on $LiMn_2O_4$. Due to the chemical bonding in ZrO_2 ALD growth on $LiMn_2O_4$ substrate via oxygen bonds ($LiMn_2O_4$-O-ZrO_2), the amorphous ZrO_2 film is apt to crystallize following the crystalline orientation or lattice fringes of $LiMn_2O_4$ under vacuum during ZrO_2 ALD growth process even at very low temperature (120°C), and thus, this epitaxial growth yields two ZrO_2 layers in HRTEM observation (Figure 4.2d). As a result, the epitaxial ZrO_2 layer inside (layer 1) has very different chemical bonding environment for Zr in comparison with amorphous ZrO_2 in the layer outside (layer 2), leading to the shift of Zr 3d peak in XPS spectrum in Figure 4.4.

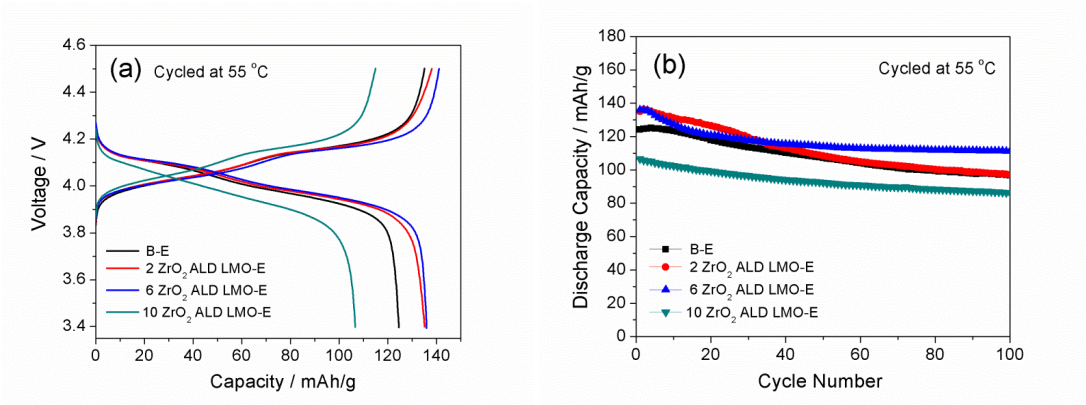

Figure 4.5 (a) 1st charge and discharge curves and (b) cycling performance of $LiMn_2O_4$ nanoparticles coated with 2, 6 and 10 ZrO_2 ALD layers in comparison with bare $LiMn_2O_4$ at a current density of 120 mA/g (~1 *C*) in a voltage range of 3.4-4.5 V at 55°C.

ZrO_2 coating on $LiMn_2O_4$-based cathode material mainly serves as an effective HF scavenger to suppress Mn dissolution and acts as an artificial interface to reduce deleterious reaction between $LiMn_2O_4$ and electrolyte for improved cycleability of $LiMn_2O_4$. Furthermore, the conformal ZrO_2 coating on $LiMn_2O_4$ particles can average distribution of electrons and lithium ions on the whole surface of $LiMn_2O_4$ particles;

hence, electrochemical polarization from electron conglomeration and concentration gradient of Li^+ can be significantly reduced in the cathode, especially under high charge/discharge rates at elevated temperature [11]. Therefore, the thickness of ZrO_2 film needs to be optimized to maximize the electrochemical performance of $LiMn_2O_4$. ZrO_2 coating with optimal thickness is supposed to be sufficiently thick to consume HF acid in electrolyte but not too thick to slow down diffusion of lithium ions at high charge/discharge rate. Our previous work has demonstrated that ultrathin ZrO_2 coating on micro-size $LiMn_2O_4$ particles for enhancing electrochemical performance of $LiMn_2O_4$ is more effective than coating on the entire composite electrode composed of $LiMn_2O_4$ particles and carbon/PVDF network, and the effect of oxide ALD coatings on improving capacity retention and increasing specific capacity of $LiMn_2O_4$ is more phenomenal at elevated temperature than at room temperature [11,22,32]. In the present work, we evaluate the effect of ZrO_2 ALD coating on $LiMn_2O_4$ nanoparticles for high-rate cycling performance at elevated temperature. In order to optimize electrochemical performance of ZrO_2-modified $LiMn_2O_4$ nanoparticles at elevated temperature (55°C), thickness of ZrO_2 coating on $LiMn_2O_4$ nanoparticles is finely tuned by using various ALD growth cycles, such as 2, 6 and 10 ALD growth cycles, corresponding to the thickness of 0.4, 1.2 and 2.0 nm, respectively. The ALD-coated composite electrodes are prepared by mixing these ALD-coated LMO particles with conductive carbon and PVDF binder at the same weight ratio of 8:1:1 (marked as 2, 6 or 10 ZrO_2 ALD LMO-E), respectively. Figure 4.5a and 5b show the initial charge and discharge curves and corresponding cycling performance of ZrO_2-modified $LiMn_2O_4$ cathodes in comparison with bare composite electrode at a high current density of 120 mA/g (~1 *C*) in a voltage range of 3.4 - 4.5 V at 55°C. Electrochemical measurements indicate that the optimal thickness of ZrO_2 coating for maximized performance of $LiMn_2O_4$ is ~1.2 nm grown via 6 ZrO_2 ALD layers. $LiMn_2O_4$ nanoparticles coated with 6 ZrO_2 ALD layers deliver a very high initial discharge capacity of 136.0 mAh/g at 1*C* at 55°C, significantly higher than that of bare $LiMn_2O_4$ (124.1 mAh/g). The improved initial capacities of 6 ZrO_2 ALD LMO-E can be attributed to the effective suppression of Mn dissolution and electrolyte decomposition at elevated temperature by conformal, uniform and complete coverage of ZrO_2 coating on the surface of individual $LiMn_2O_4$ particle. After 100 electrochemical cycles at elevated temperature, 6 ZrO_2 ALD LMO-E retains a specific capacity of 111.3 mAh/g, corresponding to an average capacity loss of 0.25 mAh/g per cycle. The sample 10 ZrO_2 ALD LMO-E only shows an initial capacity of 106. 6 mAh/g, illustrating that ZrO_2 coating thicker than 2 nm can significantly affect diffusion of lithium ions. On the other hand, 2 ZrO_2 ALD layers with the thickness of 0.4 nm on $LiMn_2O_4$ particles are not sufficient to completely scavenge the HF acid, resulting in the apparent capacity fading from 135.1 to 97.1 mAh/g after 100 electrochemical cycles, similar to the case of B-E. It is thus found that electrochemical performance of $LiMn_2O_4$ nanoparticles modified by ZrO_2 ALD layers is very sensitive to the coating thickness. The remarkable cycling stability of 6 ZrO_2 ALD LMO-E after the 50^{th} cycle indicates that the residual ZrO_2 protective film after consumption of HF acid is facile for lithium ion diffusion and can effectively

alleviate decomposition of electrolyte and reduce electrochemical polarization on the surface of $LiMn_2O_4$ particles.

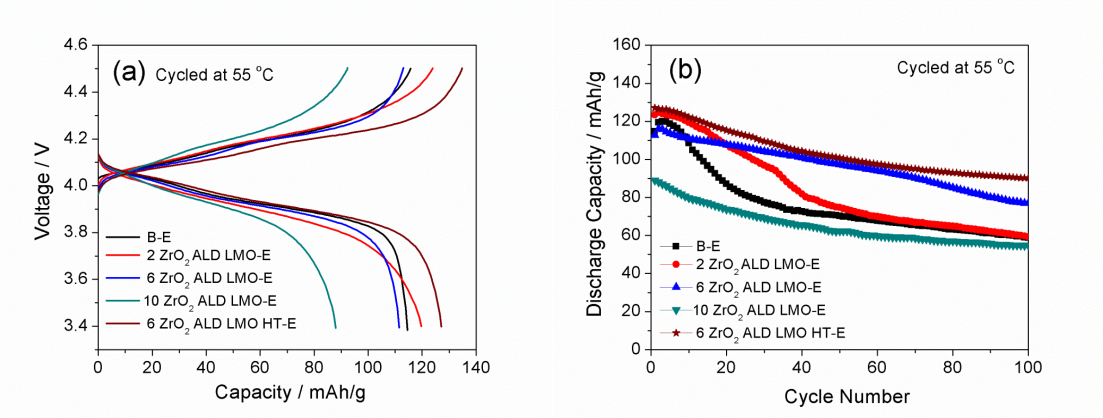

Figure 4.6 (a) 1st charge and discharge curves and (b) cycling performance of $LiMn_2O_4$ nanoparticles coated with 2, 6 and 10 ZrO_2 ALD layers in comparison with bare $LiMn_2O_4$ and heat-treated 6 ZrO_2 ALD coated $LiMn_2O_4$ at a current density of 600 mA/g (~5 *C*) in a voltage range of 3.4-4.5 V at 55°C.

The effect of tuning ZrO_2 ALD coating thickness on improving capacity retention of $LiMn_2O_4$ is even more phenomenal at high charge/discharge rate at elevated temperature. Figure 4.6a and 6b present electrochemical performance of ZrO_2-modified $LiMn_2O_4$ cathodes subject to a very high current density of 600 mA/g (~5 C) at 55°C. The 2 ZrO_2 ALD LMO-E delivers the highest initial discharge capacity of 123.4 mAh/g, higher than 112.7 mAh/g from 6 ZrO_2 ALD LMO-E and 88.5 mAh/g from 10 ZrO_2 ALD LMO-E as well as 114.6 mAh/g from B-E, indicating that thickness of ZrO_2 coating significantly influences diffusion of lithium ions under such a high current density. During subsequent electrochemical cycles at elevated temperature, B-E suffers from faster capacity fading as shown in Figure 4.6b due to the attack from acidic HF and decomposition of electrolyte on the surface of $LiMn_2O_4$ nanoparticles. In contrast, $LiMn_2O_4$ nanoparticles coated with 6 ZrO_2 ALD layers retain a discharge capacity of 76.9 mAh/g after 100 cycles, corresponding to a capacity retention of 68.2%, while bare $LiMn_2O_4$ nanoparticles exhibit a final capacity of 58.8 mAh/g and a capacity retention of only 51.4%. 2 ZrO_2 ALD LMO-E shows poor capacity retention after 100 cycles, as 2 ZrO_2 ALD layers with a thickness of 0.4 nm are not sufficient to scavenge the acidic HF. On the other hand, 10 ZrO_2 ALD LMO-E exhibits excellent cycling stability but low capacity, because 10 ZrO_2 ALD layers are overly thick and slow down diffusion of lithium ions. $LiMn_2O_4$ nanoparticles coated with 6 ZrO_2 layers with heat treatment further remain a discharge capacity of 90.3 mAh/g and a capacity retention of 71.1% after 100 cycles. The improved cycling stability of 6 ZrO_2 ALD LMO HT-E can be probably ascribed to the enhanced texture of ZrO_2 coating layer via post-heat treatment. Therefore, 6 ZrO_2 ALD layers (as thin as 1.2 nm) demonstrate to have the optimal thickness for maximized electrochemical performance of $LiMn_2O_4$ nanoparticles for applications in high-power lithium ion batteries at elevated temperature.

4.5 Conclusions

Ultrathin and highly-conformal ZrO_2 coatings have been facilely deposited on $LiMn_2O_4$ nanoparticles using atomic layer deposition. Epitaxial growth of ZrO_2 on underlying $LiMn_2O_4$ nanoparticles has been observed using HRTEM and XPS measurements. Crystalline ZrO_2 ALD coating can grow first on the surface of $LiMn_2O_4$ nanoparticles following the crystalline orientation of $LiMn_2O_4$ in low temperature ALD process followed by growth of amorphous ZrO_2 ALD film, yielding two distinguishing layers in the ZrO_2 coating. The thickness of ZrO_2 coating can be precisely tailored at ~2 Å per ALD cycle. The optimal thickness of ZrO_2 coating for maximized electrochemical performance of $LiMn_2O_4$ nanoparticles is 1.2 nm (6 ZrO_2 ALD layers). $LiMn_2O_4$ nanoparticles coated with the optimal 6 ZrO_2 ALD layers deliver an initial discharge capacity of 136.0 mAh/g at 1*C* and 112.7 mAh/g at 5*C* at 55°C. Surface modification of $LiMn_2O_4$ nanoparticles with ZrO_2 coating has led to the remarkably enhanced high-rate electrochemical performance of $LiMn_2O_4$ at elevated temperature.

4.6 References

1. O. K. Park, Y. Cho, S. Lee, H. C. Yoo, H.-K. Song, J. Cho, Who Will Drive Electric Vehicles, Olivine or Spinel? *Energy & Environmental Science* 4 (2011) 1621-1633.

2. L. Zhou, D. Zhao, X. Lou, $LiNi_{0.5}Mn_{1.5}O_4$ Hollow Structures as High-Performance Cathodes for Lithium-Ion Batteries. *Angewandte Chemie International Edition* 51 (2012) 239-241.

3. R. Mukherjee, R. Krishnan, T. M. Lu, N. Koratkar, Nanostructured Electrodes for High-Power Lithium Ion Batteries. *Nano Energy* 1 (2012) 518-533.

4. S. L. Candelaria, Y. Shao, W. Zhou, X. Li, J. Xiao, J. Zhang, Y. Wang, J. Liu, J. Li, G. Cao, Nanostructured carbon for energy storage and conversion. *Nano Energy* 1 (2012) 195-220.

5. K. M. Shaju, P. G. Bruce, A Stoichiometric Nano-$LiMn_2O_4$ Spinel Electrode Exhibiting High Power and Stable Cycling. *Chemistry of Materials* 20 (2008) 5557-5562.

6. H. W. Lee, P. Muralidharan, R. Ruffo, C. M. Mari, Y. Cui, D. K. Kim, Ultrathin Spinel $LiMn_2O_4$ Nanowires as High Power Cathode Materials for Li-Ion Batteries. *Nano Letters* 10 (2010) 3852-3856.

7. W. Tang, X. J. Wang, Y. Y. Hou, L. L. Li, H. Sun, Y. S. Zhu, Y. Bai, Y. P. Wu, K. Zhu, T. V. Ree, Nano $LiMn_2O_4$ as Cathode Material of High Rate Capability for Lithium Ion Batteries. *Journal of Power Sources* 198 (2012) 308-311.

8. Y. Matsuo, R. Kostecki, F. McLarnon, Surface Layer Formation on Thin-Film $LiMn_2O_4$ Electrodes at Elevated Temperatures. *Journal of The Electrochemical Society* 148 (2001) A687-A692.

9. T. Doi, M. Inaba, H. Tsuchiya, S. K. Jeong, Y. Iriyama, T. Abe, Z. Ogumi, Electrochemical AFM Study of $LiMn_2O_4$ Thin Film Electrodes Exposed to Elevated Temperatures. *Journal of Power Sources* 180 (2008) 539-545.

10. K. Y. Chung, H. S. Lee, W. S. Yoon, J. McBreen, X. Q. Yang, Studies of $LiMn_2O_4$ Capacity Fading at Elevated Temperature Using In Situ Synchrotron X-Ray Diffraction. *Journal of The Electrochemical Society* 153 (2006) A774-A780.

11. J. Zhao, Y. Wang, Ultrathin Surface Coatings for Improved Electrochemical Performance of Lithium Ion Battery Electrodes at Elevated Temperature. *The Journal of Physical Chemistry C* 116 (2012) 11867-11876.

12. S. T. Myung, K. Amine, Y. K. Sun, Surface Modification of Cathode Materials from Nano- to Microscale for Rechargeable Lithium-Ion Batteries. *Journal of Materials Chemistry* 20 (2010) 7074-7095.

13. M. Hirayama, H. Ido, K. Kim, W. Cho, K. Tamura, J. Mizuki, R. Kanno, Dynamic Structural Changes at $LiMn_2O_4$/Electrolyte Interface during Lithium Battery Reaction, *Journal of The American Chemical Society* 132 (2010) 15268-15276.

14. C. Qing, Y. Bai, J. Yang, W. Zhang, Enhanced Cycling Stability of $LiMn_2O_4$ Cathode by Amorphous $FePO_4$ Coating. *Electrochimica Acta* 56 (2011) 6612-6618.

15. S. Lee, Y. Cho, H. K. Song, K. T. Lee, J. Cho, Carbon-Coated Single-Crystal $LiMn_2O_4$ Nanoparticle Clusters as Cathode Material for High-Energy and High-Power Lithium-Ion Batteries. *Angewandte Chemie International Edition* 51 (2012) 8748-8752.

16. C. Li, H. P. Zhang, L. J. Fu, H. Liu, Y. P. Wu, E. Rahm, R. Holze, H. Q. Wu Cathode Materials Modified by Surface Coating for Lithium Ion Batteries. *Electrochimica Acta* 51 (2006) 3872-3883.

17. S. B. Park, H. C. Shin, W. G. Lee, W. I. Cho, H. Jang, Improvement of Capacity Fading Resistance of $LiMn_2O_4$ by Amphoteric Oxides. *Journal of Power Sources* 180 (2008) 597-601.

18. K. A. Walz, C. S. Johnson, J. Genthe, L. C. Stoiber, W. A. Zeltner, M. A. Anderson, M. M. Thackeray, Elevated Temperature Cycling Stability and Electrochemical Impedance of $LiMn_2O_4$ Cathodes with Nanoporous ZrO_2 and TiO_2 Coatings. *Journal of Power Sources* 195 (2010) 4943-4951.

19. S. Lim, J. Cho, PVP-Assisted ZrO_2 Coating on $LiMn_2O_4$ Spinel Cathode Nanoparticles Prepared by MnO_2 Nanowire Templates. *Electrochemical Communications* 10 (2008) 1478-1481.

20. J. S. Kim, C. S. Johnson, J. T. Vaughey, S. A. Hackney, K. A. Walz, W. A. Zeltner, M. A. Anderson, M. M. Thackeray, The Electrochemical Stability of Spinel Electrodes Coated with ZrO_2, Al_2O_3, and SiO_2 from Colloidal Suspensions. *Journal of The Electrochemical Society* 151 (2004) A1755-A1761.

21. H. Şahan, H. Göktepe, Ş. Patat, A. Ülgen, Effect of the Cr_2O_3 coating on Electrochemical Properties of Spinel $LiMn_2O_4$ as a Cathode Material for Lithium Battery Applications. *Solid State Ionics* 181 (2010) 1437-1444.

22. J. Zhao, Y. Wang, Surface Modifications of Li-Ion Battery Electrodes with Various Ultrathin Amphoteric Oxide Coatings for Enhanced Cycleability. *Journal of Solid State Electrochemistry* 17 (2012) 1049-1058.

23. J. D. Ferguson, A. W. Weimer, S. M. George, Atomic Layer Deposition of SiO_2 Films on BN Particles Using Sequential Surface Reactions. *Chemistry of Materials* 12 (2000) 3472-3480.

24. J. D. Ferguson, A. W. Weimer, S.M. George, Atomically Controlled Growth of Tungsten and Tungsten Nitride Using Sequential Surface Reactions. *Applied Surface Science* 162-163 (2000) 280-292.

25. J. D. Ferguson, A. W. Weimer, S. M. George, Atomic Layer Deposition of Ultrathin and Conformal Al_2O_3 Films on BN Particles. *Thin Solid Films* 371 (2000) 95-104.

26. Y. S. Jung, A. S. Cavanagh, L. A. Riley, S. H. Kang, A. C. Dillon, M. D. Groner, S. M. George, S. H. Lee, Ultrathin Direct Atomic Layer Deposition on Composite Electrodes for Highly Durable and Safe Li-Ion Batteries. *Advanced Materials* 22 (2010) 2172-2176.

27. I. D. Scott, Y. S. Jung, A. S. Cavanagh, Y. Yan, A. C. Dillon, S. M. George, S. H. Lee, Ultrathin Coatings on Nano-$LiCoO_2$ for Li-Ion Vehicular Applications. *Nano Letters* 11 (2011) 414-418.

CHAPTER 5. HIERARCHICAL FUNCTIONAL LAYERS ON HIGH-CAPACITY LITHIUM-EXCESS CATHODES FOR SUPERIOR LITHIUM ION BATTERIES

5.1 Introduction

Recently, Li-excess layered $Li[Li_xM_{1-x}]O_2$ (M = Mn, Ni, and Co) materials have attracted much research attention due to its high theoretical capacity (>250 mAh/g) and high operating potential (>4.5 V) [1-24]. The Li-excess oxide can be considered as either a solid solution or a composite oxide consisting of Li_2MnO_3 and $LiMO_2$ (M = Mn, Ni, and Co), in which $LiMO_2$ shares the same close-packing oxygen structure from a robust Mn-based layered structure of Li_2MnO_3 [5,7,22,23]. The structural compatibility between $LiMO_2$ and Li_2MnO_3 as layered rock-salt structures allows for their structural integration. The high capacity of Li-excess layered cathode material has been demonstrated from electrochemical activation of inert Li_2MnO_3 at the initial charge to 4.8 V vs. Li/Li^+. In this electrochemical activation process oxygen will be irreversibly lost together with lithium ion extraction as lithia when Li_2MnO_3 is decomposed to Li_2O and MnO_2. Hence, the oxidation state of the transition metal ions is decreased in comparison with that in the initial material at the end of the first discharge to 2.0 V vs. Li/Li^+ [6,13,25].The initial Li_2MnO_3 activation contributes to the high capacity of Li-excess layered cathode in the subsequent electrochemical cycles but also the low Coulombic efficiency of the first cycle. However, the easy oxidation in transition metal redox pairs during the initial Li_2MnO_3 activation induces severe decomposition of electrolyte. Subsequently, phase transformation and transition metal dissolution occur in the layered structure of Li-excess cathode due to the elimination of oxygen ion vacancies via atomic rearrangements, resulting in significant irreversible capacity loss and structural instability of working electrode [17]. In spite of the high capacity, these layered cathode materials suffer from significant irreversible capacity loss in the initial charge/discharge, inferior rate capability and poor reversibility. The unfavorable cycling performance of Li-excess layered cathode materials at high charge/discharge rates can be attributed to structural rearrangement, poor electronic conductivity and severe side reactions on the cathode surface [6,7,15,19,24,25]. These factors summarized above together hinder the commercial application of Li-excess layered cathode materials.

Several approaches have been reported to solve the issues of Li-excess layered cathode materials mentioned above via metal ion doping, surface modification, preparing nanocomposite, and fabricating nano-sized materials [14,26-36]. Surface modification is extensively utilized due to its simplicity and effectiveness. A variety of surface coatings have been synthesized to ameliorate properties of underlying Li-excess cathodes, and thus improve its reversibility, rate capability and cycleability [5,37]. The coating materials can be divided into two categories: Li-active and Li-inert materials. To date, Li-inert coating materials reported in literature include metal oxides [25,28], metal fluorides [26,27], metal phosphates [26,29], carbon-based materials [24,36], and so on. Among these inert coating materials, surface

modification via oxide coatings (e.g., Al_2O_3, ZnO, ZrO_2, MgO, MnO, SnO_2 and CeO_2) has been demonstrated as one of the most effective approaches to improve cycling performance of Li-excess layered cathodes [12,26,28,33]. The oxide coating not only serves as a physical protection barrier that prevents cathode from direct contact with non-aqueous electrolyte but also as a HF scavenger that reduces acidity of electrolyte. In addition, the oxide film can act as a solid framework to restrict the disordered phase transformation, leading to better structural stability [25,38,39]. However, surface modifications with electrochemically inactive materials will decrease the energy and volumetric densities of active cathode materials and affect lithium ion and electron transfer in working electrodes [40]. Compared to thick and incomplete oxide coatings prepared by traditional wet chemical methods, films grown using atomic layer deposition (ALD) are uniform, dense, homogenous, pinhole-free, and extremely conformal to the underlying substrate, and the thickness of coatings can be precisely controlled at atomic level [41-46]. ALD is an thin film deposition subjected to a sequence of chemisorption and self-terminating surface reactions. ALD oxide coatings have been used to enhance electrochemical performance of common cathode materials, such as $LiCoO_2$ [41,42] and $LiMn_2O_4$ [43,46]. However, there are only a few reports investigating the effect of oxide ALD coatings on Li-excess layered cathode materials [25].

On the other hand, fabrication of core-shell structures via "wet-chemical" methods is a common route to introduce Li-active materials as shells on the surface of core materials [14,21,40,47-52]. The electrochemically-active shells can improve electronic conductivity, lithium ion diffusivity, thermal stability, and cycling stability of core Li-excess cathode materials. In order to improve cycling stability, X. Yang *et al.* employed Li-rich $Li_{1.15}[Ni_{1/4}Mn_{3/4}]_{0.85}O_2$ as the shell enwrapping core $Li_{1.15}[Ni_{1/3}Co_{1/3}Mn_{1/3}]_{0.85}O_2$. The as-prepared core-shell composite shows significantly enhanced cycling performance, due to better structural stability of the core-shell structure [51]. D. Kim *et al.* introduced spinel Li-poor $Li_{0.5}Mn_{0.65}Ni_{0.35}O_2$ shell on core $0.3Li_2MnO_3{\cdot}0.7LiMn_{0.5}Ni_{0.5}O_2$ cathode, which can decrease lithium content in the parent 'layered-layered' structure and enhance its electrochemical property [14]. Q. Qiao *et al.* have reported that coating $LiMnPO_4$ on the surface of Li-rich layered $Li[Li_{0.17}Ni_{0.25}Mn_{0.58}]O_2$ followed by heat treatment can increase reaction kinetics and structural stability of core material, resulting in better rate capability and cycleability in comparison with bare cathode [52]. Overall, core-shell structured composites have been designed to combine advantages from both core and shell materials for enhanced electrochemical performance.

5.2 Objectives of Project

Among solid solutions of layered cathode materials, $Li[Li_{0.2}Mn_{0.54}Ni_{0.13}Co_{0.13}]O_2$ in a two component notation as $0.5\ Li_2MnO_3{\cdot}0.5\ LiMn_{1/3}Ni_{1/3}Co_{1/3}O_2$ (hereafter marked as LMNCO) has received particular interest, due to its higher theoretical capacity of 321 mAh/g, better cycling stability and rate capability than other Li-rich analogues; thus it is an excellent candidate as cathode for applications in superior

lithium ion batteries with high energy and high power [53,54]. As shown in Figure 5.1, hierarch functional layers on LMNCO cathode are designed in this work and expected to achieve a synergetic effect from ALD oxide coating and core-shell structure for superior battery performance. We first synthesize $Li[Li_{0.2}Mn_{0.54}Ni_{0.13}Co_{0.13}]O_2$ nanoparticles by using surfactant-assisted dispersion. The triblock co-polymer F127 serves as the dispersant in sol-gel method. In comparison with micro-sized materials, nanomaterials offer more active sites for lithium ion insertion and extraction due to the larger surface-to-volume ratio, and provide more flexibility for volume expansion/contraction during lithiation/delithiation process, resulting in higher specific capacity and improved cycleability. Furthermore, nanomaterials provide larger electrode/electrolyte contact area and shorter lithium ion diffusion path, leading to superior rate capability. However, associated with these benefits, the high surface area and complex structure of nanomaterials will exacerbate undesirable side reactions in terms of decomposition of electrolyte and dissolution of transition metal ions [37].

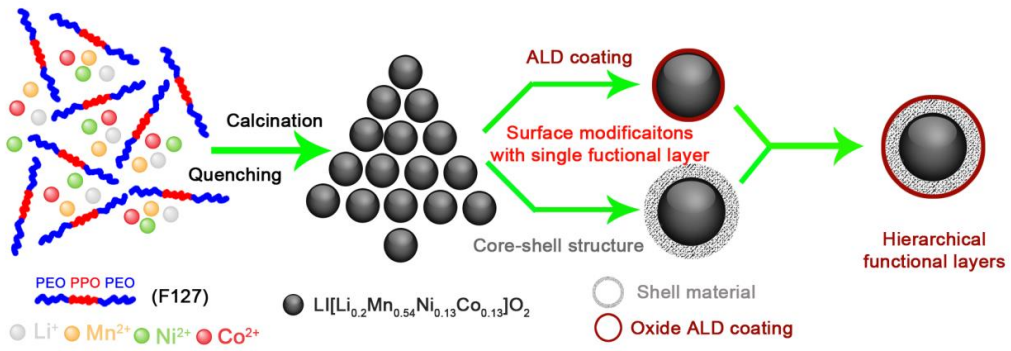

Figure 5.1 Schematic diagram showing preparation and surface modifications of $Li[Li_{0.2}Mn_{0.54}Ni_{0.13}Co_{0.13}]O_2$ nanoparticles.

In order to improve cycleability and rate capability of Li-excess layered LMNCO nanomaterials, we systematically evaluate the effects of ALD oxide coatings on LMNCO nanoparticles (marked as *n* M_xO_y ALD@LMNCO, M=Zn, Zr, and Al, *n* is the ALD coating layers) via tuning ALD coating thickness and composition. In addition, we synthesize core-shell-structured composite cathode consisting of Li-stoichiometric materials (LiM_xO_y, M=Mn and Co) as shell and Li-excess LMNCO as core material (marked as LM_xO_y-X@LMNCO, M=Mn and Co, X is the weight content of shell materials) and optimize the performance of core-shell cathode by tailoring weight content of shell and changing composition of shell materials. Finally, electrochemical performance of LMNCO cathode can be maximized by depositing hierarch functional layers on LMNCO nanoparticles consisting of 10 wt.% $LiCoO_2$ as a shell followed by coating six ZrO_2 ALD layers (marked as 6 ZrO_2 ALD@LCO-10@LMNCO). The 6 ZrO_2 ALD@LCO-10@LMNCO composite shows superior cycling stability and rate capacity due to the synergic and cooperative

effects from $LiCoO_2$ shell (~10 nm thickness) and ultrathin ZrO_2 coating (~1 nm thickness) that improve the electronic conductivity of cathode and reduce side reactions during electrochemical cycling.

5.3 Experimental Section

5.3.1 Synthesis of Li-excess $Li[Li_{0.2}Mn_{0.54}Ni_{0.13}Co_{0.13}]O_2$ nanoparticles

The Li-excess $Li[Li_{0.2}Mn_{0.54}Ni_{0.13}Co_{0.13}]O_2$ nanoparticles were synthesized by using surfactant-assisted dispersion. We first prepared three precursor solutions: 5.4 mmol F127 ($EO_{106}PO_{70}EO_{106}$) as the dispersant in 50 ml ethanol, 0.1 mol transition metal acetates (a molar ratio of Mn^{2+}:Ni^{2+}:Co^{2+}=0.54:0.13:0.13) in 50 ml ethanol, and 0.12 mol lithium hydroxide in 20 ml distilled water. The molar ratio of F127/Mn^{2+} was set to 0.01. The transition metal precursor solution was dropwisely dropped into F127/ethanol solution under continuous stirring at 40°C, and then the lithium precursor solution was added. The mixed solution was heated at 80°C until the solvent was completely evaporated. Afterwards, the mixture was dried in air at 120°C for 12h. The heat treatment of dried mixture was carried out in air at 300°C for 3h, followed by sintering at 900°C for 12h and quenching in distilled water. The $Li[Li_{0.2}Mn_{0.54}Ni_{0.13}Co_{0.13}]O_2$ nanoparticles were collected after being completely dried in vacuum over overnight.

5.3.2 Atomic layer deposition of different ultrathin oxide coatings on $Li[Li_{0.2}Mn_{0.54}Ni_{0.13}Co_{0.13}]O_2$ nanoparticles

Atomic layer deposition of different oxide coatings on LMNCO nanoparticles was performed in a Savannah 100 ALD system (Cambridge NanoTech Inc.) at 120 °C. ZnO ALD coating was carried out using $Zn(CH_2CH_3)_2$ (diethylzinc, DEZ) and H_2O as precursors with exposure time of 0.03 and 0.03 s, waiting time of 10 and 10 s, purge time of 40 and 40 s, respectively. ZrO_2 ALD coating was obtained by using $Zr(OC(CH_3)_3)_4$ (Zirconium tert-butoxide, ZTB) and H_2O as precursors with exposure time of 0.03 and 0.5 s, waiting time of 10 and 10 s and purge time of 40 s and 60 s, respectively. Al_2O_3 ALD coating was achieved applying $Al(CH_3)_3$ (Trimethylalumium, TMA) and H_2O as precursors with exposure time of 0.02 and 0.02 s, waiting time of 10 and 10 s and purge time of 40 s and 40 s, respectively. The principle of oxide ALD growth from H_2O and metallic precursors is subjected to the two self-terminating reactions, which can be referred from our previous works [38,39,46].

5.3.3 $LiCoO_2$@$Li[Li_{0.2}Mn_{0.54}Ni_{0.13}Co_{0.13}]O_2$ core-shell structure

Stoichiometric molar ratio of lithium acetate and cobalt acetate were first dissolved in distilled water. $Li[Li_{0.2}Mn_{0.54}Ni_{0.13}Co_{0.13}]O_2$ powders were dispersed in the above solution. The mixed solution was sonicated for 30 minutes, and then stirred at 80 ℃ to evaporate the distilled water. After being dried in air overnight at 120 ℃,

the mixture composed of LMNCO powders and Li and Co precursor was sintered in air at 750 ℃ for 12h. The weight ratio of core $Li[Li_{0.2}Mn_{0.54}Ni_{0.13}Co_{0.13}]O_2$ and shell $LiCoO_2$ can be controlled via tuning the mass of $Li[Li_{0.2}Mn_{0.54}Ni_{0.13}Co_{0.13}]O_2$ powders and Li and Co precursors. The same procedure was used to prepare $LiMn_2O_4$ and $LiCoMnO_4$ as shell materials on core $Li[Li_{0.2}Mn_{0.54}Ni_{0.13}Co_{0.13}]O_2$ by using corresponding transition metal precursors.

5.3.4 Hierarchical Functional Layers coating on core $Li[Li_{0.2}Mn_{0.54}Ni_{0.13}Co_{0.13}]O_2$ nanoparticles

To deposit hierarchical functional layers on core $Li[Li_{0.2}Mn_{0.54}Ni_{0.13}Co_{0.13}]O_2$ nanoparticles, the as-prepared core-shell structure was coated with ALD oxide film. The $Li[Li_{0.2}Mn_{0.54}Ni_{0.13}Co_{0.13}]O_2$ nanoparticles was modified with 10 wt.% $LiCoO_2$ shell, followed by coating of 6 ZrO_2 ALD layers.

5.3.5 Characterizations

The crystallographic structure of $Li[Li_{0.2}Mn_{0.54}Ni_{0.13}Co_{0.13}]O_2$ nanoparticles was examined by X-ray diffraction (XRD) using a Rigaku MiniFlex X-ray diffractometer with Cu K_α radiation at a scan rate of 2^o/min. Morphology and particle size of LMNCO nanoparticles were observed using a FEI Quanta 3D FEG field emission scanning electron microscopy (FESEM). Transmission electron microscopy (TEM) images were captured on a JEM-2010 instrument microscope at an acceleration voltage of 200 kV, to examine morphology and structure of bare and surface modified LMNCO nanoparticles.

5.3.6 Electrochemical measurements

The working electrodes were composed of 75 wt.% bare or surface modified $Li[Li_{0.2}Mn_{0.54}Ni_{0.13}Co_{0.13}]O_2$ nanoparticles, 20 wt.% acetylene black (conductive carbon, Alfa Aesar, 99.5%), and 5 wt.% poly-vinylidenefluoride (PVDF, Alfa Aesar) as the binder. These cathodes were assembled into two-electrode CR2032-type coin cells for electrochemical measurements, with metallic lithium foil as anode, Celgard-2320 membrane as separator; electrolyte was 1 M $LiPF_6$ dissolved in ethylene carbonate (EC) and dimethyl carbonate (DMC) and diethyl carbonate (DEC) at a volumetric ratio of 1:1:1. Galvanostatic charge and discharge were performed at different current densities in a voltage range of 2.0-4.8 V using an 8-channel battery analyzer (MTI Corporation). Theoretical capacities of bare and surface modified $Li[Li_{0.2}Mn_{0.54}Ni_{0.13}Co_{0.13}]O_2$ cathode materials are all set to 250 mAh/g, i.e., current density corresponding to 1*C* is 250 mA/g. Electrochemical storage capacities of working electrodes were calculated based on the mass of active cathode materials. Cyclic voltammetric (CV) curves of different cathodes were recorded at a scanning rate of 0.1mV/s between 2.0 and 4.8 V using an electrochemical analyzer (CHI 605C).

5.4 Results and Discussion

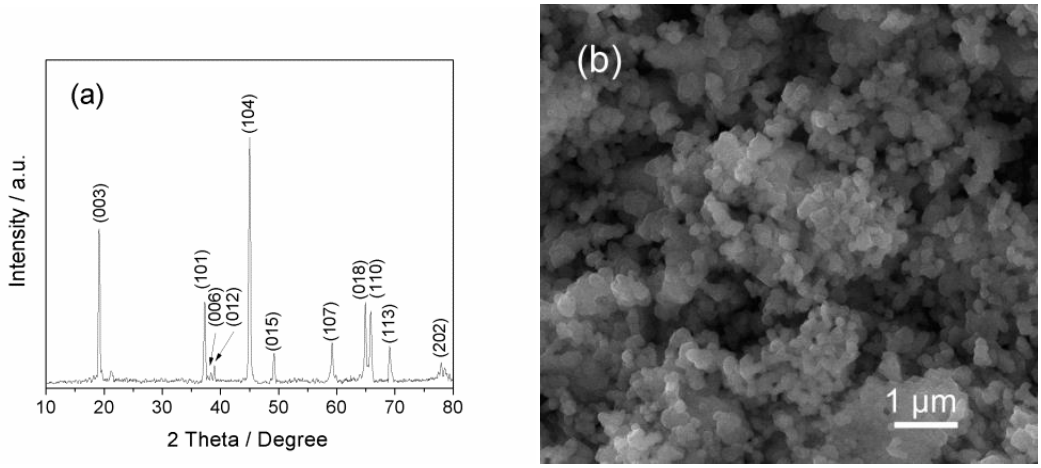

Figure 5.2 (a) XRD pattern and (b) scanning electron microscopic (SEM) image of $Li[Li_{0.2}Mn_{0.54}Ni_{0.13}Co_{0.13}]O_2$ powders.

The pristine $Li[Li_{0.2}Mn_{0.54}Ni_{0.13}Co_{0.13}]O_2$ can be considered as a solid solution composite, composed of Li-inactive Li_2MnO_3 and Li-active $LiMn_{1/3}Ni_{1/3}Co_{1/3}O_2$ two phases with a molar ratio of 1:1 in an integrated layered structure [9,29]. XRD pattern in Figure 5.2a illustrates the predominant layered structure of LMNCO with group space *R-3m*. The weak diffraction peak located around 2θ=20-25º indicates the super lattice structure, which is resulted from the $LiMn_6$ cation arrangement in the transition metal layers of Li_2MnO_3 component (group space *C2m*) [10,18,22]. The Li-excess layered LMNCO nanoparticles with an average particle size of ~250 nm have been facilely prepared via using surfactant dispersion, as shown in SEM image (Figure 5.2b) and TEM image (Figure 5.3a).

5.4.1 Improving and optimizing electrochemical performance of LMNCO via oxide ALD coatings

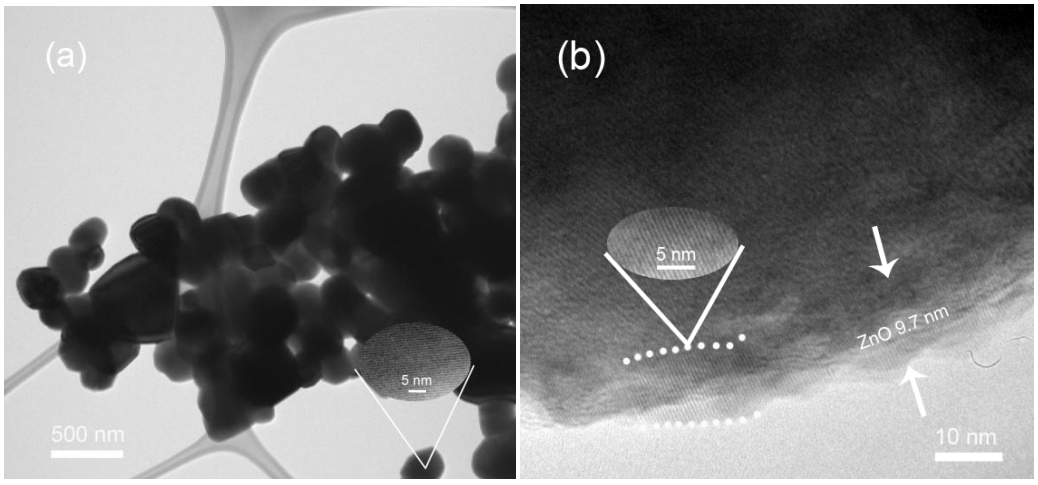

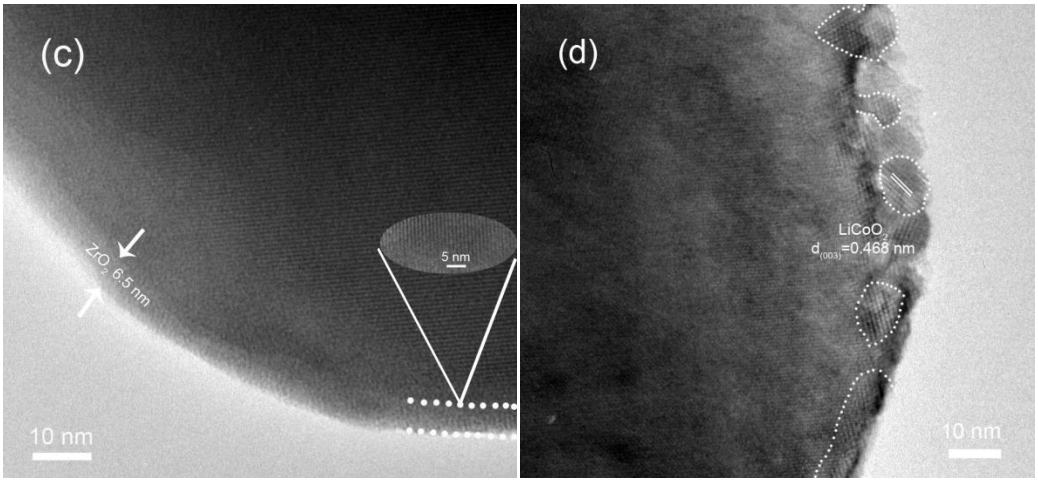

Figure 5.3 Transmission electron microscopic (TEM) images with inserted high-resolution lattice fringes of (a) bare $Li[Li_{0.2}Mn_{0.54}Ni_{0.13}Co_{0.13}]O_2$ nanoparticles, and $Li[Li_{0.2}Mn_{0.54}Ni_{0.13}Co_{0.13}]O_2$ particle coated with (b) 50 ZnO ALD layers, (c) 50 ZrO_2 ALD layers and (d) 10 wt.% $LiCoO_2$ shell.

In this section, the optimal thickness for maximizing cycling performance is determined via tailoring ZnO ALD coatings on LMNCO nanoparticles, and effects of various ALD oxide coatings on improving electrochemical properties of LMNCO cathode are compared for the first time. TEM images in Figure 5.3b and 3c show ZnO and ZrO_2 ALD coatings that are conformal, homogeneous, uniform and crystalline. 50 ALD growth cycles contribute to the thickness of 9.7 nm for ZnO and 6.5 nm for ZrO_2 on the surface of LMNCO nanoparticles, corresponding to the ALD growth rate of 1.94 Å/cycle for ZnO, 1.30 Å/cycle for ZrO_2, respectively.

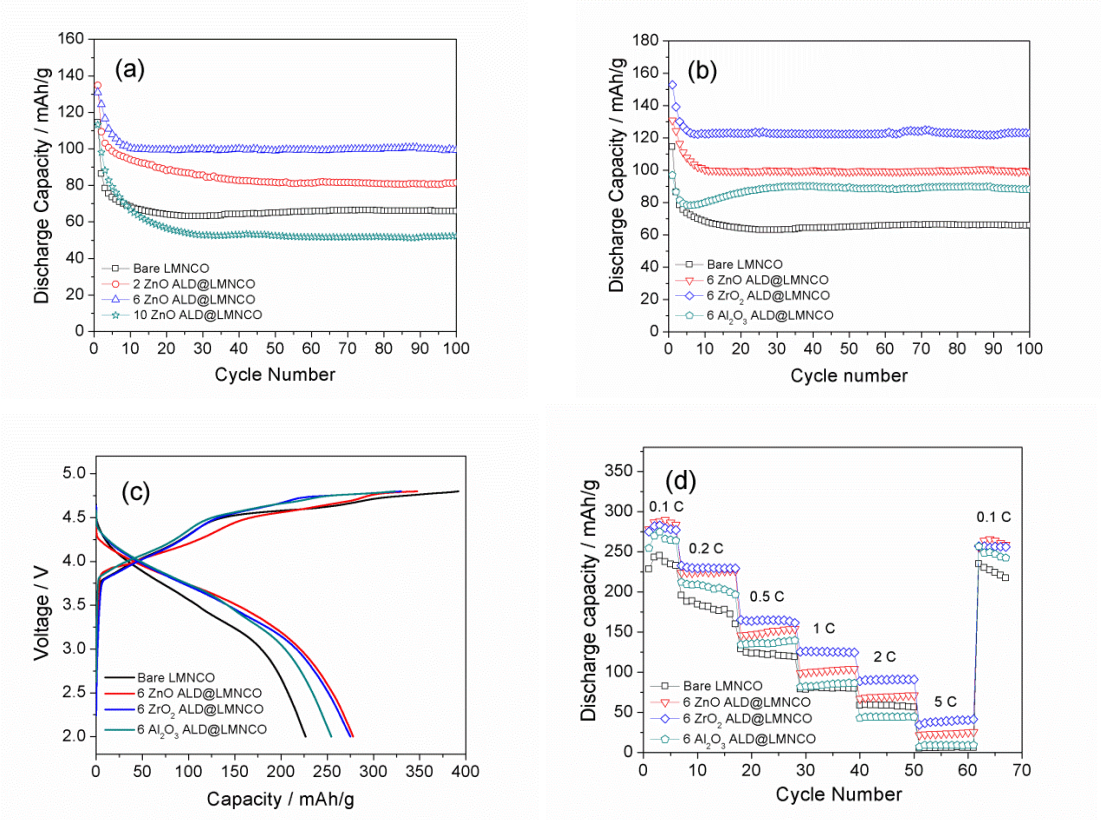

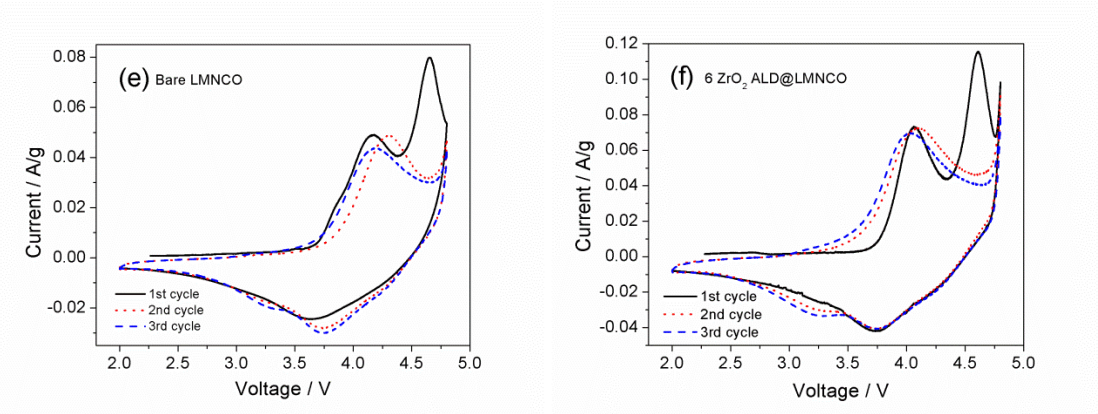

Figure 5.4 Electrochemical performances of different ALD-modified $Li[Li_{0.2}Mn_{0.54}Ni_{0.13}Co_{0.13}]O_2$ electrodes in a voltage range of 2.0-4.8 V *vs.* Li/Li^+: (a) Cycling performances of $Li[Li_{0.2}Mn_{0.54}Ni_{0.13}Co_{0.13}]O_2$ nanoparticles coated with 2, 6 and 10 ZnO ALD layers in comparison with bare electrode at a current density of 250 mA/g (1*C*); (b) Cycling performances at a current density of 250 mA/g (1*C*), (c) the initial charge and discharge curves at a current density of 25 mA/g (0.1*C*) and (d) rate performances at different current densities of $Li[Li_{0.2}Mn_{0.54}Ni_{0.13}Co_{0.13}]O_2$ nanoparticles coated with 6 ZnO, 6 ZrO_2 and 6 Al_2O_3 ALD layers in comparison with bare electrode; the first three CV profiles of (e) bare electrode and (f) $Li[Li_{0.2}Mn_{0.54}Ni_{0.13}Co_{0.13}]O_2$ nanoparticles coated with 6 ZrO_2 ALD layers at a scanning rate of 0.1 mV/s. "Bare LMNCO": bare $Li[Li_{0.2}Mn_{0.54}Ni_{0.13}Co_{0.13}]O_2$ nanoparticles; "*n* M_xO_y ALD@LMNCO (M=Zn, Zr and Al)": $Li[Li_{0.2}Mn_{0.54}Ni_{0.13}Co_{0.13}]O_2$ nanoparticles coated with *n* M_xO_y ALD layers.

Figure 5.4 summarizes the effects of ultrathin oxide ALD coatings on LMNCO nanoparticles on improving electrochemical performance via tuning ALD coating thickness and composition. Thus, we compare cycling performances of LMNCO nanoparticles coated with two, six, and ten ZnO ALD layers, and those of LMNCO modified with ZnO, ZrO_2 and Al_2O_3 ALD coatings. As shown in Figure 5.4a, bare LMNCO suffers from drasitic capacity fading from the initial discharge capacity of 114.5 mAh/g to 65.9 mAh/g after 100 electrochemical cycles at 1*C* (250 mA/g). On the contrary, LMNCO coated with ZnO ALD film exhibits improved capacity retentions in comparison with bare cathode. The enhanced electrochemical performance can be attributed to the protective ZnO ALD coating that reduces decomposition of electrolyte and preserves structural stability of LMNCO cathode. Six ZnO ALD layers demonstrate to have optimal thickness (1.14 nm via 6 ALD growth layers) for the best performance of LMNCO nanoparticles, consistent with the optimal Al_2O_3 ALD coatings on the surface of LMNCO via 6 ALD growth cycles in the reported work [25]. We speculate that two ZnO ALD layers (0.388 nm thick) are too thin to provide sufficient mechanical protection and to consume the HF in electrolyte, while thicker ZnO coating composed of ten ZnO ALD layers (1.94 nm thick) may slow down the lithium ion diffusion at a high current density of 250 mAh/g [38].

Figure 5.4b-4d compare initial charge/discharge capacities and rate performances of bare LMNCO and LMNCO nanoparticles coated with 6 ZnO, 6 ZrO_2 and 6 Al_2O_3 ALD layers. It can be seen that all ALD modified LMNCO cathodes show improved cycleability, Coulombic efficiencies in the initial cycle and rate capability than bare cathode. In particular, six ZrO_2 ALD layers demonstrate as the most effective coating, followed by ZnO and Al_2O_3, on improving performance of LMNCO especially at high charge/discharge rates as shown in Figure 5.4d. Bare LMNCO delivers an initial charge capacity of 397.1 mAh/g and discharge capacity of 228.4 mAh/g at 0.1*C* (Figure 5.4c), corresponding to a very low Coulombic efficiency of 58.3%. The high irreversible capacity loss of pristine LMNCO can be ascribed to intense decomposition of organic electrolyte on the large surface of LMNCO nanoparticles together with structural disorder of LMNCO caused by transition metal dissolutions in LMO_2 (M=Mn, Ni and Co) and irreversible oxygen loss in Li_2MnO_3 component. In contrast, LMNCO coated with 6 ZrO_2 ALD layers (~1 nm thick) exhibit a much higher Coulombic efficiency of 83.3% and specific discharge capacity of 274.9 mAh/g, due to the conformal and complete coverage of ALD film on individual LMNCO nanoparticle. The 6 ZrO_2 ALD@LMNCO also shows improved cycling stability in comparison with that of bare LMNCO by retaining a discharge capacity of 123.0 mAh/g after 100 cycles at 1*C* and delivering a capacity retention of 80.4%, while bare LMNCO nanoparticles exhibit a final capacity of 65.9 mAh/g and a capacity retention of only 65.6% (Figure 5.4b). Compared to ZnO and Al_2O_3 coated LMNCO cathodes, better high-rate cycling performance of 6 ZrO_2 ALD@LMNCO in Figure 5.3d may be attributed to the formation of lithium ion conductive interphase, Li-Zr-O or Li-M-Zr-O (M=Mn, Ni and Co), between LMNCO bulk and ZrO_2 coating [25,46]. However, ZrO_2 ALD coating for enhancing rate capability of LMNCO cathode is limited by the inferior conductivity of LMNCO nanoparticles and semi-conductivity of ZrO_2 coating. As for Al_2O_3 ALD coating, although Al_2O_3 ALD coating has been demonstrated to improve electrochemical performance of LMNCO cathodes at low current densities less than 1*C* (Figure 5.4c), which has also been reported in others' [25], the electronically insulating Al_2O_3 coating affects high-rate capacities of Al_2O_3 ALD modified LMNCO cathodes when the current density is higher than 2*C*, as shown in Figure 5.4d.

Cyclic Voltammetric (CV) performances are then carried out to understand the effect of ZrO_2 ALD coating on electrochemical performance of LMNCO cathode, as presented in Figure 5.4e-4f. The peaks in CV curves correspond to oxidation and reduction of transition metal redox pairs that occur upon lithium ion extraction and insertion in LMNCO layered structure. Figure 5.4e reveals the first three cycles of CV measurement of bare LMNCO cathode. The first anodic peak at 4.16 V in the initial charge curve is associated with the oxidation of Ni^{2+} to Ni^{4+} followed by Co^{3+} to Co^{4+}, whereas Mn still remains as tetravalent in $LiMn_{1/3}Ni_{1/3}Co_{1/3}O_2$ structure [31,55]. The second anodic peak at 4.65 V corresponds to the decomposition of Li_2MnO_3 to Li_2O and MnO_2, along with the unavoidable decomposition of electrolyte and the formation of solid electrolyte interphase (SEI) at such high potential > 4.5 V [35]. Such electrochemical activation process of Li_2MnO_3 would result in the low Coulombic

efficiency in the first cycle and high capacity of Li-excess layered cathode materials via simultaneously losing oxygen irreversibly as Li_2O and yielding Li-active MnO_2 component. In the initial discharge curve of the same sample, reduction of Co^{4+} to Co^{3+} and Ni^{4+} to Ni^{2+} occurs at 3.63 V, and the cathodic peak at 3.26 V can be assigned to the reduction of Mn^{4+} to Mn^{3+} from the as-activated MnO_2 component [35]. The anodic and cathodic peaks in the first CV cycle are consistent with the voltage plateaus in the first charge/discharge profiles of LMNCO in Figure 5.4c. It can be seen from the second and third CV cycles in Figure 5.4e that the peak observed at 4.65 V in the initial CV curve disappears leaving only one anodic peak at 4.16 V. The corresponding cathodic peak associated with reduction of Ni^{2+}/Ni^{4+} and Co^{3+}/Co^{4+} redox pairs shifts obviously towards the higher voltage region at 3.75 V, and the cathodic peak related to reduction of Mn^{3+}/Mn^{4+} redox at 3.26 V becomes more distinct, indicating better reversibility of transition metal redox pairs in bare LMNCO cathode after the initial activation process. In the case of the CV curves of LMNCO coated with six ZrO_2 ALD layers (~1 nm thick) as shown in Figure 5.4f, the anodic peak in the first CV cycle related to oxidation of Ni^{2+}/Ni^{4+} and Co^{3+}/Co^{4+} redox pairs is sharper with even higher current in comparison with that of pristine LMNCO. It can also be found that the subsequent initial activation peak separates two sharp anodic peaks at 4.60 V and around 4.8 V. The former peak is attributed to the activation of Li_2MnO_3 and the latter can probably be ascribed to decomposition of electrolyte and formation of SEI film on the surface of electrode. Such intriguing electrochemical phenomenon indicates that ZrO_2 coating can effectively reduce decomposition of electrolyte during the activation procedure of Li_2MnO_3, and thus facilitates complete activation of Li_2MnO_3, leading to less electrochemical polarization, higher specific capacity and better structural stability of LMNCO cathode. However, decomposition of electrolyte cannot be avoided due to the high oxidation abilities of Mn^{3+}/Mn^{4+}, Ni^{2+}/Ni^{4+} and Co^{3+}/Co^{4+} redox pairs. The corresponding reduction of Ni^{2+}/Ni^{4+} and Co^{3+}/Co^{4+} redox pairs at 3.75 V is more reversible, resulting in smaller overpotential of 0.32 V than 0.53 V of bare LMNCO (Figure 5.4e). The cathodic peak at 3.20 V becomes sharper in the second and third CV cycles, indicating easier reduction of Mn^{3+}/Mn^{4+} redox in later cycles. Furthermore, CV profiles of 6 ZrO_2 ALD@LMNCO in the second and third cycles are almost identical to each other, though both lose the irreversible activation peak from the CV curve of the first cycle, demonstrating the remarkable improved reversibility of 6 ZrO_2 ALD@LMNCO in comparison with bare LMNCO.

Overall, electrochemical performances of various electrodes in Figure 5.4 illustrate that surface modifications of Li-excess layered cathode material - $Li[Li_{0.2}Mn_{0.54}Ni_{0.13}Co_{0.13}]O_2$ and tailoring oxide ALD coatings can effectively reduce decomposition of electrolyte in the initial activation process of Li_2MnO_3 and alleviate structural degradation in subsequent cycles. The ALD-modified LMNCO cathodes show increased Coulombic efficiency in the initial cycle, higher specific capacity and enhanced cycleability in comparison with bare LMNCO electrode. The optimal thickness of ALD oxide coating for LMNCO nanoparticles is ~1 nm composed of 6 oxide ALD layers. ZrO_2 is the most effective oxide coating to improve performance of

LMNCO electrodes, followed by ZnO and Al_2O_3. However, ZrO_2 ALD coating does not show significant effect in improving rate capability of LMNCO coated due to poor electronic conductivity of ZrO_2 coatings as shown in Figure 5.4d. Hence, an alternative surface modification approach is used to improve high-rate performance of Li-excess layered cathode materials.

5.4.2 Improving and optimizing electrochemical performance of LMNCO via fabricating core-shell structures

The low electronic conductivity and lithium ion diffusivity of Li-excess layered $Li[Li_{0.2}Mn_{0.54}Ni_{0.13}Co_{0.13}]O_2$ cathode material impedes the improvement of high rate capability. The effort of reducing the particle size of LMNCO to nano-sized particles has been achieved in Figure 5.2b and 6.3a in order to decrease the path way of lithium ion diffusion for enhanced rate capability of LMNCO cathode. However, the electrochemical performance in Figure 5.4 shows inferior high-rate cycling performance of pristine LMNCO nanoparticles when charged at high current densities larger than 1*C*. Although ultrathin and conformal ZrO_2 ALD coating with the optimal thickness of ~1 nm has been demonstrated to enhance the electrochemical performance of LMNCO nanoparticles, the electrochemically inert ZrO_2 is unfavorable for facilitating both lithium ion diffusion and interfacial charge transfer of the electrode. One solution is to introduce more conductive Li-active phase on the surface of LMNCO nanoparticles for improved rate capacities of LMNCO. Herein, we deposit Li-stoichiometric layered $LiCoO_2$, spinel $LiMn_2O_4$ and layered-spinel $LiCoMnO_4$ as shells on LMNCO core to improve rate capability of LMNCO cathode. The three shell materials all have better electronic conductivity and lithium ion diffusivity than that of LMNCO core [56]. Electrochemical performance of such nanoarchitected composites are evaluated and optimized at 1*C*, by varying the composition and weight content of shell materials.

Figure 5.5a and 5b summarize cycling performances of LM_xO_y-X@LMNCO electrodes with different weight fraction and composition of shell materials. It can be seen that $LiCoO_2$ as shell in a series of 5 wt.%, 10 wt.%, 25 wt.%, and 50 wt.% can all effectively improve specific capacities in comparison with bare LMNCO nanoparticles, while 10 wt.% of $LiCoO_2$ shell is the optimal weight percentage and shows the most significant effect in improving performance of LMNCO. Figure 5.3d presents HRTEM image of LCO-10@LMNCO displaying the core-shell structure, with crystalline $LiCoO_2$ nanoparticles on the surface of LMNCO particle forming a ~10 nm thick coverage. Composition of $LiCoO_2$ is confirmed by lattice fringes in the HRTEM image. The core-shell LCO-10@LMNCO delivers better performance than bare LMNCO, due to better electronic conductivity and higher Li-ion diffusivity of $LiCoO_2$. For example, LCO-10@LMNCO delivers a high initial discharge capacity of 187.5 mAh/g and retains 132.8 mAh/g after 100 electrochemical cycles, much higher than the initial discharge capacity of 114.5 mAh/g and final capacity of 65.9 mAh/g at 100^{th} cycle from bare LMNCO. LMNCO coated by thicker 50 wt.% $LiCoO_2$ shell exhibits the highest discharge capacity of 188.2 mAh/g but show poor capacity

retention. The rapid capacity fading of LCO-50@LMNCO can be attributed to two possible reasons as follows: (1) The layered $LiCoO_2$ cathode suffers from structural instability when cycled at high voltage up to 4.8 V; (2) Thicker shell composed of more $LiCoO_2$ nanoparticles can be more easily detached from LMNCO than thin shell during electrochemical cycling due to mechanical stress in repeated charge/discharge cycles. In contrast, LMNCO coated with $LiCoO_2$ shell in a low amount of 5 wt.% reveals both low specific capacity and poor capacity retention, probably because $LiCoO_2$ coverage on LMNCO particles is low due to the low amount of $LiCoO_2$.

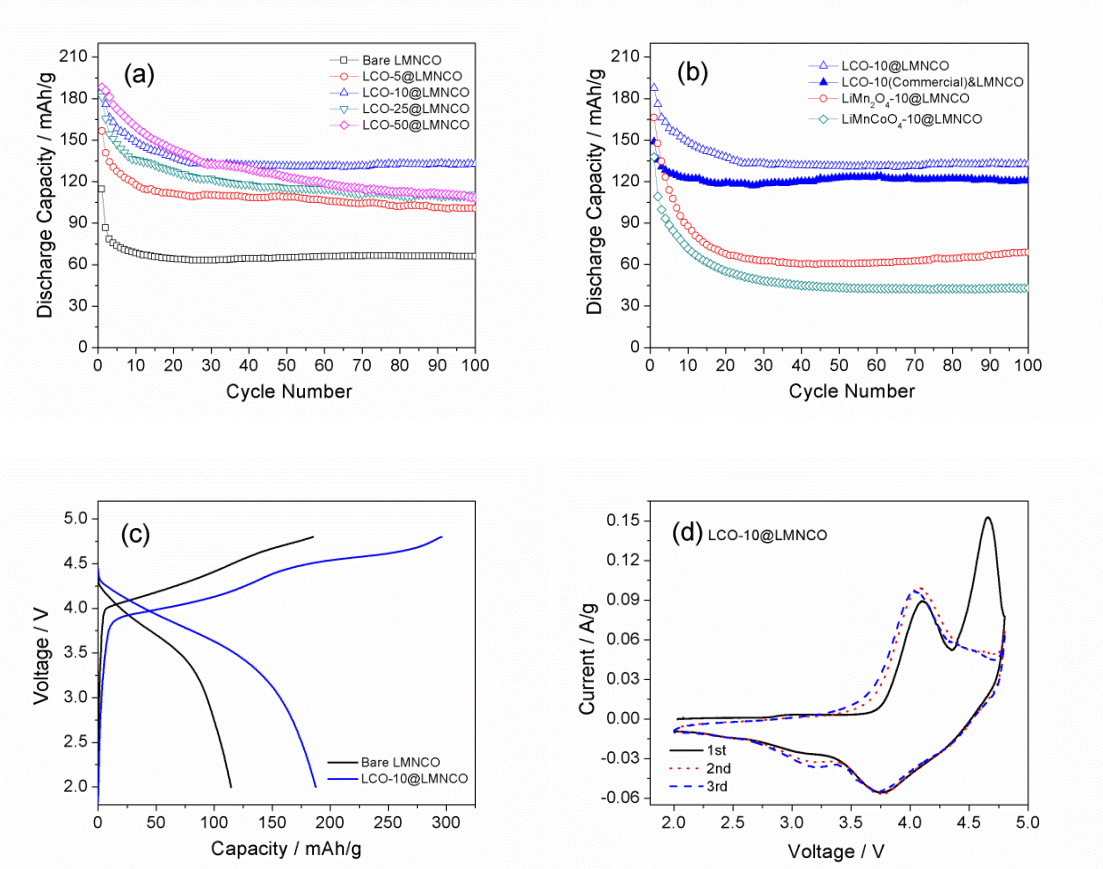

Figure 5.5 Electrochemical performances of different core-shell-structured $Li[Li_{0.2}Mn_{0.54}Ni_{0.13}Co_{0.13}]O_2$ electrodes in a voltage range of 2.0-4.8 V *vs.* Li/Li^+: Cycling performances of $Li[Li_{0.2}Mn_{0.54}Ni_{0.13}Co_{0.13}]O_2$ nanoparticles modified with (a) $LiCoO_2$ shell of 5 wt.%, 10 wt.%, 25 wt.%, and 50 wt.% in comparison with bare electrode and (b) different shells ($LiCoO_2$, $LiMn_2O_4$ and $LiCoMnO_4$) of 10 wt.% in comparison with the physical mixture of $Li[Li_{0.2}Mn_{0.54}Ni_{0.13}Co_{0.13}]O_2$ and commercial $LiCoO_2$ in the same weight ratio at a current density of 250 mA/g (1*C*); (c) Initial charge and discharge curves at a current density of 250 mA/g (1*C*) and (d) the first three CV profiles of $Li[Li_{0.2}Mn_{0.54}Ni_{0.13}Co_{0.13}]O_2$ nanoparticles modified with 10 wt.% $LiCoO_2$ shell at a scanning rate of 0.1 mV/s. "Bare LMNCO": bare $Li[Li_{0.2}Mn_{0.54}Ni_{0.13}Co_{0.13}]O_2$ nanoparticles; "LM_xO_y-X@LMNCO (M=Mn and Co, X is the weight content of shell materials": $Li[Li_{0.2}Mn_{0.54}Ni_{0.13}Co_{0.13}]O_2$ nanoparticles modified with LiM_xO_y shell of X wt.%.

Figure 5.5b compares cycling performances of LMNCO coated with different shell materials ($LiCoO_2$, $LiMn_2O_4$ and $LiCoMnO_4$) at 10 wt.% and simple mixture of LMNCO and 10 wt.% $LiCoO_2$. It can be seen that LMNCO coated with $LiCoO_2$ shell exhibits much better performance than LMNCO coated with $LiMn_2O_4$ and $LiCoMnO_2$. In addition, the LCO-10@LMNCO core-shell structure shows better performance than the physical mixture of LMNCO nanoparticles and $LiCoO_2$ nanoparticles in the same weight ratio, demonstrating the superiority of core-shell structure which have better structural comparability between $LiCoO_2$ shell and LMNCO core in the integrated "layered-layered" composite (Figure 5.3d).

The electrochemical polarization of LMNCO cathode can be effectively reduced via coating ~10 nm $LiCoO_2$ shell on core LMNCO material, resulting in high reversibility of lithium ion insertion and extraction. As shown in Figure 5.5c, the initial charge and discharge of LCO-10@LMNCO deliver high specific capacities of 295.8 mAh/g and 187.5 mAh/g at 1*C*, respectively, much higher than the initial charge/discharge capacity (185.2 mAh/g and 114.5 mAh/g) from bare LMNCO. The overpotential between charge and discharge curves is also obviously decreased owing to the conductive $LiCoO_2$ shell on the core LMNCO nanoparticles. In comparison with CV profile of pristine LMNCO cathode in Figure 5.4e, CV profiles of LCO-10@LMNCO in Figure 5.5d demonstrate better reversibility of core-shell-structured composite. The first anodic peak at 4.11 V in the initial CV cycle is associated with oxidation of Ni^{2+}/Ni^{4+} redox only from LMNCO cathode and Co^{3+}/Co^{4+} redox from both $LiCoO_2$ shell and LMNCO core. The second peak at 4.67 V can be ascribed to electrochemical activation of Li_2MnO_3 region together with inevitable decomposition of electrolyte due to the high oxidation abilities of Mn^{4+}, Ni^{4+} and Co^{4+} ions. Two corresponding cathodic peaks at 3.75 V and 3.17 V are related to combined reduction in Ni^{2+}/Ni^{4+} and Co^{3+}/Co^{4+} and reducing Mn^{4+} to Mn^{3+}, respectively. The overpetential between main anodic and cathodic peaks related to oxidation and reduction in Ni^{2+}/Ni^{4+} and Co^{3+}/Co^{4+} is reduced to 0.37 V, smaller than 0.53 V from CV profile of bare LMNCO in Figure 5.4e. After initial electrochemical activation, LCO-10@LMNCO shows significantly improved reversibility in subsequent CV cycles, resulting in high capacity and good capacity retention during high-rate cycling. However, the core-shell structure still shows a large irreversible capacity loss in the initial charge/discharge cycle corresponding to a low Coulombic efficiency of 63.5% (Figure 5.5c), indicating $LiCoO_2$ shell cannot alleviate the initial capacity loss. Fabrication of the core-shell structure in this work can be generalized to other shell materials such as high-voltage spinel cathode material (e.g., $LiMn_{1.5}Ni_{0.5}O_4$) which can be used to reduce initial capacity loss of LMNCO cathode during the first electrochemical cycle. Employing high-voltage spinel cathode material as the shell can improve the structural stability of core-shell structure, because $LiMn_{1.5}Ni_{0.5}O_4$ is more stable than $LiCoO_2$ and LMNCO under the high voltage up to 4.8V [57]. Another alternative approach is to prepare LiM_xO_y (M=Mn, Co and Ni) shell via ALD from Li_2O and M_xO_y via oxygen bonds, followed by heat treatment, which thus can restrict the oxygen evolution and structural rearrangement of LMNCO cathode in the initial cycle [46].

5.4.3 Hierarchical functional layers coated on LMNCO nanoparticles for maximized performance

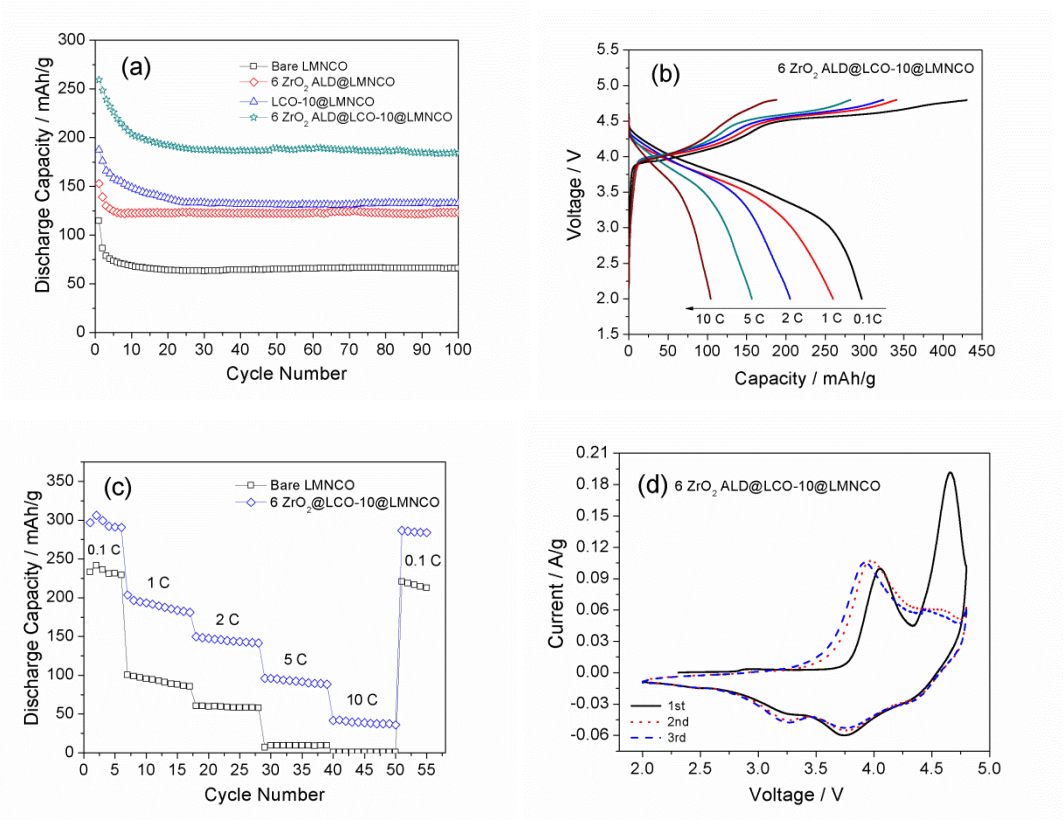

Figure 5.6 Electrochemical performances of $Li[Li_{0.2}Mn_{0.54}Ni_{0.13}Co_{0.13}]O_2$ nanoparticles modified with 10 wt.% $LiCoO_2$ shell followed by coating with 6 ZrO_2 ALD layers cycled in a voltage range of 2.0-4.8 V: (a) cycling performances at a current density of 250 mA/g (1*C*) in comparison with bare and $Li[Li_{0.2}Mn_{0.54}Ni_{0.13}Co_{0.13}]O_2$ nanoparticles coated 10 wt.% $LiCoO_2$ shell (LCO-10@LMNCO) or 6 ZrO_2 ALD layers (6 ZrO_2 ALD@LMNCO); (b) Initial charge and discharge curves and (c) Rate performance at a series of current densities; and (d) The first three CV profiles at a scanning rate of 0.1 mV/s. "Bare LMNCO": bare $Li[Li_{0.2}Mn_{0.54}Ni_{0.13}Co_{0.13}]O_2$ nanoparticles; "6 ZrO_2 ALD@LCO-10@LMNCO": $Li[Li_{0.2}Mn_{0.54}Ni_{0.13}Co_{0.13}]O_2$ nanoparticles modified with $LiCoO_2$ shell of 10 wt.%, followed by being coated with 6 ZrO_2 ALD layers.

In order to reduce the initial capacity loss and improve cycleability and rate capability at high charge/discharge rates all together, we combine the ALD coating with the core-shell structure. As discussed above, six ZrO_2 ALD layers can effectively restrict electrolyte composition and stabilize the rearranged layered structure after initial activation of LMNCO, and thus improve initial Coulombic efficiency and cycleability of LMNCO. On the other hand, 10 wt.% $LiCoO_2$ shell can increase capacities of LMNCO at high charge/discharge rates, due to enhanced electronic conductivity from $LiCoO_2$. Hence, we combine ALD and core-shell structure and fabricate hierarchical functional layers on LMNCO by depositing 10 wt.% $LiCoO_2$

(~10 nm thick) on LMNCO first followed by deposition of six ZrO_2 ALD layers (~1 nm thick) (marked as 6 ZrO_2 ALD@LCO-10@LMNCO).

Figure 5.6a compares cycling performances of ALD-coated core-shell structure, core-shell structure, ALD-coated LMNCO, and bare LMNCO. Corresponding results are also summarized in Table 1.

Table 5.1 Initial discharge capacity and final capacity after 100 electrochemical cycles delivered by $Li[Li_{0.2}Mn_{0.54}Ni_{0.13}Co_{0.13}]O_2$ nanoparticles modified with 10 wt.% $LiCoO_2$ shell followed by coating with six ZrO_2 ALD layers in comparison with bare cathode and different surface modified cathodes.

Electrodes cycled at 1*C*	Initial discharge capacity / mAh/g	100^{th} discharge capacity / mAh/g	Reference
6 ZrO_2 ALD@ LCO-10@LMNCO	259.8	184.0	This work
LCO-10@LMNCO	187.5	132.8	This work
6 ZrO_2 ALD@LMNCO	152.9	123.0	This work
Bare LMNCO	114.5	65.9	This work
LMNCO coated with 2 wt.% $AlPO_4$+3 wt.% Al_2O_3	~230	N/A	Ref. 29
LMNCO coated with 2 wt.%$CoPO_4$+3 wt.% Al_2O_3	~225	N/A	Ref. 29
LMNCO treated with 50 wt.% $Na_2S_2O_8$	194.8	173.3 at 50^{th} cycle	Ref. 30
LMNCO enwrapped with 4.9 wt.% graphene at 0.5*C*	~200	~165	Ref. 24

Obviously, 6 ZrO_2 ALD@LCO-10@LMNCO delivers the highest initial discharge capacity of 259.8 mAh/g at 1*C*, significantly higher than 187.5 mAh/g of LCO-10@LMNCO, 152.9 mAh/g of 6 ZrO_2 ALD@LMNCO and 114.5 mAh/g of bare LMNCO. This result is also better than the capacity of LMNCO coated with double shells (2 wt.% $AlPO_4$+3 wt.% Al_2O_3 or 2 wt.% $CoPO_4$+3 wt.% Al_2O_3) [29] and other surface-modified LMNCO cathodes reported in literature [24,31]. It is also noted that ALD-coated core-shell structure delivers a final capacity of 184.0 mAh/g after 100 electrochemical cycles, which is three times that from bare LMNCO (65.9 mAh/g). The remarkably increased capacity and enhanced cycleability of 6 ZrO_2 ALD@LCO-10@LMNCO can be attributed to combined effects from $LiCoO_2$ shell and ZrO_2 coating in improving performance of LMNCO. Figure 5.6b and 6c reveal

the superior rate capability of this nanoarchitected composite cathode modified with nano-sized $LiCoO_2$ shell (~10 nm) and sub-nano-sized ZrO_2 coating (~1 nm). As shown in Figure 5.6b, 6 ZrO_2 ALD@LCO-10@LMNCO shows initial discharge capacities of 296.4, 259.8, 156.6 and 104.2 mAh/g at 0.1*C*, 1*C*, 5*C* and 10*C*, which are higher than capacities of LMNCO based cathodes reported previously, such as graphene-enwrapped LMNCO hybrid cathode [24,36], LMNCO coated with oxides [12,25,33], persulfate treated LMNCO [30] and LMNCO coated with double shells [29]. Figure 5.6c compares rate performances of 6 ZrO_2 ALD@LCO-10@LMNCO and bare LMNCO, which clearly shows significantly enhanced rate capability, cycleability and reversibility of LMNCO coated with hierarchical functional layers.

The improved electrochemical property of 6 ZrO_2 ALD@LCO-10@LMNCO can be understood from its CV curves in Figure 5.6d. After initial activation of 6 ZrO_2 ALD@LCO-10@LMNCO in the first CV cycle, the overpotential of the predominant pair of anodic/cathodic peaks is 0.17 V in subquent second and third CV cycles, which is much smaller than 0.28 V from LCO-10@LMNCO (Figure 5.5d), 0.30 V from 6 ZrO_2 ALD@LMNCO (Figure 5.4e) and 0.43 V from bare LMNCO (Figure 5.4f), indicating better reversibility of Ni^{2+}/Ni^{4+} and Co^{3+}/Co^{4+} redox in 6 ZrO_2 ALD@LCO-10@LMNCO. The second cathodic peak related to reduction in $Mn^{3+/}Mn^{4+}$ is very sharp and shifts to the higher voltage at 3.25 V, suggesting the enhanced contribution of active MnO_2 component in lithiation and delithiation after initial activation of 6 ZrO_2 ALD@LCO-10@LMNCO in the first cycle. Better reversibility of transition metal redox pairs can be mainly attributed to the improved electronic conductivity from $LiCoO_2$ shell. A weak anodic/cathodic peak pair appears around ~4.5 V, different from CV profiles of LCO-10@LMNCO (Figure 5.5d), 6 ZrO_2 ALD@LMNCO (Figure 5.4e) and bare LMNCO (Figure 5.4f). Such extra anodic and cathodic peaks at ~4.5 V may be due to a cumulative effect from hierarch functional coatings to preserve oxygen ion vacancies for reversible insertion and extraction of lithium ions after electrochemical activation of Li_2MnO_3 region. Overall, CV measurement reveals that ZrO_2 ALD coating on core-shell-structured LCO-10@LMNCO can effectively inhibit the rearrangement of metal ions and thus restrict structural degradation of core LMNCO cathode, resulting in high reversibility, cycleabilitiy and rate capability of Li-excess layered cathode material.

5.5 Conclusions

Surface modifications on $Li[Li_{0.2}Mn_{0.54}Ni_{0.13}Co_{0.13}]O_2$ nanoparticles have been demonstrated to improve electrochemical performance of Li-excess layered cathode materials. Ultrathin and conformal ALD oxide coatings can effectively restrict decomposition of electrolyte and stabilize the layered structure of LMNCO, and thus reduce initial capacity loss and enhance cycleability of LMNCO. ZrO_2 is the most effective oxide coating for improved electrochemical performance of LMNCO electrodes, followed by ZnO and Al_2O_3. The optimal thickness of ZrO_2 coating for LMNCO is ~1 nm via 6 ALD growth layers. LMNCO nanoparticles coated with six ZrO_2 ALD layers delivers an initial discharge capacity of 274.9 mAh/g at 0.1*C* with a

high Coulombic efficiency of 83.3%, while bare LMNCO shows a lower initial discharge capacity of 228.4 mAh/g and Coulombic efficiency of only 58.3%. In addition, rate capability of LMNCO can be improved by fabricating core-shell structure with LMNCO as core and Li-stoichiometric active material ($LiCoO_2$, $LiMn_2O_4$, and $LiCoMnO_4$) as shell and $LiCoO_2$ shell is found to have the best effect. The optimal weight content of $LiCoO_2$ shell is 10 wt.% for maximized performance of core-shell electrode, yielding a ~10 nm thick $LiCoO_2$ shell delicately integrated on the surface of LMNCO particles. LCO-10@LMNCO shows the initial discharge capacity of 187.5 mAh/g at 1*C* and retains 132.8 mAh/g after 100 electrochemical cycles, which are much higher than the initial discharge capacity of 114.5 mAh/g and final capacity of 65.9 mAh/g from bare LMNCO, due to enhanced electronic conductivity from $LiCoO_2$ and reduced electrochemical polarization of core-shell structure during cycling. Finally, ALD is combined with core-shell structure and hierarch functional layers are fabricated on LMNCO by depositing 10 wt.% $LiCoO_2$ (~10 nm thick) on LMNCO first followed by deposition of six ZrO_2 ALD layers (~1 nm thick). Such nanoarchitected cathode exhibits a very high initial discharge capacity of 259.8 mAh/g at 1*C* and retains a final capacity of 184.0 mAh/g after 100 electrochemical cycles which is three times that from bare LMNCO (65.9 mAh/g). Such results are also higher than capacities of other surface modified LMNCO reported in literature. It is also noted that surface modification via hierarch functional layers can be applied to other cathode materials or anode materials for advanced lithium ion batteries.

5.6 References

1. J. B. Goodenough, K. S. Park, The Li-ion Rechargeable Battery: A Perspective. *Journal of American Chemical Society* 135 (2013) 1167-1176.

2. R. Mukherjee, R. Krishnan, T. M. Lu, N. Koratkar, Nanostructured Electrodes for High-Power Lithium Ion Batteries. *Nano Energy* 1 (2012) 518-533.

3. L. Hu, N. Liu, M. Eskilsson, G. Zheng, J. McDonough, L. Wågberg, Y. Cui, Silicon-Conductive Nanopaper for Li-ion Batteries, *Nano Energy* 2 (2013) 138-145.

4. I. Meschini, F. Nobili, M. Mancini, R. Marassi, R. Tossici, A. Savoini, M. L. Focarete, F. Croce, High-Performance Sn@Carbon Nanocomposite Anode for Lithium Batteries. *Journal of Power Sources* 226 (2013) 241-248.

5. P. He, H. Yu, D. Li, H. Zhou, Layered Lithium Transition Metal Oxide Cathodes towards High Energy Lithium-Ion Batteries. *Journal of Materials Chemistry* 22 (2012) 3680-3695.

6. A. R. Armstrong, M. Holzapfel, P. Novák, C. S. Johnson, S. H. Kang, M. M. Thackeray, P. G. Bruce, Demonstrating Oxygen Loss and Associated Structural

Reorganization in the Lithium Battery Cathode $Li[Ni_{0.2}Li_{0.2}Mn_{0.6}]O_2$. *Journal of The American Chemical Society* 128 (2006) 8694-8698.

7. T. A. Arunkumar, Y. Wu, A. Manthiram, Factors Influencing the Irreversible Oxygen Loss and Reversible Capacity in Layered $Li[Li_{1/3}Mn_{2/3}]O_2$-$Li[M]O_2$ (M = $Mn_{0.5-y}Ni_{0.5-y}Co_{2y}$ and $Ni_{1-y}Co_y$) Solid Solutions. *Chemistry of Materials* 19 (2007) 3067-3073.

8. T. A. Arunkumar, E. Alvarez, A. Manthiram, Structural, Chemical, and Electrochemical Characterization of Layered $Li[Li_{0.17}Mn_{0.33}Co_{0.5-y}Ni_y]O_2$ Cathodes. *Journal of The Electrochemical Society* 154 (2007) A770-A775.

9. Y. Wu, A. Manthiram, Structural Stability of Chemically Delithiated Layered $(1-z)Li[Li_{1/3}Mn_{2/3}]O_2$-$zLi[Mn_{0.5-y}Ni_{0.5-y}Co_{2y}]O_2$ Solid Solution Cathodes. *Journal of Power Sources* 183 (2008) 749-754.

10. K. A. Jarvis, Z. Deng, L. F. Allard, A. Manthiram, P. J. Ferreira, Atomic Structure of a Lithium-Rich Layered Oxide Material for Lithium-Ion Batteries: Evidence of a Solid Solution. *Chemistry of Materials* 23 (2011) 3614-3621.

11. E. S. Lee, A. Huq, H. Y. Chang, A. Manthiram, High-Voltage, High-Energy Layered-Spinel Composite Cathodes with Superior Cycle Life for Lithium-Ion Batteries. *Chemistry of Materials* 24 (2012) 600-612.

12. W. He, J. Qian, Y. Cao, X. Ai, H. Yang, Improved Electrochemical Performances of Nanocrystalline $Li[Li_{0.2}Mn_{0.54}Ni_{0.13}Co_{0.13}]O_2$ Cathode Material for Li-Ion Batteries. *RSC Advances* 2 (2012) 3423-3429.

13. S. H. Yu, T. Yoon, J. Mun, S. Park, Y. S. Kang, J. H. Park, S. M. Oh, Y. E. Sung, Continuous Activation of Li_2MnO_3 Component upon Cycling in $Li_{1.167}Ni_{0.233}Co_{0.100}Mn_{0.467}Mo_{0.033}O_2$ Cathode Material for Lithium Ion Batteries. *Journal of Materials Chemistry A* 1 (2013) 2833-2839.

14. D. Kim, G. Sandi, J. R. Croy, K. G. Gallagher, S. H. Kang, E. Lee, M. D. Slater, C. S. Johnson, M. M. Thackeray, Composite 'Layered-Layered-Spinel' Cathode Structures for Lithium-Ion Batteries. *Journal of The Electrochemical Society* 160 (2013) A31-A38.

15. Y. Wang, X. Bie, K. Nikolowski, H. Ehrenberg, F. Du, M. Hinterstein, C. Wang, G. Chen, Y. Wei, Relationships between Structural Changes and Electrochemical Kinetics of Li-Excess $Li_{1.13}Ni_{0.3}Mn_{0.57}O_2$ during the First Charge. *The Journal of Physical Chemistry C* 117 (2013) 3279-3286.
16. B. Xu, C. R. Fell, M. Chi, Y. S. Meng, Identifying Surface Structural Changes in Layered Li-Excess Nickel Manganese Oxides in High Voltage Lithium Ion

Batteries: A Joint Experimental and Theoretical Study. *Energy & Environmental Science* 4 (2011) 2223-2233.

17. N. Yabuuchi, K. Yoshii, S. T. Myung, I. Nakai, S. Komaba, Detailed Studies of a High-Capacity Electrode Material for Rechargeable Batteries, Li_2MnO_3−$LiCo_{1/3}Ni_{1/3}Mn_{1/3}O_2$. *Journal of The American Chemical Society* 133 (2011) 4404-4419.

18. M. Jiang, B. Key, Y. S. Meng, C. P. Grey, Electrochemical and Structural Study of the Layered, "Li-Excess" Lithium-Ion Battery Electrode Material $Li[Li_{1/9}Ni_{1/3}Mn_{5/9}]O_2$. *Chemistry of Materials* 21 (2009) 2733-2745.

19. J. Hong, H. D. Lim, M. Lee, S. W. Kim, H. Kim, S. T. Oh, G. C. Chung, K. Kang, Critical Role of Oxygen Evolved from Layered Li–Excess Metal Oxides in Lithium Rechargeable Batteries. *Chemistry of Materials* 24 (2012) 2692-2697.

20. M. Gu, I. Belharouak, J. Zheng, H. Wu, J. Xiao, A. Genc, K. Amine, S.Thevuthasan, D. R. Baer, J. G. Zhang, N. D. Browning, J. Liu, C. Wang, Formation of the Spinel Phase in the Layered Composite Cathode Used in Li-Ion Batteries. *ACS Nano* 7 (2013) 760-767.

21. D. Wang, I. Belharouak , G. Zhou, K. Amine, Nanoarchitecture Multi-Structural Cathode Materials for High Capacity Lithium Batteries. *Advanced Functional Materials* 23 (2013) 1070-1075.

22. A. Boulineau, L. Simonin, J.-F.Colin, E. Canévet, L. Daniel, S. Patoux, Evolutions of $Li_{1.2}Mn_{0.61}Ni_{0.18}Mg_{0.01}O_2$ during the Initial Charge/Discharge Cycle Studied by Advanced Electron Microscopy. *Chemistry of Materials* 24 (2012) 3558-3566.

23. F. Amalraj, M. Talianker, B. Markovsky, D. Sharon, L. Burlaka, G. Shafir, E.Zinigrad, O. Haik, D. Aurbach, J. Lampert, M. S. Dobrick, A. Garsuch, Study of the Lithium-Rich Integrated Compound $xLi_2MnO_3{\cdot}(1\text{-}x)LiMO_2$ (x around 0.5; M=Mn,Ni,Co;2:2:1) and Its Electrochemical Activity as Positive Electrode in Lithium Cells. *Journal of The Electrochemical Society* 160 (2012) A324-A337.

24. K. C. Jiang, X. L. Wu, Y. X. Yin, J. S. Lee, J. Kim, Y. G. Guo, Superior Hybrid Cathode Material Containing Li-Excess Layered Material and Graphene for Lithium-Ion Batteries. *ACS Applied Materials & Interfaces*, 4 (2012) 4858-4863.

25. Y. S. Jung, A. S. Cavanagh, Y. Yan, S. M. George, A. Manthiram, Effects of Atomic Layer Deposition of Al_2O_3 on the $Li[Li_{0.20}Mn_{0.54}Ni_{0.13}Co_{0.13}]O_2$ Cathode for Lithium-Ion Batteries. *Journal of The Electrochemical Society* 158 (2011) A1298-A1302.

26. Y. Wu, A. Manthiram, Effect of Surface Modifications on the Layered Solid Solution Cathodes (1-z)Li[$Li_{1/3}Mn_{2/3}$]O_2-(z)Li[$Mn_{0.5-y}Ni_{0.5-y}Co_{2y}$]$O_2$. *Solid State Ionics* 180 (2009) 50-56.

27. G. R. Li, X. Feng, Y. Ding, S. H. Ye, X. P. Gao, AlF3-Coated Li($Li_{0.17}Ni_{0.25}Mn_{0.58}$)$O_2$ as Cathode Material for Li-Ion Batteries. *Electrochimica Acta* 78 (2012) 308-315.

28. Y. Liu, S. Liu, Y. Wang, L. Chen, X. Chen, Effect of MnO_2 Modification on Electrochemical Performance of $LiNi_{0.2}Li_{0.2}Mn_{0.6}O_2$ Layered Solid Solution Cathode. *Journal of Power Sources* 222 (2013) 455-460.

29. Q. Y. Wang, J. Liu, A. Vadivel Murugan, A. Manthiram, High Capacity Double-Layer Surface Modified Li[$Li_{0.2}Mn_{0.54}Ni_{0.13}Co_{0.13}$]$O_2$ Cathode with Improved Rate Capability. *Journal of Materials Chemistry* 19 (2009) 4965-4972.

30. J. Zheng, S. Deng, Z. Shi, H. Xu, H. Xu, Y. Deng, Z. Zhang, G. Chen, The Effects of Persulfate Treatment on the Electrochemical Properties of Li[$Li_{0.2}Mn_{0.54}Ni_{0.13}Co_{0.13}$]$O_2$ Cathode Material. *Journal of Power Sources* 221 (2013) 108-113.

31. T. Zhao, S. Chen, L. Li, X. Zhang, R. Chen, I. Belharouak, F. Wu, K. Amine, Synthesis, Characterization, and Electrochemistry of Cathode Material Li[$Li_{0.2}Co_{0.13}Ni_{0.13}Mn_{0.54}$]$O_2$ Using Organic Chelating Agents for Lithium-Ion Batteries. *Journal of Power Sources* 228 (2013) 206-213.

32. H. Yim, W. Y. Kong, Y. C. Kim, S. J. Yoon, J. W. Choi, Electrochemical Properties of Li[$Li_{0.2}Mn_{0.54}Co_{0.13}Ni_{0.13}$]$O_2$ Cathode Thin Film by RF Sputtering for All-Solid-State Lithium Battery. *Journal of Solid State Chemistry* 196 (2012) 288-292.

33. S. J. Shi, J. P. Tu, Y. Y. Tang, X. Y. Liu, Y. Q. Zhang, X. L. Wang, C. D. Gu, Enhanced Cycling Stability of Li[$Li_{0.2}Mn_{0.54}Ni_{0.13}Co_{0.13}$]$O_2$ by Surface Modification of MgO with Melting Impregnation Method. *Electrochimica Acta* 88 (2013) 671-679.

34. J. Wang, B. Qiu, H. Cao, Y. Xia, Z. Liu, Electrochemical Properties of 0.6Li[$Li_{1/3}Mn_{2/3}$]O_2-0.4$LiNi_xMn_yCo_{1-x-y}O_2$ Cathode Materials for Lithium-Ion Batteries. *Journal of Power Sources* 218 (2012) 128-133.

35. S. K. Martha, J. Nanda, G. M. Veith, N. J. Dudney, Electrochemical and Rate Performance Study of High-Voltage Lithium-Rich Composition: $Li_{1.2}Mn_{0.525}Ni_{0.175}Co_{0.1}O_2$. *Journal of Power Sources* 199 (2012) 220-226.

36. Z. He, Z. Wang, H. Guo, X. Li, X. Wu, P. Yue, J. Wang, A Simple Method of Preparing Graphene-Coated $Li[Li_{0.2}Mn_{0.54}Ni_{0.13}Co_{0.13}]O_2$ for Lithium-Ion Batteries. *Materials Letters* 91 (2013) 261-264.

37. Z. Chen, Y. Qin, K. Amine, Y. K. Sun, Role of Surface Coating on cCathode Materials for Lithium-Ion Batteries. *Journal of Materials Chemistry* 20 (2010) 7606-7612.

38. J. Zhao, Y. Wang, Ultrathin Surface Coatings for Improved Electrochemical Performance of Lithium Ion Battery Electrodes at Elevated Temperature. *The Journal of Physical Chemistry C* 116 (2012) 11867-11876.

39. J. Zhao, Y. Wang, Surface Modifications of Li-Ion Battery Electrodes with Various Ultrathin Amphoteric Oxide Coatings for Enhanced Cycleability. *Journal of Solid State Electrochemistry* 17 (2012) 1049-1058.

40. J. Lu, Q. Peng, W. Wang, C. Nan, L. Li, Y. Li, Nanoscale Coating of $LiMO_2$ (M=Ni,Co,Mn) Nanobelts with Li^+-Conductive Li_2TiO_3: Toward Better Rate Capabilities for Li-Ion Batteries. *Journal of The American Chemical Society* 135 (2013) 1649-1652.

41. Y. S. Jung, A. S. Cavanagh, L. A. Riley, S. H. Kang, A. C. Dillon, M. D. Groner, S. M. George, S. H. Lee, Ultrathin Direct Atomic Layer Deposition on Composite Electrodes for Highly Durable and Safe Li-Ion Batteries. *Advanced Materials* 22 (2010) 2172-2176.

42. I. D. Scott, Y. S. Jung, A. S. Cavanagh, Y. Yan, A. C. Dillon, S. M. George, S. H. Lee, Ultrathin Coatings on Nano-$LiCoO_2$ for Li-Ion Vehicular Applications. *Nano Letters* 11 (2011) 414-418.

43. X. Meng , X. Q. Yang, X. Sun, Emerging Applications of Atomic Layer Deposition for Lithium-Ion Battery Studies. *Advanced Materials* 24 (2012) 3589-3615.

44. S. Boukhalfa, K. Evanoff, G. Yushin, Atomic Layer Deposition of Vanadium Oxide on Carbon Nanotubes for High-Power Supercapacitor Electrodes. *Energy & Environmental Science* 5 (2012) 6872-6879.

45. H. Lee, J. K. Hwang, J. W. Nam, S. U. Lee, J. T. Kim, S. M. Koo, A. Baunemann, R. A. Fischer, M. M. Sung, Low-Temperature Atomic Layer Deposition of Copper Metal Thin Films: Self-Limiting Surface Reaction of Copper Dimethylamino-2-propoxide with Diethylzinc. *Angewandte Chemie International Edition* 48 (2009) 4536-4539.

46. J. Zhao, G. Qu, J. C. Flake, Y. Wang, Low Temperature Preparation of Crystalline

ZrO_2 Coatings for Improved Elevated-Temperature Performances of Li-Ion Battery Cathodes. *Chemical Communications* 48 (2012) 8108-8110.

47. Y. K. Sun, Z. Chen, H. J. Noh, D. J. Lee, H. G. Jung, Y. Ren, S. Wang, C. S.Yoon, S. T. Myung, K. Amine, Nanostructured High-Energy Cathode Materials for Advanced Lithium Batteries. *Nature Materials* 11 (2012) 942-947.

48. Y. Cho, S. Lee, Y. Lee, T. Hong, J. Cho, Spinel-Layered Core-Shell Cathode Materials for Li-Ion Batteries. *Advanced Energy Materials* 1 (2011) 821-828.

49. S. T. Myung, K. S. Lee, D. W. Kim, B. Scrosati, Y. K. Sun, Spherical Core-Shell $Li[(Li_{0.05}Mn_{0.95})_{0.8}(Ni_{0.25}Mn_{0.75})_{0.2}]_2O_4$ Spinels as High Performance Cathodes for Lithium Batteries. *Energy & Environmental Science* 4 (2011) 935-939.

50. Y. K. Sun, D. H. Kim, C. S. Yoon, S. T. Myung, J. Prakash, K. Amine, A Novel Cathode Material with a Concentration-Gradient for High-Energy and Safe Lithium-Ion Batteries. *Advanced Functional Materials* 20 (2010) 485-491.

51. X. Yang, X. Wang, Q. Wei, H. Shu, L. Liu, S. Yang, B. Hu, Y. Song, G. Zou, L. Hu, L. Yi, Synthesis and Characterization of a Li-Rich Layered Cathode Material $Li_{1.15}[(Mn_{1/3}Ni_{1/3}Co_{1/3})_{0.5}(Ni_{1/4}Mn_{3/4})_{0.5}]_{0.85}O_2$ with Spherical Core-Shell Structure. *Journal of Materials Chemistry* 22 (2012) 19666-19672.

52. Q. Q. Qiao, H. Z. Zhang, G. R. Li, S. H. Ye, C. W. Wang, X. P. Gao, Surface Modification of Li-Rich Layered $Li(Li_{0.17}Ni_{0.25}Mn_{0.58})O_2$ Oxide with Li-Mn-PO_4 as the Cathode for Lithium-Ion Batteries. *Journal of Materials Chemistry A* 1 (2013) 5262-5268.

53. F. Amalraj, D. Kovacheva, M. Talianker, L. Zeiri, J. Grinblat, N. Leifer, G. Goobes, B. Markovsky, D. Aurbach, Synthesis of Integrated Cathode Materials $x Li_2MnO_3 \cdot (1\text{-}x)\, LiMn_{1/3}Ni_{1/3}Co_{1/3}O_2$ $(x = 0.3, 0.5, 0.7)$ and Studies of Their Electrochemical Behavior. *Journal of The Electrochemical Society* 157 (2010) A1121-A1130.

54. Y. Wu, A. Manthiram, High Capacity, Surface-Modified Layered $Li[Li_{(1-x)/3}Mn_{(2-x)/3}Ni_{x/3}Co_{x/3}]O_2$ Cathodes with Low Irreversible Capacity Loss. *Electrochemical and Solid-State Letters* 9 (2006) A221-A224.

55. T. H. Cho, Y. Shiosaki, H. Noguchi, Preparation and Characterization of Layered $LiMn_{1/3}Ni_{1/3}Co_{1/3}O_2$ as a Cathode Material by an Oxalate Co-Precipitation Method. *Journal of Power Sources* 159 (2006) 1322-1327.

56. M. Park, X. Zhang, M. Chung, G. B. Less, A. M. Sastry, A Review of Conduction Phenomena in Li-Ion Batteries. *Journal of Power Sources* 195 (2010) 7904-7929.

57. X. Zhang, F. Cheng, J. Yang, J. Chen, $LiNi_{0.5}Mn_{1.5}O_4$ Porous Nanorods as High-Rate and Long-Life Cathodes for Li-Ion Batteries. *Nano Letters* 13 (2013) 2822-2825.

CHAPTER 6. ION-EXCHANGE PROMOTED PHASE TRANSITION IN LI-EXCESS LAYERED CATHODE MATERIAL FOR HIGH-PERFORMANCE LITHIUM-ION BATTERIES

6.1 Introduction

Rechargeable lithium-ion batteries have attracted tremendous attention as "green" technology for electric transportation and portable electronic devices. Performance of lithium-ion batteries crucially relies on electrochemical characteristics of electrode materials, i.e., anode and cathode materials [1]. Various alternative anode materials have recently been developed, including silicon-based composites [2,3], nano-scale transition metal oxides [4,5], titanium-based materials [6,7], and graphene-based sulfide [8], etc. These materials have demonstrated excellent rate capability and specific capacities several times higher than conventional graphite anodes. Since capacities of cathode materials are usually much lower than those of anodes, cathode is considered as the limiting factor for lithium-ion batteries. To a great extent, development of new-generation lithium ion batteries is limited by the low energy density, low operating voltage and poor rate capability of cathode materials [9,10,11].

Recently, the emerging Li-excess layered oxides have attracted a great deal of research efforts due to their high capacities. These cathode materials can be cycled over a broad voltage range between 2.0 and 4.8 V *vs.* Li/Li^+ and deliver specific capacities higher than 250 $mAhg^{-1}$. They also offer many other advantages such as low cost, environmental benignity, and safety [12-25]. A representative example is Li-excess ternary manganese-nickel-cobalt oxide, composed of three common transition metal ions and excess lithium ions with the formula $Li[Li_xM]O_2$ (M=Mn, Co and Ni) [23,24]. For instance, $Li[Li_{0.2}Mn_{0.54}Ni_{0.13}Co_{0.13}]O_2$ (marked as LMNCO) in this category shows an impressive theoretical capacity of 321 mAh/g with operating voltage up to 4.8 V *vs.* Li/Li^+ [25]. As reported in literatures [13-15], LMNCO is composed of two components, i.e., layered lithium-inactive Li_2MnO_3 (space group *C2/m*) integrated in the parent phase of layered lithium-active $LiMn_{1/3}Ni_{1/3}Co_{1/3}O_2$ (space group *R-3m*) with a molar ratio of 1:1 ($0.5Li_2MnO_3 \cdot 0.5LiMn_{1/3}Ni_{1/3}Co_{1/3}O_2$). The high capacity of LMNCO can be achieved via electrochemical activation of inert Li_2MnO_3 during the initial charge above 4.5 V *vs.* Li/Li^+. During such activation process, Li_2MnO_3 is decomposed to Li_2O and MnO_2 due to electrochemical extraction of lithium ions. Simultaneously, this process results in an irreversible oxygen loss and creation of lithium ion vacancies in the layered structure of LMNCO [13,17]. Although Mn^{3+}/Mn^{4+} redox pair is activated in the resulted MnO_2 andthis process can improve capacity in subsequent electrochemical cycles, overall the electrochemical activation leads to a significant irreversible capacity loss of LMNCO, i.e., low Coulombic efficiency in the initial charge/discharge cycle [13].

Another phenomenon occurred during subsequent electrochemical cycles of activated LMNCO is the unavoidable and continuous layered-to-spinel phase conversion [14-16]. Li_2MnO_3 and $LiMn_{1/3}Ni_{1/3}Co_{1/3}O_2$ components simultaneously

undergo such phase transitions via different pathways. Within the Li_2MnO_3 domain, removal of Li^+ and O^{2-} during initial electrochemical activation creates lithium ion and oxygen ion vacancies and thus triggers the layered-to-spinel phase transition. Consequently, layered Li_2MnO_3 transforms to numerous spinel grains integrated in an amorphous matrix [16]. Structural rearrangement within the $LiMn_{1/3}Ni_{1/3}Co_{1/3}O_2$ region takes place via migration of transition metal ions to lithium ion layers, in which sufficient amount of lithium ion vacancies were created due to extensive extraction of lithium ions in the highly-charged status of LMNCO. As a result, spinel grains are developed at the surface of layered $LiMn_{1/3}Ni_{1/3}Co_{1/3}O_2$ initially, and then successively grow inwards during long-term electrochemical cycling [26,27]. Such a phase transition is highly feasible due to structural compatibility of cubic close-packed oxygen arrays in layered and spinel structures [14,16,20,26,28]. The newly formed spinel phase can significantly contribute to the high-rate capability, due to its lithium-active characteristics, higher electronic conductivity and facile lithium ion diffusivity [14,15,29]. On the other hand, the formation of spinel structures breaks down the parent layered lattice and induces lattice strains, causing structural instability during lithiation/delithiation and poor electrochemical reversibility of Li-excess layered cathode materials [16]. There have been quite a few reports examining the unavoidable layered-to-spinel phase transformation in LMNCO during in-situ electrochemical cycling [13-15,23,24]. However, the effects of these phase transformations on electrochemical performance of LMNCO remain very complicated and LMNCO still suffers from drastic capacity degradation, which limits its practical applications. Therefore, it would be very intriguing to purposely and controllably induce a layered-to-spinel phase transformation in LMNCO, in order to explore fundamental mechanism of the layered-to-spinel phase transition and crystal structure of the resultant spinel phase. It would also be very interesting to evaluate electrochemical performance of the resultant spinel structure for use in superior lithium-ion batteries. Therefore, we develop an ex-situ route in this work to realize a layered-to-spinel phase transition of Li-excess layered transition metal oxides for high-performance batteries.

6.2 Objectives of Project

It can be seen that generation of sufficient lithium ion vacancies in lithium ion layers is the prerequisite for inducing migration of transition metal cations within layered LMNCO and thus promotes the formation of spinel phase [15,27]. Herein, we report a new approach involving ex-situ generation of high concentration of lithium ion vacancies within LMNCO, to induce a complete phase transition of layered $Li[Li_{0.2}Mn_{0.54}Ni_{0.13}Co_{0.13}]O_2$ to $Li_4Mn_5O_{12}$-type spinel phase. This approach allows a comprehensive study on the complete growth of a spinel phase within LMNCO and its electrochemical effects for the first time. As shown in the schematics in Figure 6.1, ex situ conversion from the initial layered oxide to the spinel phase is first carried out by protonation of LMNCO in acidic solution (HCl), i.e., Li^+-H^+ exchange (marked as LHMNCO obtained after protonation of the pristine LMNCO). Subsequently, these

protons are substituted using tetrabutylammonium (TBA^+) cations under violent vortex (donated as LHMNCO TBA obtained after substituting protons of LHMNCO in TBAOH solution), resulting in an exquisite nanoflower-shaped LHMNCO TBA as the intermediate. Detailed procedures can be found in the "Experimental Section" of this chapter.

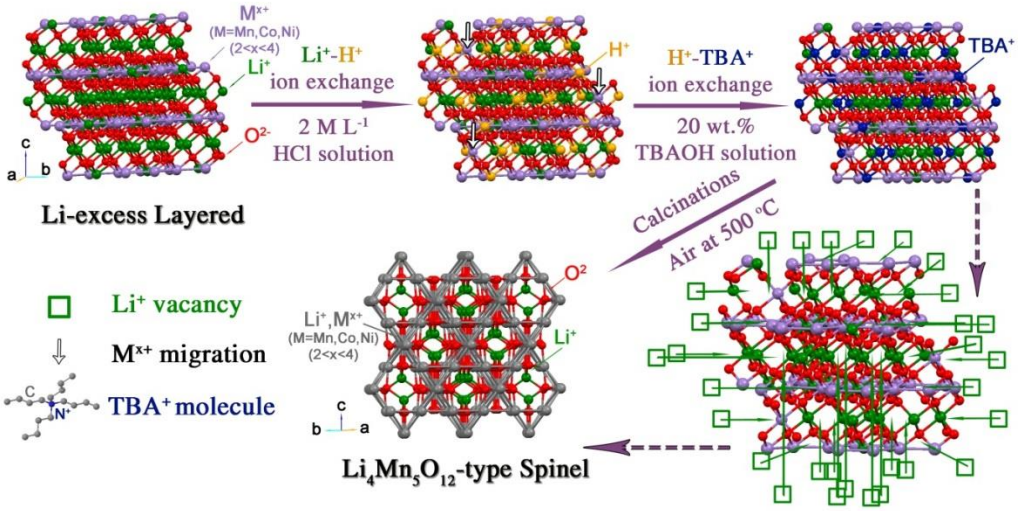

Figure 6.1 Schematics showing structural reconstruction of Li-excess layered $Li[Li_{0.2}Mn_{0.54}Ni_{0.13}Co_{0.13}]O_2$ to realize a $Li_4Mn_5O_{12}$-type spinel phase via ion-exchange processes in two steps, followed by calcinations.

Afterwards, the complete phase transition is realized after decomposition of the embedded TBA^+ by air calcinations, i.e., generation of sufficient lithium ion vacancies at a time, leading to a hierarchical mesoporous derivative named as LHMNCO TBA HT. The optimal temperature for sintering LHMNCO TBA is identified as 500°C. Sintering at this temperature yields a final product with a spinel structure and $Li_4Mn_5O_{12}$-type characteristics, which are demonstrated by using ex-situ/in-situ XRD patterns and electrochemical profiles. Morphological and structural reconstructions simultaneously take place during the aforementioned processes. The real-time structural evolution from the original layered to the spinel structure is recorded and examined using in-situ XRD, in-situ high resolution TEM and selected area electron diffraction (SAED) patterns. Most importantly, the final spinel cathode delivers much higher specific capacity and significantly enhanced rate capability in comparison with original Li-excess layered cathode materials.

6.3 Experimental Section

6.3.1 Synthesis of Li-excess $Li[Li_{0.2}Mn_{0.54}Ni_{0.13}Co_{0.13}]O_2$ nanoparticles and $Li_4Mn_5O_{12}$ particles

Li-excess $Li[Li_{0.2}Mn_{0.54}Ni_{0.13}Co_{0.13}]O_2$ nanoparticles were synthesized using surfactant-assisted dispersion in a sol-gel method. We first prepared three precursor

solutions: 5.4 mmol F127 ($EO_{106}PO_{70}EO_{106}$) in 50 mL ethanol, 0.08 mol transition metal acetate tetrahydrates (a molar ratio of Mn^{2+}:Ni^{2+}:Co^{2+}=0.54:0.13:0.13) in 50 mL ethanol, and 0.12 mol lithium hydroxide in 20 mL DI water. The molar ratio of F127/Mn^{2+} was 0.01. The transition metal precursor solution was added dropwise into the F127/ethanol solution under continuous stirring at 40°C, and then the lithium precursor solution was added. The mixed solution was heated at 80°C until the solvent was completely evaporated. Afterwards, the mixture was dried in air at 120°C for 12 h. Heat treatment of the dried mixture was carried out in air at 300°C for 3 h, followed by sintering at 900°C for 12 h. $Li[Li_{0.2}Mn_{0.54}Ni_{0.13}Co_{0.13}]O_2$ nanoparticles were collected after cooling to room temperature.

$Li_4Mn_5O_{12}$ particles were synthesized by a sol-gel method. We first prepared two precursor solutions: 0.02 mol manganese acetate tetrahydrate in 50 mL DI water, and 0.016 mol lithium hydroxide in 15 mL DI water. The manganese precursor solution was added dropwise into the lithium precursor solution under continuous stirring. The mixed solution was heated at 80°C until the solvent was completely evaporated. Afterwards, the mixture was dried in air at 120°C for 12 h. Heat treatment of dried mixture was carried out in air at 500°C for 3 h. $Li_4Mn_5O_{12}$ particles were collected after cooling to room temperature.

6.3.2 Ion exchanges in Li-excess layered $Li[Li_{0.2}Mn_{0.54}Ni_{0.13}Co_{0.13}]O_2$, and post-heat treatment of its ion-exchanged derivatives

The H^+-Li^+ ion exchange of $Li[Li_{0.2}Mn_{0.54}Ni_{0.13}Co_{0.13}]O_2$ particles (1 g) was performed in aqueous HCl (150 mL, 2M) at ambient temperature. In order to promote the protonation, the HCl solution was changed every 2 days for 10 days. As a result, a brown suspension was obtained, consisting of residual protonated intermediates in 150 mL aqueous HCl. The second (TBA^+-H^+) exchange was conducted employing a 20 wt.% aqueous tetrabutylammonium (TBAOH) solution (Sigma Aldrich). A 1 mL suspension was added to a 5 mL TBAOH solution and mixed in a vortex stirrer for 30 min. The resulting ion-exchanged particles were washed with DI water and collected via centrifugation three times, followed by heating at 80°C in vacuum overnight. Finally, heat treatment of the ion-exchanged derivative was carried out at 500°C for 3h in air. A temperature ramp of 1°C min^{-1} was used to achieve the required temperature.

6.3.3 Characterizations

Crystallographic structures of pristine Li-excess layered material and its derivatives were examined by a Panalytical X'pert Diffractometer with Cu K_α radiation. Raman spectra were collected using a 532 nm single-frequency diode laser with ~10 mW power, a triple monochromator and a 1340 × 100 pixel liquid nitrogen-cooled CCD detector (Princeton Instruments). The entrance slit width was 100 μm. Pellets prepared from a mixture of 10 wt.% of sample in KBr were used, and Raman data of multiple spots on the pellets were collected. Morphology and particle

size of different samples were observed using a Hitachi S2500 field emission scanning electron microscopy (FESEM). Transmission electron microscopic (TEM) images were captured on a FEI Tecnai G2 FEG instrument at an acceleration voltage of 300 kV, to examine structures of different samples. Specific surface area of powders was measured by nitrogen adsorption/desorption at 77 K on a Quantachrome AS-1 instrument using the Brunauer-Emmet-Teller (BET) method. Chemical compositions of specimens were determined with inductively coupled plasma atomic emission spectrometry (ICP-AES) on a SPCTRO CIROS elemental analyzer. Thermogravimetric (TG) and differential thermal analyses (DTA) were performed on a SII STA7300 analyzer at a heating rate of 1°C/min in air. In situ high temperature X-Ray Diffraction (XRD) measurement was performed on a Bruker D8 Advance Diffractometer equipped with an Anton Paar HTK 1200N high temperature attachment, Vantec-1 high speed PSD detector and Cu anode X-ray tube. The scanning rate was set to 1.25 °/min, and the heating rate was 1 °C/min. The furnace chamber was flushed with flowing air at 100 mL/min during all the measurements. In situ high-resolution TEM (HRTEM) images and selected-area electron diffraction (SAED) patterns were recorded on a Hitachi H-9500 environmental TEM instrument equipped with a Gatan Orius 832 CCD camera. A Hitachi gas injection-heating specimen holder was used to heat a specimen while injecting gas to the specimen area for real-time in situ TEM observation at an acceleration voltage of 300 kV. In this work, the heating was set from room temperature to 500ºC. Air was injected into the chamber and the gas pressure was kept at 0.04 Pa around the specimen.

6.3.4 Electrochemical measurements

The working electrodes were composed of 80 wt.% pristine $Li[Li_{0.2}Mn_{0.54}Ni_{0.13}Co_{0.13}]O_2$ cathode material or its derivatives, 10 wt.% acetylene black (conductive carbon, Alfa Aesar, 99.5%), and 10 wt.% poly-vinylidenefluoride (PVDF, Alfa Aesar) as the binder. These cathodes were assembled into two-electrode CR2032-type coin cells for electrochemical measurements, with metallic lithium foil as anode, and Celgard-2320 membrane as separator. The electrolyte was 1 M $LiPF_6$ dissolved in ethylene carbonate (EC), dimethyl carbonate (DMC) and diethyl carbonate (DEC) at a volumetric ratio of 1:1:1. Galvanostatic charge and discharge were performed at different current densities in a voltage range of 2.0 - 4.8 V *vs.* Li/Li^+ using an 8-channel battery analyzer (MTI Corporation). Theoretical capacities of different cathode materials are all set to 250 mAh/g, i.e., current density corresponding to 1 *C* is 250 mA/g. Cyclic voltammetric (CV) curves of cathodes were recorded at a scanning rate of 0.1 mV/s between 2.0 and 4.8 V *vs*. Li/Li^+ using an electrochemical analyzer (CHI 605C).

6.4 Results and Discussion

6.4.1 Substitution of lithium ions in LMNCO via two-step ion exchanges

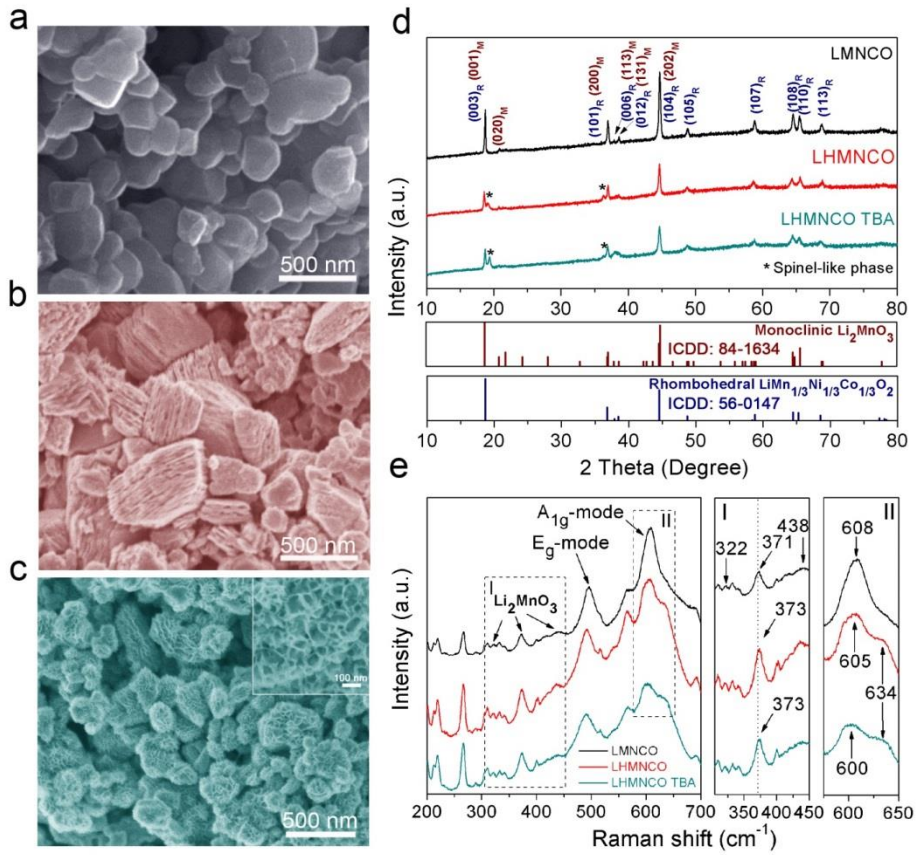

Figure 6.2 Morphological and structural evolutions of Li-excess layered $Li[Li_{0.2}Mn_{0.54}Ni_{0.13}Co_{0.13}]O_2$ nanoparticles via ion exchanges. SEM images of (a) original nanoparticles (marked as LMNCO), (b) the intermediate after the first Li^+-H^+ exchange in LMNCO in 2 M HCl solution (marked as LHMNCO), and (c) the derivative after the second H^+-TBA^+ exchange in LHMNCO in 20 wt.% TBA·OH aqueous solution (marked as LHMNCO TBA); (d) XRD patterns and (e) Raman spectra of ion-exchanged LHMNCO and LHMNCO TBA powders in comparison with those of pristine Li-excess layered LMNCO.

Li-excess $Li[Li_{0.2}Mn_{0.54}Ni_{0.13}Co_{0.13}]O_2$ (LMNCO) precursor was prepared by a sol-gel precipitation of transition metal ions in alkaline LiOH solution at a molar ratio of Li:Mn:Ni:Co=1.2:0.54:0.13:0.13, with the triblock co-polymer F127 as the dispersant. LMNCO nanoparticles were obtained after sintering the resultant precursor in air at 900°C for 12 h, exhibiting polyhedral shapes and an average particle size of ~250 nm (Figure 6.2a). Substitution of lithium ions in LMNCO by foreign cations was then carried out in two steps. First, LMNCO nanoparticles was protonated in 2 M acidic HCl solution with vigorous stirring at room temperature, in which lithium ions were replaced with protons [23,30]. Inductively coupled plasma atomic emission spectroscopy (ICP-AES) elemental analysis indicates that 45% of lithium ions in LMNCO were substituted, accompanied by slight dissolution of nickel element during protonation in the acidic environment. Nickel loss can probably be attributed to Li^+-Ni^{2+} cation mixing, since Ni^{2+} ions with similar radius to Li^+ tend to occupy lithium ion sites in the as-prepared pristine LMNCO [27]. Johnson and Kang

et al. have reported that H^+-Li^+ exchange prefers to take place within Li_2MnO_3 rather than in $LiMn_{1/3}Ni_{1/3}Co_{1/3}O_2$ [23,30]. In this case, Li_2MnO_3 component in $0.5Li_2MnO_3 \cdot 0.5LiMn_{1/3}Ni_{1/3}Co_{1/3}O$ has undergone at least partial protonation, because the theoretical fraction of lithium ions in $LiMn_{1/3}Ni_{1/3}Co_{1/3}O_2$ component is only 33.3%, less than the 45% of the exchanged lithium ions.

Protonation is the prerequisite for the second ion-exchange process, which also results in a distinct morphological change in the LHMNCO derivative and induces formation of a detectable spinel phase within a predominant layered structure. The SEM image in Figure 6.2b shows distinct layered cake-shaped LHMNCO blocks, which are drastically different from solid polyhedrons of the original LMNCO (Figure 6.2a). An ordered layered structure in Li-excess layered oxides would induce formation of a multilayer morphology in LHMNCO when subject to the extensive protonation (45% in this case), while limited H^+-Li^+ exchange (20.3% in Ref. 23) only resulted in pitted regions on the surface of LMNCO particles. Structural compatibility of cubic close-packed oxygen arrays in layered and spinel configurations is the principal factor that facilitates phase transition in LMNCO [20,26]. Figure 6.2d displays an ex-situ XRD pattern of protonated LHMNCO powder in comparison with that of original LMNCO, revealing appearance of the spinel-like phase after pronation. In good agreement with other XRD patterns of Li-excess layered materials [14,15,24,25], pristine LMNCO exhibits typical XRD peaks showing intergrowth of monoclinic Li_2MnO_3 with C2/m symmetry and rhombohedral $LiMn_{1/3}Ni_{1/3}Co_{1/3}O_2$ with R-3m symmetry within an ordered layered structure [14]. Two coupled peaks of $(006)_R$-$(012)_R$ reflections at 2θ = 36 - 38º and $(108)_R$-$(110)_R$ reflections at 2θ = 64 - 66º are characteristic of the predominant layered structure of $LiMn_{1/3}Ni_{1/3}Co_{1/3}O_2$. The weak $(020)_M$ reflection at 2θ = 20 - 23º is representative of the layered Li_2MnO_3 phase, the superstructure grown within the parent layered structure [24]. The integrated growth of these two layered components can be inferred from the other five peaks at 2θ = 18.7º, 36.9º, 37.9º, 38.5ºand 44.5º, which combine diffraction effects from $(001)_M$/$(003)_R$, $(200)_M$/$(101)_R$, $(113)_M$/$(006)_R$, $(131)_M$/$(012)_R$, and $(202)_M$/$(104)_R$, respectively. In contrast, the XRD pattern of LHMNCO shows a spinel-like impure phase marked with asterisks, consistent with results reported in literature [14,29]. As such, the merger of well-separated $(113)_M$/$(006)_R$ and $(131)_M$/$(012)_R$ doublets indicates a certain degree of distortion in the layered structure, while the peak splits of $(108)_R$-$(110)_R$ pair are preserved, showing that the layered structure is mainly retained in the protonated intermediate [29].

Since the Raman response of Mn-O bonding in the layered structure is different from that in the spinel phase, Raman spectroscopy is also used to confirm the formation of spinel structure. Figure 6.2e presents ex-situ Raman spectra with selected enlarged portions. The pristine LMNCO shows peaks at 322, 372 and 431 cm^{-1} that are typical of monoclinic Li_2MnO_3 component. Two strong peaks at 486 and 608 cm^{-1} can be ascribed to the bending E_g and stretching A_{1g} modes, respectively [24,31,32]. After H^+-Li^+ exchange, a shoulder peak at 634 cm^{-1} appears in the LHMNCO sample, which can be attributed to Mn-O vibration in a MnO_6 octahedron in the cubic spinel phase, again revealing the beginning of the phase transition [31,32].

The characteristic peak of Li_2MnO_3 at 372 cm^{-1} slightly shifts to the higher wavelength, indicating chemical activation of this component.

The second ion exchange takes places in 20 wt.% TBAOH aqueous solution, in which protons in the layered intermediate LHMNCO are further substituted by larger TBA^+ cations. As reported in the literature [33-39], TBAOH molecules have been extensively employed to tear up pre-protonated layered materials to form ultrathin two-dimensional (2D) "graphene-like" nanosheets under continuous stirring for several days. Here, we modify such a TBA^+ exfoliation technique by utilizing violent vortexes to shake the LHMNCO/HCl mixture (i.e., LHMNCO powders dispersed in HCl solution after protonation) in a TBAOH aqueous solution at a volumetric ratio of 1:5 for only 30 minutes. The XRD pattern of LHMNCO TBA reveals a small amount of spinel phase within the parent layered structure, since the intensity of the representative XRD peak at $2\theta = 19.3^o$ (marked with an asterisk in Figure 2d) from the newly-formed spinel phase increases. It is was reported that Raman responses at 600/605 cm^{-1} and 635 cm^{-1} are from diacritical vibration effects of Mn-O bonding in layered and spinel phases, respectively [32]. Therefore, the phase transition and growth of the spinel phase are also indicated by the increased intensity ratio of the Raman peaks (I_{634}/I_{600}=0.93) of LHMNCO TBA in comparison with I_{634}/I_{605}=0.87 of LHMNCO (Fig. 2e). Very interestingly, even with this modest chemical transformation, TBA^+-H^+ exchange under vortex mixing drastically alters the morphology of LHMNCO TBA, yielding exquisite nanoflower-shaped particles that are relatively monodisperse. This phenomenon can probably be attributed to the synergistic effects of the TBA-assisted exfoliation and the turbulence-induced reaction environment. The SEM image in Figure 6.2c shows that an individual nanoflower is composed of many ultrathin nano-petals in a honeycomb-like structure. Such distinct morphological reconstruction helps to significantly increase surface area of LHMNCO TBA nanoflowers to 11.1 m^2/g, almost five times that of pristine LMNCO nanoparticles (2.3 m^2/g). In summary, a variety of characterizations indicate that substitution of lithium ions in Li-excess layered cathode materials by foreign cations (H^+ and TBA^+) triggers formation of some cubic spinel phase within the parent layered structure and causes significant morphological changes.

6.4.2 Conversion of ion-exchanged layered derivative to spinel-structured material via calcinations

Although substitutions of lithium ions in LMNCO by H^+ and TBA^+ cations have induced formation of spinel domains, foreign cations still occupy the lithium ion sites between the transition metal layers and a predominantly layered atomic arrangement remains. As mentioned above, the existence of lithium ion vacancies in the lithium ion layers facilitates the migration of transition metal ions, which is the atomic level mechanism of layered-to-spinel phase transformation of LMNCO [16]. In order to generate sufficient lithium ion vacancies within an ion-exchanged layered material at a time and promote the layered-to-spinel phase transition to a maximum extent, we remove the embedded TBA^+ cations, protons and/or other byproducts (e.g., hydrates

and OH^- anions), by calcination of LHMNCO TBA nanoflowers in air at 500°C. Formation of the final nearly-perfect spinel-structured product was then investigated using a wide range of characterizations including Thermogravimetric and Differential Thermal Analyses (TG/DTA), ex/in-situ XRD patterns, ex-situ Raman spectra, and in-situ HRTEM observations with SAED patterns.

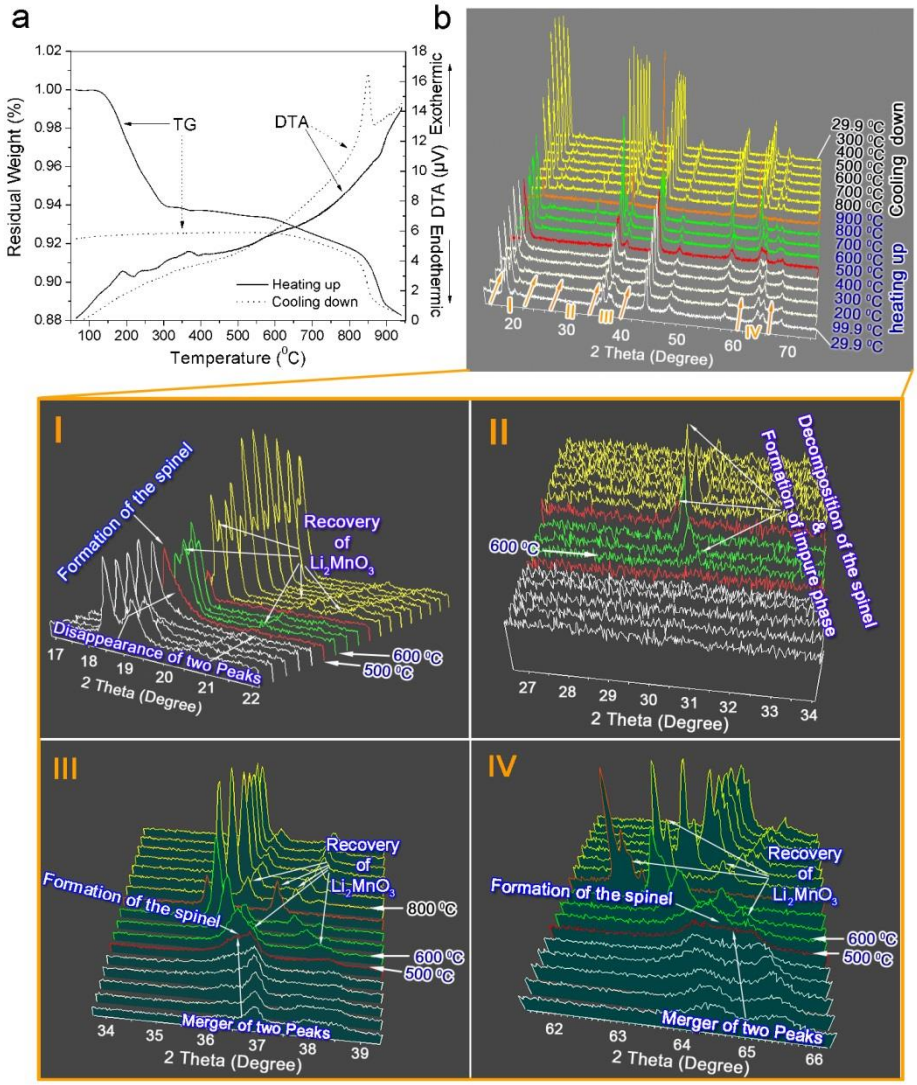

Figure 6.3 In-situ characterizations to identify phase transition of LHMNCO TBA during heat treatments. (a) TG/DTA curves showing weight loss and heat transfer when LHMNCO TBA is heated from room temperature to 950°C (solid lines) and cooled back to ambient temperature (dashed lines) in air, (b) in-situ XRD patterns of LHMNCO powders when heated to 900°C and subsequently cooled down to room temperature, with selected portions shown from I to IV.

Figure 6.3a shows TG/DTA curves of LHMNCO TBA heated from room temperature to 950°C (solid lines), and subsequently cooled to ambient temperature (dashed lines) in air. In order to determine the intermediate phases during the heating-cooling cycle, the dynamic structure of LHMNCO TBA was characterized via

in-situ XRD accordingly as shown in Figure 6.3b. The major weight loss of 6.1% in TG heating curve between 150 and 300°C is mostly attributed to pyrolysis of TBA^+ ions and removal of residual H^+, OH^-, hydrates, etc. As a result, numerous vacancies are generated at the original lithium ion sites via burning away foreign substituents, which facilitates and accelerates migrations of transition metal ions into these vacant sites, leading to a distinct layered-to-spinel phase transformation. As temperature increases, one TG plateau with a corresponding broad concave DTA peak appears at 300-600°C, indicating possible formation of a stable spinel structure in this temperature range.

The in-situ XRD patterns in Figure 6.3b demonstrate stabilization of the pure spinel phase at ~500°C. The continuous phase conversions can be more easily observed from the enlarged selected 2θ portions (I to IV) in Figure 6.3. As shown in portion I, the complete merger of the two peaks at 2θ = 18 - 20º at 300°C results in one characteristic XRD peak representing (111)s crystal planes in the cubic spinel phase. The slight shift of the (111)s peak to a lower 2θ can be ascribed to the thermal expansion effect in the crystal structure at elevated temperature during in-situ XRD characterizations [40]. Furthermore, the intensity of the $(020)_M$ peak at 2θ = 20.8º continues to decrease when the temperature is increased up to 500°C, indicating consumption of the layered Li_2MnO_3 component. As shown in Figure 6.2c, the predominantly ordered layered structure of the $LiMn_{1/3}Ni_{1/3}Co_{1/3}O_2$ component can be inferred from peak splitting in the $(006)_R$-$(012)_R$ and $(108)_R$-$(110)_R$ doublets. In contrast, it is found that these two pairs of well-separated peaks are combined into broad $(222)_S$ and $(440)_S$ peaks at 500°C in portions III and IV, respectively, revealing a complete layered-to-spinel phase transformation [29]. Increasing the annealing temperature above 600°C causes undesired decomposition of the newly-formed spinel structure, resulting in a $MnCo_2O_4$ impurity and recovery of layered Li_2MnO_3, which is consistent with the continuous mass reduction in the TG curves during the heating segment. Formation of $MnCo_2O_4$ is apparently detected at 600°C in portion II at 2θ = 30 - 31º, and the restored layered Li_2MnO_3 is confirmed by the obvious intensity increase of its XRD peaks in portions I, III and IV. After cooling down to ambient temperature, the in-situ XRD pattern of the final product indicates the coexistence of three phases: spinel-structured compound, layered Li_2MnO_3, and $MnCo_2O_4$ impurity. The regained mass in TG response (dashed line) during the cooling segment can probably be attributed to reformation of the layered Li_2MnO_3 phase, because there is a corresponding highly exothermic DTA peak (dashed line) around 850°C during the cooling process [40].

Additionally, in-situ HRTEM was used to examine the real-time layered-to-spinel phase transformation. As shown in Figure 6.4a and Figure 6.5, the layered structure in LHMNCO TBA nanoflowers is gradually transformed to the spinel phase from the surface inwards. The HRTEM images clearly show the continuous rearrangement of transition metal ions, causing the d-space distance change from 0.47 nm in an initial layered structure to 0.46 nm in a converted spinel phase. Surprisingly, we found that the transition occurred at 100°C under an air pressure of 0.04 Pa in the TEM chamber, which is much lower than that indicated in

the TG curve and in-situ XRD characterizations in Figure 6.3. Since HRTEM imaging is focused on localized areas of the specimen, the knock-on mechanism of the 300 kV electron beam combined with the very low air pressure environment might accelerate decomposition of the substitutes to generate lithium ion vacancies, and thus promotes phase conversion aggressively even at a low annealing temperature. Such phase transition has also been confirmed in another LHMNCO TBA sample as shown in Figure 6.5. The SAED pattern and HRTEM image of the fresh specimen (Figure 6.5a) clearly reveal a perfect layered structure at 25°C, while predominantly spinel features are subsequently captured from the SAED pattern and HRTEM image at 100°C (Figure 6.5b).

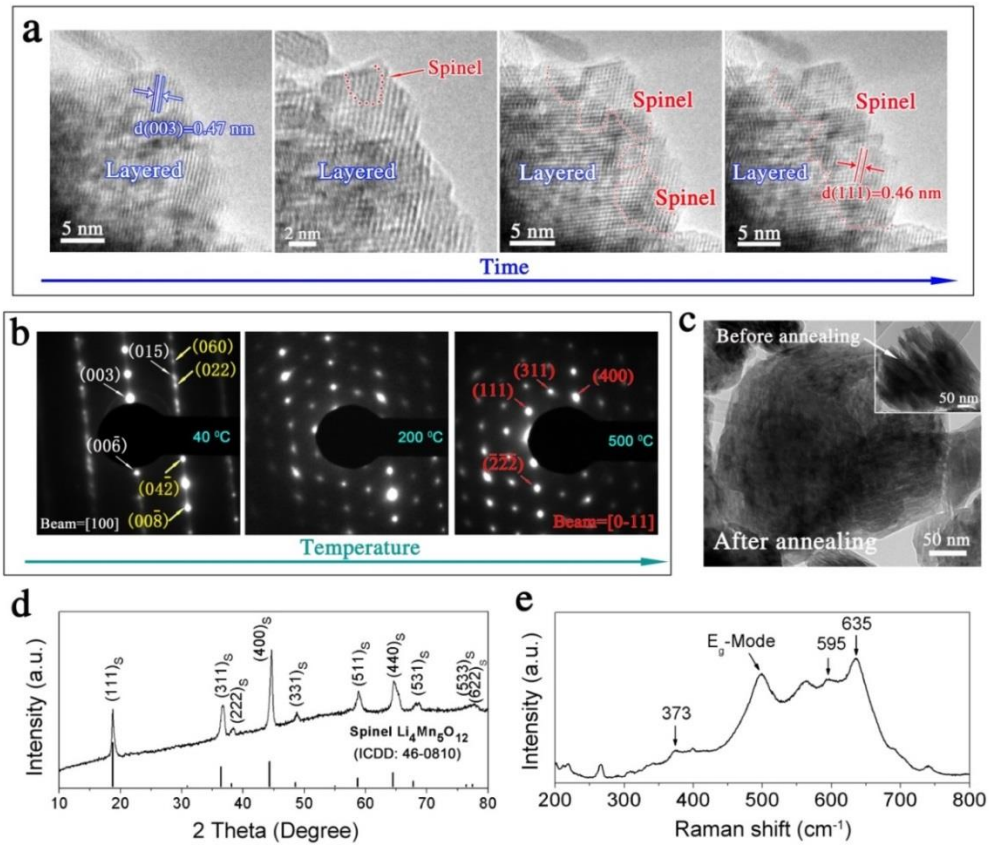

Figure 6.4 Phase transition and structural reconstruction of ion-exchanged LHMNCO TBA in a predominant layered structure to the spinel-structured material (marked as LHMNCO TBA HT) via calcinations. (a) Real-time phase transformation in LHMNCO TBA from original layered to newly-formed spinel phase captured by in-situ HRTEM observations at 100°C with an air pressure around 0.04 Pa; (b) SAED patterns recorded on the other LHMNCO TBA specimen subjected to increasing temperature (from 40°C to 200°C to 500°C) during in-situ TEM measurements, showing live migrations of transition metal cations to lithium ion layers in LHMNCO TBA and final formation of spinel-structured LHMNCO TBA HT at 500°C; (c) TEM image, (d) XRD pattern and (e) Raman spectrum of LHMNCO TBA HT after annealing LHMNCO TBA particles at 500°C for 3h.

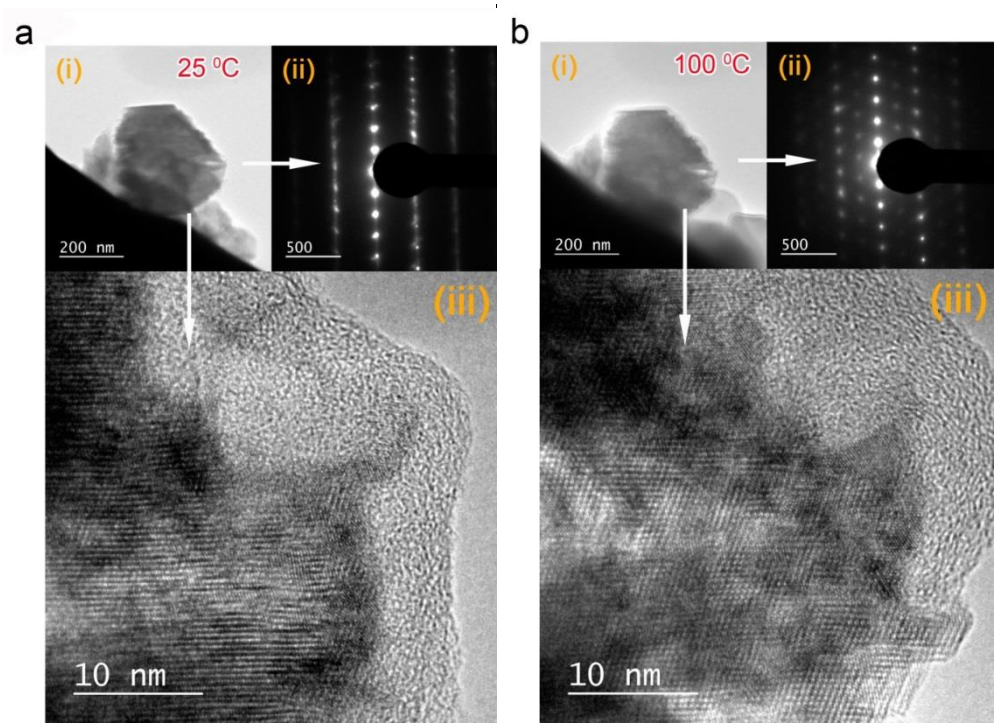

Figure 6.5 Phase transition and structural reconstruction of ion-exchanged LHMNCO TBA during in-situ TEM measurements at different temperature, 25°C and 100°C, respectively. (a) TEM observations of LHMNCO TBA at 25°C, showing the layered structure of the specimen: (i) bright-field TEM image, (ii) corresponding SAED pattern, and (iii) HRTEM image; and (b) subsequent TEM observations of LHMNCO TBA at 100°C, showing the predominantly spinel structure of the specimen when subjected to the increasing temperature: (i) bright-field TEM image, (ii) corresponding SAED pattern, and (iii) HRTEM image.

In addition, Figure 6.4b displays SAED patterns with characteristics changing from layered to layered-spinel composite to spinel structures (left to center to right) captured from the other pristine LHMNCO TBA sample subjected to the increasing temperature from 40 to 200 to 500°C, respectively. Since lithium and oxygen are too light to be visualized in SAED patterns, Figure 6.4b only shows atomic rearrangements of transition metal ions. Such changes in the SAED patterns of the specimen when heated also demonstrate the gradual migration of transition metal ions into lithium ion layers. The indexed SAED pattern captured at 40°C clearly illustrates integrated growth of two layered components, Li_2MnO_3 (yellow indexes) and $LiMn_{1/3}Ni_{1/3}Co_{1/3}O_2$ (white indexes), along the [100] direction in the ion-exchanged LHMNCO TBA nanoflowers, which is in agreement with the ex-situ XRD result in Figure 6.2c. At 200°C, the displacements of transition metal ions into the dark lithium ion layers are detected, indicating that a layered-spinel composite structure is formed. The resultant SAED pattern recorded at 500°C can be well indexed to the $Li_4Mn_5O_{12}$ spinel phase (ICDD: 46-0810), revealing phase transitions of both layered Li_2MnO_3 and $LiMn_{1/3}Ni_{1/3}Co_{1/3}O_2$ into one spinel phase. Therefore, the optimal annealing

temperature for sintering LHMNCO TBA nanoflowers to achieve a stable and highly pure spinel-structured material (LHMNCO TBA HT) is 500°C. Significant morphological and structural reconstructions take place during calcinations due to removal of embedded foreign substituents and atomic rearrangements. As shown in Figure 6.4c, petals of LHMNCO TBA nanoflowers (Figure 6.2c) are completely folded after heating, resulting in an intriguing mesoporous structure of LHMNCO TBA HT with a surface area of 13.7 m^2/g higher than the LHMNCO TBA nanoflowers.

Figure 6.4d shows the ex-situ XRD pattern after sintering LHMNCO TBA nanoflowers at 500°C in air for 3 h. The resulted product can be indexed as a spinel $Li_4Mn_5O_{12}$ phase with an *Fd-3m* space group. The Raman spectrum of LHMNCO TBA HT in Figure 6.4e also confirms formation of a $Li_4Mn_5O_{12}$-type spinel-structured phase [41]. The two strong Raman signals at 595 and 635 cm^{-1} are associated with the symmetric Mn-O stretching modes in the spinel $Li_4Mn_5O_{12}$ structure, in contrast to 580 and 625 cm^{-1} from $LiMn_2O_4$ [42]. The higher stretching frequency is attributed to the shorted Mn-O bonding length in $Li_4Mn_5O_{12}$ spinel. All the representative peaks of Li_2MnO_3 disappear except a weak one at 373 cm^{-1}. Both SAED pattern at 500°C in Figure 6.4b and the ex-situ XRD in Figure 6.4d can be indexed as a pure $Li_4Mn_5O_{12}$-type spinel phase without showing any characteristics of layered structures. However, the spinel structure of LHMNCO TBA HT cannot be considered perfect, since the Raman spectrum in Figure 6.4e exhibits a weak peak that does not belong to the spinel structure and can probably be attributed to partial decomposition of newly-formed $Li_4Mn_5O_{12}$-type spinel to the Li-rich spinel $Li_{1+x}Mn_{2-x}O_4$ and layered Li_2MnO_3 [43]. In addition, the existence of Ni and Co elements in LHMNCO TBA HT results in a more complex structure of the $Li_4Mn_5O_{12}$-based spinel. Overall, the desired phase transition has been achieved in Li-excess layered oxides, yielding a highly-pure spinel-structured material with $Li_4Mn_5O_{12}$-type characteristics after ion-exchanges and calcinations.

6.4.3 Electrochemical performance of the final spinel cathode material for high-performance lithium-ion batteries

Electrochemical performance of the newly-formed cathode material reveals typical spinel characteristics in a voltage range of 2.0 - 4.8 V *vs.* Li/Li^+, as shown in Figure 6.6. Figure 6.6a records cyclic voltammetric (CV) profiles of the spinel LHMNCO TBA HT in the first three cycles. In comparison with the CV curves of pristine layered LMNCO (Figure 6.7b), two extra redox pairs around 2.8 and 4.6 V are found in the CV curves of LHMNCO TBA HT, and the intensity of redox at 4.0 V is reduced considerably. The predominant redox pair, anodic peak at 3.03 V and cathodic peak at 2.64 V, can be ascribed to oxidation and reduction processes of Mn^{3+}/Mn^{4+} redox pair, related to extraction and insertion of lithium ions on 16c sites in the spinel structure [1]. The dominant Mn^{3+}/Mn^{4+} redox indicates significant displacements of tetravalent manganese cations and lithium ions in both layered Li_2MnO_3 and $LiMn_{1/3}Ni_{1/3}Co_{1/3}O_2$ components have been transformed to spinel in the final product.

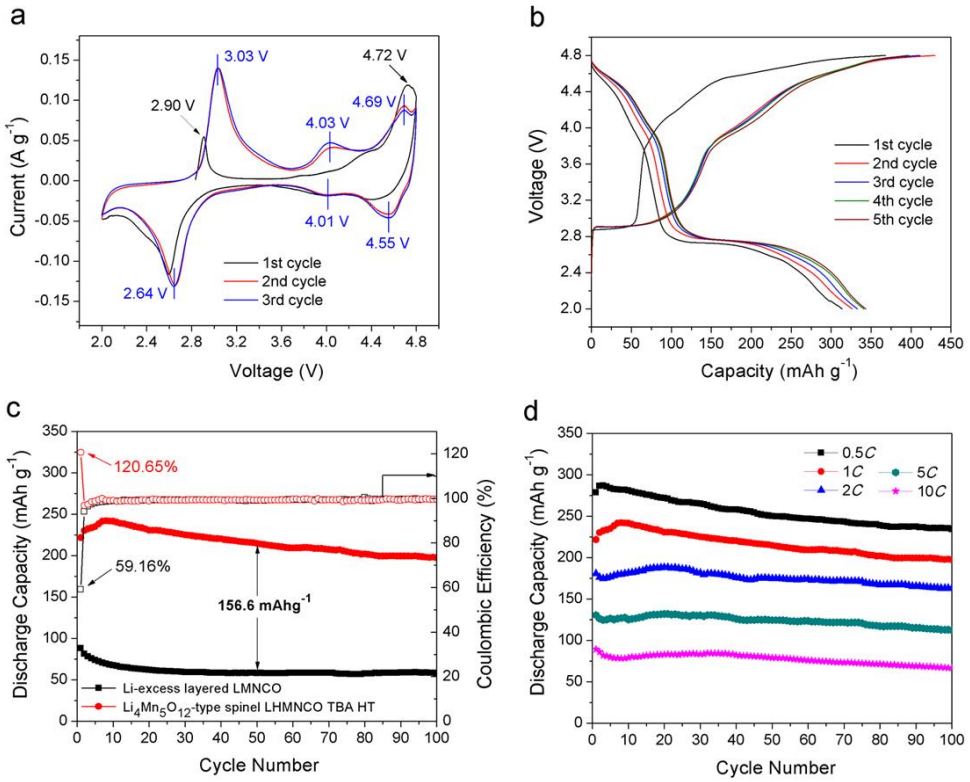

Figure 6.6 Electrochemical performance of spinel LMNCO TBA HT cathode material cycled in a voltage range of 2.0-4.8 V *vs.* Li/Li$^+$. (a) Cyclic voltammetric (CV) profiles in the first three cycles at a scanning rate of 0.1 mV/s, (b) charge and discharge curves in the first five cycles at 0.1 *C* (1*C* = 250 mA/g), (c) cycling performance at 1 *C* with corresponding Coulombic efficiency in comparison with that of a pristine layered LMNCO cathode, and (d) cycling performance at various charge/discharge rates showing high-rate performance up to 10 *C*.

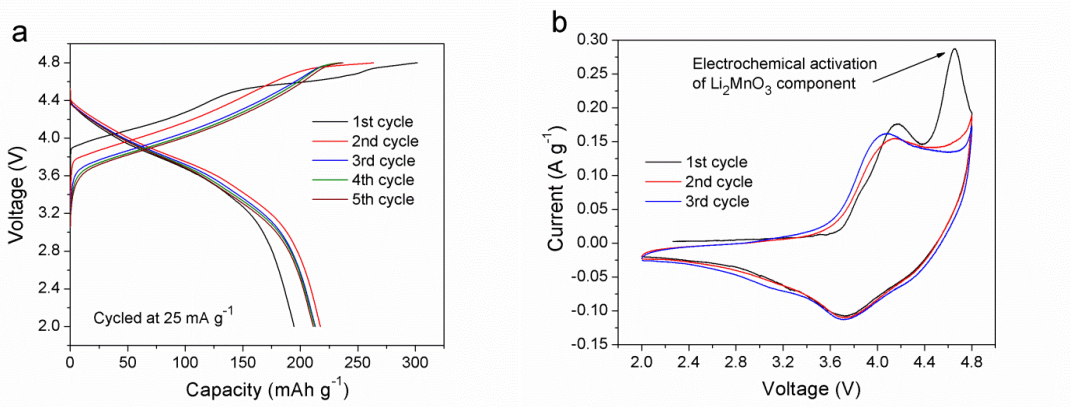

Figure 6.7 Electrochemical performance of pristine Li-excess layered $Li[Li_{0.2}Mn_{0.54}Ni_{0.13}Co_{0.13}]O_2$ cathode material in a voltage range of 2.0-4.8 V *vs.* Li/Li$^+$. (a) Charge and discharge curves in the first five cycles at 0.1 *C* (1 *C* = 250 mA/g), and (b) cyclic Voltammetric (CV) curves in the first three cycles at a scanning rate of 0.1 mV/s.

Accordingly, Figure 6.8b and Figure 6.9b show CV profiles of commercial $LiMn_2O_4$ and the as-prepared $Li_4Mn_5O_{12}$ spinel cathode materials, respectively. It is found that CV curves of $LiMn_2O_4$-type spinel materials, such as $LiMn_2O_4$ (Figure 6.8b), $LiMn_{1.5}Ni_{0.5}O_4$ [10] and $Li[Mn_{1.5}Ni_{0.425}Co_{0.075}]O_2$ [21], show a major redox around 4.0 V as well as a minor one near 3.0 V. In contrast, CV curve of $Li_4Mn_5O_{12}$-type spinel shows a significantly predominant redox around 3.0 V and a redox pair with much lower intensity at 4.0 V (Figure 6.9b). The CV characteristics of LHMNCO TBA HT are consistent with the as-prepared $Li_4Mn_5O_{12}$ spinel rather than $LiMn_2O_4$-type spinel cathode materials, and also significantly different from that of pristine LMNCO. As such, LHMNCO TBA HT cathode material very likely has the $Li_4Mn_5O_{12}$-type spinel structure, which contributes to a capacity even higher than the theoretical capacity of pristine Li-excess layered cathode $Li[Li_{0.2}Mn_{0.54}Ni_{0.13}Co_{0.13}]O_2$.

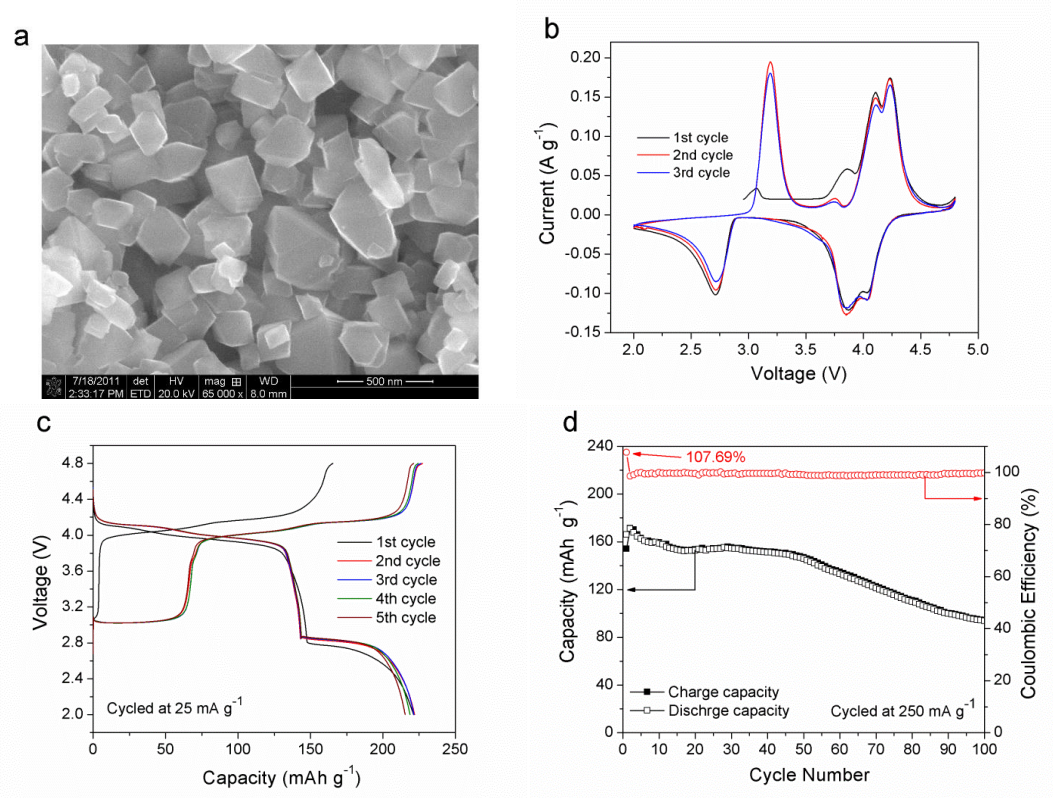

Figure 6.8 Morphology and electrochemical performance of Li-stoichiometric spinel $LiMn_2O_4$ (MTI Corp.) cathode material in a voltage range of 2.0-4.8 V *vs.* Li/Li^+. (a) SEM image of $LiMn_2O_4$ nanoparticles with an average particle size of ~250 nm, (b) cyclic voltammetric (CV) profiles in the first three cycles at a scanning rate of 0.1 mV/s, (c) charge and discharge curves in the first five cycles at 0.1 *C* (1*C* = 250 mA/g), and (d) cycling performance at 1 *C* with corresponding Coulombic efficiency. The initial Coulombic efficiency reaches 107.69%. After 100 electrochemical cycles, the $LiMn_2O_4$ cathode retains a final discharge capacity of 93.8 mA/g, corresponding to a capacity retention of 56.5%.

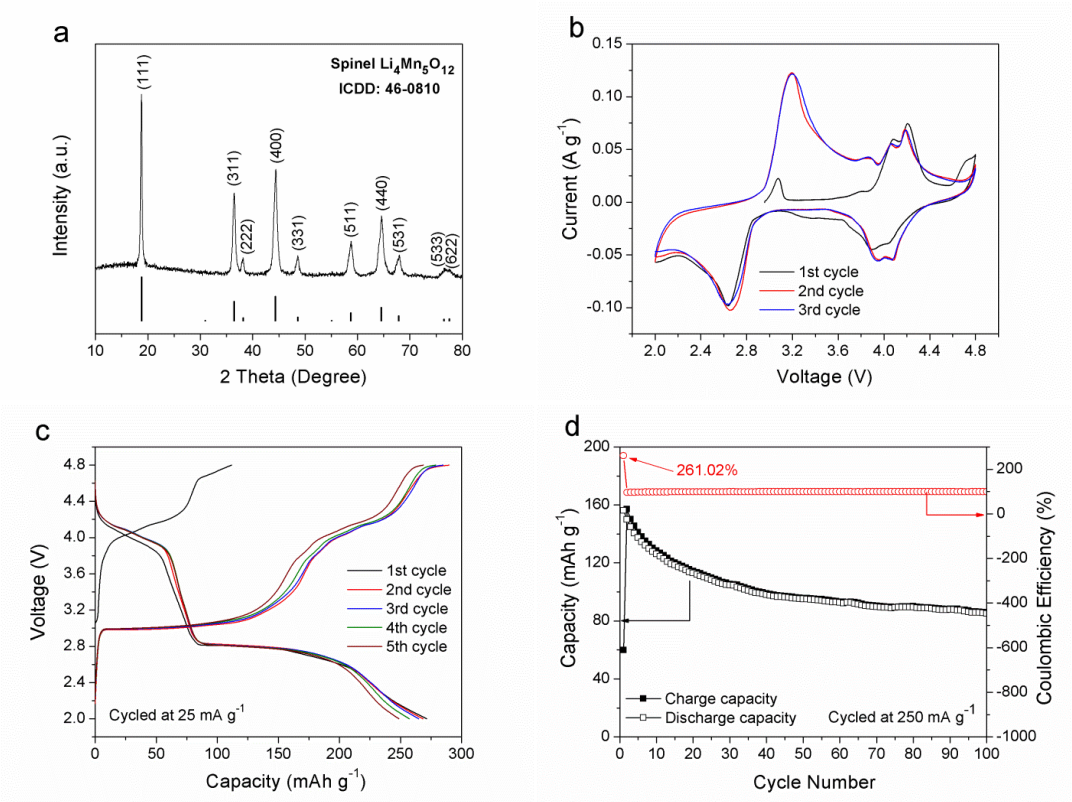

Figure 6.9 XRD pattern and electrochemical performance of the as-prepared spinel $Li_4Mn_5O_{12}$ cathode material in a voltage range of 2.0-4.8 V *vs.* Li/Li^+. (a) XRD pattern of $Li_4Mn_5O_{12}$ powders prepared by a sol-gel method, (b) cyclic voltammetric (CV) profiles in the first three cycles at a scan rate of 0.1 mV/s, (c) charge and discharge curves in the first five cycles at 0.1 *C* (1 *C* = 250 mA/g), and (d) cycling performance at 1 *C* with corresponding Coulombic efficiency. The initial Coulombic efficiency reaches 261.02%. After 100 electrochemical cycles, the $Li_4Mn_5O_{12}$ cathode retains a final discharge capacity of 85.0 mAg^{-1}, corresponding to a capacity retention of 54.4%.

Figure 6.6b shows the galvanostatic charge/discharge curves of LHMNCO TBA HT in the first five cycles at 0.1 *C* (1 *C* = 250 mA/g). It is noted that there are also capacity contributions from Ni^{2+}/Ni^{4+} redox at 4.6 V and Co^{3+}/Co^{4+} redox at 4.0 V in the reconstructed spinel structure. Since charge/discharge curves of the fourth and fifth cycle are almost identical, it is suggested that the cathode becomes stable after five electrochemical cycles. Such $Li_4Mn_5O_{12}$-type spinel cathode delivers a remarkable discharge capacity of 343.2 mAh/g in the fifth cycle at 0.1 *C*, much higher than that exhibited from the pristine Li-excess layered LMNCO cycled at the same rate (211.3 mAh/g) (Fig. S2a) or the theoretical capacity of LMNCO (321 mAh/g). In other words, additional capacity of 131.9 mAh/g is developed after layered-to-spinel phase transition accompanied by morphological and structural reconstructions of LMNCO (Figure 6.2c and Figure 6.4c).

It can be seen that the initial charge curves in CV and charge/discharge profiles of LHMNCO TBA HT are significantly different from those in the second and third

cycles, possibly due to the $Li_4Mn_5O_{12}$-type spinel characteristics in LHMNCO TBA HT. Since Mn^{4+} in $Li_4Mn_5O_{12}$ spinel cannot be further oxidized, anodic peaks at 2.90 and 4.72 V in the initial CV charge arise from the decomposition products of $Li_4Mn_5O_{12}$, $Li_{1+x}Mn_{2-x}O_4$ and Li_2MnO_3, respectively, which is in agreement with the Raman spectra (Figure 6.4e). In the subsequent initial discharge, extra Li^+ will be inserted into vacant 16c sites in $Li_4Mn_5O_{12}$, contributing to the predominant redox reaction around 3.0 V and unexpected high capacities. As a result, the initial Columbic efficiency of LHMNCO TBA HT cycled at 1 *C* reaches 120.65% (Figure 6.6c), because more lithium ions can be inserted into $Li_4Mn_5O_{12}$ spinel during initial discharge than those extracted in the initial charge reaction. On the other hand, pristine Li-excess layered LMNCO only shows a Columbic efficiency of 59.16% in the first cycle due to irreversible electrochemical activation of the inert Li_2MnO_3 component. The high initial Columbic efficiency of LHMNCO TBA HT is similar to that of the as-prepared $Li_4Mn_5O_{12}$ (261.02%, Figure 6.9d). Moreover, when cycled at 1 *C* in a voltage range of 2.0 - 4.8 V *vs.* Li/Li^+, such $Li_4Mn_5O_{12}$-type spinel cathode not only exhibits extra capacity contribution of ~150 mAh/g in comparison with the original LMNCO (Figure 6.6c), but also delivers a much higher capacity and better cycleability than both as-prepared $Li_4Mn_5O_{12}$ (Figure 6.9d) and commercial $LiMn_2O_4$ spinel (Figure 6.8d). It is suggested that the existence of Ni and Co elements in LHMNCO TBA HT as well as its mesoporous structure helps to stabilize the basic $Li_4Mn_5O_{12}$ spinel structure, and thus contributes to the desirable cycleability. Furthermore, Figure 6.6d shows the excellent rate capability of the converted spinel cathode, delivering initial discharge capacities of 267.2, 203.9, 180.7, 126.3, and 89.4 mAh/g at 0.5, 1, 2, 5, and 10 *C*, respectively. This material also demonstrates outstanding cycling stabilities.

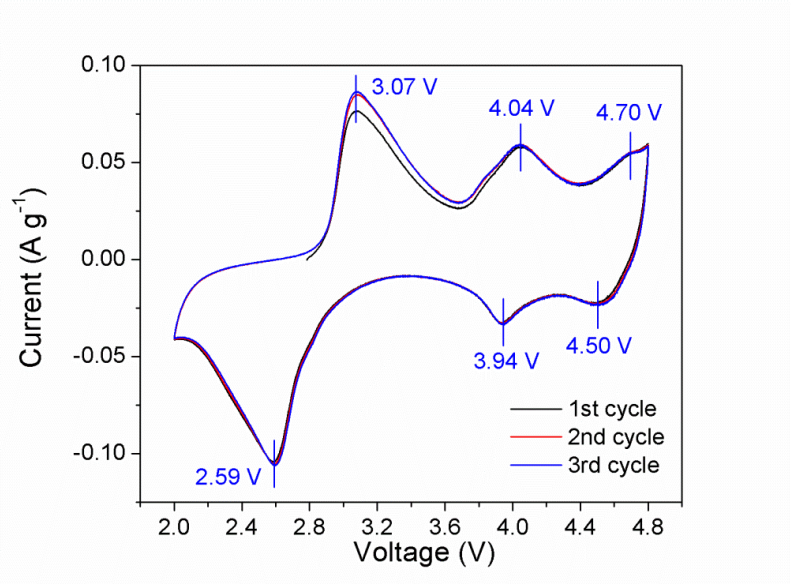

Figure 6.10 Electrochemical performance of newly-formed LHMNCO TBA HT spinel cathode in a voltage range of 2.0-4.8 V *vs.* Li/Li^+. Cyclic Voltammetric (CV) curves in the first three cycles at a scanning rate of 0.1 mV/s recorded after the sample was cycled by 100 electrochemical cycles at 1 *C*.

Figure 6.10 presents the first three cycles of CV curves from LHMNCO TBA HT cathode which has already undergone 100 charge/discharge cycles by chronopotentiometry. The three CV curves are almost overlapped with each together, demonstrating its remarkable structural stability and electrochemical reversibility. In summary, the ex-situ ion-exchange promoted phase transition in LMNCO contributes to unexpectedly high capacity, excellent rate capability, and remarkable cycling reversibility of the newly-formed $Li_4Mn_5O_{12}$-type spinel cathode.

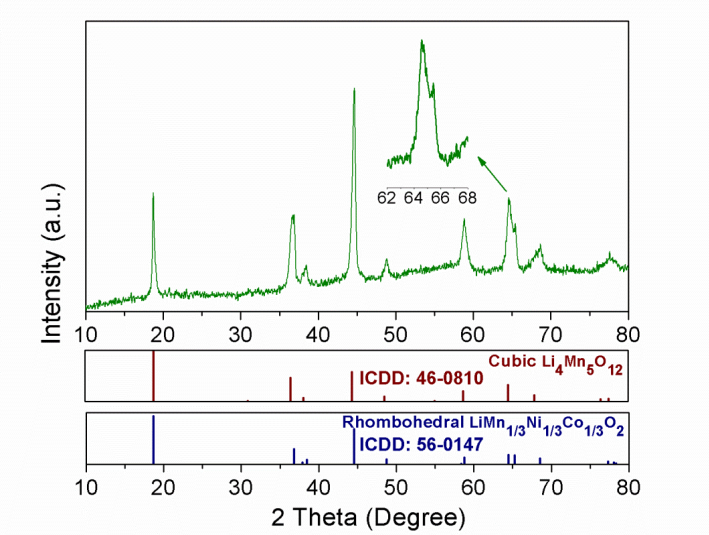

Figure 6.11 XRD pattern of the resultant powder after annealing LHMNCO at 500°C in air for 3 h. In the inset shows the enlarged portion at 2θ = 62-68º.

As reported in literatures [23,30], chemical activations of LMNCO can be accomplished in an acidic environment, in which protonation causes release of Li_2O from the inert Li_2MnO_3 component to yield lithium-active MnO_2, resulting in significantly improved specific capacity and initial Coulombic efficiency in the first cycle. Although such irreversible lithium ion extraction together with oxygen loss induces formation of the spinel phase via migrating transition metal cations into lithium ion layers, the amount of spinel-structured domains is very limited on the surface of LMNCO. Furthermore, the phase transition continuously occurs within partially activated spinel-layered composite cathodes during subsequent electrochemical cycles, giving rise to structural instability and inferior cycleability [30]. In the present work, we employed TBAOH molecules for the second step of ion exchange to the protonated LMNCO under violent vortex to achieve a complete phase transition to spinel structures. As mentioned previously, alkylammonium hydroxide, such as TBAOH and tetramethylammonium hydroxide (TMAOH), has been extensively used to exfoliate protonated-layered materials into two-dimensional (2D) nanosheets [34,36,37]. However, as shown in Figure 6.2c, three-dimensional (3D) nanoflower-shaped LHMNCO TBA derivatives have been achieved by precisely controlling the volumetric ratio of the LHMNCO/HCl mixed suspension to the TBAOH solution, under vortex mixing instead of the mild stirrings as reported in literature [36]. The formation of the spinel structure on the surface of the protonated

layered LHMNCO may impede extensive exfoliation within LHMNCO upon TBA^+-H^+ exchange, resulting in 3D nanoarchitectured LHMNCO TBA nanoflowers instead of the usual 2D nanosheets. Using a controlled dose of TBAOH solution and vortex treatment are two crucial factors for obtaining such exquisite monodisperse nanoflowers rather than other coarse morphologies and agglomerated nanosheets reported in the literature [37]. Furthermore, exfoliation time in our designed approach is 30 min, much shorter than those reported by other groups [34]. In addition, applying TBA^+ cations with a larger molecular size to replace protons during the second ion-exchange process helps to increase the *c*-axis lattice distance between transition metal layers. Such expanded layered structure contributes to the favorable generation of lithium ion vacancies and subsequent displacement by transition metal cations after the removal of TBA^+ via calcinations in air, and thus leads to a complete layered-to-spinel phase transition. On the other hand, it is found that a complete phase transition cannot be achieved via direct annealing of LHMNCO after H^+-Li^+ ion exchange. Figure 6.11 shows the XRD pattern of the resultant powder after annealing LHMNCO at 500°C in air for 3h. The splitting XRD doublets at 2θ = 64 - 66º indicates some preserved layered feature.

This work not only reports a complete phase transformation from Li-excess layered to $Li_4Mn_5O_{12}$-type spinel oxide via ex-situ ion-exchange processes, but also provides detailed characterizations of the reconstructed spinel phase. It should be noted that the spinel structure obtained in this work is different from the spinel structures prepared via other routes such as in-situ electrochemical cycling [16]. For example, Gu et al. reported that after 300 electrochemical cycles the spinel formed at the surface of cycled layered cathode materials shows a $LiMn_2O_4$-type diffraction feature. In their work, only SAED characterization is used for exploring the spinel phase, which may be not sufficient to identify their specific structure. This is because the SAED patterns diffracted from $LiMn_2O_4$-type, $LiMn_{1.5}Ni_{0.5}O_4$-type and $Li_4Mn_5O_{12}$-type spinel materials are mostly identical. On the other hand, Song and co-workers produced a spinel phase on the surface of LMNCO by reacting it with Super P (carbon black), and suggested that its structure is different from either $LiMn_2O_4$ or $LiMn_{1.5}Ni_{0.5}O_4$ [14]. In our work, the converted spinel has been demonstrated to be $Li_4Mn_5O_{12}$-type by ex-situ XRD patterns and Raman spectrum (Figure 6.4) as well as its electrochemical characteristics (Figure 6.6). Simultaneously, ex-situ chemical activation of high-capacity LMNCO is realized through phase transition, resulting in significantly improved electrochemical reversibility and rate capability while retaining high capacity and remarkable cycling stability. Such excellent electrochemical performances of $Li_4Mn_5O_{12}$-type spinel-structured cathodes can be attributed to the following factors: (1) The reconstructed spinel structure offers 3D channels for lithium ion diffusion while the original layered cathode material only has 2D pathways [14]; (2) The newly-formed $Li_4Mn_5O_{12}$-type spinel material exhibits unexpected structural stability and electrochemical reversibility (Figure 6.6 and Figure 6.10) due to the coexistence of Ni and Co elements within the $Li_4Mn_5O_{12}$ spinel; (3) As shown in Figure 6.4c, the nanoarchitectured spinel cathode has a mesoporous structure that provides maximum electrochemical active sites, facilitates

accommodation of electrolyte and effectively releases strains during lithiation/delithiation processes. Improved capacity may also be attributed to absorption and desorption of lithium ions within the porous structure [44-46].

6.5 Conclusions

In summary, the present work sheds light on fundamental understanding of layered-to-spinel phase transition within Li-excess layered oxides. A $Li_4Mn_5O_{12}$-type spinel-structured material has been converted from Li-excess layered $Li[Li_{0.2}Mn_{0.54}Ni_{0.13}Co_{0.13}]O_2$ via ion-exchange promoted phase transitions. During this process, both Li_2MnO_3 and $LiMn_{1/3}Ni_{1/3}Co_{1/3}O_2$ components in a Li-excess layered oxide undergo layered-to-spinel phase transformations by first replacing lithium ions with protons in aqueous acid and further substitution of the embedded protons by TBA^+ ions under violent vortex. According to in-situ XRD, HRTEM and SAED characterizations, the optimal annealing temperature for such an ion-exchanged layered intermediate is determined as 500°C, at which a nearly-perfect spinel phase with a mesoporous structure is obtained. It is suggested that the generation of sufficient lithium ion vacancies within LMNCO at a time is critical for such a complete phase evolution. In comparison with the pristine LMNCO, the newly-converted spinel cathode exhibits improved electrochemical reversibility and extra capacity in the initial cycle, and delivers high specific capacity, excellent rate capability and favorable cycleabiltiy in successive electrochemical cycles. This work opens up new routes to maximize electrochemical performance of Li-excess layered cathode materials for applications in superior lithium ion batteries.

6.6 References

1. J. B. Goodenough, K. S. Park, The Li-ion Rechargeable Battery: A Perspective. *Journal of American Chemical Society* 135 (2013) 1167-1176.

2. H. Wu, G. Yu, L. Pan, N. Liu, M. T. McDowell, Z. Bao, Y. Cui, Stable Li-Ion Battery Anodes by In-Situ Polymerization of Conducting Hydrogel to Conformally Coat Silicon Nanoparticles. *Nature Communications* 4 (2013) 1943.

3. A. Magasinki, P. Dixon, B. Hertzberg, A. Kvit, J. Ayala, G. Yushin, High-Performance Lithium-Ion Anodes Using a Hierarchical Bottom-Up Approach. *Nature Materials* 9 (2010) 353-358.

4. P. Poizot, S. Laruelle, S. Grugeon, L. Dupont, J. M. Tarascon, Nano-Sized Transition-Metal Oxides as Negative-Electrode Materials for Lithium-Ion Batteries. *Nature* 407 (2000) 496-499.

5. M. V. Reddy, G. V. Subba Rao, B. V. Chowdari, Metal Oxides and Oxysalts as Anode Materials for Li Ion Batteries. *Chemical Reviews* 113 (2013) 5364-5457.

6. Z. Chen, I. Belharouak, Y. K. Sun, K. Amine, Titanium-Based Anode Materials for Safe Lithium-Ion Batteries. *Advacned Functional Materials* 23 (2013) 959-969.

7. H. G. Jung, M. W. Jang, J. Hassoun, Y. K. Sun, B. Scrosati, A High-Rate Long-Life $Li_4Ti_5O_{12}/Li[Ni_{0.45}Co_{0.1}Mn_{1.45}]O_4$ Lithium-Ion Battery. *Nature Communications* 2 (2011) 516.

8. W. Ai, L. Xie, Z. Du, Z. Zeng, J. Liu, H. Zhang, Y. Huang, W. Huang, T. Yu, A Novel Graphene-Polysulfide Anode Material for High-Performance Lithium-Ion Batteries. *Scienticfic Reports* 3 (2013) 2341.

9. Y. K. Sun, S. T. Myung, B. C. Park, J. Prakash, I. Belharouak, K. Amine, High-Energy Cathode Material for Long-Life and Safe Lithium Batteries. *Nature Materials* 8 (2009) 320-324.

10. A. Manthiram, K. Chemelewski, E. S. Lee, A Perspective on the High-Voltage $LiMn_{1.5}Ni_{0.5}O_4$ Spinel Cathode for Lithium-Ion Batteries. *Energy & Environmental Science* 7 (2014) 1339-1350.

11. L. H. Hu, F. Y. Wu, C. T. Lin, A. N. Khlobystov, L. J. Li, Graphene-Modified $LiFePO_4$ Cathode for Lithium Ion Battery beyond Theoretical Capacity. *Nature Communications* 4 (2013) 1687.

12. M. Jiang, B. Key, Y. S. Meng, C. P. Grey, Electrochemical and Structural Study of the Layered, "Li-Excess" Lithium-Ion Battery Electrode Material $Li[Li_{1/9}Ni_{1/3}Mn_{5/9}]O_2$. *Chemistry of Materials* 21 (2009) 2733-2745.

13. N. Yabuuchi, K. Yoshii, S. T. Myung, I. Nakai, S. Komaba, Detailed Studies of a High-Capacity Electrode Material for Rechargeable Batteries, Li_2MnO_3-$LiCo_{1/3}Ni_{1/3}Mn_{1/3}O_2$. *Journal of The American Chemical Society* 133 (2011) 4404-4419.

14. B. Song, H. Liu, Z. Liu, P. Xiao, M. O. Lai, L. Lu, High Rate Capability Caused by Surface Cubic Spinels in Li-Rich Layer-Structured Cathodes for Li-Ion Batteries. *Scientific Reports* 3 (2013) 3094.

15. M. N. Ates, Q. Jia, A. Shah, A. Busnaina, S. Mukerjee, K. M. Abraham, Mitigation of Layered to Spinel Conversion of A Li-Rich Layered Metal Oxide Cathode Material for Li-Ion Batteries. *Journal of The Electrochemical Society* 161 (2013) A290-A301.

16. M. Gu, I. Belharouak, J. Zheng, H. Wu, J. Xiao, A. Genc, K. Amine, S. Thevuthasan, D. R. Baer, J. G. Zhang, N. D. Browning, J. Liu, C. Wang,

Formation of the Spinel Phase in the Layered Composite Cathode Used in Li Ion Batteries. *ACS Nano* 7 (2013) 760-767.

17. S. Hy, F. Felix, J. Rick, W. N. Su, B. J. Hwang, Direct In Situ Observation of Li_2O Evolution on Li-Rich High-Capacity Cathode Material, $Li[Ni_xLi_{(1-2x)/3}Mn_{(2-x)/3}]O_2$ (0<=x<=0.5). *Journal of The Amecian Chemical Society* 136 (2014) 999-1007.

18. K. A. Jarvis, Z. Deng, L. F. Allard, A. Manthiram, P. J. Ferreira, Atomic Structure of a Lithium-Rich Layered Oxide Material for Lithium-Ion Batteries: Evidence of a Solid Solution. *Chemistry of Materials* 23 (2011) 3614-3621.

19. C. R. Fell, D. Qian, K. J. Carroll, M. Chi, J. L. Jones, Y. S. Meng, Correlation between Oxygen Vacancy, Microstrain, and Cation Distribution in Lithium-Eexcess Layered Oxides during the First Electrochemical Cycle. *Chemistry of Materials* 25 (2013) 1621-1629.

20. D. Mohanty, S. Kalnaus, R. A. Meisner, K. J. Rhodes, J. Li, E. A. Payzant, D. L. Wood III, C. Daniel, Structural Transformation of A Lithium-Rich $Li_{1.2}Co_{0.1}Mn_{0.55}Ni_{0.15}O_2$ Cathode during High Voltage Cycling Resolved by In Situ X-Ray Diffraction. *Journal of Power Sources* 229 (2013) 239-248.

21. E. S. Lee, A. Huq, H. Y. Chang, A. Manthiram, High-Voltage, High-Energy Layered-Spinel Composite Cathodes with Superior Cycle Life for Lithium-Ion Batteries. *Chemistry of Materials* 24 (2012) 600-612.

22. S. Hy, W. N. Su, J. M. Chen, B. J. Hwang, Soft X-Ray Absorption Spectroscopic and Raman Studies on $Li_{1.2}Ni_{0.2}Mn_{0.6}O_2$ for Lithium-Ion Batteries. *The Journal of Physical Chemistry C* 116 (2012) 25242-25247.

23. C. S. Johnson, N. Li, C. Lefief, J. T. Vaughey, M. M. Thackeray, Synthesis, Characterization and Electrochemistry of Lithium Battery Electrodes: $xLi_2MnO_3{\cdot}(1\text{-}x)LiMn_{0.333}Ni_{0.333}Co_{0.333}O_2$. *Chemistry of Materials* 20 (2008) 6095-6106.

24. F. Amalraj, D. Kovacheva, M. Talianker, L. Zeiri, J. Grinblat, N. Leifer, G. Goobes, B. Markovsky, D. Aurbach, Synthesis of Integrated Cathode Materials $xLi_2MnO_3{\cdot}(1\text{-}x)\,LiMn_{1/3}Ni_{1/3}Co_{1/3}O_2$ $(x = 0.3,0.5,0.7)$ and Studies of Their Electrochemical Behavior. *Journal of The Electrochemical Society* 157 (2010) A1121-A1130.

25. Y. Wu, A. Manthiram, High Capacity, Surface-Modified Layered $Li[Li_{(1-x)/3}Mn_{(2-x)/3}Ni_{x/3}Co_{x/3}]O_2$ Cathodes with Low Irreversible Capacity Loss. *Electrochemical and Solid-State Letters* 9 (2006) A221-A224.

26. F. Lin, I. M. Markus, D. Nordlund, T. C. Weng, M. D. Asta, H. L. Xin, M. M. Doeff, Surface Reconstruction and Chemical Evolution of Stoichiometric Layered Cathode Materials for Lithium-Ion Batteries. *Nature Communications* 5 (2014) 3529.

27. A. Boulineau, L. Simonin, J.-F.Colin, E. Canévet, L. Daniel, S. Patoux, Evolutions of $Li_{1.2}Mn_{0.61}Ni_{0.18}Mg_{0.01}O_2$ during the Initial Charge/Discharge Cycle Studied by Advanced Electron Microscopy. *Chemistry of Materials* 24 (2012) 3558-3566.

28. J. Lee, A. Urban, X. Li, D. Su, G. Hautier, G. Ceder, Unlocking the Potential of Cation-Disordered Oxides for Rechargeable Lithium Batteries. *Science* 343 (2014) 519-522.

29. D. Wang, I. Belharouak, G. Zhou, K. Amine, Nanoarchitecture Multi-Structural Cathode Materials for High Capacity Lithium Batteries. *Advanced Functional Materials* 23 (2013)1070-1075.

30. S. H. Kang, C. S. Johnson, J. T. Vaughey, K. Amine, M. M. Thackeray, The Effects of Acid Treatment on the Electrochemical Properties of $0.5Li_2MnO_3 \cdot 0.5LiNi_{0.44}Co_{0.25}Mn_{0.31}O_2$ Electrodes in Lithium Cells. *Journal of The Electrochemical Society* 153 (2006) A1186-A1192.

31. F. Amalraj, M. Talianker, B. Markovsky, D. Sharon, L. Burlaka, G. Shafir, E.Zinigrad, O. Haik, D. Aurbach, J. Lampert, M. S. Dobrick, A. Garsuch, Study of the Lithium-Rich Integrated Compound $xLi_2MnO_3 \cdot (1-x)LiMO_2$ (x around 0.5; M=Mn,Ni,Co;2:2:1) and Its Electrochemical Activity as Positive Electrode in Lithium Cells. *Journal of The Electrochemical Society* 160 (2012) A324-A337.

32. S. F. Amalraj, B. Markovsky, D. Sharon, M. Talianker, E. Zinigrad, R. Persky, O. Haik, J. Grinblat, J. Lampert, M. Schulz-Dobrick, A. Garsuch, L. Burlaka, D. Aurbach, Study of the Electrochemical Behavior of the "Inactive" Li_2MnO_3. *Electrochimica Acta* 78 (2012) 32-39.

33.G. B. Saupe, C. C. Waraksa, H. N. Kim, Y. J. Han, D. M. Kaschak, D. M. Skinner, T. E. Mallouk,Nanoscale Tubules Formed by Exfoliation of Potassium Hexaniobate. *Chemistry of Materials* 12 (2000) 1556-1562.

34. Y. Omomo, T. Sasaki, L. Wang, M. Watanabe, Redoxable Nanosheet Crystallites of MnO_2 Derived via Delamination of a Layered Manganese Oxide. *Journal of American Chemical Society* 12 (2003) 3568-3575.

35. Y. Kobayashi, H. Hata, M. Salama, T. E. Mallouk, Scrolled Sheet Precursor Route to Niobium and Tantalum Oxide Nanotubes. *Nano Letters* 7 (2007) 2142-2145.

36. E.J. Oh, T. W. Kim, K. M. Lee, M. S. Song, A. Y. Jee, S. T. Lim, H. W. Ha, M. Y. Lee, J. H. Choy, S. J. Hwang, Unilamellar Nanosheet of Layered Manganese Cobalt Nickel Oxide and Its Heterolayered Film with Polycations. *ACS Nano* 8 (2010) 4437-4444.

37. K. M. Lee, Y. R. Lee, I. Y. Kim, T. W. Kim, S. Y. Han, S. J. Hwang, Heterolayered Li^{+}–MnO_2–$[Mn_{1/3}Co_{1/3}Ni_{1/3}]O_2$ Nanocomposites with Improved Electrode Functionality: Effects of Heat Treatment and Layer Doping on the Electrode Performance of Reassembled Lithium Manganate. The *Journal of Physical Chemistry C* 116 (2012) 3311-3319.

38. Y. Yao, G. S. Chaubey, J. B. Wiley, Fabrication of Nanopeapods: Scrolling of Niobate Nanosheets for Magnetic Nanoparticle Chain Encapsulation. *Journal of The Amecian Chemical Society* 134 (2012) 2450-2452.

39. V. Nicolosi, M. Chhowalla, M. G. Kanatzidis, M. S. Strano, J. N. Coleman, Liquid Exfoliation of Layered Materials. *Science* 340 (2013)1226419-1-18.

40. M. G. Lazarraga, L. Pascual, H. Gadjov, D. Kovacheva, K. Petrov, J. M. Amarilla, R. M. Rojas, A. M. Martin-Luengo, J. M. Rojo, Nanosize $LiNi_yMn_{2-y}O_4$ ($0<y<=0.5$) Spinels Synthesized by a Sucrose-Aided Combustion Method. Characterization and Electrochemical Performance. *Journal of Materials Chemistry* 14 (2004)1640-1647.

41. C. M. Julien, K. Zaghib, Electrochemistry and Local Structure of Nano-Sized $Li_{4/3}Me_{5/3}O_4$ (Me=Mn, Ti) Spinels. *Electrochimica Acta* 50 (2004) 411-416.

42. C. V. Ramana, M. Massot, C. M. Julien, XPS and Raman Spectroscopic Characterization of $LiMn_2O_4$ Spinels. *Surface and Interface Analysis* 37 (2005) 412-416.

43. W. Choi, A. Manthiram, Influence of Fluorine Substitution on the Electrochemical Performance of 3 V Spinel $Li_4Mn_5O_{12-\eta}F_\eta$ Cathodes. *Solid State Ionics* 178 (2007) 1541-1545.

44. A. Vu, Y. Qian, A. Stein, Porous Electrode Materials for Lithium-Ion Batteries - How to Prepare Them and What Makes Them Special. *Advanced Engergy Materials* 2 (2012) 1056-1085.

45. J. Wang, Y. Li, X. Sun, Challenges and Opportunities of Nanostructured Materials for Aprotic Rechargeable Lithium-Air Batteries. *Nano Energy* 2 (2013) 443-467.

46. Q. Zhang, E. Uchaker, S. L. Candelaria, G. Cao, Nanomaterials for Energy Conversion and Storage. *Chemical Society Reviews* 42 (2013) 3127-3171.

CHAPTER 7. HIGH-CAPACITY FULL LITHIUM-ION CELLS BASED ON NANOARCHITECTURED TERNARY MANGANESE-NICKEL-COBALT CARBONATE AND ITS LITHIATED DERIVATIVE

7.1 Introduction

The rapid development of electronic devices and electric transportations requires energy conversion/storage systems that offer high energy and powder densities, long service life and assuring safety. Rechargeable lithium-ion battery is one of the most promising energy conversion and storage systems. However, current lithium-ion batteries suffer from limited specific capacity and poor rate performance of both anode and cathode materials [1-5]. For example, the theoretical capacity of graphite as traditional anode material is only 372 mAh/g, and the other drawback of graphite anode is low volumetric energy density [5]. On the other hand, cathode materials, such as layered $LiCoO_2$, $LiMn_{1/3}Co_{1/3}Ni_{1/3}O_2$, spinel $LiMn_2O_4$ and olivine $LiFePO_4$, typically deliver low practical capacities below 200 mAh/g with acceptable cycling stabilities [3,6]. Rate capability and operating voltage of current cathode materials are also far from performance demand for electric and hybrid electric vehicles and microminiaturization of electronic devices. Electrochemical performances of lithium-ion batteries critically rely on properties and characteristics of electrode materials, which are expected to provide high practical capacity, wide operating voltage range, excellent cycling stability, remarkable rate capability, and safety [5,7]. It is imperative to develop both alternative anode and cathode materials for superior lithium-ion batteries.

Transition metal carbonates MCO_3 (M=Mn, Co, Ni, etc.) can be used for lithium storage via a conversion reaction mechanism, in which active materials decompose into metals (M^0) and lithium carbonate (Li_2CO_3) in the process of lithiation and subsequently restore to the original phase upon delithiation. Such reversible transition allows transition metal carbonates to serve as anode materials in lithium-ion batteries [4,8-13]. Theoretical capacity of carbonate anodes can be calculated based on number of electrons and molar mass of transition metal M^0 according to the conversion reaction mechanism. For example, $MnCO_3$ and $CoCO_3$ can theoretically deliver maximum capacities of 466 and 451 mAh/g, respectively, equivalent to storage of two moles of lithium per mole of active material, which are significantly higher than that of graphite anode [8,12]. Formation of amorphous Li_2CO_3 matrix is not only favorable for releasing reaction strain during lithium intercalation/deintercalation processes but also restricts agglomeration of reduced metal particles, thus promises better cycling stability of carbonate anode materials [9].Transition metal carbonates as anode materials in lithium-ion batteries always show much higher practical capacity than the theoretical value, and three possible mechanisms were suggested accounting for this phenomenon. As reported in literature, Su et al. proposed an electrochemically catalytic conversion mechanism for lithium storage in $CoCO_3$ microcubes [12].The newly-formed Co nanoparticles in discharge reaction can act as electrochemical catalysis to realize reduction of C^{4+} in CO_3^{2-} anions to C^0 or other lower-valence C. In

subsequent charge process, oxidations of both Co^{2+}/Co^0 redox from transition metal and $C^{4+/}C^{(4-x)+}$ ($0<x<4$) redox from carbon material take place, contributing to the higher initial reversible capacity of $CoCO_3$ microcubes than 1000 mAh/g. Tirado's group also reported extra capacity delivered by submicron $MnCO_3$, which was assigned to non-Faradaic capacity, i.e., capacitive capacity contribution [9].Another reason for extra capacity from carbonate anodes can be referred to the similar phenomenon found in transition metal oxide anodes in MO/Li batteries (M = transition metals). Laruelle and co-workers stated that the origin of extra electrochemical capacity can be attributed to a reversible formation/dissolution of a polymeric gel-like film on the surface of oxide anodes during the conversion reaction [14]. Transition metal carbonates have shown good promises for use as anode materials in high-capacity lithium-ion batteries owning to its facile synthesis, high practical capacity and acceptable capacity retention. Another advantage of carbonate materials is that they can serve as versatile precursors for producing corresponding cathode materials. For example, lithiation of carbonate materials can yield conventional spinel $LiMn_2O_4$ and emerging high-capacity Li-excess layered cathode materials [15-17].

On the other hand, breakthroughs in the present lithium-ion battery technology focus on overcoming the limited reversible specific capacity and low operating voltage in cathode materials [2, 3]. In this regard, Li-excess layered cathode materials, $Li[Li,Mn,Ni,Co]O_2$, consisting of layered Li_2MnO_3 and $LiMO_2$ (M =Mn, Ni, and Co) components have become attractive since they offer significantly high operating voltage up to 4.8 V *vs.* Li/Li^+ and practical capacity larger than 250 mAh/g [18-30]. The high capacity of Li-excess layered cathodes is attributed to electrochemical activation of lithium-inactive Li_2MnO_3 component during the initial charge, in which inert Li_2MnO_3 decomposes into lithium-active MnO_2 and Li_2O via lithium ion extraction, accompanying with irreversible loss of oxygen from the lattice. Such activation process lowers the oxidation state of transition metal ions at the end of initial discharge, resulting in high capacity but also an undesirable irreversible capacity loss in the initial cycle. In despite of the high theoretical capacity, such Li-excess cathode materials exhibit unfavorable rate capability and cycling stability [19,31]. One representative in this category of cathode materials is $Li[Li_{0.2}Mn_{0.54}Ni_{0.13}Co_{0.13}]O_2$ (marked as LMNCO), which possesses a very high theoretical capacity of 321 mAh/g and wide operating voltage range between 2.0 and 4.8 V *vs.* Li/Li^+. LMNCO is composed of two components, lithium-inactive Li_2MnO_3 (space group *C2/m*) and lithium-active $LiMn_{1/3}Ni_{1/3}Co_{1/3}O_2$ (space group *R-3m*) at a molar ratio of 1:1, i.e., $0.5Li_2MnO_3 \cdot 0.5LiMn_{1/3}Ni_{1/3}Co_{1/3}O_2$ [19,32].

7.2 Objectives of Project

Battery performance depends on not only intrinsic characteristics but also the designed morphologies and structures of electrode materials. One approach to realize combination of high energy and high power in battery is to assemble high-capacity electrode materials in nanoarchitectures, which can provide efficient charge and

lithium ion transport, maximized electrochemical activity, and structural porosity and stability [7,23,33,34]. Among various synthetic approaches, solvothermal method is a very effective approach to tailor electrode materials in various morphologies and structures, such as spheres, cubes, urchin-like architecture, nanorods, nanowires, nanosheets, etc [12,35-41]. In this study, ternary transition metal carbonates are prepared in multi-shell spherical structure, which is composed of numerous primary nanoparticles. Such nanoarchitectured anode material reveals higher lithium storage capacity together with outstanding cycleability and rate capability in comparison with monodispersed solid carbonate spheres. Li-excess layered cathode material in yolk-shell structure can be further achieved from nanostructured carbonate after lithiation. Accordingly, yolk-shell-structured cathode material delivers much higher capacity and better high-rate performance in comparison with well-dispersed nanoparticles. For the first time, a full lithium-ion battery is constructed using nanostructured ternary manganese-nickel-cobalt electrode materials with carbonate compound as anode and Li-excess oxide as cathode, which demonstrates high practical capacity for advanced lithium-ion batteries.

7.3 Experimental Section

7.3.1 Synthesis of $Mn_{0.54}Ni_{0.13}Co_{0.13}(CO_3)_{0.8}$ carbonates and Li-excess $Li[Li_{0.2}Mn_{0.54}Ni_{0.13}Co_{0.13}]O_2$ oxides using solvothermal methods

$Mn_{0.54}Ni_{0.13}Co_{0.13}(CO_3)_{0.8}$ carbonates of different morphologies were synthesized via a solvothermal route using different solvents, i.e., distilled water and ethylene glycol, respectively. Urea (NH_2CONH_2) was used as the precipitant in this process. Six mmol transition metal acetates (a molar ratio of Mn^{2+}:Ni^{2+}:Co^{2+}=0.54:0.13:0.13) were dissolved in 10 ml solvent under continuous stirring at 40°C for 30 minutes, followed by adding 22.5 mmol urea. Additional solvent was replenished to form a total 15 ml solution. The resultant solution was transferred into a 23 ml Teflon container and placed within a sealed stainless steel autoclave (Parr, Inc.). Heat treatment of the autoclave was carried out in an oven at 200°C for 10 h. After cooling down to room temperature, the resultant powders were centrifuged and washed with distilled water for three times, and were collected after drying at 120°C in vacuum overnight. In order to obtain Li-excess $Li[Li_{0.2}Mn_{0.54}Ni_{0.13}Co_{0.13}]O_2$ oxide, 9 mmol lithium acetate was dissolved in solvent together with transition metal acetates and urea for the same solvothermal process. The whole mixture in Teflon container after heating was transferred to a beaker to completely evaporate the solvent at 80°C. $Li[Li_{0.2}Mn_{0.54}Ni_{0.13}Co_{0.13}]O_2$ was obtained after annealing the dried mixture at 500°C for 3 h at a temp. ramp of 1°C/min, followed by heating up to 900°C for 12 h at 5°C/min. Due to the use of two different solvents (distilled water and ethylene glycol), two carbonates in different morphologies and two corresponding Li-excess oxides in different morphologies are resulted, respectively.

7.3.2 Characterizations

Crystal structure of $Mn_{0.54}Ni_{0.13}Co_{0.13}(CO_3)_{0.8}$ carbonate and Li-excess $Li[Li_{0.2}Mn_{0.54}Ni_{0.13}Co_{0.13}]O_2$ powders were examined by X-ray diffraction (XRD) using a Rigaku MiniFlex X-ray diffractometer with Cu K_α radiation at a scan rate of 2^o/min. Morphology and size of the as-prepared particles were observed using a FEI Quanta 3D FEG field emission scanning electron microscopy (FESEM) after coating with Pt. Transmission electron microscopy (TEM) images were captured on a JEM-2010 instrument microscope at an acceleration voltage of 200 kV, to examine the structures of different samples.

7.3.3 Electrochemical measurements

The anode was composed of 70 wt.% $Mn_{0.54}Ni_{0.13}Co_{0.13}(CO_3)_{0.8}$ carbonate, 20 wt.% acetylene black (conductive carbon, Alfa Aesar, 99.5%), and 10 wt.% poly-vinylidenefluoride (PVDF, Alfa Aesar) as the binder. The cathode was composed of 80 wt.% $Li[Li_{0.2}Mn_{0.54}Ni_{0.13}Co_{0.13}]O_2$ particles, 10 wt.% acetylene black (conductive carbon, Alfa Aesar, 99.5%), and 10 wt.% poly-vinylidenefluoride (PVDF, Alfa Aesar) as the binder. As for half battery cell testing, carbonate anode or Li-excess oxide cathode was assembled into two-electrode CR2032-type coin cells for electrochemical measurements, with metallic lithium foil as the counter electrode, Celgard-2320 membrane as the separator. The electrolyte was 1 M $LiPF_6$ dissolved in ethylene carbonate (EC), dimethyl carbonate (DMC) and diethyl carbonate (DEC) at a volumetric ratio of 1:1:1. Chronopotentiometric (CP) charge and discharge were performed at various specific currents in a voltage range of 0.01 - 3.0 V *vs*. Li/Li^+ for carbonate anode and 2.0 - 4.8 V *vs*. Li/Li^+ for Li-excess oxide cathode using an 8-channel battery analyzer (MTI Corporation). Lithium storage capacities of working electrodes were calculated based on the mass of active anode or cathode materials. As for the full battery, $Mn_{0.54}Ni_{0.13}Co_{0.13}(CO_3)_{0.8}$ carbonate was used as anode in combination with $Li[Li_{0.2}Mn_{0.54}Ni_{0.13}Co_{0.13}]O_2$ oxide as cathode within a coin cell. The operating voltage range is set between 0.1 and 4.0 V. Cyclic voltammetric (CV) curves of both half and full batteries were recorded at a scan rate of 0.1 mV/s in corresponding voltage ranges using an electrochemical workstation (CHI 605C).

7.4 Results and Discussion

7.4.1 Synthesis and characterization of $Mn_{0.54}Ni_{0.13}Co_{0.13}(CO_3)_{0.8}$ carbonates in different morphologies and subsequently derived Li-excess $Li[Li_{0.2}Mn_{0.54}Ni_{0.13}Co_{0.13}]O_2$ oxides in different structures

Figure 7.1 presents schematics illustrating two different synthetic processes to obtain ternary transition metal carbonates (the molar ratio of Mn:Ni:Co=0.54:0.13:0.13) of different morphologies by using a solvothermal method. In these processes, differences in the polarity of solvents (distilled water and ethylene

glycol) may induce self-assembly of transition metal cations and acetate anions into different structures during heating under high pressure in the autoclave. The acetate anions act like the surfactant to assemble transition metal cations in different solvents. As illustrated in the upper synthetic route, transition metal acetates prefer to assemble linearly in aqueous solution, since organic CH_3- groups at the outmost top of acetate anions are hydrophobic, and thus they tend to attract each other in distilled water. Such assembly leads to distinct arrangement of transition metal cations within water-based solvent. In contrast, because ethylene glycol has a polarity similar to organic chains (CH_3COO) in acetate anions, as shown in the lower synthetic route, CH_3COO ions are apt to stretch towards the surrounding ethylene glycol solvent, resulting in transition metal cations encapsulated within acetate anions. Subsequent precipitation of transition metal cations to form carbonate compound is attributed to decomposition of urea, which can release carbonate anions at elevated temperature in the autoclave [12].

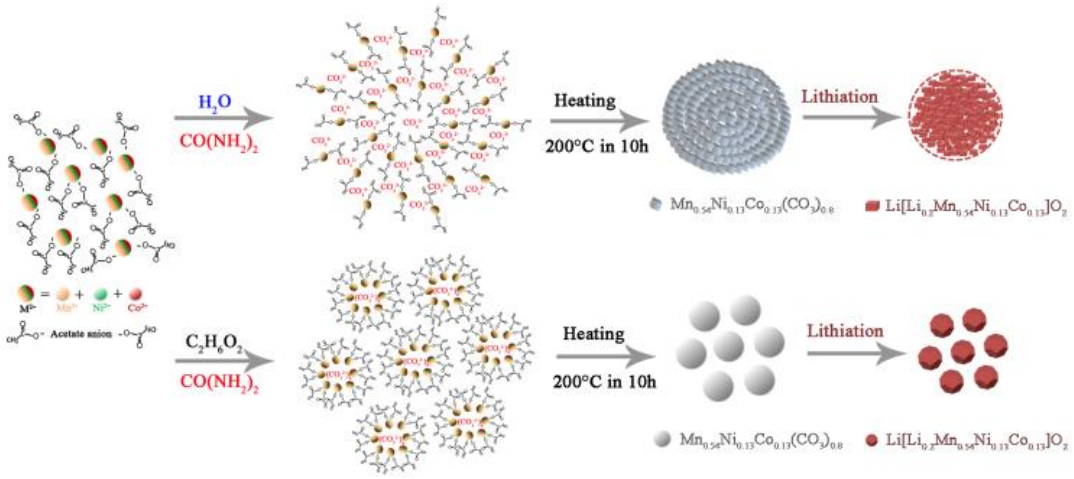

Figure 7.1 Schematics showing solvothermal growth of ternary manganese-nickel-cobalt carbonate compound and subsequent Li-excess oxide in nanoarchitecture (upper synthetic route) and in the form of solid spheres (lower synthetic route) using different solvents, distilled water and ethylene glycol, respectively. Urea can release CO_3^{2-} anions to react with transition metal cations. The upper reaction mechanism yields multi-shell spherical carbonate ($MNCCO_3$ MS) and yolk-shell Li-excess oxide (LMNCO YS) after lithiation, and the lower route produces monodispersed solid spherical carbonate ($MNCCO_3$ SS) and Li-excess oxide nanoparticles (LMNCO NP).

As a result, carbonate materials of different morphologies are obtained via using distilled water or ethylene glycol as the solvent, respectively: carbonate resulted from water-based solution shows multi-shell spherical structure composed of numerous cuboid-shaped carbonate particles (marked as $MNCCO_3$ MS), while the ethylene-glycol-based solution yields carbonate in the form of monodispersive solid spheres (marked as $MNCCO_3$ SS). Carbonates can be used as the precursor to prepare corresponding Li-excess layered oxides through lithiation during calcinations.

Decomposition of carbonates causes the release of a large amount of CO_2 gas during lithiation, which may account for distinct morphology and structure changes in lithiated oxides in comparison with the original carbonates [11]. Lithiation of multi-shell spherical structure of $MNCCO_3$ MS leads to yolk-shell-structured Li-excess oxide (marked as LMNCO YS), while monodispersive $MNCCO_3$ SS results in well-dispersed Li-excess oxide nanoparticles (marked as LMNCO NP).

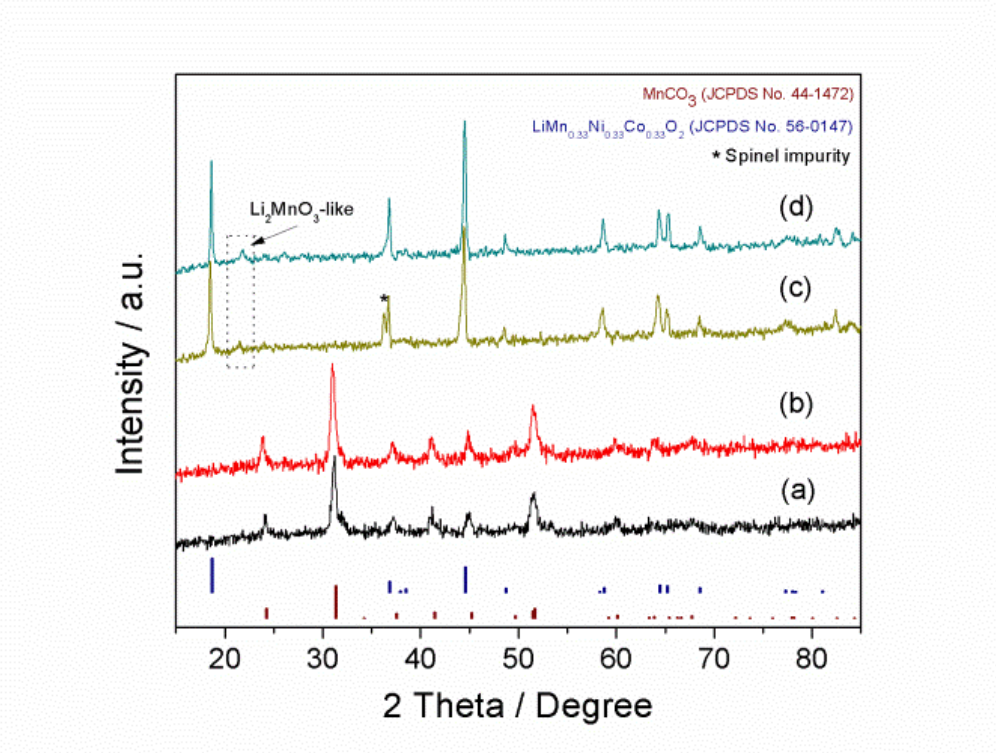

Figure 7.2 XRD patterns of (a) $MNCCO_3$ MS, (b) $MNCCO_3$ SS, (c) LMNCO YS and (d) LMNCO NP.

Figure 7.2 reveals XRD patterns of the as-prepared carbonates and corresponding Li-excess oxides. All major XRD peaks of $MNCCO_3$ MS and $MNCCO_3$ SS are identical; both can be indexed to Rhodochrosite $MnCO_3$ in a space group of *R-3c* (JCPDS #. 44-1472), but have slight shifts to the larger diffraction angle due to nominal cobalt and nickel substitutions [9]. No impurity phases, such as transition metal oxides (M_xO_y) and hydroxides ($M(OH)_2$) (M=Mn, Co and Ni) are detected. XRD characterizations indicate that changing the solvent in the solvothermal method affects morphology and microstructure/nanostructure of ternary manganese-nickel-cobalt carbonate but has little effect on its elemental composition and crystal phase. However, when transition metal carbonates of different morphologies react with the same lithium precursor to form Li-excess oxides, one impurity with spinel-like crystal structure is detected in LMNCO YS sample (a peak marked with asterisk at $2\theta = 36 - 37^0$ in XRD pattern in Figure 8.2(c) [24], while LMNCO NP shows higher purity in layered crystal phase. Formation of spinel-like phase in LMNCO YS may possibly be attributed to more difficult diffusion of lithium ions into the center of $MNCCO_3$ MS through multiple shells during lithiation than

diffusing in the entire bulk of $MNCCO_3$ SS sphere. Except this extra XRD peak in LMNCO YS, XRD patterns of two lithiated oxides are consistent, in good agreement with that of Li-excess layered cathode materials reported in literature [19,31]. The presentence of weak peaks at $2\theta = 20 - 22^{\circ}$ (enclosed in a rectangle in dashed lines) in the XRD patterns of LMNCO YS and LMNCO NP (Figure 7.2(c) and (d)) can be attributed to the existence of Li_2MnO_3 component, in which Li^+ and Mn^{4+} cations are integrated in the transition metal layers in $LiMn_{1/3}Ni_{1/3}Co_{1/3}O_2$ component, indicating the lithium-rich characteristics of both samples [42]. In summary, XRD patterns clearly show formations of ternary transition metal carbonates and corresponding Li-excess oxides.

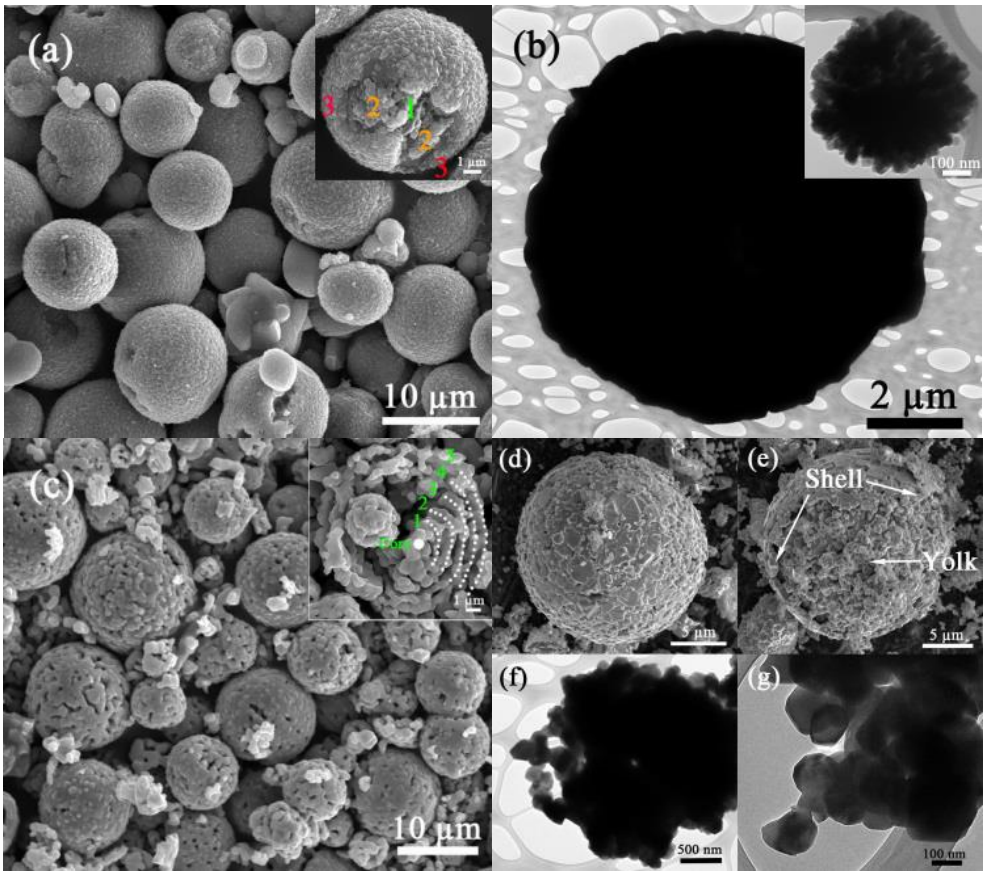

Figure 7.3 Morphology and structure of nanostructured ternary transition metal carbonate compound and its derivatives: (a) SEM image and (b) TEM image of $MNCCO_3$ MS; (c) SEM image of cage-like derivative after sintering $MNCCO_3$ MS in air at 900°C for 12 h; (d) and (e) SEM images, and (f) and (g) TEM images of LMNCO YS after lithiation of $MNCCO_3$ MS.

Figure 7.3a and 3b display morphological and structural characteristics of nanoarchitectured carbonate ($MNCCO_3$ MS), which is prepared via the upper synthetic route in Figure 7.1 by using distilled water as the solvent. It is found that concentration of transition metal acetates, reaction temperature and heating time can significantly affect morphology, particle size and particle size distribution of ternary

transition metal carbonate products in a solvothermal process. As shown in Figure 7.3a and 3b, $MNCCO_3$ MS carbonate can be tailored into regular spherical shape with a diameter in the range of 5-10 μm. Individual carbonate sphere with a micron size is assembled by numerous primary nanoparticles when all transition metal cations react with carbonate anions, yielding precipitated carbonate products in aqueous solution in formation of multiple shells and rough surface of $MNCCO_3$ MS (Figure 7.1). Since TEM technique has its limitations on studying detailed structures of micron-sized specimens and a few smaller carbonate spheres with submicron size do exist in the final $MNCCO_3$ MS product, we observe the distinct structure of carbonate compound from a smaller sphere as inserted in Figure 7.3b, which clearly demonstrates the nanofabrication of $MNCCO_3$ MS. Moreover, a broken sphere shown in the inset image of Figure 7.3a reveals at least three internal shells which are labelled by number 1, 2, 3, within the hierarchical structure. In order to confirm this multi-shell nanoarchitecture, carbonate microspheres are sintered at a very high temperature of 900°C in air for 12 h, resulting in porous cage-structured derivative. As shown in Figure 8.3c, the spherical shape of each microsphere is fully preserved after sintering, though carbonate material is completely decomposed to oxide and CO_2 during calcination [11], indicating structural integrity and solidness of ternary transition metal carbonate. One representative cross-section view of the cage-like derivative is inserted in Figure 7.3c. The distinctive multi-shell morphology is well retained from original nanoarchitectured $MNCCO_3$ MS after heat treatment, in which the core is hierarchically encapsulated by five shells from the center to the outmost. Hence, multi-shell structure of ternary transition metal carbonate has been validated, similar to core-shell-structured $Ni_{0.25}Mn_{0.75}CO_3$ reported in literature [16].

The nanostructured transition metal carbonate has been demonstrated as a favorable template and precursor to prepare corresponding Li-containing oxides with retained morphology and structure [15,17]. In order to achieve similarly nanoarchitectured Li-excess $Li[Li_{0.2}Mn_{0.54}Ni_{0.13}Co_{0.13}]O_2$ oxide, lithium acetate as lithium source is directly introduced in the solvothermal process with the same procedure for preparing $Mn_{0.54}Ni_{0.13}Co_{0.13}(CO_3)_{0.8}$ carbonate. However, Li-excess oxide cannot be directly obtained after solvothermal treatment, only yielding a mixture of carbonate spheres and Li^+-contained solution. The lithiated $Li[Li_{0.2}Mn_{0.54}Ni_{0.13}Co_{0.13}]O_2$ can only be formed after drying and sintering the resultant mixture. As a result, Li-excess oxide preserves spherical shape as shown in Figure 7.3d, but also shows some collapsed structure, which may be attributed to particle growth and further volumetric expansion during lithiation. It is interesting to find that yolk-shell structure in LMNCO YS is achieved after lithiation of $MNCCO_3$ MS in multi-shell nanoarchitecture. SEM image in Figure 7.3e and TEM image in Figure 7.3f reveal a yolk-shell structure, in which the shell is composed of slab-shaped particles and the yolk is composed of numerous nanoparticles in smaller particle size of ~200 nm (Figure 7.3g). As arrowed in Figure 7.3e, a broken LMNCO YS sphere clearly reveals the yolk structure inside and the broken shell outside in the hierarchical structure.

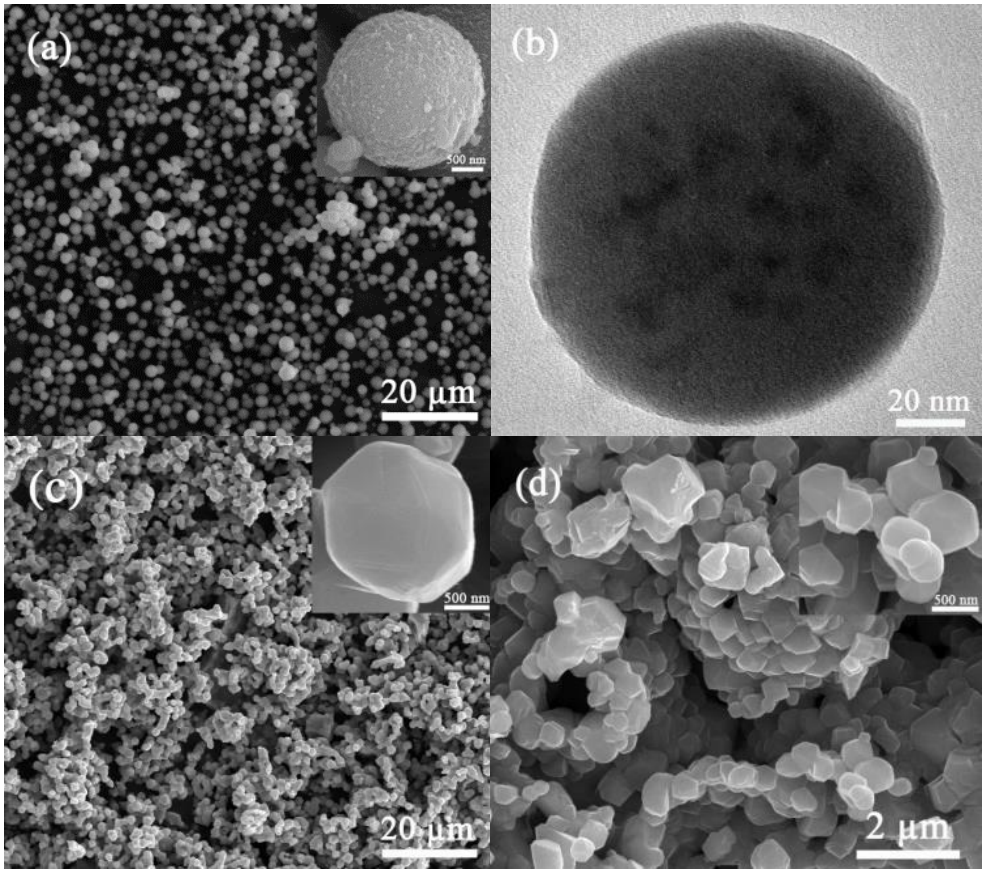

Figure 7.4 Morphology and structure of monodispersed ternary transition metal carbonate microspheres and its derivatives: (a) SEM image and (b) TEM image of $MNCCO_3$ SS; (c) SEM image of well-dispersed derivative after sintering $MNCCO_3$ SS in air at 900°C in 12 h; (d) SEM image of LMNCO NP after lithiation of $MNCCO_3$ SS.

For comparison purpose, monodispersive solid microspheres of carbonate and corresponding Li-excess nanoparticles are also prepared via replacing distilled water with ethylene glycol as the solvent in the solvothermal synthesis (the reaction row in the lower part of Figure 7.1). Although XRD characterizations have proved the same crystal phase in $MNCCO_3$ SS and $MNCCO_3$ MS, they show different morphological features. Figure 7.4a presents the evidently monodispersive carbonate microspheres. The inserted SEM image showing individual sphere in Figure 7.4a reveals that $MNCCO_3$ SS carbonate has a very uniform diameter of ~2 µm, indicating better particle size distribution in comparison with nanoarchitectured $MNCCO_3$ MS (Figure 7.3a). As aforementioned in Figure 7.3b, a smaller sphere is chosen for TEM observation. TEM image in Figure 7.4b reveals the solidity of individual $MNCCO_3$ SS sphere. Accordingly, as shown in Figure 7.4c, such solid structure is retained after $MNCCO_3$ SS is subject to sintering at 900°C in air for 12h, yielding well-dispersed derivatives (Figure 7.4c). In contrast, as shown in Figure 7.4d, lithium-richened lithiation of $MNCCO_3$ SS microspheres results in irregular morphology and agglomeration of Li-excess nanoparticles to some extent, due to the decomposition of

carbonate materials during calcination without the favorable structure-retaining effect from the nanoarchitecture discussed above. LMNCO NP displays an average particle size around 500 nm, larger than nanoparticles in the core of LMNCO YS.

7.4.2 Electrochemical evaluation of $Mn_{0.54}Ni_{0.13}Co_{0.13}(CO_3)_{0.8}$ carbonate as lithium-ion battery anode material via half battery cell testing

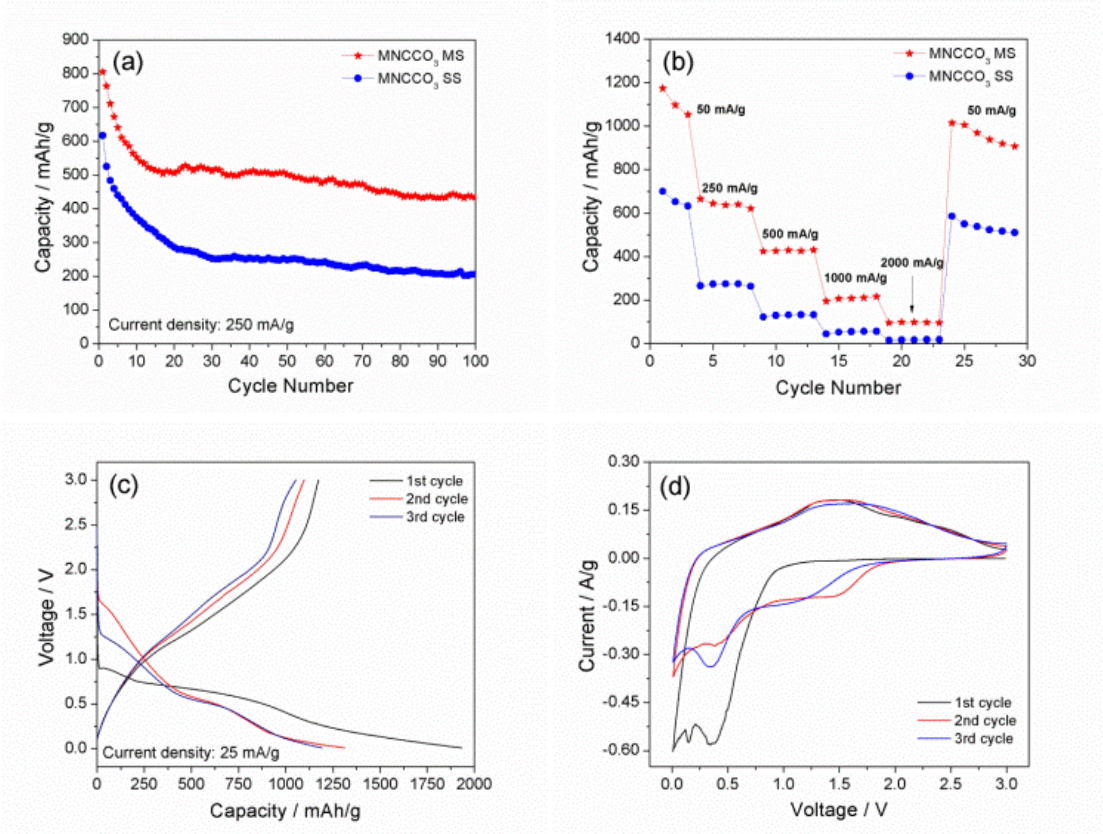

Figure 7.5 Electrochemical performances of $MNCCO_3$ MS and $MNCCO_3$ SS as lithium-ion battery anode materials during half battery cell testing with lithium metal as the counter electrode in a voltage range of 0.01-3.0 V *vs.* Li/Li^+: (a) cycling performance at a specific current of 250 mA/g, and (b) rate capability at various specific currents. CP and CV curves of $MNCCO_3$ MS: (c) CP discharge and charge curves in the first three cycles at a specific current of 25 mA/g, and (d) CV curves in the first three cycles at a scan rate of 0.1 mV/s.

Transition metal carbonates have been demonstrated as high-capacity anode materials for lithium-ion batteries, due to its ability in lithium storage via the conversion reaction similar to metal oxides but with lower molecular weight for larger capacity [9,12,13]. In order to improve electrochemical performance of carbonate anodes, we have prepared nanostructured ternary $Mn_{0.54}Ni_{0.13}Co_{0.13}(CO_3)_{0.8}$ carbonate compounds (Figure 7.3a and 3b). The beneficial effect of nanoarchitectures on electrochemical performance of ternary transition metal carbonates has been studied in comparison with solid microspheres of carbonate (Figure 7.4a and 4b). Figure 7.5

shows electrochemical performances of manganese-nickel-cobalt carbonate compounds as anode materials in a lithium-ion half battery testing with lithium metal foil as the counter electrode. Theoretical capacity of $Mn_{0.54}Ni_{0.13}Co_{0.13}(CO_3)_{0.8}$ for lithium storage can be calculated as 461 mAh/g based on the molar ratio of $MnCO_3$ (466 mAh/g), $CoCO_3$ (451 mAh/g), and $NiCO_3$ (451 mAh/g). Figure 7.5a and 5b demonstrate much better cycling stability and rate capability of multi-shell- structured carbonate anode than monodispersive solid carbonate spheres. Although both carbonate anodes show higher specific capacity than its theoretical capacity when cycled at a specific current of 250 mA/g, $MNCCO_3$ MS delivers an initial charge capacity of 806.2 mAh/g, much higher than 617.4 mAh/g from $MNCCO_3$ SS (Figure 7.5a); the capacity higher by 188.8 mAh/g from $MNCCO_3$ MS is probably attributed to its nanoarchitecture. As shown in Figure 7.3a-3c, the multi-shell $MNCCO_3$ MS is structurally robust and porous. Such nanoarchitecture is favorable for accommodating extra lithium ions, restricting agglomeration of active materials, and stabilizing the working electrode, and thus contributes to higher capacity and better cycleability in comparison with monodispersive micron-sized $MNCCO_3$ SS spheres. Additionally, the effect of nanoarchitectured structure on enhancing rate performance of carbonate anodes is more phenomenal when they are cycled at high specific currents (Figure 7.5b).

The charge/discharge curves and CV profiles in initial three cycles are shown in Figure 7.5c and 5d, respectively, for studying electrochemical behavior of $MNCCO_3$ MS in details. At a low specific current of 25 mA/g, $MNCCO_3$ MS shows high initial discharge and charge capacities of 1932.2 and 1173.1 mAh/g, more than twice its theoretical capacity and also higher than the reported capacities for $MnCO_3$ [8,11], $CoCO_3$ [12] and $Mn_xCo_{1-x}CO_3$ [9]. As mentioned before, there are three main capacity contributions for transition metal carbonate anodes: Faradic capacity (practical capacity from reduction and oxidation of transition metal and/or other redox pairs within the conversion reaction) [12], non-Faradic capacity (capacitive capacity, such as capacity contribution from electrical double layer and pores via reversible absorption and desorption of lithium ions, etc.) [11], and extra capacity caused by reversible formation and dissolution of a gel-like polymer film on the surface of anode materials during lithiation and delithiation [14]. In the case of multi-shell-structured carbonate material, its extremely high capacity can be attributed to Faradic capacity delivered by transition metal redox pairs and additional lithium storage capacity from the as-formed gel-like polymer film on the surface of carbonate anode during electrochemical cycling. The large irreversible capacity loss in the initial cycle is mainly ascribed to the decomposition of electrolyte and formation of solid-electrolyte interphase (SEI) film on the surface of anodes. $MNCCO_3$ MS shows improved reversibility in the subsequent second and third electrochemical cycles (Figure 7.5c) and tends to stabilize after ten cycles (Figure 7.5a).

The apparent profile changes of CV curves in initial three cycles indicate the conversion reaction of ternary $Mn_{0.54}Ni_{0.13}Co_{0.13}(CO_3)_{0.8}$ carbonate with multi-shell structure, consistent with changes in charge/discharge curves. The first cathodic peak at 0.35 V in the initial CV pattern can be attributed to the reduction of transition metal

ions (M^{2+}, M=Mn, Ni and Co) to the metallic state M^0 in carbonate compound, accompanying with the formation of amorphous Li_2CO_3 matrix [11]. The inevitable decomposition of electrolyte and formation of SEI film contribute to the other broad cathodic peak below 0.25 V. The appearance of a small but sharp peak at 0.15 V is not very clear, possibly due to the reduction of $C^{4+}/C^{(4-x)+}$($0<x<4$) redox within carbonate anions trigged by the newly-formed M^0 as reported by Su and co-workers [12]. In the subsequent oxidation process, two broad anodic peaks at 0.25 and 1.45 V correspond to oxidations of $C^{(4-x)+}$ ($0<x<4$) and M^0, respectively. The cathodic CV curves in the second and third electrochemical cycles are obviously different from those in the initial CV curve. We speculate that ternary carbonate compound can be separate into three components: $MnCO_3$, $NiCO_3$ and $CoCO_3$, after initial charge/discharge. Due to different potentials of Mn^{2+}/Mn^0, Ni^{2+}/Ni^0, and Co^{2+}/Co^0 redox pairs, reductions of different transition metal ions take place in different voltage ranges, which may also result in different profiles of charge/discharge curves in the first three cycles in Figure 7.5c. In the second CV cycle, the first cathodic reaction occurs between 1.0 and 1.9 V, corresponding to the combined effect from reductions of Ni^{2+}/Ni^0 and Co^{2+}/Co^0 redox, which is consistent with the slope in the second discharge curve at higher voltage. Reduction of Mn^{2+} to Mn^0 results in the second cathodic peak in the voltage range of 0.3 - 0.6 V, followed by continuous formation of SEI film and negligible reversible reaction from $C^{4+}/C^{(4-x)+}$($0<x<4$) redox. In the third cycle, Mn^{2+}/Mn^0 redox contributes to the main discharge capacity owing to its highest fraction in the mixture of transition metal carbonates, which can be seen from increased current density of cathodic peak at 0.35 V in CV profile in comparison with that in the second cycle. The CV features from the second and third oxidation processes are almost identical, indicating acceptable cycling stability of carbonate anodes after the initial cycle. Overall, ternary manganese-nickel-cobalt carbonate compound in multi-shell spherical structure shows high practical capacity, desirable cycleability and rate capacity in comparison with monodispersive carbonate, which can be considered as a promising anode material for high-energy lithium-ion batteries. Another advantage of transition metal carbonate is that they can serve as a versatile precursor for preparing oxides as anode materials and lithium-containing cathode materials via lithiation. The converted ternary transition metal oxide as anode material for lithium-ion batteries will be published elsewhere, and the derived Li-excess oxide as cathode material is discussed below.

7.4.3 Electrochemical evaluation of Li-excess $Li[Li_{0.2}Mn_{0.54}Ni_{0.13}Co_{0.13}]O_2$ as lithium-ion battery cathode material via half battery cell testing

Li-excess $Li[Li_{0.2}Mn_{0.54}Ni_{0.13}Co_{0.13}]O_2$ oxide can be facilely achieved after lithiation of $Mn_{0.54}Ni_{0.13}Co_{0.13}(CO_3)_{0.8}$ carbonate via heat treatment in air. XRD patterns in Figure 7.2 have confirmed layered structure and Li-rich characteristics of $Li[Li_{0.2}Mn_{0.54}Ni_{0.13}Co_{0.13}]O_2$. SEM and TEM images show the mostly retained morphology and structure from nanoarchitectured carbonate compound, resulting in yolk-shell-structured LMNCO YS (Figure 7.3) and monodispersive LMNCO NP nanoparticles (Figure 7.4). Figure 7.6 illustrates electrochemical performance of

Li-excess layered $Li[Li_{0.2}Mn_{0.54}Ni_{0.13}Co_{0.13}]O_2$ cathode materials in lithium-ion half batteries with lithium metal as anode. It can be seen that yolk-shell-structured Li-excess layered cathode material shows better cycling and high-rate performance than well-dispersed nanoparticles of Li-excess layered material.

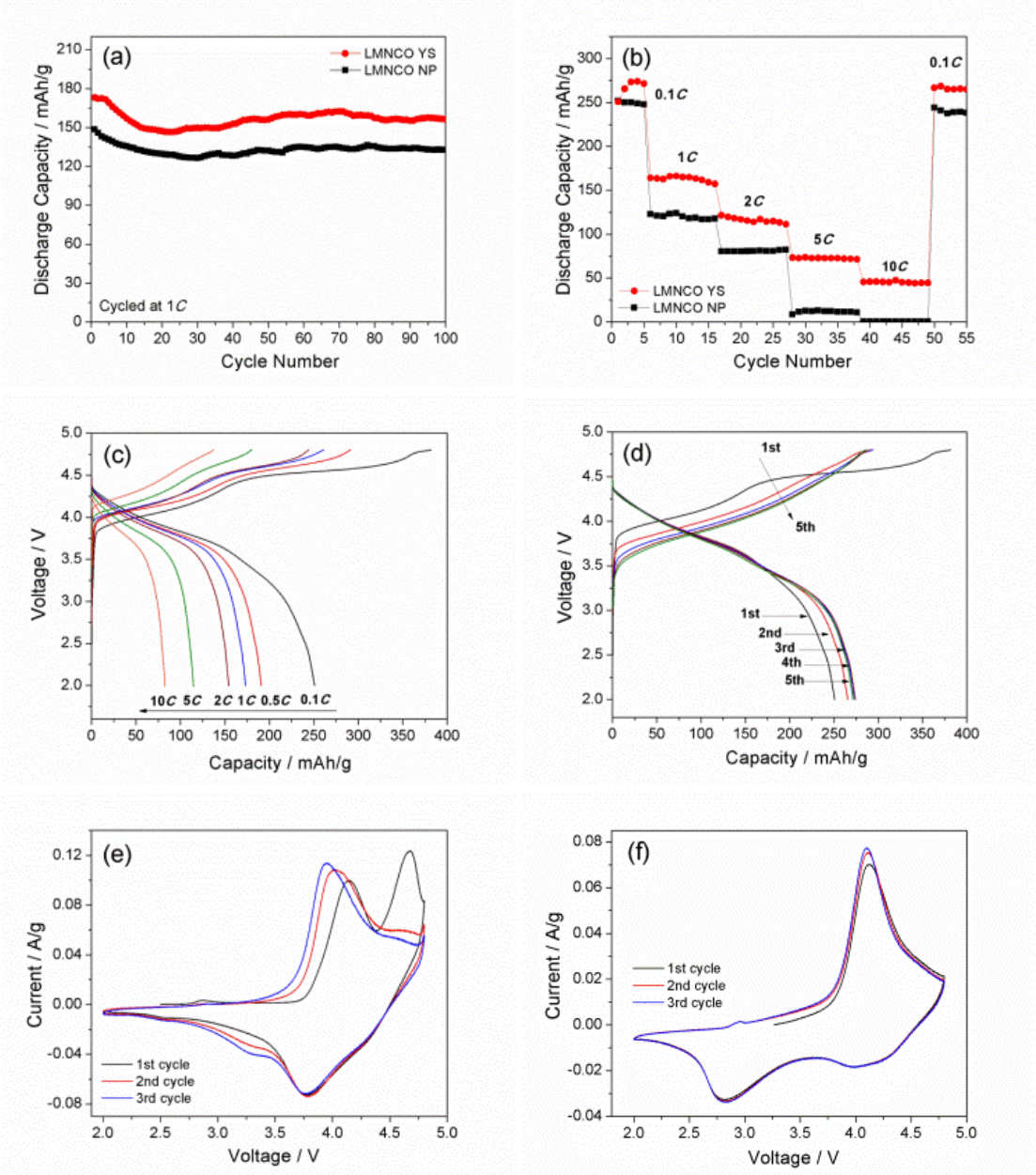

Figure 7.6 Electrochemical performances of LMNCO YS and LMNCO NP as lithium-ion battery cathode materials during half battery cell testing with lithium metal as counter electrode in a voltage range of 2.0-4.8 V *vs.* Li/Li^+: (a) cycling performance at 1*C* (1*C* = 250 mA/g) and (b) rate capability at various *C* rates. CP and CV curves of LMNCO YS: (c) initial discharge and charge curves at various *C*-rates, (d) discharge and charge curves in the first five cycles at 0.1 *C*, and CV curves in the first three cycles of (e) pristine cathode and (f) cycled cell after 100 electrochemical cycles at 0.5 *C* at a scanning rate of 0.1 mV/s.

As shown in Figure 7.6a, LMNCO YS delivers an initial discharge capacity of 170.0 mAh/g and retains 156.3 mAh/g at 1 *C* (1*C* = 250 mA/g) after 100 cycles, higher than 148.6 and 132.7 mAh/g in LMNCO NP, respectively. Although these two cathodes show the similar outstanding capacity retention of ~90%, nanoarchitectured LMNCO YS may offer more volume accommodation and larger contact area between cathode material and electrolyte than dispersed LMNCO nanoparticles. The effect of nanoarchitecture on enhancing rate capability of Li-excess cathode material is more distinct as shown in Figure 7.6b. In comparison with poor rate performance of LMNCO NP, LMNCO YS exhibits much better rate capability up to 10 *C*, and better electrochemical performance is also observed in nanoarchitectured carbonate anode.
Figure 6c exhibits initial charge/discharge curves of LMNCO YS cathode at different specific currents, showing specific discharge capacities of 250.7, 190.7, 173.0 154.2, 114.4 and 80.9 mAh/g at 0.1, 0.5, 1, 2, 5 and 10 *C*, respectively. More details can be found from Figure 7.6d-6e when Li-excess cathode material with hierarchical yolk-shell structure is subject to chronopotentiometric (CP) charge/discharge at a low specific current of 0.1 *C* and cyclic voltammetric (CV) measurement at a scan rate of 0.1 mV/s. As shown in Figure 7.6d, the initial charge/discharge profile is different from that of subsequent cycles, which can be attributed to the initial electrochemical activation of lithium-inactive Li_2MnO_3 component [32], contributing to a capacity higher than 250 mAh/g at the corresponding discharge. Initial activation of Li-excess layered cathode material can lead to oxygen loss and lithium vacancies in layered structure and consequent phase transition from a layered to a spinel phase due to transition metal migrations during electrochemical cycles. Whether this phase transformation is favorable for improving cycleability and rate capability of Li-excess layered cathode materials or not [24,43], nanostructured Li-excess cathode material has demonstrated enhanced electrochemical performance in comparison with nanoparticles (Figure 8.6a and 6b). The charge/discharge curves from the second to the fifth cycle indicate increased capacities with better reversibility, which can probably be attributed to complete penetration of electrolyte to immerse all nanoparticles in yolk component in LMNCO YS. The identical curve patterns between the fourth and the fifth cycle reveal actual discharge capacity of yolk-shell $Li[Li_{0.2}Mn_{0.54}Ni_{0.13}Co_{0.13}]O_2$ higher than 270 mAh/g after the initial electrochemical activation.

CV records of the first three cycles in Figure 7.6e show consistent responses compared to CP charge/discharge curves in Figure 7.6d. Two anodic peaks at 4.15 and 4.65 V are observed in the initial cycle, respectively, in good agreement with two voltage plateaus in the first CP charge curve. The first anodic peak corresponds to the oxidation of Ni^{2+} to Ni^{4+}, followed by Co^{3+} to Co^{4+}, whereas Mn remains as tetravalent in $LiMn_{1/3}Ni_{1/3}Co_{1/3}O_2$ component.[31] No CV response is from the impure phase in LMNCO YS as detected in XRD characterization (Figure 7.2). The second peak at 4.65 V is associated with the electrochemical activation of Li_2MnO_3, along with the unavoidable decomposition of electrolyte and formation of SEI film at such high voltage > 4.5 V. The corresponding reductions of Ni^{4+}/Ni^{3+}, Ni^{3+}/Ni^{2+} and Co^{4+}/Co^{3+} redox pairs occur at 3.78 V in subsequent discharge process. After initial activation of LMNCO YS, the anodic peak at 4.65V disappears in the second and

third CV cycle. The anodic peak related to the oxidation of Ni^{3+}/Ni^{2+} Ni^{4+}/Ni^{3+}, and Co^{4+}/Co^{3+} redox shifts to the lower voltage at 3.95 V in the third cycle, and cathodic peaks in the three cycles are completely overlapped. Such electrochemical behaviors in CV measurements indicate improved cyclic reversibility, which is again consistent with charge/discharge curves in Figure 7.6d. The continuous growth of broad cathodic peak around 3.3 V is due to the contribution from activated Mn^{4+}/Mn^{3+} redox from inert Li_2MnO_3 component. In order to evaluate effects from phase transition on electrochemical performance of Li-excess layered cathode materials, we record CV curves after LMNCO YS was cycled for 100 cycles at 0.5 *C*. The CV profiles and cycling performance before CV is taken are shown in Figure 7.6f and Figure 7.7, respectively.

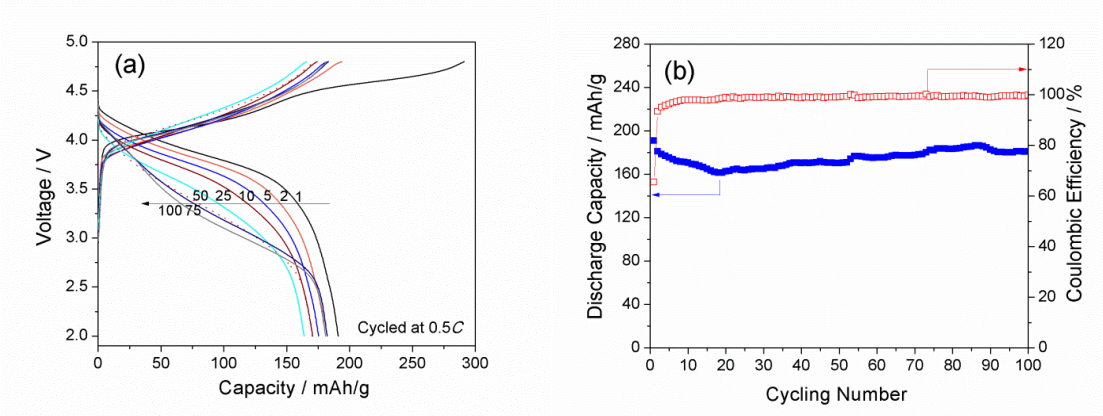

Figure 7.7 Cycling performance of yolk-shell-structured Li-excess $Li[Li_{0.2}Mn_{0.54}Ni_{0.13}Co_{0.13}]O_2$ as lithium-ion battery cathode material in half battery testing with lithium metal as the counter electrode at 0.5 *C* (1*C*=250 mA/g) in a voltage range of 2.0-4.8 V *vs*. Li/Li^+: (a) charge and discharge curves at the 1, 2, 5, 10, 25, 50, 75 and 100^{th} cycle, and (b) capacity retention and Coulombic efficiency as a function of cycle number.

In comparison with CV patterns in Figure 7.6e recorded from the pristine cathode, electrochemical cycles have induced a phase transition and consequent formation of spinel phase from original layered phase. An apparent pair of broad cathodic peak and weak anodic peak appears around 2.80 V, which is a typical feature resulted from reduction and oxidation of Mn^{4+}/Mn^{3+} redox of newly-formed spinel phase within Li-excess layered cathode [22]. As displayed in Figure 7.7a, changes of charge/discharge curves at the 1, 2, 5, 10, 25, 50, 75 and 100^{th} cycle correspond to such phase transition. The unique spinel characteristics can be obviously observed after 50 cycles, and actually it compensates the capacity loss resulted from the gradual degradation of layered structure in LMNCO YS during cycling performance (Figure 7.7b); hence, we tend to conclude that phase transition from original layered phase to spinel phase within parent layered structure helps to improve the capacity retention of Li-excess layered cathode materials. In summary, such desirable cycleabilitiy and rate

capability of LMNCO YS cathode material can be attributed to its yolk-shell nanoarchitecture and additional capacity contribution resulted from layered-to-spinel phase transition during electrochemical cycling.

7.4.4 Electrochemical performance of a lithium-ion full battery cell consisting of $Mn_{0.54}Ni_{0.13}Co_{0.13}(CO_3)_{0.8}$ anode and $Li[Li_{0.2}Mn_{0.54}Ni_{0.13}Co_{0.13}]O_2$ cathode

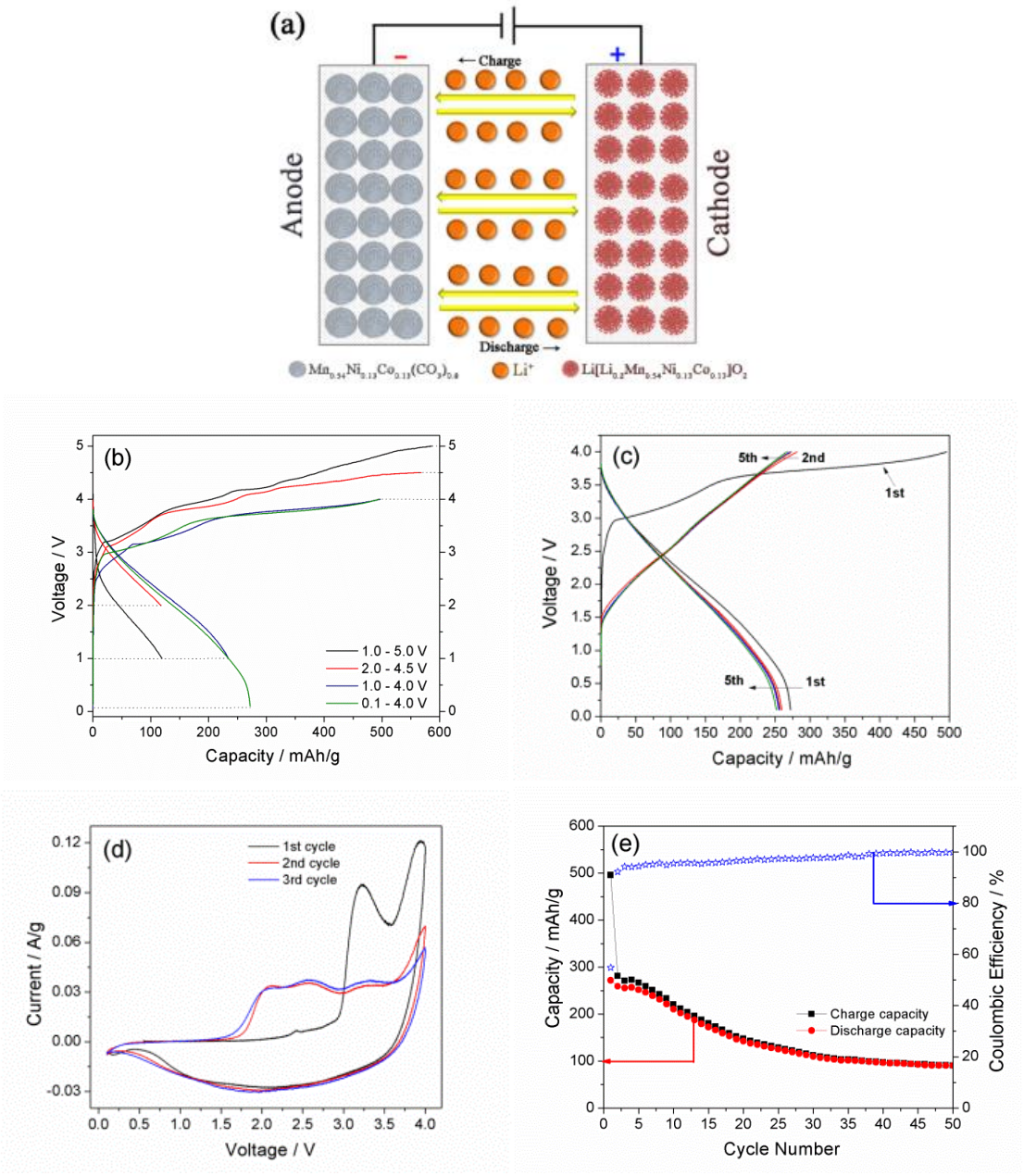

Figure 7.8 Electrochemical performance of a full lithium-ion battery with $MNCCO_3$ MS as anode and LMNCO YS as cathode: (a) schematic diagram of the full battery cell, (b) initial charge and discharge curves in various voltage ranges, and (c) charge and discharge curves in the first five cycles at a specific current of 0.1 *C*, (d) CV curves in the first three cycles at a scan rate of 0.1 mV/s and (d) cycling performance at 0.1 *C* in a voltage range of 0.1-4.0 V.

As both nanoarchitectured carbonate anode and Li-excess layered cathode demonstrate excellent electrochemical performances in half battery testing, we assembly them into a full lithium-ion battery as shown in Figure 8.8a, in which yolk-shell $Li[Li_{0.2}Mn_{0.54}Ni_{0.13}Co_{0.13}]O_2$ serves as cathode material and multi-shell $Mn_{0.54}Ni_{0.13}Co_{0.13}(CO_3)_{0.8}$ as anode material. It should be noted that the capacity of a full lithium-ion battery is limited by the cathode since cathode usually has much lower capacity than anode material, and charge/discharge rate of 1 *C* for the full battery is also equal to 250 mA/g as in the case of $Li[Li_{0.2}Mn_{0.54}Ni_{0.13}Co_{0.13}]O_2$ cathode. The compatibility of voltage range between Li-excess cathode (2.0 - 4.8 V *vs*. Li/Li^+) and transition metal anode (0.01 - 3.0 V *vs*. Li/Li^+) is very critical for achieving acceptable electrochemical performance in a full lithium-ion battery. The voltage range can be optimized between 0.1 and 4.0 V in comparison with other selected voltage cut-offs. Figure 7.8b compares initial charge/discharge curves in different voltage ranges of 0.1 - 4.0 V, 1.0 - 4.0 V, 2.0 - 4.5 V, and 1.0 - 5.0 V. The voltage higher than 4.0 V may help to promote more complete electrochemical activation of Li-excess layered cathodes but results in deteriorative polarization in electrodes due to severe decomposition of electrolyte and continuous formation of SEI film. On the other hand, the full battery can be charged down to 0.1 V because of the low discharge voltage of Li-excess layered cathode material and high charge voltage of carbonate anode material, contributing to high capacity in such full battery. Figure 7.8c shows charge/discharge CP curves of full LMNCO YS/$MNCCO_3$ MS battery at 0.1 *C* in the optimal voltage range of 0.1 - 4.0 V, which delivers a high practical discharge capacity above 250 mAh/g in the first five cycles, much higher than those reported for full lithium or sodium ion batteries based on various electrode materials [44-47]. The CV curves in Figure 7.8d reveal desirable compatibility of Li-excess layered cathode material and ternary transition metal carbonate anode in a full cell cycled in a voltage range of 0.1 - 4.0 V in the first three cycles, consistent with charge/discharge curves. In comparison with shaper anodic peaks, broad cathodic peak even across the whole voltage range indicates more complex potential matching between cathode and anode during discharge process. In addition, as shown in Figure 7.6f and Figure 7.7, the unavoidable formation of spinel phase within the cycled Li-excess layered cathode materials lowers the operating voltage of LMNCO YS cathode, which may account for rapid capacity degradation of LMNCO YS/$MNCCO_3$ MS full battery during the first twenty cycles (Figure 7.8e). Overall, more research efforts are deserved to understand the compatibility of carbonate anode and Li-excess cathode for high-capacity full lithium-ion batteries.

7.5 Conclusions

High-capacity lithium-ion full battery has been fabricated, in which multi-shell spherical ternary manganese-nickel-cobalt carbonate compound serves as anode material and yolk-shell-structured Li-excess layered oxide as cathode material, respectively. It is found that nanoarchitecture of these electrode materials contributes to higher practical capacity, better cycleability and rate capability than those of

monodispersed carbonate anode and Li-excess cathode materials. Ternary transition metal carbonate in multi-shell structure has demonstrated as a promising anode material that can be used in lithium-ion batteries, which delivers a remarkably high initial charge capacity of 1173.1 mAh/g at a specific current of 25 mA/g possibly due to extra capacity contribution from its nanoarchitecture, as well as improved cycling stability and rate capability in comparison with monodispersed carbonate microspheres. Such versatile carbonate allows for preparing Li-containing cathode materials via lithiation. Yolk-shell structure is obtained in the derived Li-excess layered cathode material after lithiating carbonate precursor; remarkable cycling and rate performance in nanoarchitectured cathode are also observed in contrast to those of well-dispersed nanoparticles. It should be noted that formation of spinel phase in Li-excess layered cathode materials during electrochemical cycling is favorable for enhanced cycling stability of cathode. Therefore, a full battery cell consisting of nanostructured transition metal carbonate anode and Li-excess cathode yields the high capacity output above 250 mAh/g in a selected voltage range of 0.1 - 4.0 V. This work may also be able to shed light on understanding high-capacity anodes with similar lithium storage reaction mechanism and/or operating voltage range, such as silicon, tin oxides and transition metal oxides, and how they work together with the emerging high-capacity Li-excess layered cathode material in new-generation full lithium ion batteries.

7.6 References

1. J. B. Goodenough, K. S. Park, The Li-ion Rechargeable Battery: A Perspective. *Journal of American Chemical Society* 135 (2013) 1167-1176.

2. J. Xu, S. Dou, H. Liu and L. Dai, Cathode materials for next generation lithium ion batteries. *Nano Energy*, 2 (2013) 439-442.

3. P. He, H. Yu, D. Li, H. Zhou, Layered Lithium Transition Metal Oxide Cathodes towards High Energy Lithium-Ion Batteries. *Journal of Materials Chemistry* 22 (2012) 3680-3695.

4. M. V. Reddy, G. V. Subba Rao, B. V. Chowdari, Metal Oxides and Oxysalts as Anode Materials for Li Ion Batteries. *Chemical Reviews* 113 (2013) 5364-5457.

5. R. Mukherjee, R. Krishnan, T. M. Lu, N. Koratkar, Nanostructured Electrodes for High-Power Lithium Ion Batteries. *Nano Energy* 1 (2012) 518-533.

6. O. K. Park, Y. Cho, S. Lee, H. C. Yoo, H.-K. Song, J. Cho, Who Will Drive Electric Vehicles, Olivine or Spinel? *Energy & Environmental Science* 4 (2011) 1621-1633.

7. Q. Zhang, E. Uchaker, S. L. Candelaria, G. Cao, Nanomaterials for Energy Conversion and Storage. *Chemical Society Reviews* 42 (2013) 3127-3171.

8. M. J. Aragón, C. Pérez-Vicente, J. L. Tirado, Submicronic Particles of Manganese Carbonate Prepared in Reverse Micelles: A New Electrode Material for Lithium-Ion Batteries. *Electrochemical Communications* 9 (2007) 1744-1748.

9. S. Mirhashemihaghighi, B. Leon, C. Perez Vicente, J. L. Tirado, R. Stoyanova, M. Yoncheva, E. Zhecheva, R. Saez Puche, E. M. Arroyo, J. Romero de Paz, Lithium Storage Mechanisms and Effect of Partial Cobalt Substitution in Manganese Carbonate Electrodes. *Inorganic Chemistry* 51 (2012) 5554-5560.

10. L. Shao, R. Ma, K. Wu, M. Shui, M. Lao, D. Wang, N. Long, Y. Ren, J. Shu, Metal Carbonates as Anode Materials for Lithium Ion Batteries. *Journal of Alloys Compounds* 581 (2013) 602-609.

11. M. J. Aragón, B. León, C. Pérez Vicente, J. L. Tirado, A New Form of Manganese Carbonate for the Negative Electrode of Lithium-Ion Batteries. *Journal of Power Sources* 196 (2011) 2863-2866.

12. L. Su, Z. Zhou, X. Qin, Q. Tang, D. Wu, P. Shen, $CoCO_3$ Submicrocube/Graphene Composites with High Lithium Storage Capability. *Nano Energy* 2 (2013) 276-282.

13. Y. Zhong, L. Su, M. Yang, J. Wei, Z. Zhou, Rambutan-Like $FeCO_3$ Hollow Microspheres: Facile Preparation and Superior Lithium Storage Performances. *ACS Applied Materials & Interfaces* 5 (2013) 11212-11217.

14. S. Laruelle, S. Grugeon, P. Poizot, M. Dolle´, L. Dupont, J-M. Tarascon, On the Origin of the Extra Electrochemical Capacity Displayed by MO/Li Cells at Low Potential. *Journal of The Electrochemical Society*149 (2002) A627-A634.

15. X. Xiao, J. Lu, Y. Li, $LiMn_2O_4$ Microspheres: Synthesis, Characterization and Use as a Cathode in Lithium Ion Batteries. *Nano Research* 3 (2010) 733-737.

16. J. Zhang, X. Guo, S. Yao, W. Zhu, X. Qiu, Tailored Synthesis of $Ni_{0.25}Mn_{0.75}CO_3$ Spherical Precursors for High Capacity Li-Rich Cathode Materials via a Urea-Based Precipitation Method. *Journal of Power Sources* 238 (2013) 245-250.

17. S. T. Myung, K. S. Lee, D. W. Kim, B. Scrosati, Y. K. Sun, Spherical Core-Shell $Li[(Li_{0.05}Mn_{0.95})_{0.8}(Ni_{0.25}Mn_{0.75})_{0.2}]_2O_4$ Spinels as High Performance Cathodes for Lithium Batteries. *Energy & Environmental Science* 4 (2011) 935-939.

18. B. Xu, C. R. Fell, M. Chi, Y. S. Meng, Identifying Surface Structural Changes in Layered Li-Excess Nickel Manganese Oxides in High Voltage Lithium Ion Batteries: A Joint Experimental and Theoretical Study. *Energy & Environmental Science* 4 (2011) 2223-2233.

19. F. Amalraj, D. Kovacheva, M. Talianker, L. Zeiri, J. Grinblat, N. Leifer, G. Goobes, B. Markovsky, D. Aurbach, Synthesis of Integrated Cathode Materials $xLi_2MnO_3 \cdot (1-x)\, LiMn_{1/3}Ni_{1/3}Co_{1/3}O_2$ $(x = 0.3\,,\, 0.5\,,\, 0.7)$ and Studies of Their Electrochemical Behavior. *Journal of The Electrochemical Society* 157 (2010) A1121-A1130.

20. N. Yabuuchi, K. Yoshii, S. T. Myung, I. Nakai, S. Komaba, Detailed Studies of a High-Capacity Electrode Material for Rechargeable Batteries, Li_2MnO_3-$LiCo_{1/3}Ni_{1/3}Mn_{1/3}O_2$. *Journal of The American Chemical Society* 133 (2011) 4404-4419.

21. K. A. Jarvis, Z. Deng, L. F. Allard, A. Manthiram, P. J. Ferreira, Atomic Structure of a Lithium-Rich Layered Oxide Material for Lithium-Ion Batteries: Evidence of a Solid Solution. *Chemistry of Materials* 23 (2011) 3614-3621.

22. E. S. Lee, A. Huq, H. Y. Chang, A. Manthiram, High-Voltage, High-Energy Layered-Spinel Composite Cathodes with Superior Cycle Life for Lithium-Ion Batteries. *Chemistry of Materials* 24 (2012) 600-612.

23. D. Wang, I. Belharouak, G. Zhou, K. Amine, Nanoarchitecture Multi-Structural Cathode Materials for High Capacity Lithium Batteries. *Advanced Functional Materials* 23 (2013)1070-1075.

24. B. Song, H. Liu, Z. Liu, P. Xiao, M. On Lai, L. Lu, High Rate Capability Caused by Surface Cubic Spinels in Li-Rich Layer-Structured Cathodes for Li-Ion Batteries. *Scientific Reports* 3 (2013) 3094.

25. B. Song, M. O. Lai, Z. Liu, H. Liu, L. Lu, Graphene-Based Surface Modification on Layered Li-Rich Cathode for High-Performance Li-Ion Batteries. *Journal of Materials Chemistry A* 1 (2013) 9954-9965.

26. M. Gu, I. Belharouak, J. Zheng, H. Wu, J. Xiao, A. Genc, K. Amine, S.Thevuthasan, D. R. Baer, J. G. Zhang, N. D. Browning, J. Liu, C. Wang, Formation of the Spinel Phase in the Layered Composite Cathode Used in Li-Ion Batteries. *ACS Nano* 7 (2013) 760-767.

27. B. Qiu, J. Wang, Y. Xia, Y. Liu, L. Qin, X. Yao, Z. Liu, Effects of Na^+ Contents on Electrochemical Properties of $Li_{1.2}Ni_{0.13}Co_{0.13}Mn_{0.54}O_2$ Cathode Materials. *Journal of Power Sources* 240 (2013) 530-535.

28. S. H. Yu, T. Yoon, J. Mun, S. Park, Y. S. Kang, J. H. Park, S. M. Oh, Y. E. Sung, Continuous Activation of Li_2MnO_3 Component upon Cycling in $Li_{1.167}Ni_{0.233}Co_{0.100}Mn_{0.467}Mo_{0.033}O_2$ Cathode Material for Lithium Ion Batteries. *Journal of Materials Chemistry A* 1 (2013) 2833-2839

29. C. R. Fell, D. Qian, K. J. Carroll, M. Chi, J. L. Jones, Y. S. Meng, Correlation between Oxygen Vacancy, Microstrain, and Cation Distribution in Lithium-Eexcess Layered Oxides during the First Electrochemical Cycle. *Chemistry of Materials* 25 (2013) 1621-1629.

30. Y. Cho, S. Lee, Y. Lee, T. Hong, J. Cho, Spinel-Layered Core-Shell Cathode Materials for Li-Ion Batteries. *Advanced Energy Materials* 1 (2011) 821-828.

31. L. Xi, C. Cao, R. Ma, Y. Wang, S. Yang, J. Deng, M. Gao, F. Lian, Z. Lu, C. Y. Chung, Layered $Li_2MnO_3 \cdot 3LiNi_{(0.5-x)}Mn_{(0.5-x)}Co_{(2x)}O_2$ Microspheres with Mn-Rich Cores as High Performance Cathode Materials for Lithium Ion Batteries. *Physical Chemistry Chemical Physics*, 2013, 15, 16579-16585.

32. J. Zhao, S. Aziz, Y. Wang, Hierarchical Functional Layers on High-Capacity Lithium-Excess Cathodes for Superior Lithium Ion Batteries. *Journal of Power Sources* 247 (2014) 95-104.

33. S. L. Candelaria, Y. Shao, W. Zhou, X. Li, J. Xiao, J. Zhang, Y. Wang, J. Liu, J. Li, G. Cao, Nanostructured carbon for energy storage and conversion. *Nano Energy* 1 (2012) 195-220.

34. Y. K. Sun, Z. Chen, H. J. Noh, D. J. Lee, H. G. Jung, Y. Ren, S. Wang, C. S.Yoon, S. T. Myung, K. Amine, Nanostructured High-Energy Cathode Materials for Advanced Lithium Batteries. *Nature Materials* 11 (2012) 942-947.

35. S. Xiong, C. Yuan, X. Zhang, B. Xi, Y. Qian, Controllable Synthesis of Mesoporous Co_3O_4 Nanostructures with Tunable Morphology for Application in Supercapacitors. *Chemistry- A European Journal* 15 (2009) 5320-5326.

36. X. Lai, J. E. Halpert, D. Wang, Recent Advances in Micro-/Nano-Structured Hollow Spheres for Energy Applications: From Simple to Complex Systems *Energy & Environmental Science* 5 2012 5604-5618.

37. A. Q. Pan, H. B. Wu, L. Zhang, X. W. Lou, Uniform V_2O_5 Nanosheet-Assembled Hollow Microflowers with Excellent Lithium Storage Properties. *Energy & Environmental Science* 6 (2013) 1476-1479.

38. X. Rui, H. Tan, D. Sim, W. Liu, C. Xu, H. H. Hng, R. Yazami, T. M. Lim, Q. Yan, Template-Free Synthesis of Urchin-like Co_3O_4 Hollow Spheres with Good Lithium Storage Properties. *Journal of Power Sources* 222 (2013) 97-102.

39. X. Xu, Y. Z. Luo, L. Q. Mai, Y.-L. Zhao, Q. Y. An, L. Xu, F. Hu, L. Zhang, Q. J. Zhang, Topotactically Synthesized Ultralong LiV_3O_8 Nanowire Cathode Materials for High-Rate and Long-Life Rechargeable Lithium Batteries. *NPG Asia Materials*, 4 (2012) e20.

40. L. Yu, H. B. Wu and X. W. Lou, Mesoporous $Li_4Ti_5O_{12}$ Hollow Spheres with Enhanced Lithium Storage Capability. *Advanced Materials* 25 (2013) 2296-2300.

41. Q. Sun, X. Q. Zhang, F. Han, W. C. Li, A. H. Lu, Controlled Hydrothermal Synthesis of 1D Nanocarbons by Surfactant-Templated Assembly for Use as Anodes for Rechargeable Lithium-Ion Batteries. *Journal of Materials Chemistry* 22 (2012) 17049-17054.

42. A. Boulineau, L. Simonin, J.-F.Colin, E. Canévet, L. Daniel, S. Patoux, Evolutions of $Li_{1.2}Mn_{0.61}Ni_{0.18}Mg_{0.01}O_2$ during the Initial Charge/Discharge Cycle Studied by Advanced Electron Microscopy. *Chemistry of Materials* 24 (2012) 3558-3566.

43. M. N. Ates, Q. Jia, A. Shah, A. Busnaina, S. Mukerjee, K. M. Abraham, Mitigation of Layered to Spinel Conversion of A Li-Rich Layered Metal Oxide Cathode Material for Li-Ion Batteries. *Journal of The Electrochemical Society* 161 (2013) A290-A301.

44. S. M. Oh, S. T. Myung, C. S. Yoon, J. Lu, J. Hassoun, B. Scrosati, K. Amine, Y. K. Sun, Advanced $Na[Ni_{0.25}Fe_{0.5}Mn_{0.25}]O_2$/C-$Fe_3O_4$ Sodium-Ion Batteries Using EMS Electrolyte for Energy Storage. *Nano Letters* 14 (2014) 1620-1626.

45. Y. Wang, Y. Wang, D. Jia, Z. Peng, Y. Xia, G. Zheng, All-Nanowire Based Li-Ion Full Cells Using Homologous Mn_2O_3 and $LiMn_2O_4$. *Nano Letters* 14 (2014) 1080-1084.

46. L. J. Xi, H. K. Wang, S. L. Yang, R. G. Ma, Z. G. Lu, C. W. Cao, K. L. Leung, J. Q. Deng, A. L. Rogach, C. Y. Chung, Single-Crystalline $Li_4Ti_5O_{12}$ Nanorods and Their Application in High Rate Capability $Li_4Ti_5O_{12}$/$LiMn_2O_4$ Full Cells. *Journal of Power Sources* 242 (2013) 222-229.

47. C. Chae, H. Park, D. Kim, J. Kim, E.-S. Oh, J. K. Lee, A Li-ion battery using LiMn2O4 cathode and MnOx/C anode. *Journal of Power Sources* 244 (2013) 214-221.

CHAPTER 8. CONCLUSIONS

In this dissertation, two strategies have been developed to significantly improve the electrochemical performance of cathode materials for lithium-ion batteries: One is surface modifications of $LiMn_2O_4$ cathodes by depositing ultrathin and conformal amphoteric oxides via atomic layer deposition (ALD) to enhance elevated-temperature performance of lithium-ion batteries; the other is to synthesize and modify emerging Li-excess layered $Li[Li_{0.2}Mn_{0.54}Ni_{0.13}Co_{0.13}]O_2$ cathode material for high-energy and high-power lithium-ion batteries.

To enhance cycling stability of $LiMn_2O_4$ especially at elevated temperature, we use atomic layer deposition (ALD) method to deposit ultra-thin and highly-conformal ZnO coatings (as thin as 0.34-1.7 nm) onto $LiMn_2O_4$ cathodes with precise thickness-control at atomic scale. We prepare two types of ALD-modified electrodes: one is electrode composed of ALD-coated $LiMn_2O_4$ particles and uncoated carbon/poly-vinylidenefluoride (PVDF) network, the other is ALD-coated $LiMn_2O_4$ composite electrode. All ALD-modified $LiMn_2O_4$ electrodes demonstrate significantly enhanced cycling performances than bare electrodes at both 25°C and 55°C. In particular, the electrode coated with 6 ZnO ALD layers (1.02 nm thick) shows the best cycling performances among electrodes coated with ALD films of different thicknesses at both 25°C and 55°C, indicating cycling performances of coated electrodes can be easily optimized by accurately tuning coating thickness via varying ALD growth cycles. Furthermore, electrode consisting of $LiMn_2O_4$ particles coated with 6 ZnO ALD layers and uncoated carbon/PVDF network shows even better electrochemical performances than electrode coated with 6 ZnO ALD layers at both 25°C and 55°C. The enhanced electrochemical performances of ALD-coated cathodes are ascribed to the high-quality ALD coatings that are highly-conformal, dense, complete, and thus effectively protect active material from Mn dissolution especially at elevated temperature.

Apart from ZnO coating, ultrathin crystalline ZrO_2 nanofilm has been facilely deposited on $LiMn_2O_4$ micron-sized particles at 120^{o}C using atomic layer deposition (ALD). The ZrO_2 coating shows high crystallinity, conformality and homogeneity, which contribute to considerably improved electrochemical performance of $LiMn_2O_4$ at elevated temperature in lithium-ion batteries. Furthermore, epitaxial ZrO_2 coating on $LiMn_2O_4$ nanoparticles using ALD also shows high conformality, uniformity and precise thickness control at atomic scale. The thickness of ZrO_2 coating can be precisely tailored at 2 Å per ALD cycle. Cycling performance of ZrO_2 ALD-modified $LiMn_2O_4$ cathode material is optimized by tuning the coating thickness via varying ALD growth cycles. The optimal thickness of ZrO_2 coating for maximized electrochemical performance of $LiMn_2O_4$ is ~1.2 nm grown via 6 ZrO_2 ALD layers. $LiMn_2O_4$ nanoparticles coated with 6 ZrO_2 ALD layers deliver a very high initial discharge capacity of 136.0 mAh/g at 1*C* (1*C* = 120 mA/g) at 55°C, significantly higher than that of bare $LiMn_2O_4$ (124.1 mAh/g). The effect of ZrO_2 ALD coating on improving capacity retention of $LiMn_2O_4$ is even more distinct at high charge/discharge rate at elevated temperature. $LiMn_2O_4$ nanoparticles coated with 6

ZrO_2 ALD layers after heat treatment retain a discharge capacity of 90.3 mAh/g after 100 cycles at 5*C* at 55°C, while bare $LiMn_2O_4$ nanoparticles exhibit a final capacity of 58.8 mAh/g. ZrO_2-ALD-modified $LiMn_2O_4$ nanoparticles show significantly improved specific capacity and enhanced cycleability at high rate at elevated temperature due to the protective effect of ultrathin and high-quality ALD surface coatings.

Compared to common $LiMn_2O_4$ cathode material, Li-excess layered transition metal oxides are emerging cathode materials with much higher theoretical capacities but suffering from drastic initial capacity loss and poor rate capability. A representative example is $Li[Li_{0.2}Mn_{0.54}Ni_{0.13}Co_{0.13}]O_2$ in this family. Novel synthesis and surface modifications are also used to enhance its cycleability and rate capability. Li-excess layered $Li[Li_{0.2}Mn_{0.54}Ni_{0.13}Co_{0.13}]O_2$ nanoparticles are facilely synthesized using a surfactant-assisted dispersion method. Ultrathin and conformal oxide coatings are deposited on the surface of individual $Li[Li_{0.2}Mn_{0.54}Ni_{0.13}Co_{0.13}]O_2$ nanoparticles via atomic layer deposition (ALD). The effect of oxide ALD coatings on improving electrochemical performance of LMNCO electrodes is evaluated and optimized via tuning the coating thickness and composition. In addition, we synthesize a novel core-shell structure cathode consisting of Li-excess LMNCO as core and Li-stoichiometric material as shell, and its electrochemical property is optimized by tailoring weight content and composition of shell materials. Finally, electrochemical performance of Li-excess cathode material can be maximized by surface modification with hierarchical functional layers composed of 10 wt.% $LiCoO_2$ shell (~10 nm thick) and 6 ZrO_2 ALD layers (~1 nm thick), which delivers very high initial discharge capacities of 296.4, 259.8, 156.6 and 104.2 mAh/g at 0.1*C*, 1*C*, 5*C*and 10*C*, and can retain 184.0 mAh/g at 1*C* (1*C* = 250 mA/g) after 100 electrochemical cycles. Such remarkably improved cycleabilitiy and rate capability of nanoarchitected Li-excess layered cathode material can be attributed to the synergic effect from hierarchical functional coatings to reduce electrochemical polarization, structural degradation and side reactions during electrochemical cycling.

Aside from nanostructure synthesis and surface modifications, another new approach has been developed to intentionally induce phase transition of emerging Li-excess layered cathode materials for applications in high-performance lithium ion batteries. In highly contrast to the limited layered-to-spinel phase transformation occurred during in-situ electrochemical cycles, we completely convert the Li-excess layered $Li[Li_{0.2}Mn_{0.54}Ni_{0.13}Co_{0.13}]O_2$ to a $Li_4Mn_5O_{12}$-type spinel product by first replacing lithium ions with protons in aqueous acid, and further substitution of embedded protons by TBA^+ ions under violent vortex, followed by a post-annealing at 500°C in air. Both Li_2MnO_3 and $LiMn_{1/3}Ni_{1/3}Co_{1/3}O_2$ components in the layered structure of $Li[Li_{0.2}Mn_{0.54}Ni_{0.13}Co_{0.13}]O_2$ undergo phase transformation from the original layered to the newly-formed spinel phase with a mesoporous structure. Such a layered-to-spinel phase conversion is demonstrated by using in-situ XRD and in-situ HRTEM. It is suggested that the generation of sufficient lithium ion vacancies within the Li-excess transition metal oxides at a time is critical for such a complete phase evolution. The newly-formed spinel material exhibits initial discharge capacities of

313.6, 267.2, 204.0 and 126.3 $mAhg^{-1}$ when cycled at 0.1, 0.5, 1 and 5 *C* (1*C* = 250 mA/g), respectively, and can retain a specific capacity of 197.5 mAh/g at 1*C* after 100 electrochemical cycles, demonstrating remarkably improved rate capability and cycling stability in comparison with the original Li-excess layered cathode materials. This work sheds light on fundamental understanding of phase transitions within Li-excess layered oxides, and provides a novel route for tailoring and maximizing electrochemical performance of Li-excess layered cathode materials for next-generation lithium ion batteries.

In addition to cathode materials, synthesis of novel anode material is also explored for new-generation lithium-ion batteries. A full lithium-ion battery cell has been assembled based on nanoarchitectured ternary manganese-nickel-cobalt compounds, in which multi-shell spherical $Mn_{0.54}Ni_{0.13}Co_{0.13}(CO_3)_{0.8}$ serves as anode and the subsequently lithiated Li-excess $Li[Li_{0.2}Mn_{0.54}Ni_{0.13}Co_{0.13}]O_2$ with a yolk-shell structure acts as cathode. Performance of a lithium-ion full battery significantly relies on electrochemical properties of both anode and cathode materials. Multi-shell carbonate anode is first tested in a half battery cell with metallic lithium as the counter electrode, revealing an unexpectedly high initial charge capacity of 1173.1 mAh/g at a specific current of 25 mA/g, which is twice higher than its theoretical capacity. Moreover, when cycled at 250 mA/g for 100 electrochemical cycles, this carbonate anode retains a final specific capacity of 434.6 mAh/g. Accordingly, yolk-shell-structured Li-excess layered cathode material has been facilely obtained through lithiation of carbonate compound, showing an initial discharge capacity of 250.7 mAh/g when cycled at 0.1 *C* (1*C* = 250 mA/g) in a half battery cell. Furthermore, this cathode retains a final capacity of 156.3 mAh/g at 1 *C* after 100 cycles and exhibits outstanding capacity retention of 90.3%. Such remarkable electrochemical properties of carbonate anode and Li-excess oxide cathode materials are attributed to their nanoarchitectures resulted from water-based solvothermal process, i.e., multi-shell and yolk-shell structures composed of numerous primary nanoparticles, in comparison with mediocre performances from monodispersive carbonate microspheres and Li-excess oxide nanoparticles synthesized via ethylene-glycol-based solvothermal method. Combination of nanostructured ternary transition metal carbonate anode and Li-excess layered cathode into a full lithium ion battery results in a remarkable specific capacity above 250 mAh/g at 0.1 *C* in a voltage range of 0.1 - 4.0 V, which demonstrates as a very promising electrochemical device for future energy conversion and storage.

In conclusion, this dissertation work provides various strategies to achieve desirable electrochemical performances of electrode materials for new-generation lithium-ion batteries. The advanced ALD technique is very effective on improving cycling performance of Mn-based spinel cathode materials. Fabrication of nanostructured electrode materials contributes to higher capacity and enhanced rate capability of both cathode and anode materials. Synthesis of nanostructured Li-excess layered cathode material and its surface modifications alleviate its initial capacity loss and improve its rate capability significantly for applications in superior lithium-ion batteries. In addition, the layered-to-spinel phase transition in Li-excess cathode

material is better understood by intentionally and controllably inducing the phase conversion via novel ex-situ ion exchange processes. More importantly, the resultant spinel product shows even better electrochemical performance than the original Li-excess layered cathode material. As such, combination of cathode and anode materials in this work would lead to high-energy high-power full battery cells worthy of future explorations. In-situ characterizations are expected to be used in future work for studying fundamental mechanisms of capacity fading when a full lithium-ion battery is subjected to electrochemical cycling. Research aspects to explore include volume changes, structural degradations and phase evolutions of electrode materials, caused by reaction strains during lithium intercalation and deinterclation processes.

APPENDIX: LETTERS OF COPYRIGHT PERMISSION

1. Permission of using published materials from publisher of Elsevier (Journal of Power Sources)

This is a License Agreement between Jianqing Zhao ("You") and Elsevier ("Elsevier") provided by Copyright Clearance Center ("CCC"). The license consists of your order details, the terms and conditions provided by Elsevier, and the payment terms and conditions.

All payments must be made in full to CCC. For payment instructions, please see information listed at the bottom of this form.

License Number	3464421140956
License date	Sep 08, 2014
Licensed content publisher	Elsevier
Licensed content publication	Journal of Power Sources
Licensed content title	Hierarchical functional layers on high-capacity lithium-excess cathodes for superior lithium ion batteries
Licensed content author	Jianqing Zhao,Saad Aziz,Ying Wang
Licensed content date	1 February 2014
Licensed content volume number	247
Licensed content issue number	n/a
Number of pages	10
Type of Use	reuse in a thesis/dissertation
Portion	full article
Format	both print and electronic
Are you the author of this Elsevier article?	Yes
Will you be translating?	No
Title of your thesis/dissertation	NOVEL SYNTHESE AND SURFACE MODIFICATIONS OF ELETRODE MATERIALS FOR SUPERIOR LITHIUM-ION BATTERIES
Expected completion date	Dec 2014
Estimated size (number of pages)	150
Elsevier VAT number	GB 494 6272 12
Permissions price	0.00 USD
VAT/Local Sales Tax	0.00 USD / 0.00 GBP
Total	0.00 USD

2. Permission of using published materials from publisher of Elsevier (Nano Energy)

This is a License Agreement between Jianqing Zhao ("You") and Elsevier ("Elsevier") provided by Copyright Clearance Center ("CCC"). The license consists of your order details, the terms and conditions provided by Elsevier, and the payment terms and conditions.

All payments must be made in full to CCC. For payment instructions, please see information listed at the bottom of this form.

License Number	
License date	
Licensed content publisher	Elsevier
Licensed content publication	Nano Energy
Licensed content title	Atomic layer deposition of epitaxial ZrO_2 coating on $LiMn_2O_4$ nanoparticles for high-rate lithium ion batteries at elevated temperature
Licensed content author	Jianqing Zhao,Ying Wang
Licensed content date	September 2013
Licensed content volume number	2
Licensed content issue number	5
Number of pages	8
Type of Use	reuse in a thesis/dissertation
Portion	full article
Format	both print and electronic
Are you the author of this Elsevier article?	Yes
Will you be translating?	No
Title of your thesis/dissertation	NOVEL SYNTHESE AND SURFACE MODIFICATIONS OF ELETRODE MATERIALS FOR SUPERIOR LITHIUM-ION BATTERIES
Expected completion date	Dec 2014
Estimated size (number of pages)	150
Elsevier VAT number	GB 494 6272 12
Permissions price	0.00 USD
VAT/Local Sales Tax	0.00 USD / 0.00 GBP
Total	0.00 USD

3. Permission of using published materials from publisher of Royal Society of Chemistry (Chemical Communications, and Journal of Materials Chemistry A)

Reproduced by permission of The Royal Society of Chemistry (RSC) for the following two papers:

1. Jianqing Zhao, Guoying Qu, John C. Flake and Ying Wang, "Low Temperature Preparation of Crystalline ZrO2 Coatings for Improved Elevated-Temperature Performances of Li-ion Battery Cathodes", Chem. Comm., 48, 8108-8110 (2012). DOI: 10.1039/C2CC33522K
http://pubs.rsc.org/en/content/articlelanding/2012/cc/c2cc33522k#!divAbstract
2. J. Q. Zhao and Y. Wang, "High-Capacity Full Lithium-Ion Cells Based on Nanoarchitectured Ternary Manganese-Nickel-Cobalt Carbonate and Its Lithiated Derivative", J. Mater. Chem. A, 2, 14947-14956 (2014). DOI: 10.1039/C4TA02574A
http://pubs.rsc.org/en/content/articlelanding/2014/ta/c4ta02574a#!divAbstract

CONTRACTS-COPYRIGHT (Contracts-Copyright@rsc.org)
To jianqing Zhao (jzhao3@tigers.lsu.edu)

Dear Jianging Zhao

The Royal Society of Chemistry (RSC) hereby grants permission for the use of your paper(s) specified below in the printed and microfilm version of your thesis. You may also make available the PDF version of your paper(s) that the RSC sent to the corresponding author(s) of your paper(s) upon publication of the paper(s) in the following ways: in your thesis via any website that your university may have for the deposition of theses, via your university's Intranet or via your own personal website. We are however unable to grant you permission to include the PDF version of the paper(s) on its own in your institutional repository. The Royal Society of Chemistry is a signatory to the STM Guidelines on Permissions (available on request).

Please note that if the material specified below or any part of it appears with credit or acknowledgement to a third party then you must also secure permission from that third party before reproducing that material.

Please ensure that the thesis states the following:

Reproduced by permission of The Royal Society of Chemistry and include a link to the paper on the Royal Society of Chemistry's website.

Please ensure that your co-authors are aware that you are including the paper in your thesis.

Regards
Gill Cockhead

Publishing Contracts & Copyright Executive
Royal Society of Chemistry,
Thomas Graham House,
Science Park, Milton Road,
Cambridge, CB4 0WF, UK
Tel +44 (0) 1223 432134

-----Original Message-----
From: Jianqing Zhao [mailto:jzhao3@tigers.lsu.edu]
Sent: 08 September 2014 22:35
To: CONTRACTS-COPYRIGHT (shared)
Subject: Website Email: Permission of using my two published papers from publisher of Royal Society of Chemistry

To: Gill Cockhead
This Email was sent from the following rsc.org page:
/Publishing/copyright/permission-requests.asp

Dear Gill Cockhead,

This is Jianqing Zhao, a PhD student at Louisiana State University. I am writing here to request a permission of using my two published papers from Royal Society of Chemistry. So I can reproduce them in my dissertation.

The information of my two published papers in RSC is as follows:

1. Jianqing Zhao, Guoying Qu, John C. Flake and Ying Wang, "Low Temperature Preparation of Crystalline ZrO2 Coatings for Improved Elevated-Temperature Performances of Li-ion Battery Cathodes", Chem. Comm., 48, 8108-8110 (2012). DOI: 10.1039/C2CC33522K

2. Jianqing Zhao and Ying Wang, "High-Capacity Full Lithium-Ion Cells Based on Nanoarchitectured Ternary Manganese-Nickel-Cobalt Carbonate and Its Lithiated Derivative", J. Mater. Chem. A, 2, 14947-14956 (2014). DOI: 10.1039/C4TA02574A

Thank you very much for your time and work. Look forward to your response.

Best regards,

Jianqing Zhao

4. Permission of using published materials from publisher of Royal Society of Chemistry (Chemical Communications, and Journal of Materials Chemistry A)

Reproduced with permission from (Jianqing Zhao and Ying Wang, Ultrathin Surface Coatings for Improved Electrochemical Performance of Li-ion Battery Electrodes at Elevated Temperature", Journal of Physical Chemistry C, 116 (22), 11867-11876 (2012), DOI: 10.1021/jp3010629.). Copyright (2012) American Chemical Society.

EIC office (eic@jpc.acs.org)
To jzhao3@tigers.lsu.edu

Greetings;

Permission is granted with the understanding that the appropriate citations of the published work must be made.

Sincerely,

Davine for
George C. Schatz
Editor-in-Chief

From: jzhao3@tigers.lsu.edu [mailto:jzhao3@tigers.lsu.edu]
Sent: Monday, September 08, 2014 3:31 PM
To: eic@jpc.acs.org
Subject: Permission of using my published paper in JPCC for my dissertation

Dear Editor,

This is Jianqing Zhao, a PhD student at Louisiana State University. I am writing here to request a permission of using my published paper in The Journal of Physical and Chemistry C. So I can reproduce it in my dissertation.

The information of my published paper in JPCC is as follows:
Jianqing Zhao and Ying Wang, Ultrathin Surface Coatings for Improved Electrochemical Performance of Li-ion Battery Electrodes at Elevated Temperature", J. Phys. Chem. C, *116* (22), 11867-11876 (2012), DOI: 10.1021/jp3010629.

Thank you very much for your time and work. Look forward to your response.

Best regards,

Jianqing Zhao

VITA

Jianqing Zhao was born in Shangyun, Zhejiang province, China in 1983. He received his Bachelor's degree in Applied Chemistry from Nanjing University of Aeronautics and Astronautics (NUAA) in 2006. After his graduation, he worked at NUAA for two years as an undergraduate administrative coordinator in the College of Material Science and Technology. He continued his study and received his Master's degree in Applied Chemistry from the Graduate School of NUAA in 2011. Jianqing joined the doctoral program in the Department of Mechanical & Industrial Engineering at Louisiana State University (LSU) in the United States in 2011 and expects to receive the Degree of Philosophy in December 2014. His PhD research concentrates on novel synthesis and surface modifications of electrode materials at nanoscale and sub-nanoscale for superior lithium-ion batteries. Jianqing Zhao's professional publications in Ph.D. program at LSU are listed as follows:

1. Jianqing Zhao and Ying Wang, High-Capacity Full Lithium-Ion Cells Based on Nanoarchitectured Ternary Manganese-Nickel-Cobalt Carbonate and Its Lithiated Derivative. *Journal of Materials Chemistry A* 2 (2014) 14947-14956.
2. Jianqing Zhao and Ying Wang, "Hierarchical Functional Layers on High-Capacity Lithium-Excess Cathodes for Superior Lithium Ion Batteries", *Journal of Power Sources* 247 (2014) 95-104.
3. Saad Aziz*, Jianqing Zhao*, Carrington Cain and Ying Wang, Nanoarchitectured $LiMn_2O_4$/Graphene/ZnO Composites as Electrodes for Lithium Ion Batteries. *Journal of Materials Science & Technology* 30 (2014) 427-433. (*equal contribution)
4. Jianqing Zhao and Ying Wang, Atomic Layer Deposition of Epitaxial ZrO_2 Coating on $LiMn_2O_4$ Nanoparticles for High-Rate Lithium Ion Batteries at Elevated Temperature. *Nano Energy* 2 (2013) 882-889.
5. Jianqing Zhao and Ying Wang, Surface Modifications of Li-Ion Battery Electrodes with Various Ultrathin Amphoteric Oxide Coatings for Enhanced Cycleability. *J. Solid State Electrochemistry* 17 (2013)1049-1058.
6. Jianqing Zhao, Guoying Qu, John C. Flake and Ying Wang, Low Temperature Preparation of Crystalline ZrO_2 Coatings for Improved Elevated-Temperature Performances of Li-ion Battery Cathodes. *Chemical Communications* 48 (2012) 8108-8110.
7. Jianqing Zhao and Ying Wang, Ultrathin Surface Coatings for Improved Electrochemical Performance of Li-ion Battery Electrodes at Elevated Temperature. The *Journal of Physical Chemistry C* 116 (2012) 11867-11876.
8. Jianqing Zhao, Ruiming Huang, Wenpei Gao, Jian-Min Zuo, Xiaofeng Zhang, Scott T. Misture, Yuan Chen, Jenny Lockard, Boliang Zhang, Shengmin Guo, M. Reza Khoshi, Kerry Dooley, Huixin He, Ying Wang, Ion-Exchange Promoted Phase Transition in Li-Excess Layered Cathode Material for High-Performance Lithium-Ion Batteries. Submitted, (2014).